Eutectic modification of Al-Si casting alloys

Dissertation zur Erlangung des Grades

des Doktors der Ingenieurwissenschaften

der Naturwissenschaftlich-Technischen Fakultät

der Universität des Saarlandes

von

Jenifer Barrirero

Saarbrücken

2019

UNIVERSITÄT DES SAARLANDES   LiU LINKÖPING UNIVERSITY

Tag des Kolloquiums: 31.10.2019

Dekan: Prof. Dr. Guido Kickelbick

Berichterstatter:

Prof. Dr.-Ing. Frank Mücklich

Prof. Dr.-Ing. Hans-Georg Herrmann

Vorsitz: Prof. Dr. Guido Kickelbick

Akad. Mitarbeiter: PD Dr.-Ing. Dr. rer. nat. Anne Jung

Weitere Teilnehmer:

Prof. Dr. Magnus Odén

Prof. Dr.-Ing. Franz-Josef Feikus

PD Dr.-Ing. Michael Marx

ahora
      en esta hora inocente
yo y la que fui nos sentamos
en el umbral de mi mirada

Alejandra Pizarnik

Abstract

The change of microstructure of eutectic silicon from plate- to coral-like in Al-Si casting alloys is well known for enhancing their ductility. This is achieved by adding low concentrations of a modifying agent. Amongst the elements proposed as modifiers, only strontium, sodium and europium induce a plate-to-coral transition, while others such as ytterbium, only refine the silicon plates. The exact mechanism for the remarkable plate-to-coral change, and the reason why certain elements only refine the structure, is still not completely understood. In this investigation, atom probe tomography and transmission electron microscopy were used to analyze and compare the crystal structure and the distribution of solute atoms in silicon at the atomic level. An unmodified alloy and alloys modified by strontium, sodium, europium and ytterbium were studied. Elements inducing silicon plate-to-coral transition were found to contain nanometer sized clusters at the defects in silicon with stoichiometries corresponding to compounds formed at the ternary eutectic reaction of each system. In contrast ytterbium, that only refines the silicon plates, is unable to form clusters in silicon. It is propose that the formation of clusters of $AlSiNa$, Al_2Si_2Sr and Al_2Si_2Eu at the silicon/liquid interface during solidification restrict silicon growth and increase growth direction diversity. The incorporation of clusters explains the high density of crystallographic defects and the structural modification.

Zusammenfassung

Die Zugabe geringer Konzentrationen eines Veredelungselementes in Al-Si-Gusslegierungen führt zu einer für die Duktilität günstigen Morphologieänderung des eutektischen Silizium. Dabei bewirken die Veredelungselemente Strontium, Natrium und Europium einen Übergang von einer platten- zu einer korallenartigen Morphologie, während andere wie Ytterbium nur das Eutektikum verfeinern. Der zu Grunde liegende Mechanismus ist noch nicht vollständig verstanden. In dieser Arbeit wurden mit Hilfe der Atomsondentomographie und der Transmissionselektronenmikroskopie die Kristallstruktur und die Verteilung der im Silizium gelösten Atome auf atomarer Ebene analysiert und verglichen. Eine unveredelte und durch Strontium, Natrium, Europium und Ytterbium veredelte Legierungen wurden untersucht. Es zeigt sich, dass Elemente, die eine korallenartige Morphologie erzeugen (Strontium, Natrium und Europium), nanometergroße Cluster an Defekten in Silizium bilden, deren Stöchiometrien den Verbindungen aus ternären eutektischen Reaktionen des jeweiligen Systems entsprechen. Im Gegensatz dazu werden durch Zusatz von Ytterbium keine Cluster im Silizium gebildet. Es wird gezeigt, dass die Bildung von Clustern aus $AlSiNa$, Al_2Si_2Sr und Al_2Si_2Eu an der Grenzfläche Silizium/Schmelze während der Erstarrung das Siliziumwachstum einschränkt und die Zahl der Wachstumsrichtungen erhöht. Die Einlagerung von Clustern in Silizium erklärt dessen hohe Dichte an kristallographischen Defekten und die Morphologieänderung.

Popular Summary

Air pollution is one of the top environmental concerns. Cars are responsible for around 12% of the total CO_2 emissions in Europe. One way to reduce CO_2 emissions and fuel consumption is to reduce the mass of vehicles, also called light-weighting. Light-weighting also plays an important role in the developing electro-mobility branch compensating for the high weight of batteries and improving energy efficiency.

To significantly reduce the weight of a vehicle, we can focus on the materials' selection, for example, by replacing some steel or cast iron parts by light-weight aluminum parts. Aluminum has one third the density of iron allowing a reduction of up to 50% weight without compromising safety. This replacement is, however, not trivial. Strong and tough alloys based on aluminum need to be designed and optimized for this purpose.

The mechanical properties and, consequently, the performance of an alloy can be controlled and improved by designing their microscopic structure. In the aluminum-silicon (Al-Si) alloys studied in this investigation, for instance, silicon grows in aluminum in the form of hard and brittle plates that can act as crack propagation paths deteriorating the resistance to fracture of the material. To enhance ductility, the morphology of silicon can be modified to a coral-like structure by adding a modifying agent. Amongst the several elements that have been proposed as potential modifiers, only strontium, sodium and europium induce the plate-to-coral transition, while other elements such as ytterbium, only refine the silicon plates. Although this modification has been used at the industrial practice in the last decades, the exact underlying mechanism for the remarkable plate-to-coral change, and the reason why certain elements only refine the structure, is still not completely understood. This lack of knowledge hinders the control of the microstructure homogeneity in more complex alloys such as Al-Si-Mg and Al-Si-Mg-Cu.

The reason why this structural modification has not been completely understood, in spite of almost 100 years of heavy investigation, is that the key of the effect lies at an extremely small length-scale. Only now with the possibility of combining two characterization methods with spatial, structural and chemical resolutions down to the atomic scale, we are capable of gaining further understanding. Atom probe tomography and transmission electron microscopy among other methods, were used in this investigation for a detailed study of the distribution of atoms in the silicon crystal of Al-Si alloys. In alloys containing elements that transform the silicon structure from plates to corals (strontium, sodium and europium), groups of atoms with fixed compositional relationships, were found inside the silicon crystal. In contrast, with the addition of ytterbium, which only refines the silicon plates, no clusters of atoms in silicon were found. We propose that the formation of clusters during the solidification of the casting parts restrict the

silicon growth. These clusters lead to increased growth direction diversity, explaining the formation of a coral-like structure.

This new understanding contributes to the future control of the microstructure evolution of complex alloys at the industrial practice and the further enhancement and optimization of aluminum casting parts.

Populärvetenskaplig sammanfattning

Luftföroreningar är en av de viktigaste miljöfrågorna. I Europa står bilar för ungefär 12% av det totala utsläppet av CO_2. Ett sätt att minska bränsleförbrukning och CO_2-utsläpp är att minska fordonets massa, så kallade lättviktskonstruktioner. Lättviktskonstruktioner spelar också en viktig roll för elektrifieringen av transportsektorn genom att kompensera för batteriernas vikt och öka energieffektiviteten.

Vikten på ett fordon kan signifikant minskas genom materialvalen, t.ex. kan vissa stål- och gjutjärnskomponenter bytas mot lättviktskomponenter i aluminium. Aluminiums densitet är ca en tredjedel av järns vilket möjliggör en viktsreduktion på 50% utan att tumma på säkerheten. Detta byte av material är dock inte trivialt. Höghållfasta och sega legering av aluminium måste designas och optimeras för detta ändamål.

De mekaniska egenskaperna och följaktligen prestandan hos en legering kan kontrolleras och förbättras genom design av dess mikrostruktur. Till exempel, i de legeringar mellan aluminium och kisel (Al-Si) som studerats i denna avhandling så växer kislet in i aluminium och bildar hårda och spröda plattor som kan verka som spricktillväxtvägar som lättare ger upphov till materialbrott. För att öka segheten så kan kislets morfologi ändras till en koralliknade morfologi genom att tillsätta en modifierare. Av de många ämnen som föreslagits som möjliga modifierare är det endast strontium, natrium och europium som inducerar den eftertraktade övergången från plattor till koraller medans andra ämnen så som ytterbium endast förfinar kiselplattorna.Trots att denna modifiering har använts industriellt de senaste årtiondena så är fortfarande de underliggande mekanismerna för denna remarkabla förändring av plattorna inte förstådd. Avsaknaden av denna kunskap hindrar att oss från att kunna kontrollera mikrostrukturen hos mer komplexa legeringar så som Al-Si-Mg och Al-Si-Cu.

Orsaken till denna strukturförändring är ännu inte förstådd, trots nästan 100 år av studier. Det beror på att nyckeleffekterna återfinns på en extremt liten längdskala. Endast nu är det möjligt att kunna studera detta genom att kombinera två karakteriseringsmetoder som tillsammans ger nödvändig spatial, strukturell och kemisk upplösning, dvs på atomär nivå. Atomsond och transmissionselektronmikroskopi, jämte andra metoder, användes i denna avhandling för detaljerade studier av atomernas placering i kiselkristallerna i Al-Si legeringar. I legeringar innehållande ämnen som modifierar Si-strukturen (strontium, natrium och europium) hittades endast dessa ämnen grupperade till små områden i kiselkristallen med en och samma sammansättning, s.k. kluster. Det står i kontrast till de ämnen som enast förfinanade kiselplattorna där sådana kluster inte kunde hittas. Vi föreslår att bildandet av kluster under framställningsprocessen av de gjutna detaljerna begränsar tillväxten av kiselkristaller. Dessa

kluster leder till en större variation i tillväxtriktning som också förklarar bildandet av en koralliknande struktur.

Denna nya förståelse bidrar till en framtida kontroll av mikrostrukturutvecklingen av gjutna komplexa aluminiumlegeringar så att förbättrade och optimerade lättviktdetaljer kan framställas industriellt.

Vereinfachte Zusammenfassung

Die Luftverschmutzung ist eines der größten Umweltprobleme. Pkw sind für rund 12% der gesamten CO_2-Emissionen in Europa verantwortlich. Eine Möglichkeit, den Kraftstoffverbrauch und damit den CO_2-Ausstoß zu reduzieren, besteht darin, die Masse der Fahrzeuge zu reduzieren, was auch als Leichtbau bezeichnet wird. In der zunehmend an Bedeutung gewinnenden Elektromobilitätsbranche spielt der Leichtbau ebenfalls eine wichtige Rolle, da er das hohe Gewicht der Batterien kompensieren und damit die Energieeffizienz verbessern kann.

Eine deutliche Reduzierung des Fahrzeuggewichts ist durch eine geeignete Materialauswahl möglich, indem beispielsweise einige Stahl- oder Eisengussteile durch leichte Aluminiumteile ersetzt werden. Aluminium hat ein Drittel der Dichte von Eisen, was eine Gewichtsreduzierung von bis zu 50% ermöglicht, ohne die Sicherheit zu beeinträchtigen. Dieser Ersatz ist jedoch nicht trivial, da feste und zähe Legierungen auf Aluminiumbasis für diesen Zweck entwickelt und optimiert werden müssen.

Die mechanischen Eigenschaften und damit die Leistungsfähigkeit einer Legierung können durch die Gestaltung ihrer Mikrostruktur, dem Gefüge, kontrolliert und verbessert werden. In den in dieser Untersuchung untersuchten Aluminium-Silizium (Al-Si) -Legierungen liegt Silizium beispielsweise in Form von harten und spröden Platten im Aluminium vor, die als Rissausbreitungspfade fungieren können und die Bruchfestigkeit des Materials beeinträchtigen. Um die Duktilität zu erhöhen, kann die Morphologie des Siliziums durch Zugabe eines sogenannten Veredelungsmittels in eine korallenartige Struktur überführt werden. Unter den zahlreichen Elementen, die als potenzielle Veredelungselemente vorgeschlagen wurden, erzeugen nur Strontium, Natrium und Europium den Übergang von einer plattenförmigen zu einer korallenförmigen Morphologie, während andere Elemente wie Ytterbium nur die Siliziumplatten verfeinern. Obwohl diese Veredelung in den letzten Jahrzehnten in der industriellen Praxis angewendet wurde, ist der genaue zugrunde liegende Mechanismus für diese bemerkenswerten Morphologieänderung und der Grund, warum bestimmte Elemente die Struktur nur verfeinern, noch nicht vollständig verstanden. Dieses fehlende Wissen behindert die Kontrolle der Mikrostrukturhomogenität bei komplexeren Legierungen wie beispielsweise Al-Si-Mg und Al-Si-Mg-Cu.

Der Grund, warum diese Morphologieänderung trotz fast 100-jähriger intensiver Forschung nicht vollständig verstanden wurde, ist, dass sich die Ursache des Effekts auf einer extrem kleinen Längenskala abspielt. Erst heute sind wir durch die Kombination zweier Charakterisierungsmethoden mit räumlichen, strukturellen und chemischen Auflösungen bis in den atomaren Bereich in der Lage, dieses Verständnis zu erweitern. Die Atomsondentomographie und die Transmissionselektronenmikroskopie wurden in dieser Untersuchung unter anderem für

eine detaillierte Untersuchung der Atomverteilung in der Siliziumphase in Al-Si-Legierungen eingesetzt. In Legierungen mit Veredelungselementen die eine korallenförmige Morphologie des Siliziums erzeugen (Strontium, Natrium und Europium), wurden in der Siliziumphase Atomcluster mit festem Verhältnis der Zusammensetzung gefunden. Im Gegensatz dazu wurden bei der Zugabe von Ytterbium, das die Siliziumplatten nur verfeinert, keine Atomcluster im Silizium gefunden. Wir schlagen vor, dass die Bildung von Clustern während der Erstarrung der Gussteile das Siliziumwachstum behindert. Diese Cluster führen zu einer erhöhten Vielfalt der Wachstumsrichtungen und erklären damit die Bildung einer korallenartigen Struktur.

Dieses neue Verständnis trägt zur zukünftigen Steuerung der Mikrostruktur komplexer Legierungen in der industriellen Praxis und zur weiteren Verbesserung und Optimierung von Aluminiumgussteilen bei.

Preface

This thesis is the result of the Joint European Doctoral Program in Advanced Materials Science and Engineering - DocMASE. The work was accomplished in the Chair of Functional Materials at the University of Saarland, Saarbrücken, Germany; and in the group of Nanostructured Materials at the Department of Physics, Chemistry and Biology (IFM) of Linköping University, Linköping, Sweden.

Included papers

Paper I.

Comparison of segregations formed in unmodified and Sr-modified Al-Si alloys studied by atom probe tomography and transmission electron microscopy.

Barrirero J., Engstler M., Ghafoor N., de Jonge N., Odén M., & Mücklich F. *Journal of Alloys and Compounds*, *611*, 410–421 (2014). https://doi.org/10.1016/j.jallcom.2014.05.121

Paper II.

Cluster formation at the Si/liquid interface in Sr and Na modified Al–Si alloys.

Barrirero J., Li J., Engstler M., Ghafoor N., Schumacher P., Odén M., & Mücklich F. *Scripta Materialia*, *117*, 16–19 (2016). https://doi.org/10.1016/j.scriptamat.2016.02.018

Paper III.

Eutectic modification by ternary compound cluster formation in Al-Si alloys.

Barrirero J., Pauly C., Engstler M., Ghanbaja J., Ghafoor N., Li J., Schumacher P., Odén M., & Mücklich F. *Scientific Reports 9*, 1-10 (2019). https://doi.org/10.1038/s41598-019-41919-2

Paper IV.

Nucleation and Growth of Eutectic Si in Al-Si Alloys with Na Addition.

Li J. H. H., Barrirero J., Engstler M., Aboulfadl H., Mücklich F., & Schumacher P. *Metallurgical and Materials Transactions A*, *46*(3), 1300–1311 (2014). https://doi.org/10.1007/s11661-014-2702-6

Paper V.

Phase selective sample preparation of Al-Si alloys for Atom Probe Tomography.

Barrirero J., Engstler M., Odén M., Mücklich F. *Practical Metallography, 56(2), 76 - 90* (2019) https://doi.org/10.3139/147.110557

My contribution to the papers

Paper I.

I was responsible for the planning of the project, prepared the samples for SEM / FIB, EBSD, APT and TEM. I performed the APT and EBSD measurements and analyses and participated in the TEM analysis. I wrote the first draft of the paper and was in charge of the submission and revision processes.

Paper II.

I was responsible for the planning of the project, prepared the samples for SEM / FIB, APT and TEM. I performed the APT measurements and analyses and participated in the TEM analysis. I wrote the first draft of the paper and was in charge of the submission and revision processes.

Paper III.

I was responsible for the planning of the project, prepared the samples for SEM / FIB, EBSD, APT and TEM. I performed the APT and EBSD measurements and analyses and participated in the TEM. I wrote the first draft of the paper and was in charge of the submission and revision processes.

Paper IV.

I prepared the samples for APT. I performed the APT measurements and analyses. I contributed to the writing of the paper.

Paper V.

I developed the method, prepared the samples, and applied it successfully in my work. I wrote the first draft of the paper and was in charge of the submission and revision processes.

Other papers not included in the thesis

Barrirero J, Engstler M, Mücklich F. Atom Probe analysis of Sr distribution in AlSi foundry alloys. In: *Light Metals 2013 - TMS*. ; 2013:291-296. doi:10.1002/9781118663189.ch50.

Liang S-M, Engstler M, Groten V, Barrirero J, Mücklich F, Bührig-Polaczek A, Schmid-Fetzer R. Key experiments and thermodynamic revision of the binary Al–Sr system. *J Alloys Compd*. 2014;610:443-450. doi:10.1016/j.jallcom.2014.05.018.

Mücklich F, Engstler M, Britz D, Barrirero J, Rossi P. Why We Need All Dimensions to Solve Both Very Old and Very New Questions in Materials at the Micro-, Nano- and Atomic Scales. *Pract Metallogr*. 2015;52(9):507-524. doi:10.3139/147.110360.

Li JH, Barrirero J, Sha G, Aboulfadl H, Mücklich F, Schumacher P. Precipitation hardening of an Mg–5Zn–2Gd–0.4Zr (wt. %) alloy. *Acta Mater*. 2016;108:207-218. doi:10.1016/j.actamat.2016.01.053.

Shulumba N, Hellman O, Raza Z, Alling B, Barrirero J, Mücklich F, Abrikosov I A, Odén M. Lattice Vibrations Change the Solid Solubility of an Alloy at High Temperatures. *Phys Rev Lett*. 2016;117(20):205502. doi:10.1103/PhysRevLett.117.205502.

Yalamanchili K, Wang F, Aboulfadl H, Barrirero J, Rogström L, Jiménez-Pique E, Mücklich F, Tasnadi F, Odén M, Ghafoor N. Growth and thermal stability of TiN/ZrAlN: Effect of internal interfaces. *Acta Mater*. 2016;121:396-406. doi:10.1016/j.actamat.2016.07.006.

Menezes CM, Bogoni N, Barrirero J, Aboulfadl H, Mücklich F, Figueroa CA. Influence of the surface chemistry-structure relationship on the nanoscale friction of nitrided and post-oxidized iron. *Surf Coatings Technol*. 2016;308:220-225. doi:10.1016/j.surfcoat.2016.07.095.

Roa JJ, Aboulfadl H, Barrirero J, Turon-Vinas M, Mücklich F, Anglada M. Chemical segregation in a 12Ce-ZrO 2 /3Y-ZrO 2 ceramic composite. *Mater Charact*. 2017;132:83-91. doi:10.1016/j.matchar.2017.07.045.

Calamba KM, Pierson JF, Bruyère S, Febvrier AL, Eklund P, Barrirero J, Mücklich F, Boyd R, Johansson Jõesaar MP, Odén M. Dislocation structure and microstrain evolution during spinodal decomposition of reactive magnetron sputtered heteroepixatial c-(Ti $_{0.37}$,Al $_{0.63}$)N/c-TiN films grown on MgO(001) and (111) substrates. *J Appl Phys*. 2019;125(10):105301. doi:10.1063/1.5051609.

El Azhari I, Barrirero J, García J, Soldera F, Llanes L, Mücklich F. Atom Probe Tomography investigations on grain boundary segregation in polycrystalline Ti(C,N) and Zr(C,N) CVD coatings. *Scr Mater*. 2019;162:335-340. doi:10.1016/j.scriptama t.2018.11.041.

Calamba KM, Barrirero J, Johansson Jõesaar MP, Bruyère S, Boyd R, Pierson JF, Le Febvrier A, Mücklich F, Odén M. Growth and high temperature decomposition of epitaxial metastable wurtzite (Ti$_{1-x}$,Al$_x$)N(0001) thin films. *Thin Solid Films*. 2019; 137414. doi.org/10.1016/j.tsf.2019.137414

Acknowledgements

First and foremost, I would like to express my gratitude to my two supervisors, Prof. Frank Mücklich and Prof. Magnus Odén.

Prof. Frank Mücklich is a leadership role model for me. I have learned from his ever positive approach and communication skills. I would like to thank him for his trust and unrestricted access to all I needed to fulfill this research.

Prof. Magnus Odén is an inspiring scientist, I learned from his experience and confidence. I would like to thank him for the fruitful discussions, academic guidance, personal advice and endless support.

I am especially grateful to Michael Engstler for believing in me, always finding a solution to whatever came up and accompanying me during all these years.

I thank all the co-authors of the publications included in this thesis. This work would not have been possible without their contributions. Thank you to Christoph Pauly for giving me insight on materials characterization and for the fruitful discussions, and to Michael Engstler, Flavio Soldera, Andrés Olguín and Pranav Nayak for proof reading the manuscript of the thesis.

Thank you to the colleagues at the Chair of Functional Materials at Saarland University and the Nanostructured Materials group at Linköping University that made all these years such an enjoyable time.

I thank the Erasmus Mundus Joint European Programme for giving me the possibility of performing my doctoral studies in two countries and working in multi-cultural international environments.

I am very grateful to Andrés Olguin for holding me in his embraces and encouraging me to go forward in difficult times.

I am particularly grateful to Roberto Tannchen who stood wholehearted by my side helping me to sail through the storm.

Thank you to Corinna Markmann for her inspiring light.

I thank my parents Carmen Caffaratti and Domingo Barrirero for their love and unconditional support. Thanks to my brother Exe Barrirero for teaching me with his strength and determination. Thanks to Caro Rey for her openness, sweetness and peace.

I am extremely grateful to all my dearest friends who are the biggest treasure that I have in this life: Pauli Kuschnir, María Laura Cenci, Anne Villamil, Moni Echeverry, Marian De Giovanni, Prisi Zanetti, Pauli Sierra, Anita Barbotti, Cele Karchesky, Juli Trivelli, Gaby Fertonani, Celi Bratovich, Hisham Aboulfadl, Fede Benedetto, Marco Francesconi, Oscar Deccó, Feli Giussani,

Acronyms and symbols

A	Solidification interface area
APT	Atom Probe Tomography
AR	Atomic Resolution
BSE	Back-Scattered Electrons
ΔHF	Enthalpy of fusion
ΔSF	Entropy of fusion
EBSD	Electron Backscattered Diffraction
EDX	Electron Dispersive X-ray
ETD	Everhart Thornley Detector
FIB	Focused Ion Beam
G	Temperature gradient
HR	High Resolution
HV	High Voltage
IIT	Impurity Induced Twinning
IPF	Inverse Pole Figure
L	Latent heat of fusion per unit volume
LEAP	Local Electrode Atom Probe
μXRF	Micro X-Ray Fluorescence
PF	Pole Figure
q	Total rate of heat extraction
R	Ideal gas contant
SE	Secondary Electrons
SEM	Scanning Electron Microscopy
SIMS	Secondary Ions Mass Spectroscopy
TEM	Transmission Electron Microscopy
ToF	Time-of-Flight
TTL	Through The Lens
UHV	Ultra-High Voltage
V	Average interface velocity
V	Growth rate
vCD	Low voltage - high Contrast Detector
VF	Volume Fraction
Z	Atomic number
α	Jackson's factor
η	Nearest neighbors at a growing solid/liquid interface
ν	Coordination number
ξ	Orientation factor

Content

1. Introduction

Improving the design of structural alloys is a never-ending task as industrial applications continuously demand increased performance. Aluminum alloys are used in a wide range of applications due to their attractive low density in comparison to steels, which offers the possibility to design light-weight components.

Aluminum alloys with silicon as the major alloying element are the most widely used for casting applications. Their excellent castability and high strength-to-weight ratio makes them an appealing material for the automotive industry [1]. Al-Si alloys have an irregular eutectic phase formed by faceted silicon in a non-faceted aluminum matrix [2–4]. During the solidification of this phase, several microstructures and growth modes can be obtained depending on the temperature gradient and cooling rate [5,6].

In the solidification processes generally used in industry, such as sand casting or die casting, eutectic silicon grows in the form of plates, also known as flakes. Since silicon plates are hard and brittle and, often act as easy paths for cracks, a microstructural modification towards rounded silicon branches is desirable [7]. Almost 100 years ago, a peculiar phenomenon was patented by Pacz [8], who found that the addition of low concentrations of alkaline fluorides, particularly sodium fluoride changed the silicon structure in these alloys from plate-like to fibrous or coral-like. This modification significantly improves ductility and therefore, it is industrially used nowadays [7]. However, challenges in its application are found when the composition of the alloy gets more complex.

In general, industrially relevant Al-Si alloys contain ternary and quaternary elements such as magnesium and/or copper. The addition of these elements can make the alloy heat treatable and improve its strength and machinability [1]. All of these alloys benefit from the modification of the eutectic microstructure, but in the case of ternary and quaternary alloys, the change is often inhomogeneous showing well-modified regions and non-modified regions with coarse silicon parts. Inhomogeneities in the microstructure are detrimental for the properties of the alloys and hinder its further development. The lack of understanding of the fundamental mechanism underlying eutectic modification impedes further improvement of these alloys.

During the last decades, several alkaline earth and rare earth metals were investigated and two groups of elements were differentiated based on their effects: (1) elements which change the silicon morphology into corals such as sodium [9,10], strontium [11,12] and europium [13]; and (2) others which only refine the plate-like silicon or can only partially change the silicon structure such as calcium [14,15], yttrium [16], ytterbium [17,18], barium [19] and most rare-earths [20]. The reason why these elements behave differently is still unknown.

1.1 Scope

The aim of this thesis is to widen our understanding of the eutectic modification in Al-Si alloys. Several investigations have been performed regarding this topic, however, no systematic research revealed and compared the three-dimensional distribution of the atoms in the silicon phase. I seek to analyze, for the first time ever, atomically resolved chemical information in these alloys by atom probe tomography (APT) and propose a model for the multiplication of crystal defects in silicon and its morphological change.

The study will focus on three cases:

- Al-Si alloy with no addition of any modifier as a reference for the identification of changes and characteristics related to addition of a modifier agent.
- Alloys with addition of the three most powerful modifiers known to date: sodium, strontium and europium. By studying and comparing the solute distribution in eutectic silicon in these alloys, it is possible to pinpoint the common characteristics to further understand the plate-to-coral transition.
- An alloy with ytterbium addition, where the silicon plate structure is refined without corals formation, to understand the differences with coral-forming elements.

1.2 Outline of the thesis

This thesis contains a background about aluminum and Al-Si alloys highlighting their relevance, classification and general applications in chapter 2. An introduction to eutectic solidification of irregular systems in general and, of Al-Si alloys in particular is given in chapter 3 and 4 respectively. Chapter 5 presents a literature review about eutectic modification. Chapter 6 goes through the sample preparation and characterization methods used during this investigation. Chapter 7 gives a summary of the papers included in the thesis and the contribution to the field, together with an outlook and suggestions for further work. Finally, the outcome of the thesis is presented in five scientific papers.

2. Aluminum casting alloys

Several useful properties make aluminum the base metal of choice for engineering solutions. It is light weight, with a density of approximately one-third that of steel; it has high electrical and heat conductivities; good corrosion resistance and can be used in wrought and casting applications. Its high recyclability also plays an important role with a remelting process out of scrap requiring only about 5 % of the energy needed to extract the same amount of primary metal from the bauxite ore [1,21].

Aluminum is the most abundant metallic element, the third most abundant element in earth's crust and the second most industrially used after iron. Surprisingly, its existence was not acknowledged until the beginning of the 19th century and it took almost until the end of the century to develop an economically viable production route [21]. Although its short history of about 200 years in comparison to thousands of years of iron use, aluminum metallurgy evolved extremely fast to cover a wide range of applications. The constant growth in the importance of aluminum is tightly related to the increasing demands for mass reduction in vehicles to improve fuel consumption and lower CO_2 emissions [1,21].

Pure aluminum has low strength and has to be alloyed for use in structural applications. The major alloying elements are copper, manganese, magnesium, silicon and zinc. The mechanical, physical and chemical properties of these alloys are determined by their composition and microstructure. Depending on the composition, manufacturing processes and mechanism of properties development, alloys can be classified into wrought or casting alloys and further into heat treatable or not heat treatable alloys. The most important difference between wrought and casting composition is the alloy's castability. Wrought parts are casted in round or rectangular cross sections with a uniform solidification front. On the contrary, casting compositions are able to achieve dimensionally accurate near-net-shape parts with complex geometries and designed properties, in order to fulfill specified requirements [1]. The good castability of aluminum castings is related to their relative high fluidity, low melting point, short casting cycles and relatively low tendency for hot cracking [22]. Since the present work focuses on the eutectic modification of casting alloys, only this type will be further described. Aluminum castings present a wide range of compositions with great versatility in the achievable properties (Table 2.1).

The most common classification of aluminum castings is based on the major alloying elements. Although no international standard nomenclature is available, the designation given by the Aluminum Association of the United States is well known [23]. This designation has four numeric digits separated by a period between the third and fourth. Table 2.2 shows the main categories defined by the first digit based on the major alloying constituent. The second and third digits do not have any significance but are unique to each alloy. The fourth digit describes whether it is

casting (0) or ingot (1, 2). For fine variations in the composition limits, a letter preceding the numbers is added (A, B, C).

Table 2.1: Range of mechanical properties for aluminum casting alloys [1]

Tensile strength	70 – 505 MPa
Yield strength	20 – 455 MPa
Elongation	< 1 – 30 %
Hardness	30- 150 HB
Electrical conductivity	18 – 60 %IACS
Thermal conductivity	85 – 175 W/m*K at 25 °C
Fatigue limit	55 – 145 MPa
Coefficient of linear thermal expansion at 20 – 100 °C	$(17.6 – 24.7) \times 10^{-6}/°C$
Shear strength	42 – 325 MPa
Modulus of elasticity	65 – 80 GPa
Specific gravity	2.57 – 2.95

Table 2.2: Casting alloys designation of the Aluminum Association (ANSI H35.1) [23]

1xx.x	pure aluminum (99% or greater)
2xx.x	aluminum-copper alloys
3xx.x	aluminum-silicon + copper and/or magnesium
4xx.x	aluminum-silicon
5xx.x	aluminum-magnesium
7xx.x	aluminum-zinc
8xx.x	aluminum-tin
9xx.x	aluminum + other elements
6xx.x	unused series

Table 2.2 summarizes the most relevant composition families for aluminum castings. Some of their remarkable characteristics and applications are [1]:

- Aluminum-copper alloys primarily fulfill requirements of strength and toughness. They exhibit high strength and hardness at room and elevated temperatures. Mostly used in the aerospace industry.
- Aluminum-silicon-copper alloys exist in a wide range of compositions. Copper is added to improve strength and machinability, while silicon contributes to the castability. They dominate the market for powertrain components such as engine blocks, cylinder heads or pistons.
- Aluminum-silicon binary alloys have excellent fluidity, castability and corrosion resistance, but limited strength and poor machinability. They show low specific gravity

and coefficients of thermal expansion. In hypoeutectic alloys, the strength, ductility and castability can be improved by modification of the eutectic phase.

- Aluminum-silicon-magnesium alloys combine remarkable casting characteristics, outstanding properties after heat treatment, good corrosion resistance and low level of thermal expansion. Eutectic modification is also used for these alloys to increase elongation.

- Aluminum-magnesium are binary alloys with moderate to high strength and toughness with excellent corrosion resistance. They have good weldability, machinability and an attractive appearance. They are used to produce high-pressure die cast automotive steering wheels and structural components.

- Aluminum-zinc-magnesium have the particularity of naturally aging, showing full strength after approximately 30 days at room temperature. Their machinability and corrosion resistance is good in general, but they often show poor castability.

- Aluminum-tin are alloys used for bearing applications. The light weight and good heat dissipation are beneficial characteristics. Alloys with 5.0 to 7.0 wt% Sn are often used when low friction, low compressive and fatigue strengths and good resistance to corrosion are needed.

The steady increase in the production of aluminum responds in a great part to its light weight. The reduction in weight by the use of aluminum alloys in automotive designs, improves the efficiency of energy consumption without compromising performance and safety, with a minimal impact on costs [21]. Castings in the transport sector are used in applications such as engine blocks, cylinder heads, pistons, wheels or suspension components, just to mention some examples. In addition to the automotive sector, aluminum alloys are also used in aerospace applications, construction, machinery, packaging, cooking utensils, and housing for electronics or pressure vessels.

All casting manufacturing methods can be applied to cast aluminum alloys. The choice of the most convenient method depends on the size, complexity of the design and number of parts to be manufactured per year [1,21]. The three most important methods are die casting, permanent mold and sand casting. Figure 2.1 shows application sectors and their relative percentages for these three casting processes.

High pressure die casting accounts for more than 50 % of aluminum castings produced [21]. It is a fast near-net shape manufacturing process well suited for large production volumes. High cooling rates are desirable to get short manufacturing cycles. This method enables the fabrication of dimensionally accurate parts with excellent surface finish [22]. The tooling and automation costs are rather high, but they are compensated by the production volume.

Permanent mold and sand castings are used for thicker wall products or for parts requiring internal hollow sections that strictly need a sand core to be fabricated (e.g. cylinder heads) [21]. These two methods show slower cooling rates than the high pressure die casting and therefore, for

Al-Si parts manufactured by these methods, the modification of the eutectic phase treated in this thesis is used to refine the structure and improve strength, ductility and machinability [22]

(a) High pressure die casting

Other, 25%   Internal combustion engine, 8%
Lawn & garden, 2%
Power tools, 3%
Aircraft, 2%
Computer & office equipment, 4%
Refrigeration/AC, 3%
Household, 4%
Motor vehicles, 49%

(b) Permanent mold and sand casting

Aircraft, 10%   Other, 15%
Instruments, 9%
Internal combustion engine, 4%
Power tools, 2%
Computer & office equipment, 2%
Refrigeration/AC, 1%
Household, 3%
Motor vehicles, 54%

Figure 2.1: Applications for aluminum cast products separated by casting process, data collected from [24].

2.1 Al-Si alloys

Al-Si alloys are the most widely used aluminum castings, especially in automotive applications. Silicon provides good castability with improved fluidity, elevated-temperature resistance to cracking and good feeding characteristics [1]. The amount of silicon depends on the desired properties but also on the casting process used to manufacture the part. Processes that need higher heat flux use higher silicon content to improve fluidity, which in turn assists the filling of narrow cavities and intricate designs. Good castability is associated with alloys of reduced solidification range. Addition of silicon also reduces the specific gravity and the coefficient of thermal expansion. Commercial alloys may contain silicon from hypoeutectic concentrations to hypereutectic with up to about 30 wt% Si [1].

Binary Al-Si alloys have low density, are weldable and resistant to corrosion although sometimes difficult to machine. Binary alloys often range between 5 to 12 wt%. Some applications include architectural panels, marine components, cooking utensils, tire molds and, medical and dental equipment. Besides the binary Al-Si, alloys with additional elements such as Al-Si-Cu, Al-Si-Mg and Al-Si-Cu-Mg are extremely relevant for industrial applications (Figure 2.2). The addition of copper to Al-Si results in good castability, higher strength and hardness, and improved machinability; but it reduces ductility and resistance to corrosion. Typical applications are in transmission cases, engine blocks, gear blocks and cases, fuel pumps and cylinder heads. Al-Si-Mg, which include the very well-known 356.0 and A356.0, have outstanding casting properties and good corrosion resistance. The remarkable combination of tensile and physical properties that can be obtained by heat treatments, makes them appealing for aerospace, machinery,

automotive and military applications. Some examples of parts produced by these alloys are automotive space frames and wheels, pump and compressor bodies, cylinder heads, impellers or missile bodies.

Finally, in some cases, the addition of both, copper and magnesium, to Al-Si is advantageous. These alloys have excellent strength and hardness, with some sacrifice in ductility and corrosion resistance. Optimal properties are achieved after heat treatment. The alloy most commonly used for pistons in passenger cars and light trucks belongs to this category (332.0-T5 / Al-9.5 wt% Si-3 wt% Cu- 1 wt% Mg), showing a good combination of mechanical and physical properties at elevated temperatures including low thermal expansion. Other applications of Al-Si-Cu-Mg are found in crankcases, structural aerospace components, air compressor pistons or compressor cases [1].
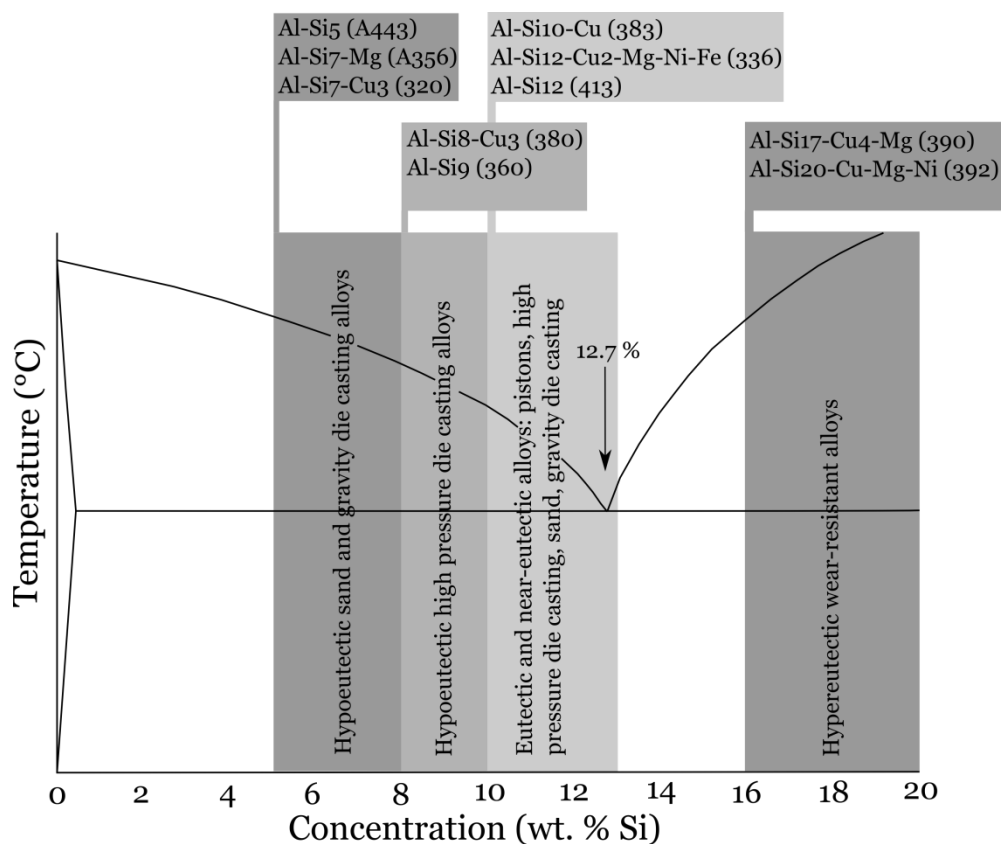
Figure 2.2: Schematic of the Al-Si phase diagram with some of the most common casting alloys. Adapted from [25].

All these general-purpose alloys may be subjected to modification of the eutectic silicon phase morphology. Ultimately, the commercial use of these materials depends on the control of the microstructure of the silicon phase. The detailed study of this modification is the focus of this thesis and will be further explained in the next sections.

3. Eutectic solidification

The microstructure of an alloy is influenced by the solidification conditions and the composition. Generally speaking, two basic growth morphologies exist during alloy solidification: dendritic and eutectic [26]. Depending on the composition on a phase diagram, one can find (a) a pure substance that can solidify in a planar or dendritic manner; (b) solid-solution dendrites; (c) dendrites with interdendritic eutectic; and (d) eutectic (Figure 3.1).

The design of casting alloys requires good castability to get small hot tearing, low shrinkage and good mold filling [1,22]. The best castability is given by pure metals, or by alloys with near eutectic compositions [26]. Multicomponent systems with an invariant eutectic point have a long history in the casting of components. These systems offer relatively low temperature melting when mixing pure elements enabling the fabrication of near-net shape parts of high performance [27]. Near eutectic compositions have a short freezing range offering better fluidity than long freezing range.
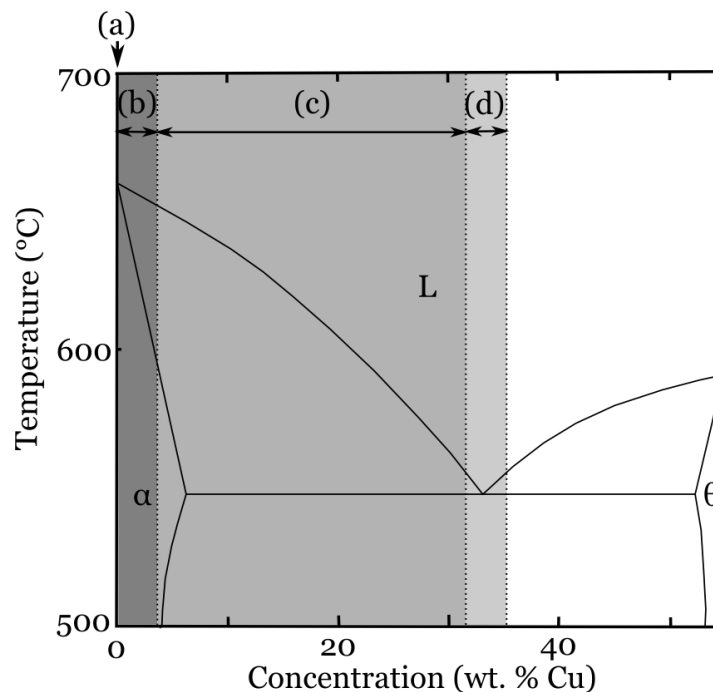
Figure 3.1: Representation of part of the Al-Cu system between aluminum and θ (Al₂Cu). Letters in the diagram highlight different microstructures depending on the composition: (a) planar or dendritic solidification of a pure component; (b) solid-solution dendrites; (c) dendrites plus interdendritic eutectic; (d) eutectic. (Adaptation from [26])

During solidification of a binary eutectic, two solid phases form cooperatively from the liquid. There are numerous morphologies in which eutectic phases may evolve depending on the growth characteristics of the individual phases [28,29]. Eutectic structures can be classified depending on

the entropy of fusion of the components, which is the difference of entropy between the liquid and the solid phases at the melting point. Jackson *et al* [30] proposed a parameter, α, to evaluate this:

$$\alpha = \frac{\eta}{\upsilon}\frac{\Delta H_F}{RT_M} = \xi\,\frac{\Delta S_F}{R}$$

where ξ is the orientation factor defined as the ratio between the number of nearest neighbors for a growth unit at the solid / liquid interface of the crystal (η) and the coordination number (ν); ΔH_F the enthalpy of fusion (or latent heat of fusion); T_M the melting temperature; R the ideal gas constant and ($\Delta S_F/R$) the dimensionless entropy of fusion. According to this factor, related to the roughening transition of a crystal surface, phases with α > 2 (high entropy of fusion) grow in a faceted manner with an atomically smooth interface, while phases with α < 2 (low entropy of fusion) grow isotropically showing no facets and atomically rough interface. Based on this, eutectic structures can be broadly classified into *regular* (or *normal*) and *irregular* (or *anomalous*). *Regular* eutectics are formed by two non-faceted phases (low entropies of fusion), while *irregular* eutectics have one faceted phase with a high entropy of fusion. Aluminum-silicon, for example, presents an irregular faceted / non-faceted eutectic, with a metallic aluminum-rich phase with α < 2 ($\Delta S_F/R$ = 1.35) and a faceted silicon α > 2 ($\Delta S_F/R$ = 7.15) [11].

Another difference that distinguishes regular and irregular eutectics is that the former generally occurs for symmetric phase diagrams with a symmetric eutectic coupled zone (Figure 3.2 (a)). The coupled zone represents the solidification conditions under which the two eutectic phases can grow together with similar velocities [31]. For two non-faceted phases, both phases have a similar undercooling and therefore, the coupled zone is symmetric. Differently, in an irregular system where one phase is faceted, its growth and consequently, that of the eutectic phase will need a higher undercooling. Dendrites of the non-faceted phase can grow faster and they can grow even at eutectic composition. Because of this reason, pure eutectic microstructures can be obtained only at hypereutectic compositions forming an asymmetrical coupled zone (Figure 3.2 (b)) [32].

A further finer classification can be done if the volume fraction (V_F) of the solute phase is considered. When the minor phase in a regular eutectic has a V_F smaller than 30%, the structure will be *rod-like*; and when the V_F is higher than that, a *lamellar* structure will form. For irregular eutectics, when V_F < 30%, the faceted phase grows with a *rod-like* or *fibrous* morphology, while for V_F > 30%, *branched flakes* or *acicular structures* are generally present. Figure 3.3 shows a schematic of the classification considering Jackson's factor (α) and V_F [26].
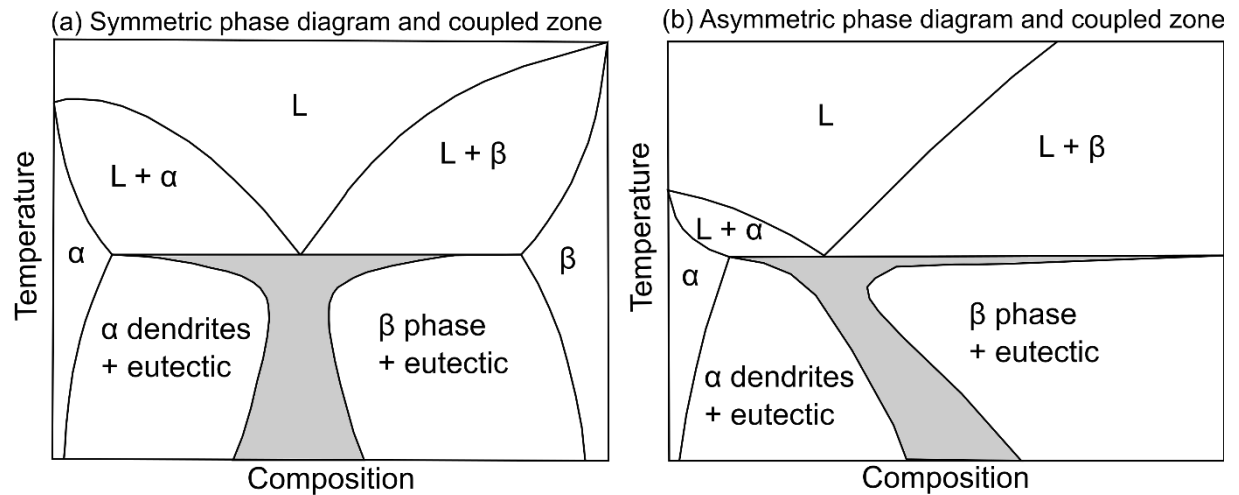
Figure 3.2: Representation of the coupled zones for: (a) eutectic system with regular structure and (b) eutectic system with irregular structure. Adapted from [32].
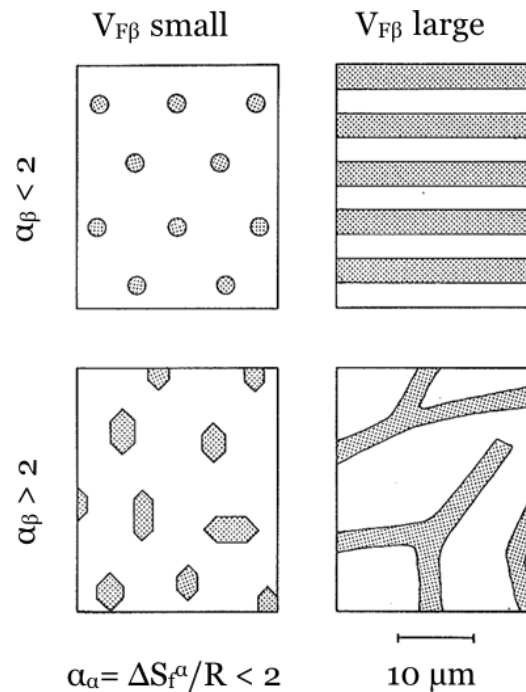
Figure 3.3: Schematic of the four broad categories of eutectic structures based on Jackson's factor, α; and volume fraction ($V_{F\beta}$). The top part shows the regular structures: rod (left) and lamellar (right); and at the bottom, the irregular structures: fibrous (left) and lamellar (right) . Reproduced from [26].

In general, rod-like or fibrous structures are formed for small V_F of one phase because the interfacial area decreases with decreasing V_F of the fibers, while it is constant for lamellae. The interfacial area of fibers is smaller than that of lamellae at V_F smaller than 30% [26]. These criteria are approximated, and lamellae can also form for lower V_F if the specific interfacial energy is strongly anisotropic. Such is the case of the irregular Al-Si system, where the silicon phase represents only about 11 % of the eutectic structure, but still forms a plate-like silicon structure.

Irregular eutectics can present a wide range of morphologies, depending on the solidification conditions [29].
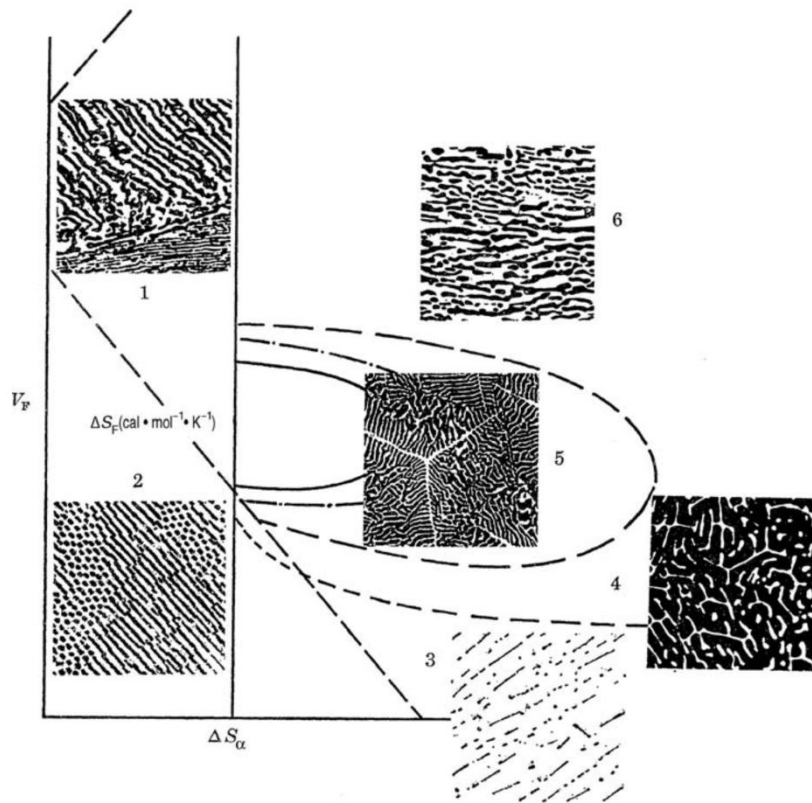
Figure 3.4: Classification of eutectic morphologies as a function of the entropy of fusion (ΔS_α) and volume fraction (V_F) for a growth rate of 5 x 10^{-4} cm/s. Six regions are shown corresponding to: (1) regular lamellar; (2) regular rod; (3) broken lamellar; (4) irregular; (5) complex regular; and (6) quasi regular. Reproduced from [28].

The α factor has considerable success in predicting whether a eutectic structure would grow in a normal or anomalous manner. However, since the eutectic structure grows from solution at a considerably lower temperature than the melting point of its pure constituents, the tendency to facet may be higher. Then, the Jackson's factor can be recalculated for the growth from solution by replacing the latent heat of fusion of the separate constituent by the latent heat of fusion of the solid solution and the melting temperature by the eutectic temperature [33]. Based on this improvement, Croker et al. [28] developed a more detailed classification of eutectic structures. In this approach, an entropy of solution of 23 J/(mol.K) was found as the transition value between non-faceting and faceting behavior. Due to the difficulty in calculating the orientation factor (η/v) for complex structures, it is advantageous to use this entropy of solution instead of the α factor. Systems with an entropy of solution $\Delta S < 23$ J/(mol.K) present a normal growth, while $\Delta S > 23$ J/(mol.K) are anomalous. The structures in each group, particularly the anomalous, depend on the V_F and the growth velocity. Figure 3.4 shows a schematic of the structures in the different regions for a growth rate of approximately 5 x 10^{-4} cm/s as presented by Croker et al. [28].

Regions (1) and (2) show regular lamellar structure and rod structure, respectively. Because of the increased surface energy anisotropy towards higher faceting tendency, the boundary V_F between regions 1 and 2 becomes smaller when ΔS rises.

Anomalous structures show a wider variety of morphologies. They can be broadly divided into four types:

(3) *broken lamellar* or sometimes fibrous ($V_F < 10\%$);

(4) *irregular phases* with a number of morphological types which may coexist. This is the region for the Al-Si eutectic structure.

(5) *complex regular,* array of regular plates or fibers over small areas and generally surrounded by a spine. This structure grows with macrofaceted cellular projections at the solid/liquid interface (V_F higher than approximately 20%)

(6) quasi-regular structure. Sheets or fibers of a non-faceted minor phase in a matrix of the faceted phase

The transitions between regions in figure 3.4 are not sharp and, in the case of anomalous eutectic structures, they also depend on growth rate. The Al-Si eutectic is an example of this dependence on solidification conditions.

4. Eutectic solidification of Al-Si alloys

The Al-Si phase diagram has a simple eutectic point with two solid solution phases: aluminum (fcc) and silicon (diamond cubic). The eutectic reaction occurs at 12.2 ± 0.1 at% Si and 577 ± 1°C [34]. The maximum solubility of silicon in aluminum at the eutectic temperature is 1.5 at%, and decreases to 0.05 at% at 300 °C. The solubility of aluminum in silicon is extremely low at about 0.04 ± 0.02 at% [35]. Figure 4.1 shows the phase diagram of the Al-Si system as presented by [34] with the metastable extensions of the liquidus and solidus lines.
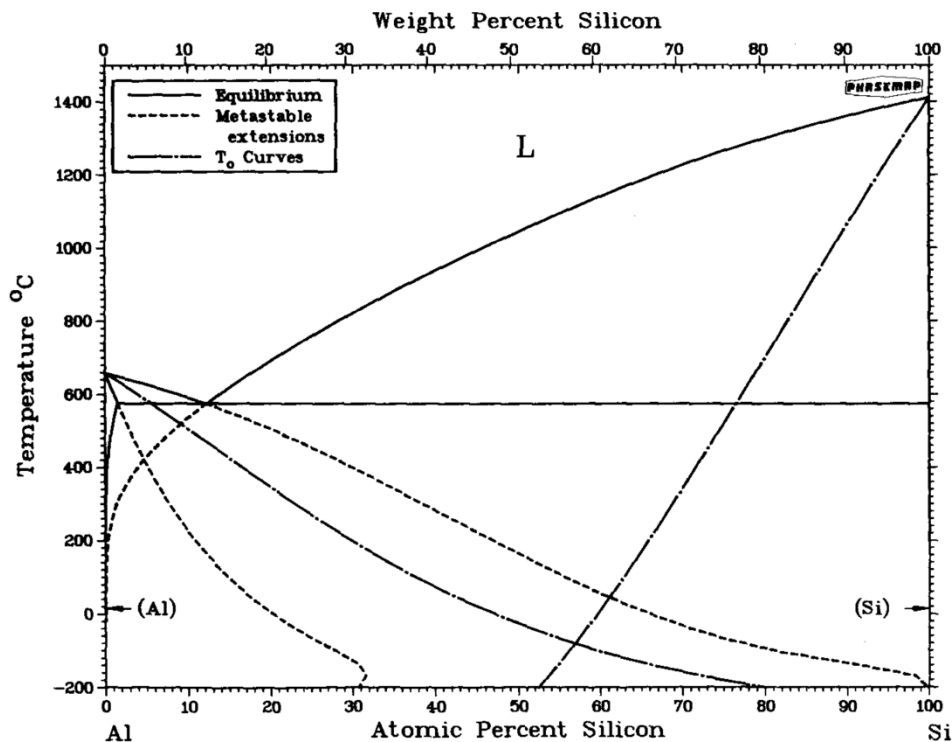
Figure 4.1: Equilibrium phase diagram of the Al-Si system with the extensions of the metastable liquidus and solidus lines. Reproduced from [34].

The formation temperature of the eutectic phase in this system is cooling rate dependent. At high cooling rates, the eutectic temperature is depressed and the eutectic point is shifted towards higher silicon concentrations [36]. This behavior is explained by the presence of an asymmetric coupled zone (introduced in section 3). Since silicon is a nonmetal that grows anisotropically in a faceted fashion forming directed covalent bonds, it needs a higher undercooling than the non-faceted aluminum phase and a growth asymmetry arises for changing solidification rates.

The irregular or anomalous Al-Si eutectic system formed by faceted silicon and non-faceted aluminum can grow with a variety of morphologies depending on the solidification conditions. Silicon is capable of several crystal growth mechanisms in metal solutions. These mechanisms

15

were rationalized and classified by Day and Hellawell [5,6]. Figure 4.2 depicts four distinctive regions as a function of temperature gradient (G) and growth rate (V).
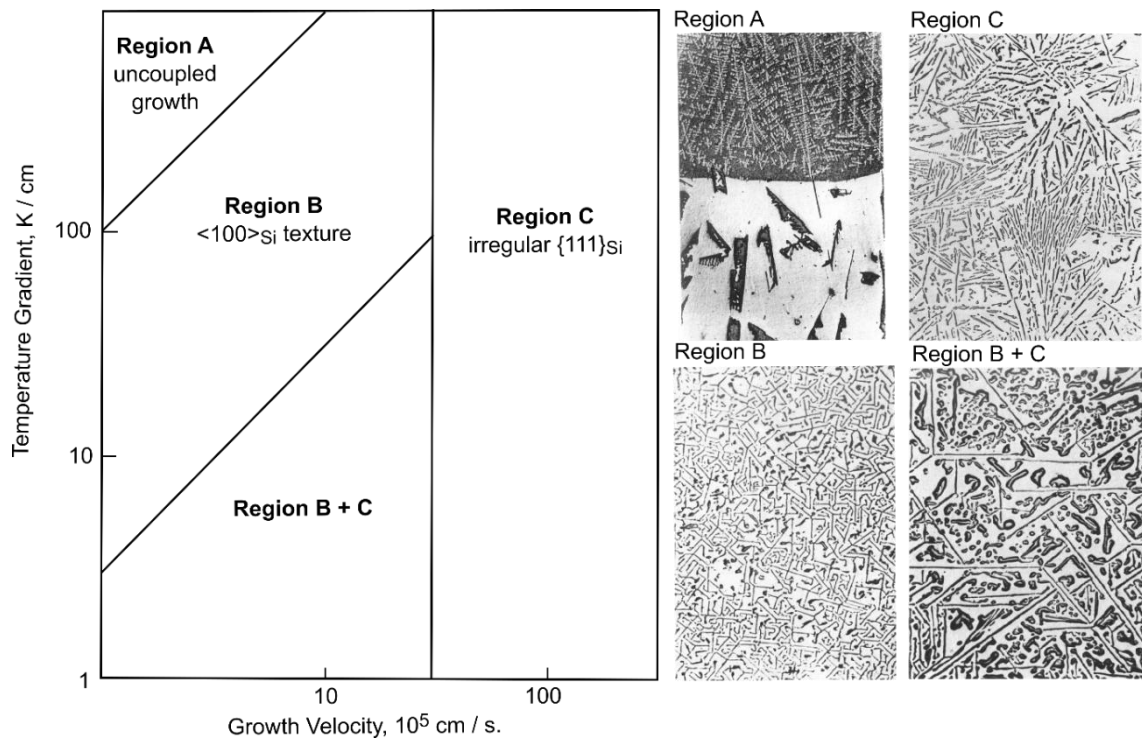
Figure 4.2: Classification of eutectic microstructures in Al-Si alloys as rationalized and presented by [5]

- **Region A**: the two eutectic phases grow independently showing a long-range-diffusion front at high G/V. The solidification front is formed by a planar metal liquid interface with uncoupled massive silicon crystals projecting forward into the liquid. The silicon crystals were showed to be interconnected and twinned in {111} planes. Several silicon particles in this region show elongation in the <110> or <211> orientations.

- **Region B**: eutectic growth with a lower G/V than region A presenting short-range diffusion. Silicon shows a variety of morphologies with highly preferred <100> texture. Two of the most common forms found in this region are thin plates with {100} faces closed at the growing end by <110> edges; and corrugated crystals with {111} faces with the axis of corrugation being the <110>. Silicon plates are inclined with a variety of angles that account for twin configurations. For these structures to be stable, the aluminum must wet the {100} external surfaces up to the aluminum-silicon-melt junction as shown in figure 4.3 (a).

- **Region C**: irregular plate-like silicon structure. This structure occurs when the growth rate is increased above a critical value where a very large undercooling is produced. Silicon flakes grow faster in the <112> orientation and project ahead of the solidification interface forming a non-isothermal front. They have {111} growth habit and contain flat twins across the plates that allow a variety of orientations. This type of growth presents a wide range of inter-particle spacing as a result of the rigid growth anisotropy.

- **Region B+C**: shows a gradual transition between <100> texture and the {111} growth habit. This transition in the morphology of the microstructure is the result of the change of growth mechanism of the faceting phase. Figure 4.3 shows the <100> texture of region B with facets on the {111} crystal faces. This type of morphology can occur only if the metal phase wets the {100} external faces of the silicon crystal up to the solid / liquid interface, that is, if the growth takes place with an iso-thermal solidification front. For decreasing G/V, the silicon phase starts to project ahead of the solidification front in a non-isothermal front and the rapidly growing {100} grow laterally giving rise to a transition structure. If the G/V decreases even further because of an increase in V, the irregular structure of region C is formed by close packed {111} faces at the external walls of the plates and at the growing end.

(a) Region B <100>Si texture   (b) Region C {111}Si growth habit
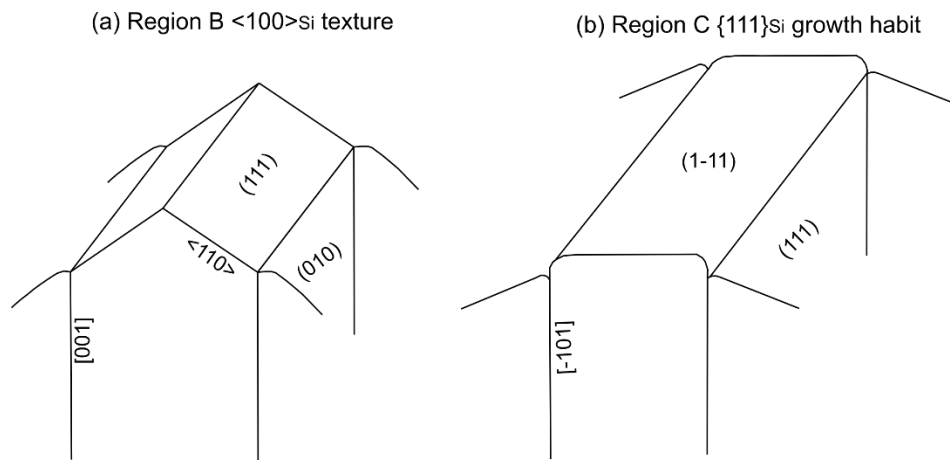
Figure 4.3: Simplified schematic view of the crystallography of eutectic silicon growing in regions B and C. Reproduced from [5].

- **Region D**: for higher freezing velocities in the range of 0.2 to 1 mm /sec., there is a further transition in the microstructure called sometimes *chill- or quench-modification* in literature [5,37]. Silicon appears as continuous irregular fibers with rounded cross-section similar to the modified structure obtained by the addition of impurity elements.

In the case of such a high cooling velocity, it is proposed that the kinetic undercooling increases sharply and eventually, an inversion at the solidification front occurs such that the silicon grows behind the metal phase [37]. This change in the front will also affect the liquid diffusion.

Some differences in the twinning of silicon in this structure has been reported. There is evidence showing some twinning mostly parallel to silicon growth axes [37,38], other showing non-faceted silicon with no twins [39,40], and considerable higher twinning density than in region C [41].

4.1 Plate-like structure and TPRE mechanism

The irregular plate-like structure from region C (Figure 4.4) corresponds to the solidification conditions most generally found in typical unmodified industrial casting processes and therefore, this type of growth deserves closer attention.
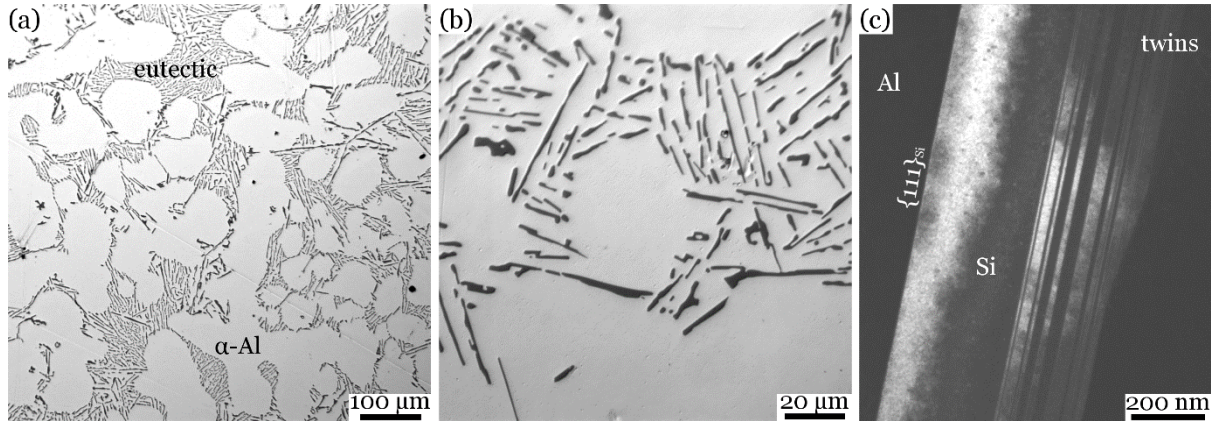
Figure 4.4: Alloy microstructure of Al-7 wt% Si. (a, b) Optical microscopy images showing α-aluminum dendrites and plate-like eutectic. (c) Dark field TEM image showing repeated parallel twinning on {111}$_{Si}$ planes in agreement with the TPRE growth mechanism.

As shown in figure 4.3 (b) and 4.4 (c), the growth rate of silicon in region C will be limited by the nucleation rate on the slow growing {111} faces. One way the crystal increases its nucleation rate is by the presence of coherent twin planes across the silicon plates. In 1960, Wagner [42], and Hamilton and Siedensticker [43] thoroughly explained the faceted growth mechanism of germanium crystals in contact with a supercooled melt, which was later also well-accepted for silicon growth. This is called the twin plane re-entrant edge (TPRE) mechanism and it is based on the formation of twin planes through the germanium or silicon lamella, generating self-perpetuating grooves that function as nucleation and growth sites. The growth on grooves is assumed to be rapid because steps are generated at the center of the grooves. The authors showed that germanium growth occurs readily if the crystal contains at least two parallel twin planes [42]. Figure 4.5 (a) shows a crystal with two twin planes bounded by {111} faces at the growth interfaces. These twinned crystals form re-entrant corners with an angle of 141°, and ridges with an angle of 219° enabling rapid growth in <211> orientations as shown in figure 4.5 (a). Considering the three <211> preferred growth orientations, six re-entrant corners are formed. Figure 4.5 (b) shows examples of nucleation events on two of these corners (sites I) and the further generation of new re-entrant corners with an angle of 109.5° between {111} planes (sites II). The simultaneous existence of two self-perpetuating re-entrant corners ensures the permanent presence of steps for a continuous growth in preferred sites.
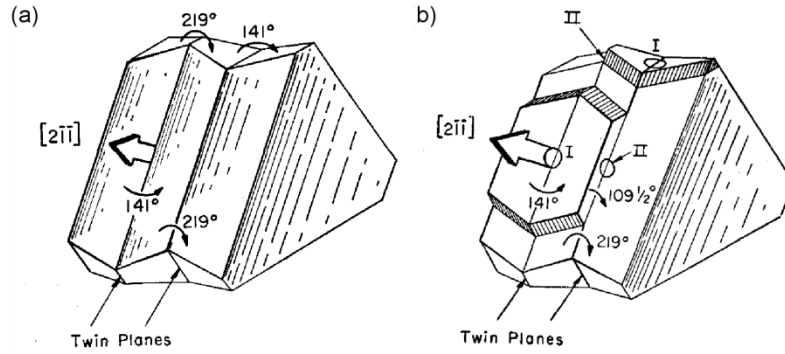
Figure 4.5: Schematic diagram of the twin plane re-entrant edge (TPRE) mechanism. (a) Re-entrant corners (141°) and ridges (219°) formed by the presence of twin planes. (b) View of the growth after nucleation in two "type I" sites, which perpetuate nucleation by the formation of "type II" corners. Reproduced from [43].

Shamsuzzoha *et al* [44] confirmed the TPRE mechanism and showed that all active {111} twin planes are cozonal or coplanar, i.e. parallel to a single <110> zone axis (Figure 4.4(c)). The growth of the silicon under these conditions is purely two-dimensional. To maintain an approximately constant average inter-plate spacing, repeated branching and direction changes occur by multiple twinning. Kobayashi and Hogan [45] explained branching by a 70.5° change in direction due to twinning at the bounding {111} plane. Figure 4.6 (a) shows a representation of a horizontal plate formed by the twinned crystals A and B, and a branch containing the twinned crystals B and C. In this example, crystal B commenced the branching nucleating on A, and the C crystals formed subsequently. Repeated branching such as in figure 4.6 (b) allow for changes in the silicon growth in almost any angle while retaining the <211> direction and the {111} surface planes.
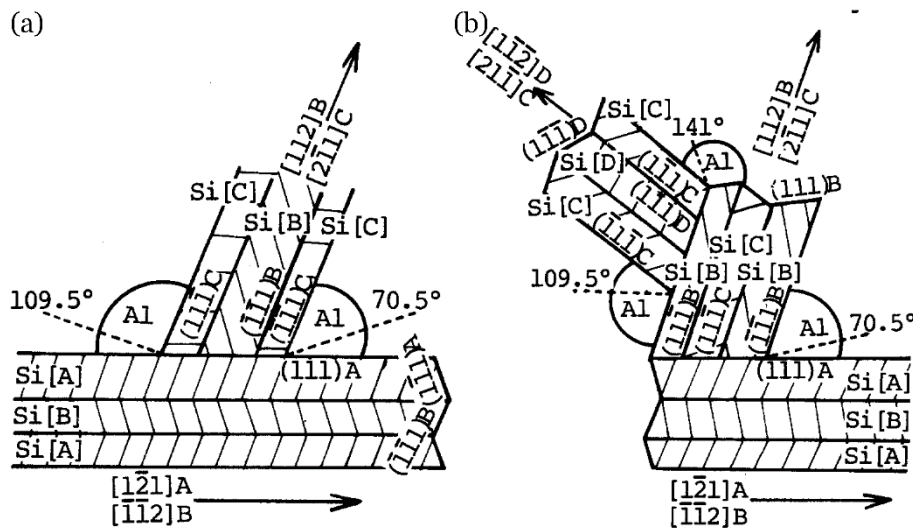
Figure4.6: Schematic representation of the high-angle branching of the eutectic silicon plate structure. (a) 70.5° branching by the formation of a twinned crystal on a {111}$_{Si}$ surface plane. (b) Repeated branching by twinning allowing for almost any growth direction [45].

Shamsuzzoha and Hogan [46] showed a further mechanism for the adjustment of the inter-plate spacing called "displacement twinning". Figure 4.7 gives a schematic representation showing two mutually twinned crystals (C and D) that stop their original growth while a new twin is formed laterally on the external {111}D face. A crystal on the C orientation protrudes and growth continues in the <121> direction parallel to the original by the formation of two further twin events with self-perpetuating grooves. Repeated displacements result in branching in any arbitrary angle.
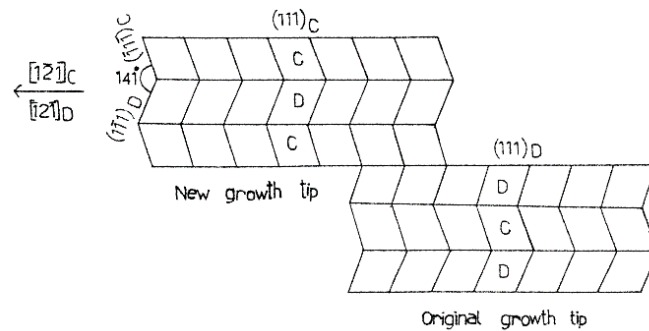
Figure 4.7: Schematic representation of displacement twinning [46]

Recently, a thorough analysis of the silicon plate-like growth done by EBSD supports the TPRE model [47]. However, in this study the authors show that, microscopically, the silicon plates elongate in a <110> direction rather than the <112> assumed in the model. They argue that a zigzag paired <112> growth from parallel twinning planes result in <110> growth habit. They explain this by an alternate disappearance and creation of 141° re-entrants, schematically shown in Figure 4.8.
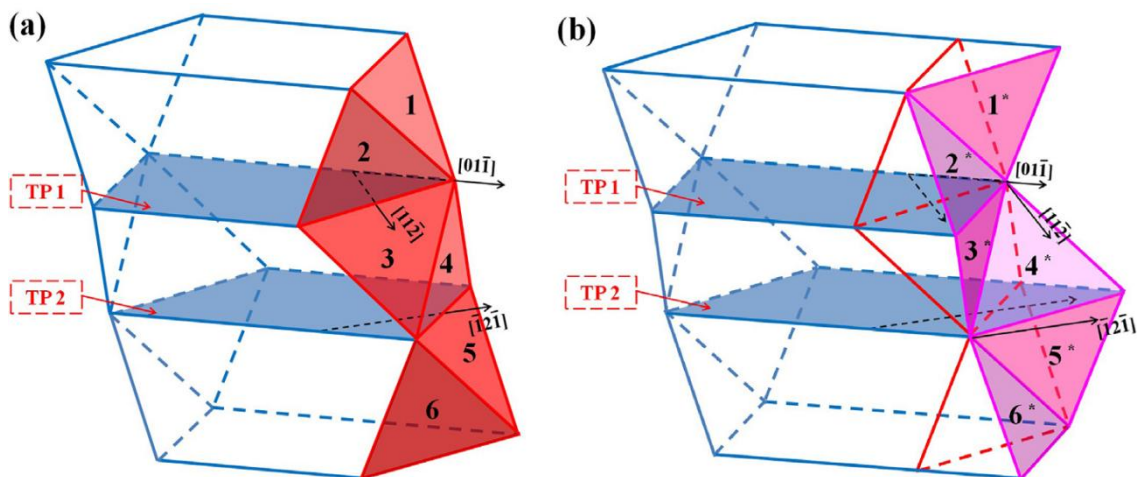
Figure 4.8: Silicon plate with two twin planes TP1 and TP2. (a) Two 141° re-entrants are shown between faces 2 and 3, and between 4 and 5, while two 219° ridges complete the structure between 1 and 4, and between 3 and 6. (b) Further growth causes the disappearance and subsequent creation of 141° re-entrants that result in a <110> growth extension. [47]

TPRE mechanism was shown experimentally for germanium crystals [42,48,49]. Figure 4.4 (c) shows several parallel twin boundaries crossing through the silicon plate and parallel to the outer $\{111\}_{Si}$ plate bounding planes. This evidence is in favor of the TPRE mechanism for silicon plate growth. It is however not possible to ensure that this mechanism is the main responsible for the plate-like growth. Lu and Hellawell [39,40] for example, showed that the spacing between twins might be too wide to be determining for the kinetics of molecular attachment and stated that the TPRE mechanism might be just incidental. Kitamura *et al* [50] argue that the TPRE mechanism was developed for perfect crystals without considering the influence of dislocations and therefore, its relevance is questionable. Although it is not completely elucidated, whether just twins or the presence of twins plus dislocation is responsible for unmodified silicon growth, in any case, twins show to readily form and aid the growth of silicon.

5. Eutectic modification of Al-Si alloys

Al-Si alloys are commercially relevant not only because of their good castability, strength-to-weight ratio or corrosion resistance, but also because the silicon microstructure can be modified by the addition of low concentrations of certain elements [7]. This *modification* is used to enhance properties such as ductility and toughness in these alloys and because of this, it was the subject of hundreds of studies since its discovery in 1921 [8].

5.1 Enhancement of mechanical Properties

Unmodified silicon adopts a plate-like structure for industrial solidifying conditions (Figure 5.1 (a,c)) [51,52]. The coarse, hard and brittle silicon plates diminish the alloy's ductility. The facets of the silicon plates are often on the cleavage plane {111} and therefore, cracks propagate easily across them [37]. The unmodified alloys' elongation is often no more than a few percent and toughness is deteriorated [53,54]. In contrast, the modified silicon structure shows a fine interconnected coral-like structure formed by fibers with rounded cross-section (Figure 5.1 (b,d)) [51,52,55]. This transformation of the silicon structure improves the elongation significantly [7,56,57]. Table 5.1 shows the modification effect on the tensile yield strength, ultimate tensile strength and elongation of some representative alloys.

The mechanical properties of Al-Si castings strongly depend on the form, size and distribution of silicon in its eutectic phase. When comparing modified and unmodified alloys, the modified structure showed a reduced amount of fractured silicon particles under the same testing conditions. This is related to the lower aspect ratio and particle size of modified silicon [54]. Larger and longer particles are more prone to cracking rapidly at low strains in coarse structures, in contrast to finer structures where the progression of particles' cracking is more gradual [58–60]. High sphericity of silicon particles is favorable to the resistance of interface debonding and plastic deformation of the aluminum matrix [61]. Fractography shows a direct relationship between the size and aspect ratio of the silicon particles and the dimples implying that the elongation of silicon particles is transmitted to the dimples and the cross-section area of the silicon particles directly influences the fracture surface geometry [62]. The mechanical properties of hypoeutectic Al-Si castings are also influenced by the grain size and the secondary dendrite arm spacing (SDAS). The combination of eutectic modification together with grain refiners and small SDAS were shown to exert a significant improvement of tensile [63–65] and impact properties [53,60,66].
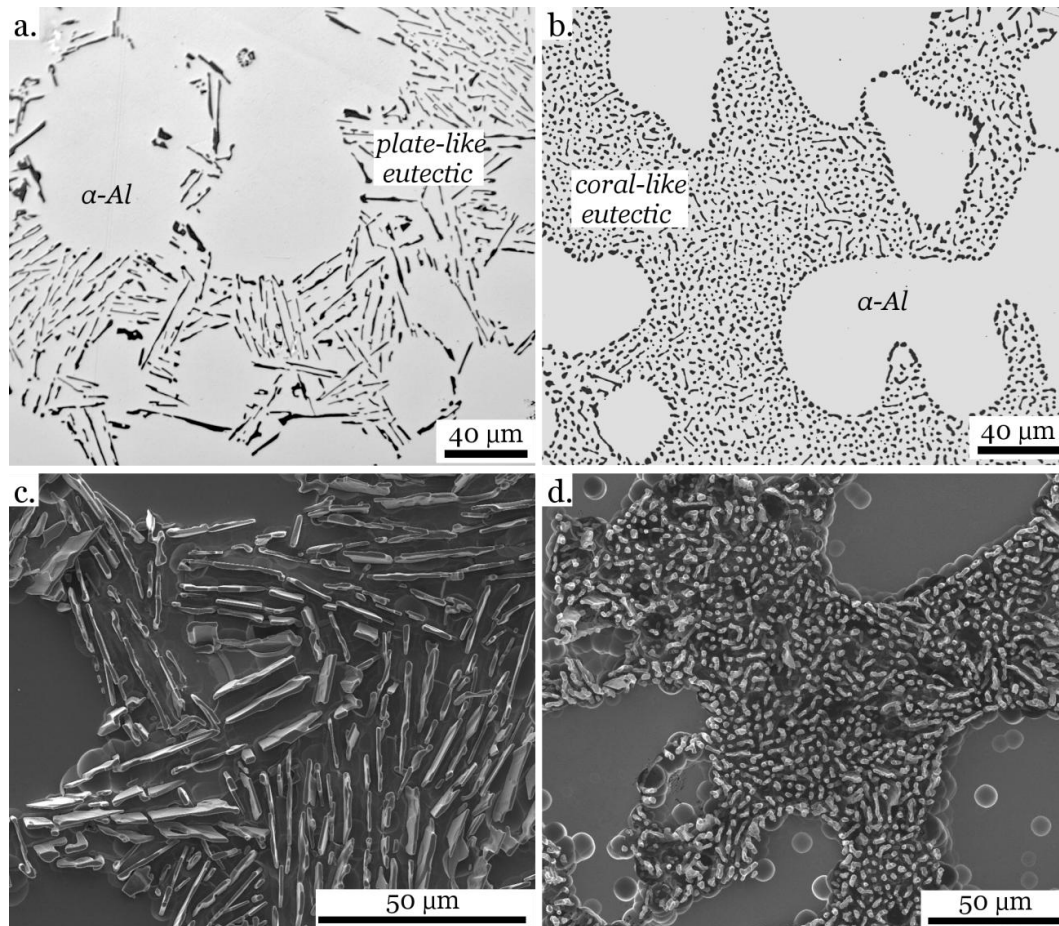
Figure 5.1: Comparison between unmodified and modified microstructure in an Al – 7 wt% Si alloy. Both images show primary α-Al dendrites surrounded by eutectic phase. (a,c) 2D and 3D images of unmodified eutectic silicon plates in an aluminum matrix. (b,d) Modified eutectic phase by the addition of 150 wt ppm Sr. 2D and 3D images of the silicon coral-like structure.

In industrial practice, ductility can also be improved by heat treatment producing a "thermal modification". During the heat treatments of Al-Si alloys, the spheroidization of silicon crystals is a time consuming part of the process. Silicon plates first break up into smaller parts, then coarsen and become spherical. If the chemical modification studied in this thesis is combined with a heat treatment, the time needed for the spheroidization can be reduced in half. The reduction in cost by shortening the heat treatment can be about 10 times the cost of strontium addition and the throughput of the furnaces doubled [67,68].

Apart from the modification of the eutectic microstructure, the addition of strontium was also reported to have an effect on iron-rich intermetallics. Iron is a common impurity in commercial alloys which often cannot be avoided. Several iron-rich intermetallics with different compositions and morphologies such as the needle/plate-like β (Al_5FeSi), Chinese script α (Al_8Fe_2Si or $Al_{15}(Fe,Mn)_3Si_2$), π ($Al_8Mg_3FeSi_6$) or δ (Al_4FeSi_2) can be formed in Al-Si alloys and they are generally detrimental to the mechanical behavior of the alloy [70–75]. The β-phase (Al_5FeSi) is brittle and cracks propagate along the boundary of its needle morphology [76]. Manganese is

often added to the alloy to inhibit the formation of coarse β phase and replace it by the less harmful α phase which is more compact, but strontium addition was also reported to lower the volume fraction of Fe-intermetallics and refine the needle-shaped β (Al_5FeSi) making it shorter and thinner [72,76,77]. Samuel *et al* [78] noted the dissolution of β in the aluminum matrix and an enhanced effect when magnesium and strontium are added together by the additional transformation of β to π phase. In wrought aluminum alloys of the 6xxx series, addition of strontium was reported to promote the formation of the α phase instead of β, leaving more excess silicon available for the precipitation of Mg_2Si during aging and, therefore, enhancing its mechanical properties [79].

Table 5.1: Comparison of mechanical properties for unmodified and modified cast alloys as presented in reference [69]

Alloy and temper	Product	Modification treatment	Tensile yield strength (MPa)	Ultimate tensile strength (MPa)	Elongation (%)
13 % Si	Sand cast test bars	None	...	124	2.0
		Na-modified	...	193	13.00
	Permanent mold test bars	None	...	193	3.6
		Na-modified	...	221	8.0
359.0	Permanent mold test bars	None	...	180	5.5
		0.07% Sr	...	210	12.0
356.0-T6	Sand cast test bars	None	208	289	2.0
		0.07% Sr	238	293	3.0
	Bars cut from chilled sand casting	None	213	284	4.4
		0.07% Sr	218	291	7.2
A356.0-T6	Sand cast test bars	None	179	226	4.8
		0.01% Sr	207	297	8.0
A444.0-T4	Permanent mold test bars	None	...	151	24.0
		0.07% Sr	...	149	30.0
A413.2	Sand cast test bars	None	112	137	1.8
		0.005-0.05% Sr	108	159	8.4
	Permanent mold test bars	None	125	168	6.0
		0.005-0.08% Sr	125	191	12.0
	Test bar cut from auto wheel	0.05% Sr	121	193	10.6
		0.06% Sr	126	193	12.8

5.2 Elements modifying eutectic silicon and their effect on the microstructure

Sodium was the first element extensively studied as a modifier [5,9,10,40,80–85]. It has a powerful effect and only around 50 ppm are enough to show full modification. The main challenge of adding sodium is its high vapor pressure and consequent tendency to fade [7,11,40]. This makes the amount of effective added sodium difficult to control and therefore not so convenient for industrial practice. For this reason, since the 1970s strontium replaced sodium and its effect on Al-Si was increasingly studied [11,12,38,86–88]. Strontium is generally added in the form of Al-Sr

master alloys [7,89,90] with almost no loss during solidification. Detailed information on the effect of sodium and strontium is reviewed in section 5.4.

On 1987, in the search for a systematic that could explain the modification of silicon, Lu and Hellawell [40] introduced the impurity induced twinning mechanism. This model considered that elements with an appropriate size would force the silicon growth to miss one close packed position and create a twin. Based on this assumption, several elements such as barium, calcium, yttrium and most rare-earths were proposed as potential modifiers. Since then, several investigations were carried out on the effect of these elements in Al-Si alloys. Calcium was found to modify the silicon structure but with a weaker effect than sodium or strontium [14–16,19,91–94]. Ludwig *et al* [14,15,94] concluded that a fully coral silicon structure cannot be achieved with calcium additions of up to 300 ppm, but a strong refinement of the silicon plates is observed. Besides silicon refinement, calcium was found to refine detrimental iron intermetallics in Al-Si alloys [95–97] and to improve elongation and impact strength, but often deteriorate ultimate tensile strength due to porosity and formation of Al-Si-Ca intermetallics. Abdollahi and Gruzleski [98], and Ludwig *et al* [94] observed that silicon modification with calcium only refines the silicon plate structure in alloys solidified with low cooling rates and achieves fibrous silicon for higher cooling rates.

Barium addition can produce a full modification of the silicon plates [16,19,40,91]. However, a relatively high amount of modifier is needed in comparison to sodium or strontium. Knuutinen *et al* [16] showed that full modification needs additions of at least 890 ppm Ba to occur, while lower additions produce only partial modification or only refinement of the silicon plates.

Rare earths were also tested as possible modifiers [20]. From all of them, only europium showed the ability to transform the silicon plates into corals, while all others showed only a refinement of the silicon plates (Figure 5.2). Besides, much lower concentrations of europium (~ 600 ppm in an Al-10 wt% Si) are enough for silicon modification compared to the amount of the other rare-earths elements needed just to refine the structure (1.3 to 3.0 wt%) [20]. Alloys modified by europium show similar characteristics as strontium modified alloys. Some of the characteristics of this modification are: high density of crystallographic defects in silicon, formation of pre-eutectic and eutectic Al_2Si_2Eu intermetallic phases, and improved ultimate tensile strength and elongation [13,56,99].

The question that remains unanswered is: why do the other rare earths only refine eutectic silicon and cannot form silicon corals. Similarly to europium, alloys with ytterbium also form Al_2Si_2Yb phases [18]. However, Nogita *et al* [17] showed by micro X-ray fluorescence (μ-XRF) that, while europium is present in the silicon phase like in the case of strontium [100], ytterbium is not. Ytterbium was tested in a wide range of concentrations from 0 to 6400 ppm in an A356.0 alloy and every composition showed only an increasingly refined silicon plate structure [16]. The absence of ytterbium in the silicon phase was pointed as one possible explanation for the lower density of twins in silicon [18].
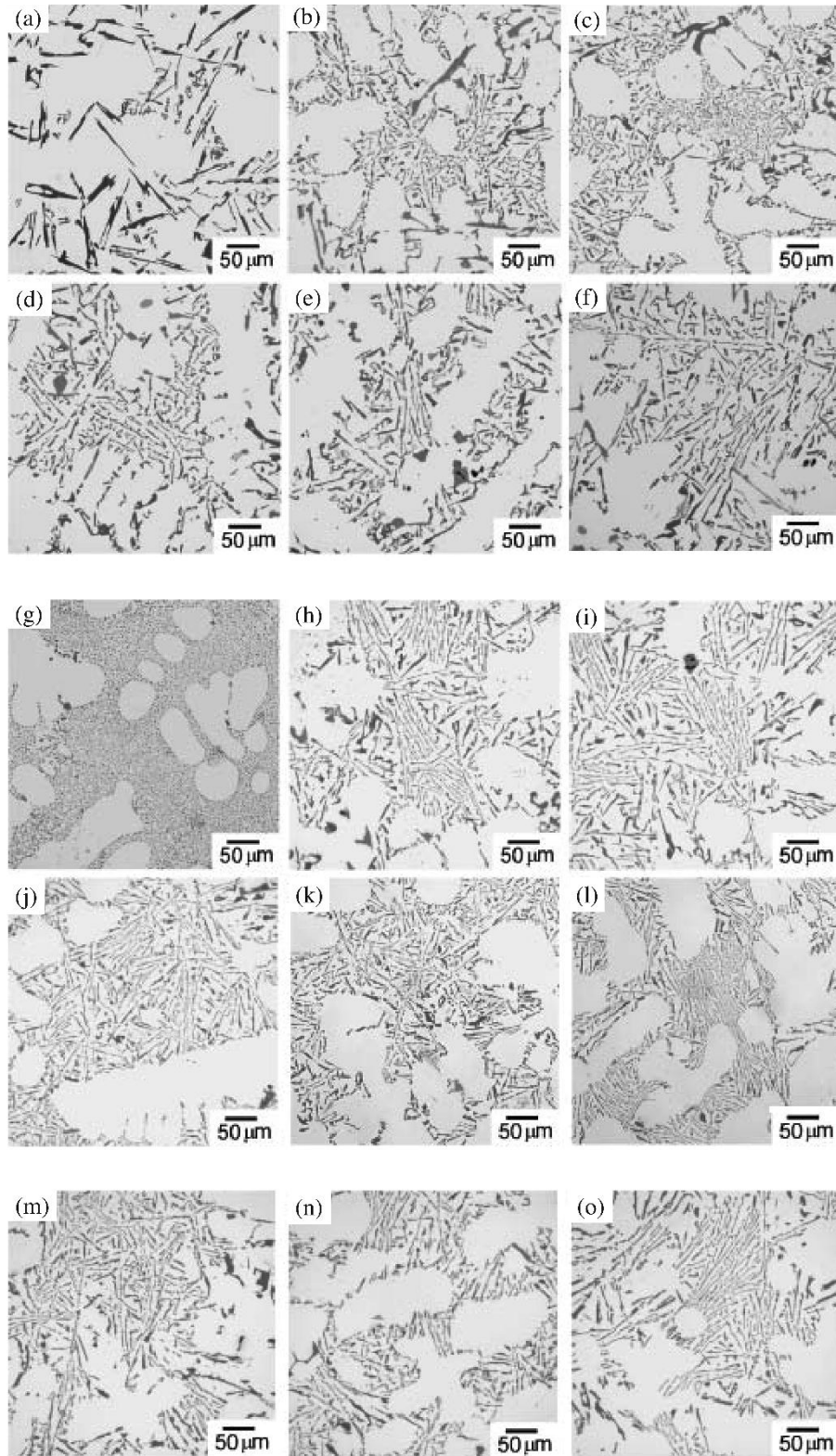
Figure 5.2: Optical micrographs of Al-Si alloys with addition corresponding to the maximum modification for each element: (a) unmodified, (b) 17300 ppm La, (c) 19700 ppm Ce, (d) 17200 ppm Pr, (e) 14800 ppm Nd, (f) 19700 ppm Sm, (g) 600 ppm Eu, (h) 30300 ppm Gd, (i) 25300 ppm Tb, (j) 14300 ppm Dy, (k) 18700 ppm Ho, (l) 17900 ppm Er, (m) 12900 ppm Tm, (n) 13900 ppm Yb, (o) 12700 ppm Lu [20].

5.3 Porosity and shrinkage

A downside of the addition of a modifying agent to Al-Si castings is the alteration of the amount, size and distribution of porosity. A considerable percentage of scrap is caused by undesirable casting defects such as porosity and shrinkage. Low elongation, loss of tensile strength or poor fatigue strength are some of the problems related to porosity and / or shrinkage [101]. An increased level of porosity is often reported for modified alloys and several approaches to find an explanation to this behavior can be found in literature [102–106]. A decrease of hydrogen solubility in the liquid was reported in strontium modified alloys [107]; degassing the melt after strontium addition was suggested to decrease the content of hydrogen [108]. Emadi *et al* [107,109] showed lower surface tension and higher viscosity of the liquid, as well as a higher volume shrinkage due to increased solid density. Inclusions such as strontium oxides (Al_2OSr_3) [105] and strontium-containing intermetallics (Al_2Si_2Sr) [110] were suggested to act as sites for heterogeneous nucleation of pores.

In alloys with a significant volume fraction of eutectic phase, porosity was showed to be redistributed from centrally located irregular and interconnected pores in unmodified alloys, to well dispersed and rounded pores in strontium and sodium modified alloys [103,104,111]. The redistribution of the porosity was explained by an alteration of the solidification mode. As it will be presented in more detail in section 5.4.3, eutectic grains in hypoeutectic unmodified alloys, which nucleate near the tip of primary dendrites, are very numerous and small; in contrast, few and very large eutectic grains nucleate independently from the dendrites in modified alloys. An "isolation" model was proposed by McDonald *et al* [103] to account for the effect of the solidification mode on porosity. Pores are showed to form after a significant amount of solidification has occurred. The authors argue that during solidification, liquid pools will become trapped and isolated from the riser when eutectic grains impinge each other. After isolation, no feeding will occur and solidification shrinkage leads to pore formation. In the unmodified alloy, the massive number and small size of the eutectic grains will allow a good permeability of the liquid until the last stage of solidification. Very small pools may form, but porosity will mainly concentrate at the center of the casting. In contrast, the dramatic decrease in number and increase in size of the eutectic grains in the modified alloys, cause the isolation of well distributed relatively large pools of liquid where rounded pores will form due to shrinkage. The impact of solidification mode on interdendritic flow was also evaluated for additions of barium, calcium, yttrium and ytterbium to Al-Si alloys [102]. Significant differences were found in the distribution of porosity in the castings that support the effect of solidification modes on the permeability of the mushy zone. On the one hand, barium and ytterbium showed nucleation of independent eutectic grains that reduced the flow paths causing small, rounded and well distributed pores similarly to strontium. While on the other hand, the eutectic phase with calcium and yttrium evolved from the surface of the casting towards the center of the hot spot and the freezing of the central path caused the formation of porosity in the center such as in unmodified alloys.

The amount of silicon plays a role on porosity in hypoeutectic and eutectic alloys. Higher silicon contents decrease the volume fraction of primary aluminum dendrites, leaving more space for feeding during a longer time. In this sense, near-eutectic Al-12.5 wt% Si alloy shows less porosity than Al- 7 wt% Si [106]. The combination of casting design together with the feeding efficiency, given by the solidification modes and the silicon content, influences the amount of porosity in these alloys [111]. Based on this knowledge, casting design can be used to promote directional solidification towards the feeder in order to get sounder castings of increased integrity [102,106].

5.4 Theories explaining eutectic modification of Al-Si alloys

Several conflicting theories have been proposed through the years showing the complexity and controversy of the subject [112]. In spite of 100 years of research, the underlying phenomena for modification are still not fully understood.

5.4.1 Early theories for eutectic modification

Shortly after the discovery of the eutectic modification in 1921 [8], one of the first explanations considered the ternary system as a key factor. Otani [80] suggested a ternary monotectic reaction in alloys modified by sodium. He proposed that, during solidification, aluminum and silicon solid phases are formed simultaneously with a small amount of a β-liquid rich in sodium. If this very small amount of β-liquid is just ignored, the invariant reaction may be taken as equivalent to the binary eutectic reaction and, as the reaction proceeds, the β-liquid gradually accumulates contiguous to the crystal hindering the free growth. Also during the 1920s, Gwyer and Phillips [113] suggested a condition of transient stability, where formation of aggregates of colloidal dimensions in the nanometer range would play an important role. Ransley and Neufeld [81] corrected the Al-Si-Na phase diagram to show that the system had a ternary eutectic instead of a monotectic reaction and found the formation of a ternary compound [AlSiNa]. At that time, they pointed out that the idea of a colloidal dispersion would provide an adequate explanation if it were assumed that this [AlSiNa] compound is the hindering agent. Later development of the ternary phase diagram of the Al-Si-Na [114] and Al-Si-Sr [115] systems confirmed ternary eutectic reactions forming ternary compounds instead of a β-liquid.

In 1949, Thall and Chalmers [82] proposed a model to explain eutectic modification based on the balance of interfacial tensions during solidification. They assumed that aluminum is the leading phase during eutectic solidification. This assumption was based on the statement that the rate of advance of the solidification interface depends on the balance between the heat flow from the liquid to the solid and the latent heat evolved during solidification. Based on this, the higher thermal conductivity and the lower the latent heat of fusion, the faster the interface will advance. Because aluminum has considerably higher thermal conductivity and lower latent heat than silicon, it was concluded that the aluminum / liquid interface would freeze in advance more rapidly than the silicon / liquid interface. The second assumption made by the authors is that a

small amount of added sodium reduces the surface energy between solid aluminum and solid silicon, which in turn increases the interfacial angle θ (Figure 5.3). They suggested that this reduction of surface energy causes the aluminum phase growing ahead of the solidification front to enclose the silicon crystal and, therefore, the silicon particle will be "sealed off" from the liquid and will need to re-nucleate repeatedly. Despite the logical train of thought of the authors, it was later showed that the silicon phase is the leading phase during eutectic solidification and silicon grows in a continuous manner instead of constantly re-nucleating [5,116,117].
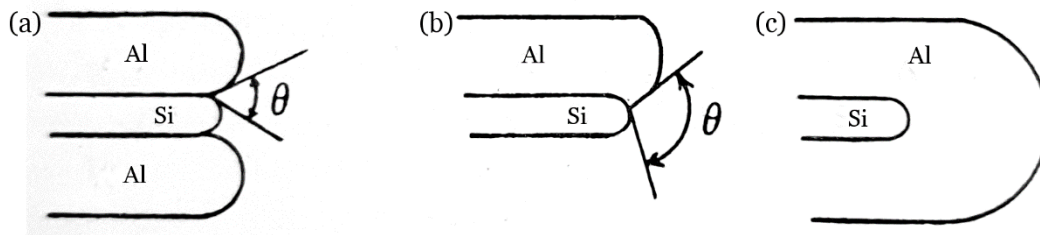
Figure5.3: Eutectic growth proposed by Thall and Chalmers: (a) Alloy with no modification. Aluminum grows in advanced of silicon. Interfacial angle θ between the growing aluminum and silicon phases. (b) Modified alloy with a reduced surface energy between the phases that translates into a larger interfacial angle θ. (c) Because of the reduced surface energy, aluminum encloses silicon which will need to re-nucleate [82].

Following the idea of Thall and Chalmers [82], Davies and West [9,84] studied interfacial energies in deeper detail. The interfacial angle between solid silicon and the melt was shown to be equal to the grain boundary energy in silicon in an unmodified alloy. For the sodium modified melt, no typical angles were found and the angle depended on the crystallographic orientation of the silicon substrate. This showed that, even though a lower surface tension was found for sodium modified alloy in comparison to unmodified [84], the change in interfacial energy cannot determine the interface profile during solidification. The authors claimed that sodium modifies the crystal habit of silicon by being incorporated into certain crystallographic facets. They showed the restriction of fast-growing crystal faces in the presence of sodium (Figure 5.4), which reduces the growth rate of the eutectic phase to that of the slowest facets in silicon. To the best of our knowledge, Davies and West [9] were the first to propose the progressive poisoning of silicon facets by sodium atoms, explaining the supercooling of the melt as the increased driving force needed by the crystal to further grow. They also concluded that the modification is found for elements with sufficient affinity for silicon to form ternary compounds confirming the early idea [80,81] that the ternary system plays a crucial role for modification.
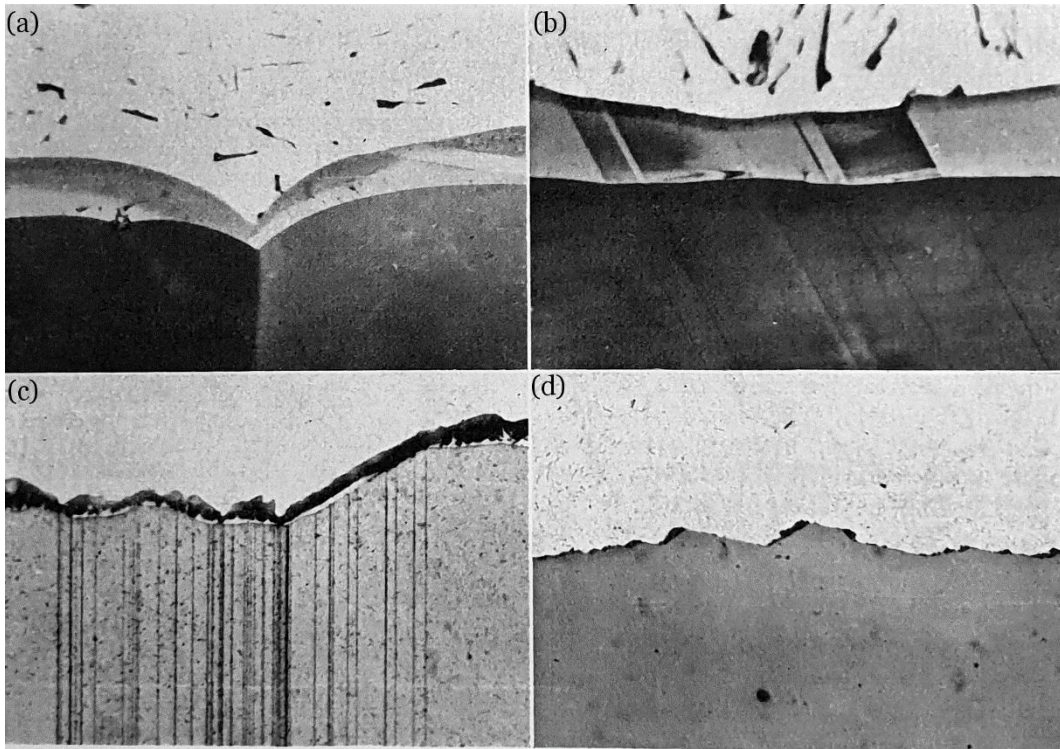
Figure 5.4: Dihedral angles at the interface between polycrystalline silicon and eutectic (Dash etch). (a) Grain boundary without sodium. (b) Twin boundaries without sodium. (c) Grain boundary and twins in presence of sodium. (d) Silicon growth layer with sodium. Apparent restriction to certain crystal faces [9].[1]

Around 1970, Day and Hellawell [5,6] agreed with the proposal of the poisoning of silicon by sodium reporting that sodium poisons re-entrant {111} twin grooves characteristic for the growth of plate-like silicon in region C (Figure 4.2). They explained that the selective adsorption of sodium retards silicon growth and increases undercooling.

From the early theories mentioned above, two hypotheses stand out:

(i)   the ternary system Al-Si-X (X = modifier) and the formation of ternary phase/s play an important role to understand modification; and

(ii)   the modifier restricts silicon growth by poisoning certain crystallographic facets.

In the following decades, hypothesis (i) was abandoned because of lack of proof and great attention was put on (ii) to understand silicon growth and its restriction. Next section presents a brief summary on this topic.

---

[1] Magnifications reported in the original publication are: (a) x450, (b) x450, (c) x450, (d) x240. Note possible small deviations from these values due to print size.

5.4.2 Modification effect on eutectic growth

Similar to Davies and West [9], and Day and Hellawell [5,6], several other studies based their models and explanations on the silicon growth restriction due to the presence of the modifier at the growth front [11,118–120]. During the 1970s and 1980s, even though some studies still used sodium to modify Al-Si alloys, more and more investigations focused on strontium modification because of strontium's low tendency to volatilize. Strontium was proven to segregate preferentially into silicon in the eutectic phase [87].

Steen and Hellawell [118] analyzed eutectic growth and reported that strontium interfered with facet formation on {111} silicon planes and increased the frequency of twinning events. They suggested that the effect of sodium and strontium is to inhibit the growth on planes other than {111} by selective adsorption of the impurity element poisoning other faces. This situation leads to faceting of other planes implying that the original plane is no longer the most slowly growing and crystal growth becomes more isotropic. Hanna *et al* [119] suggested that the inhibition of molecular attachment on the most rapidly growing sites would increase the undercooling until growth could occur in less advantageous planes.

Jenkinson and Hogan [11] as well as Steen and Hellawell [118] concluded that modification occurs due to a limited diffusion process at the solidification front, caused by accumulation of the impurity element at the solid-liquid interphase up to a concentration where the undercooling and growth profile are affected. If the solubility of silicon in the melt is reduced, the attachment of silicon to the crystal surface is also reduced until silicon and aluminum growth velocities are equalized and both phases form by an isothermal continuous growth.

The isotropic growth front in modified alloys was shown in several studies [10,85,86,119] by comparing the shape of the solidification front in unmodified and sodium-modified eutectics. While unmodified eutectic has an irregular solidification front with silicon growing ahead, the sodium-modified alloy shows a very smooth one. In 1981, Flood and Hunt [85] emphasized that not only the growth of silicon was affected by the addition of sodium, but also the nucleation. From the imaging of quenched samples, these authors arrived at the conclusion that in an unmodified alloy, nucleation can occur on dendrites ahead of the main eutectic front, but when sodium is added these nucleation events are inhibited and growth occurs in a smooth front (Figure 5.5). Some years later, Hanna *et al* [119] polished successive layers on similarly quenched samples and showed that, in the unmodified alloy, eutectic colonies do not necessarily originate as nucleation events in the liquid, but are connected to the main growth front by outlying extensions of flake silicon. Although the conclusion of a restricted nucleation given by Flood and Hunt [85] was rebutted, their analysis still holds. In their study, the growth front of the sodium modified alloy was 18 times smaller than the growth front of the unmodified alloy. Because the rate of heat extraction from the solidification front should be similar for both alloys, the average interface velocity of the modified alloy must be much greater. The authors suggested that the higher

interface velocity due to the smaller interface area, accounted for the refinement of the microstructure and consequent smaller spacing between silicon branches.
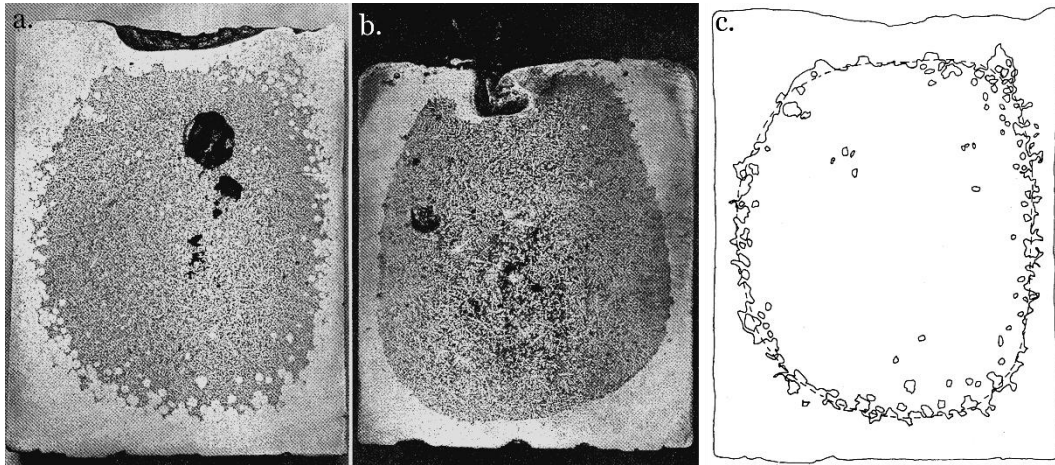
Figure 5.5: Solid / liquid interfaces after quenching molds during solidification: (a) Unmodified Al-Si eutectic alloy; (b) Sodium modified Al-Si eutectic alloy; (c) solid line showing the solid / liquid interface in (a) and dashed line showing the expected smooth interface [85].

The reason for the change in morphology of the solidification front remained unclear and the next step forward to understand eutectic modification came with the development and increasing popularity of transmission electron microscopy (TEM). Modified silicon revealed a remarkably imperfect crystallography with a massive increase in the twin density [12]. TEM imaging and diffraction were extensively used to study the presence of twins and to understand whether they are important or incidental for the growth of silicon and the modification process [38,39,88,121]. Frequent twinning in the silicon crystal was proposed to enable an isotropic growth by allowing repeated changes of growth orientation [12,38–40,88].

Shamsuzzoha and Hogan [12,38,88], and Jenkinson and Hogan [11] performed TEM studies on silicon fibers modified by strontium and showed that modified silicon has fiber axes in the <100> and <110> orientations and exhibit multiple {111} twinning from at least two {111} planes simultaneously. The high twin population allows frequent branching and flexible growth. This permits the axes of the corals to change and maintain the necessary inter-coral distance. Similarly, Lu and Hellawell [39,40] showed that silicon in a sodium modified alloy is heavily twinned with the silicon fibers having a principal axis along a <100> direction, with the four twin systems involved and side branches extending in <211> directions at an angle of 35.3° to the principal axis. They observed that modified fibers have rough or microfaceted external surfaces, and that multiple steps and grooves are expected at the solid / liquid front as twins emerge.

Shamsuzzoha and Hogan [12] postulated that the increased twin density is the result of sodium or strontium adsorption on {111} $_{Si}$ surfaces lowering the {111} twin energy. Based on TEM images, they proposed a zigzag growth model. Figure 5.6 (a) shows how the local growth directions [$\bar{1}\bar{1}2$]A and [11$\bar{2}$]B are repeatedly alternated with [11$\bar{2}$]C and [$\bar{1}\bar{1}2$]B. If twins are nucleated such that each

growth segment is of equal length, the resultant fiber axis will be [00$\bar{1}$] in terms of the common B orientation. Figure 5.6 (b) shows a similar case but in this case the fiber axis is [110] in terms of A. The difference between figure 5.6 (a) and (b) is given by the twin alternative configurations forming angles of 70.5° and 109.5° between the crystals, respectively. The <100> and <110> fiber orientations are extreme cases. The fiber axis can vary anywhere between <100> to <112> to <110> if the lengths of the crystal segments are unequal. Based on this model, Shamsuzzoha and Hogan [12] also explained the branching of the fibers as an extension of the same mechanism with the twin configuration governed by the local diffusion conditions.

Figure 5.6: Schematic representation of the "zigzag" growth in a strontium modified alloy. Orientation relationships in a fiber with effective [00$\bar{1}$] (a)and [110] (b) growth axes [12]

Following the idea of the adsorption of the modifying element on {111}$_{Si}$ facets, in 1987, Lu and Hellawell [40] proposed the impurity induced twinning (IIT) model. In this model, the authors looked for a common trait that could explain which elements modify the eutectic silicon. They considered in detail the possible relevance of the atomic radius of the modifying agent by calculating what would be a suitable size of the impurity atom to change the {111} stacking sequence and promote the formation of a twin when adsorbed on the solid-liquid interface. The authors assumed silicon growth by extension of step sources across the {111} planes. The modifier "poisons" the growth by the accumulation of adatoms at those steps. Figure 5.7 shows a 011 projection where an impurity atom of appropriate size forces the next silicon atom to miss one regular close packed position and so, continue in the alternative stacking sequence creating a twin. The geometrical calculation of the necessary hard sphere size to fulfil this condition resulted in a radius ratio of $r_{(modifier)}/r_{(silicon)} \approx 1.646$. Table 5.2 shows a line between ytterbium (Yb) and lanthanum (La) for this "ideal" ratio and a cross (x) for elements that were reported to have some kind of influence on the eutectic phase.

At the time when the impurity induced twinning (IIT) model was proposed, there were no characterization methods with enough chemical resolution to prove the hypothesis by direct observation. This model was considered a valid explanation for the formation of twin in the silicon phase although there were incongruencies with experimental evidence. Sodium, for example, is

much more effective than calcium [14,15] although it has a larger difference from the "ideal"; and ytterbium and lanthanum only refine the silicon plates instead of forming the beneficial coral structure seen with sodium or strontium additions [16–18,20]. Factors other than the atomic radius -such as melting points, vapor pressures or oxide formation-, were also qualitatively considered by Lu and Hellawell [40], but they were rather inconclusive.

Table 5.2: Possible modifying additions in order of atomic radii as proposed by Lu and Hellawell [40]

Element	At. Rad r (Å)	r/r_{si}	mp (K)	VP at 1000 K (atm.)	$-\Delta G$ Oxide (kJ/mol 1000 K)	K $\frac{[MO][Al]}{[Al_2O_3][M]}$	Effect
Cs	2.63	2.37	301	1.675	156		
Rb	2.44	2.08	311	1.451	185		
K	2.31	1.97	336	0.732	209		
Ba	2.18	1.85	998	$5 \cdot 10^{-5}$	482	20	x
Sr	2.16	1.84	1042	$1 \cdot 10^{-3}$	480	15	x
Eu	2.02	1.72	1095	$1.8 \cdot 10^{-4}$	~500		x
Ca	1.97	1.68	1112	$2.6 \cdot 10^{-4}$	509	$4 \cdot 10^2$	x
Yb r^*	1.93	1.65	1097	$5.6 \cdot 10^{-3}$	~500	$1.5 \cdot 10^2$	?
La	1.87	1.59	1193	10^{-6}	487		x
Na	1.86	1.58	371	0.2	367	$2.7 \cdot 10^{-5}$	xx
Ce	1.83	1.56	1071	10^{-16}	497		x
Pr	1.82	1.55	1204	10^{-13}	524		x
Nd	1.82	1.55	1283	10^{-11}	452		x
Sm	1.81	1.54	1345	10^{-5}	510		
Y	1.81	1.54	1796	10^{-15}	506		
Gd	1.79	1.52	1584	10^{-14}			
Tb	1.77	1.51	1633				
Mo	1.76	1.50	1743	10^{-10}			
Er	1.75	1.49	1795	10^{-11}			
Li	1.52	1.29	454	10^{-3}	560		
Al	1.4310	1.22	933	$5.3 \cdot 10^{-11}$	457	comparison	
Si	1.1755	1.00	1683	$8.9 \cdot 10^{-17}$	354		

x signifies reported modifying effect. The horizontal line corresponds to the hard sphere radius ratio for impurity induced twinning, r^*.
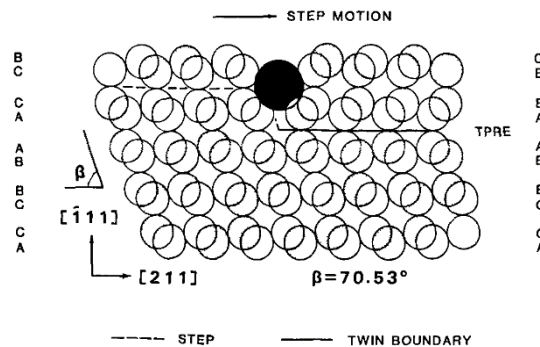
Figure 5.7: Schematic showing the impurity induced twinning model on a 011 plane projection. Impurity atom (modifying agent) with an appropriate size would promote the formation of a twin by forcing silicon to grow on the alternative {111} stacking sequence [40].

5.4.3 Modification effect on eutectic nucleation

The addition of a modifying element also influences the nucleation of the eutectic phase in Al-Si alloys. The study of the cooling curves during solidification shows a depression of the nucleation temperature (T_N), minimum temperature before recalescence (T_{Min}) and growth temperature (T_G)

in modified alloys (Figure 5.8) [119,122–124]. Thermal analysis is routinely used to study the effect of modification on nucleation and growth enabling the identification of phase formation. This analysis is made by the combination of the cooling curve (temperature over time) and its first derivative showing the solidification rate of the alloy. The nucleation temperature (T_N) of the eutectic phase is defined as the point where the first silicon crystals are formed and start to grow releasing latent heat. This temperature is identified by a change in the slope of the cooling curve that can be clearly identified by the first derivative of the cooling curve [16]. The minimum temperature (T_{Min}) shows the point where the latent heat due to eutectic growth equals the heat flow out of the system. This depends on the cooling rate and the heat capacity of the system [18]. After this point, the release of latent heat is higher than the heat extraction from the system and the temperature rises until the growth temperature is reached (T_G). The growth temperature corresponds to the nearly horizontal part of the eutectic arrest and is defined as the maximum reaction temperature after recalescence [123]. The difference $\Delta T = T_G - T_{Min}$ is known as the recalescence of the eutectic arrest. Thall and Chalmers [82], and Hanna *et al* [119] showed depressions of ≈6 K in the nucleation and growth temperatures of sodium modified alloys. They also showed a depression of primary silicon nucleation in modified hyper-eutectic alloys, while primary aluminum remains unchanged. They concluded that the depression in the nucleation of the eutectic phase is predominantly related to a change in the nucleation of the silicon phase. Another distinctive characteristic of the modified alloy is that, while the eutectic arrest is depressed, the melting temperature remains almost unaffected [82,83,119]. The difference between melting and freezing temperatures was shown to be dependent on the amount of modifier in the sample. Higher concentrations of the modifier in an alloy result in higher differences between melting and freezing temperatures [83]. Thall and Chalmers [82] pointed out that when the modifier content was very low, the eutectic solidification took place in two stages: the first at the normal temperature and the second at a lower temperature characteristic of a modified alloy. Several studies have confirmed the depression of the eutectic reaction temperatures for additions of strontium [100,122–124], calcium [14–16], barium [16], europium [13,17,56], yttrium [16] and rare earth metals [16–18,20]

Thermal analyses of Al-Si alloys clearly depict a retarding effect of the eutectic nucleation by the addition of modifying elements. However, for a complete analysis of the eutectic nucleation, it is essential to consider the role of phosphorus. Phosphorus is deliberately added in hypereutectic Al-Si alloys to refine primary silicon by an increased silicon nucleation on aluminum phosphide (AlP) [7,125,126]. Contrarily, in the eutectic phase, silicon is coarsened in the presence of phosphorous [123,127,128]. Phosphorus content also affects the modification of the eutectic silicon and larger modifier concentrations are needed in alloys with higher phosphorus levels [7,125]. Thus, the control of the phosphorus content is a major key to ensure the reproducibility of the modification treatment.
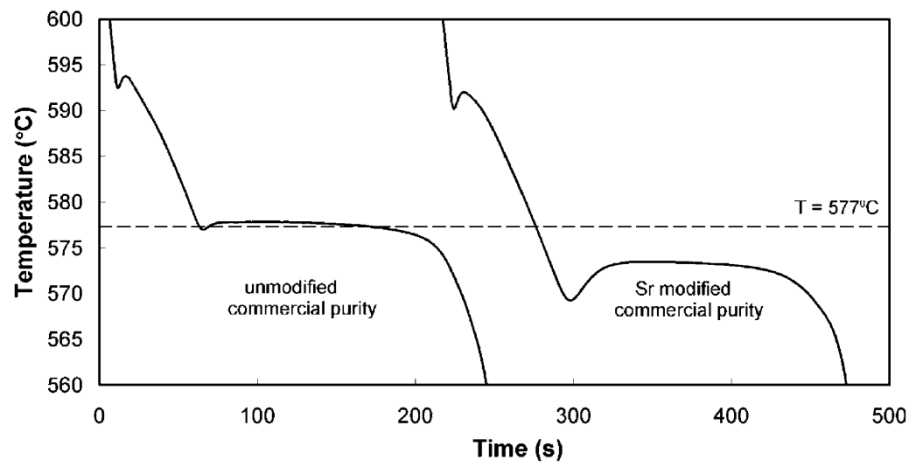
Figure 5.8: Comparison of cooling curves from unmodified and Sr-modified hypoeutectic Al-10 wt% Si alloys with commercial purity. The primary aluminum reaction presents almost no change, while the eutectic reaction is depressed to lower T_N, T_{Min} and T_G and higher recalescence [123]

The Al-Si-P ternary system and particularly the L → (Al) + Si + AlP ternary reaction was calculated showing a phosphorus concentration threshold value between zero and 7.4 ppm for all hypoeutectic compositions [129,130]. For Al-7 wt% Si-P with phosphorus contents higher than 3.7 ppm, AlP forms prior to eutectic silicon acting as nucleation sites. For phosphorus contents lower than 3.7 ppm this is not possible, with silicon starting its precipitation before AlP [131]. Ludwig *et al* [128] showed that increasing the phosphorus concentration from 2 to 3 ppm resulted in a transition from nucleation on the mold walls with planar front and a strong dependence of the thermal gradient, to nucleation in the vicinity of the primary aluminum dendrites with a dramatic increase in the number of grains.

Because the threshold level of phosphorus that exert a significant difference in eutectic nucleation is extremely low and the presence of further impurities also play a role on nucleation, the entrained droplet experiment is often used to study nucleation kinetics in these alloys [13,127,132–134]. In this setup, impurities can be isolated and clean heterogeneous nucleation can be studied. The technique consists of two stages: first, the alloy is rapidly solidified by melt spinning to produce a microstructure consisting of finely dispersed eutectic droplets embedded in a higher melting point aluminum matrix; and subsequently, the low melting point eutectic droplets are re-melted and slowly cooled in a thermal analyzer to record the solidification characteristics of the eutectic phase. The advantage of this setup is that impurities segregate into a small number of droplets, leaving a large number of droplets where clean nucleation conditions can be studied. The nucleation undercooling can then be quantified by differential scanning calorimetry (DSC). A DSC is a thermal analysis technique that shows the change of heat capacity of a material as a function of temperature. In the case of Al-Si eutectic, the DSC curve shows normally two exotherms: one first sharp peak that corresponds to the solidification of eutectic droplets at the grain boundaries, and a second broader peak at lower temperature that corresponds to the entrained droplets. The undercooling of this second exotherm is related to the ability of heterogeneous nucleation in clean conditions. Ho and Cantor [127] used this method in

1995 to show a strongly increased undercooling when the content of phosphorus was decreased to less than 2 ppm in Al-3 wt% Si. Commercial purity alloys (up to 10 ppm P) showed centrally located particles containing aluminum and phosphorus consistent with AlP and increasingly higher nucleation undercoolings with decreasing amount of phosphorus [122,124,128]. Insufficient number of AlP particles to effectively nucleate silicon heterogeneously causes a strong reduction in the number of eutectic grains and considerable refinement of the microstructure (Figure 5.9 (a,b)) [123,127]. The refinement is explained by the higher solidification front interface velocity derived from the low number of nucleation events. Given a constant rate of heat extraction, the inverse relationship between the solid-liquid interface velocity and surface area of the eutectic grains results in a finer eutectic structure [122,123,128]. The addition of modifying elements to commercially pure alloys was shown to have a comparable effect than decreasing the phosphorus content (comparison of Figure 5.9 (a, b and c)). In alloys with sodium addition, DSC analyses showed increased undercooling for eutectic nucleation. A possible explanation is the formation of the competing phase Na_3P that consumes phosphorus, decreasing AlP nucleation sites. Similarly, other competing phases were proposed in alloys with other modifiers such as Sr_3P_2 [133,134] or YbP [18]. However, no direct evidence of these phases was ever shown.

The effect of strontium was extensively studied in literature depicting a density of eutectic grains two orders of magnitude lower than in the equivalent unmodified alloy [122,124] and the size of the eutectic grains at least one order of magnitude larger [123,135]. The local structure of strontium was shown to be that of Al_2Si_2Sr by means of synchrotron based extended X-ray absorption fine structure (EXAFS) spectroscopy [136]. Several studies proposed the poisoning or removal of AlP by the formation of Al_2Si_2Sr [122,124]. Pre-eutectic Al_2Si_2Sr surrounding a P-rich particle was shown by EDX analysis on a TEM sample [137]. The formation of pre-eutectic Al_2Si_2Sr was corroborated by DSC and Scheil simulation with Thermo-Calc [133,134]. Eiken *et al* [131] showed a critical threshold of strontium of 80 ppm in hypoeutectic alloys with 7 wt% Si and 5 ppm P. If the strontium content is lower than 80 ppm, AlP solidifies before eutectic silicon. However, for higher strontium contents, the Al_2Si_2Sr phase precipitates before eutectic silicon and after AlP, leaving a solidification sequence L → (Al) → AlP → Al_2Si_2Sr → Si. This calculation agrees with the postulate that Al_2Si_2Sr can nucleate on AlP particles reducing silicon's nucleation potential. DSC analysis of Al-5 wt% Si modified with 500 ppm Eu also showed the formation of pre-eutectic Al_2Si_2Eu phases suggesting the possibility of poisoning of AlP also in this system [13].

As an alternative for AlP nucleation sites of the eutectic phase, Shankar *et al* [138] proposed that eutectic silicon nucleates on β-(Al,Si,Fe) phases forming ahead of primary aluminum dendrites. The addition of strontium increases the viscosity of the eutectic liquid ahead of the α-aluminum dendrites [139]. Since the viscosity is proportional to the surface tension, the authors argue that the presence of strontium changes the wetting angle between the eutectic liquid and the β-(Al,Si,Fe) particles. If the viscosity is sufficiently high, the eutectic phases cannot nucleate at the eutectic temperature and significant undercooling of the melt occurs. However, Lu and Dahle [72]and Li *et al* [134] could not find evidences suggesting that β needles nucleate eutectic silicon. On the contrary, it was proven by Cho *et al* [137] that both, pre-eutectic β-Al_5FeSi and eutectic

silicon, nucleate on phosphorus-rich nuclei. Higher phosphorus contents cause an increase in the nucleation temperature of β-Al$_5$FeSi suggesting that this iron-rich intermetallic nucleates at lower undercooling because of the larger number of phosphorus-based nuclei. The Al-Si eutectic nucleation frequency decreases further when the iron concentration in the alloy increases. This means that the AlP particles are consumed by both, Al$_2$Si$_2$Sr and β-Al$_5$FeSi, before eutectic solidification. Shankar *et al* [139] showed a depression of the eutectic nucleation temperature for higher iron content that supports these results. The inter-relationship between strontium and iron on eutectic nucleation events shows that eutectic growth undercooling is not an exclusive characteristic of strontium modification, but is strongly related to the presence of additional impurities in commercial alloys as it was stated before by McDonald *et al* [123] based on the analysis of cooling curves.
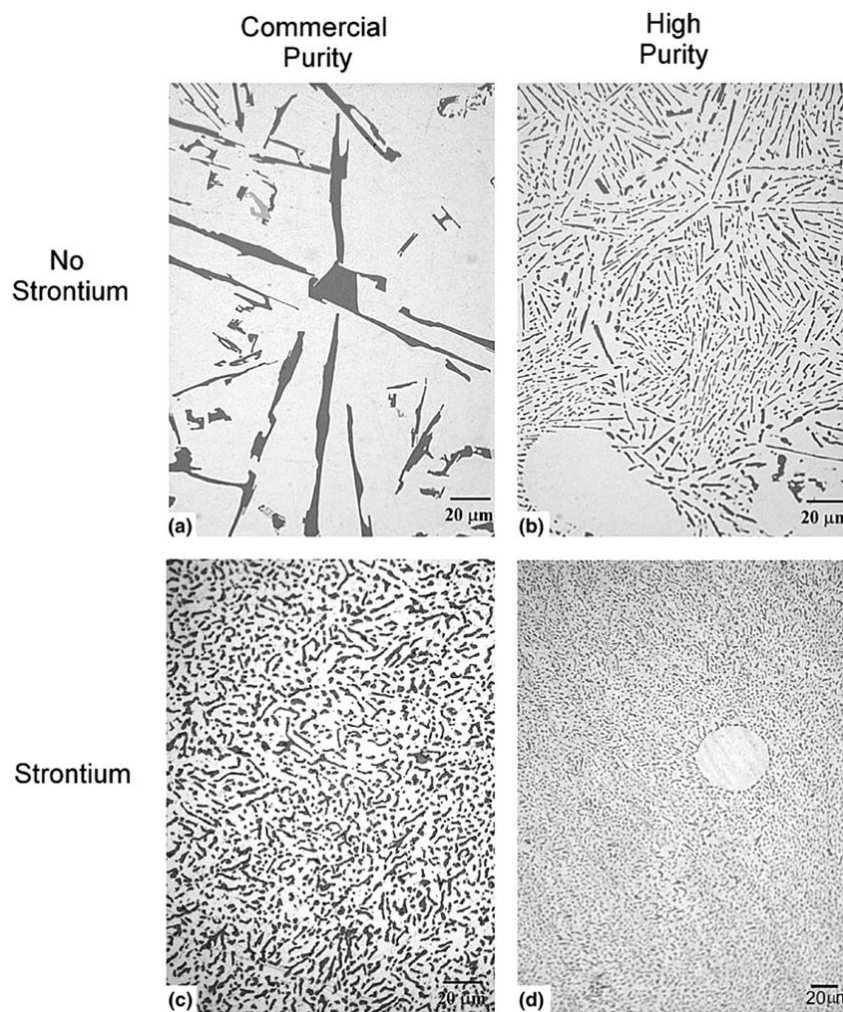
Figure 5.9: Eutectic microstructures: unmodified alloys with (a) commercial purity, and (b) high purity; strontium modified alloys with (c) commercial purity, and (d) high purity [123]

The decrease in eutectic nucleation frequency is accompanied by changes in the nucleation mode. Dahle *et al* [140] showed three solidification modes (figure 5.10): (a) nucleation at or adjacent to the wall, and growth opposite to thermal gradient; (b) nucleation of the eutectic phase on primary

aluminum dendrites; and (c) heterogeneous eutectic nucleation on nucleant-particles in the interdendritic liquid. Quenched samples showed growth type (b) in hypoeutectic unmodified alloys with the eutectic phase formed close to the tips of the dendrites (figure 5.10(b)). In this case, primary and eutectic aluminum had the same crystallographic orientation [122,124,135,140,141]. In contrast, alloys with 70 and 110 ppm Sr showed eutectic grains starting solidification at the center of interdendritic channels in an "independent" nucleation as depicted in figure 5.10 (c) [122,124,135,140]. Small eutectic aluminum grains in these modified samples showed no orientation relationship to the surrounding aluminum dendrites [141]. Interestingly, a sample modified with 500 ppm Sr exhibited growth associated to the dendrites, like unmodified alloys (figure 5.10 (b)). The authors argue that strontium containing particles such as Al_2Si_2Sr in samples with a low strontium level, might promote independent nucleation, while these particles become too large at higher strontium levels causing the reversion in nucleation mode [140].

(a) (b) (c)
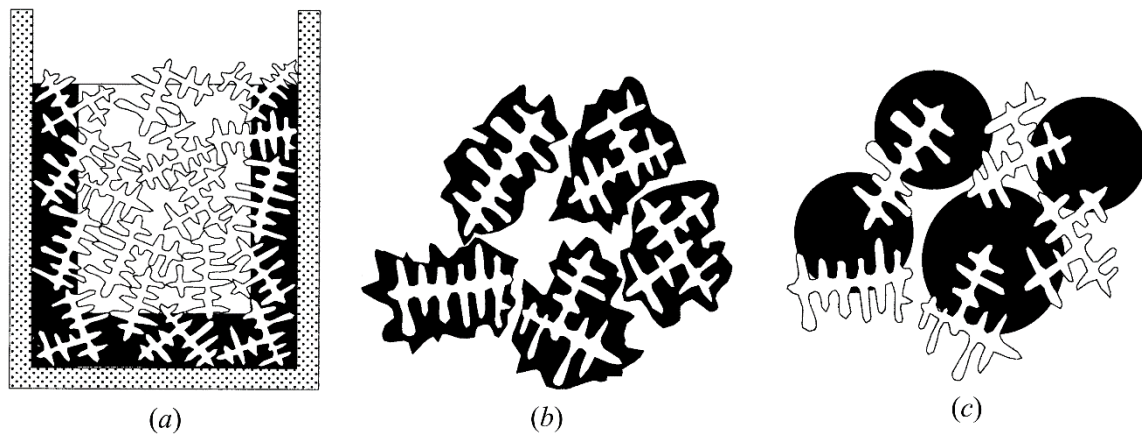
Figure 5.10: Possible eutectic growth modes in Al-Si alloys (eutectic phase illustrated in black): (a) front growth opposite to the thermal gradient; (b) nucleation on primary aluminum dendrites; and (c) independent heterogeneous nucleation in interdendritic spaces. [140]

In summary, it has been shown by several studies, that the nucleation of the eutectic phase is inhibited by the addition of a modifying element. Considering the following equation:

$$q = \bar{V}AL$$

where q is the total rate of heat extraction, $\bar{V}$ the average interface velocity, A the solidification interface area and L the latent heat of fusion per unit volume. If fewer eutectic grains are nucleated in a modified alloy, the solid / liquid interface area (A) will be smaller than in the unmodified case. In order to maintain a constant rate of heat extraction (q), the interface velocity ($\bar{V}$) of the modified alloy will increase to compensate for the decrease in area (A). The higher interface velocity has been accounted in literature for the refinement of the structure inside the eutectic grains. Several elements, for example all rare earths (except for europium) only refine the eutectic microstructure but are not able to produce the coral-like growth of silicon [20]. The plate-

to-coral transition is believed to be independent of the change in the nucleation mode [123,131,140] and it is rather a consequence of the additional effect of the modifier during growth.

5.4.4. Recent developments

Efforts to reveal the distribution of the modifier elements in the eutectic phase show sub-micrometer strontium-rich intermetallics (most likely Al_2Si_2Sr) adjacent to eutectic silicon crystals [100,142]. A relatively homogeneous distribution of strontium and sodium is shown to be exclusively incorporated into the silicon phase [100,142,143]. Although these studies were able to confirm the relevance of the modifier in the silicon phase, the reported lateral resolutions of about 50 nm are not enough to disclose how crystallographic defects in this phase are formed.

The first APT results showing the local distribution of the modifying element in the Al-Si eutectic showed segregations of strontium together with aluminum and silicon [144−147]. These studies showed segregations with varying compositions of 2.6-2.8 at% Sr, 6.2-11 at% Al and 86.4-91 at% Si, and proposed the formation of $SrAl_4Si_{33}$ or $SrAl_2Si_{88}$ intermetallic phases to cause the multiplication of twins and restrict silicon growth. These phases have never been shown for the Al-Si-Sr system, although several ternary phases were calculated [148]. Nevertheless, these early investigations proved the potential of APT to study eutectic modification.

6. Sample preparation and Characterization

A combination of characterization techniques has been used in this thesis for the study of the eutectic modification in Al-Si alloys. This chapter gives a basic description of the sample preparation and the methods used including: mechanical polishing, SEM, EDX, EBSD, FIB, (S)TEM and APT.

6.1 Al-Si alloys

The compositions of the analyzed alloys are summarized in Table 6.1.

Table 6.1: List of the alloys analyzed in this thesis.

Modification	Si (wt%)	X = Sr, Na, Eu, Yb (wt. ppm)	Al	
Unmodified	7	--	Balance	Directional solidification
Unmodified	5	--	Balance	Conventional casting
Strontium	7	150	Balance	Directional solidification
Sodium	5	19	Balance	Conventional casting
Sodium	5	160	Balance	Conventional casting
Europium	5	500	Balance	Conventional casting
Ytterbium	5	6100	Balance	Conventional casting

6.1.1 Al – 7 wt% Si

Al-7 wt.% Si with and without 150 wt. ppm Sr were produced at the Foundry Institute at RWTH Aachen by directional solidification in a Bridgman furnace at a cooling rate of 0.25 K/s and a temperature gradient of 15 K/mm. High purity silicon and aluminum (Al5N5) were melted at the corresponding proportions. An aluminum master alloy containing 15 wt% Sr was added to modify the samples with 150 wt. ppm Sr.

6.1.2 Al – 5 wt% Si

Al – 5 wt% Si with no additions and with 19 wt. ppm Na, 160 wt. ppm Na, 500 wt. ppm Eu and 6100 wt. ppm Yb were manufactured with high purity silicon chips (5N) and Al (5N). Sodium was added using elemental sodium (2N8, 99.8) supplied in vacuum-packed aluminum foils. Europium and Ytterbium were added by the aluminum master alloys Al - 2 wt% Eu and Al – 5 wt% Yb.

Conventional casting samples were produced by electric resistance melting of the charge material in a boron-nitride coated clay-graphite crucible at 720 °C - 750 °C and then casted using gravity

die casting. Prior to casting, no degassing treatment was performed. The average cooling rate was about 20 K / min (20 C / min).

6.2 Scanning electron microscopy – SEM

Scanning electron microscopy (SEM) is a standard technique to characterize alloys from nanometer to micrometer length scales. The sample is irradiated with a high energy (1 – 30kV) focused electron beam that interacts with the electrons of the atoms in the sample analyzed. Secondary electron, backscattered electrons and characteristic x-rays are produced from the interaction of the primary electron beam with the sample [149]. For this investigation, a FIB / SEM Dual-station Helios 600 (FEI company) was used.

6.2.1 Secondary electron imaging – SE

Secondary electrons (SE) are generated from a narrow volume near the primary beam impact area and, therefore, the imaging resolution can approximate the size of the focused electron beam. Secondary electrons are loosely bound outer shell electrons from the specimen atoms that are excited by the inelastic scattering of beam electrons. They have low energy of less than 50 eV, with 90 % of them emitted with less than 10 eV. The important consequence of their low kinetic energy is the shallow escape depth in the order of few nanometers [149]. SE imaging was performed at a voltage of 5 kV and currents in the range of 86 pA to 1.4 nA. Two secondary electrons detectors were used during this investigation: an Everhart-Thornley detector (ETD) and a through-the-lens detector (TTL).

ETD uses a scintillator to convert electrons to light and transmit them through reflection in a light guide to a photomultiplier. Photons are then transformed back into electrons multiplied in a cascade until they reach the final collector. The face of the scintillator is metal coated with a bias positive potential to accelerate the SE to a sufficient energy to generate light in the scintillator. The scintillator is surrounded with a Faraday cage with a separate bias potential to increase the collection of SE with higher geometric efficiency.

The TTL detector is a scintillator with a high bias positioned above the objective lens. Only the SE that pass through the lens bore are detected. The disposition of the detector completely eliminates the SE coming from remotely produced electrons from BSE colliding with the bottom of the lens and chamber walls. The TTL detector is especially advantageous when used together with the "snorkel"-type lens. The strong magnetic field of this lens extends from the polepiece directly to the specimen below the physical lens. Lens aberrations are small due to the reduced working distance (reduced focal length) and, therefore, high-resolution images are possible [149].

6.2.2 Backscattered electron imaging – BSE

Backscattered electrons (BSE) are beam electrons that interacted with the electrical field of the specimen atoms and were elastically scattered along new trajectories with small or no loss of kinetic energy. The beam electron can suffer several deflections before leaving the specimen backscattered. Because of these repeated deflections, the interaction volume from which BSE emerge is larger than the size of the incident beam and, consequently, the resolution lower than SE. However, the important characteristic of BSE is that the probability of elastic scattering increases with the atomic number (Z) by a relationship of approximately Z^2. Primary electrons interact strongly with the positive charge of the nucleus of heavy atoms. This characteristic allows for compositional contrast or also called Z contrast. Due to their penetration depth, BSE can carry information from subsurface features of the specimen and therefore, this signal is generally not considered surface-sensitive [149]. BSE imaging was performed at voltages of 5 and 10kV and currents in the range of 0.34 to 1.4nA.

A high sensitivity solid state backscattered detector was used for this investigation (low-voltage / high-contrast detector - vCD). Silicon diode detectors operate on the principle of electron-holes production induced in a semiconductor by energetic electrons. They have the form of a thin wafer placed parallel to the surface of the specimen below the electron column.

Figure 6.1 compares SE and BSE contrasts for the eutectic phase in unmodified and strontium modified Al- 7 wt% Si-0.3 wt% Mg alloys. The compositional and channeling contrasts of BSE electron allows for the clear identification of eutectic Al_2Si_2Sr ternary phases and twin boundaries in silicon.
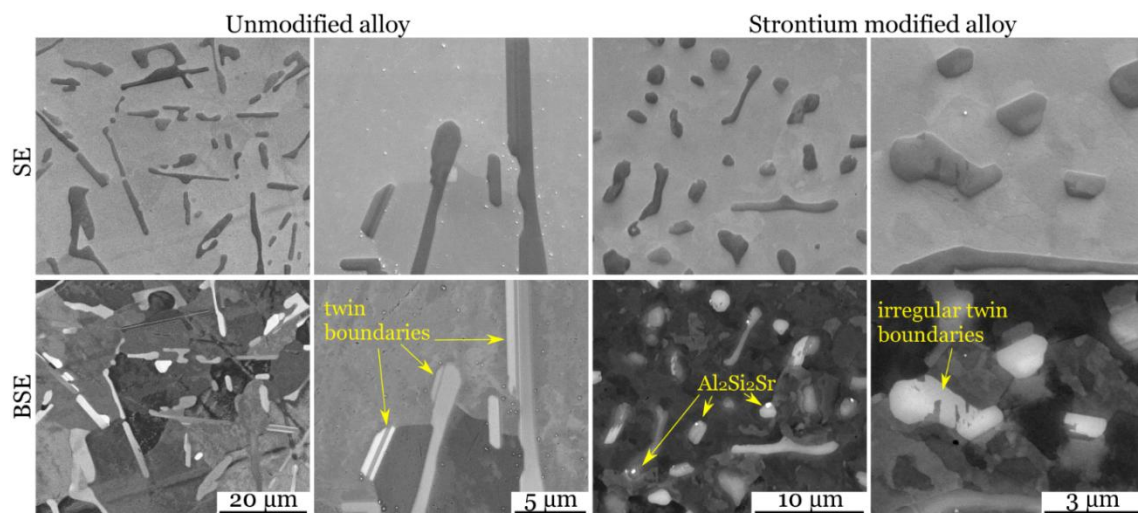
Figure 6.1: Scanning electron microscopy images of unmodified and strontium modified Al-7 wt% Si-0.3 wt% Mg alloys. Comparison of secondary electron (SE) and back-scattered electrons (BSE) contrasts.

6.2.3 Energy dispersive X-ray spectroscopy – EDX

Beam electrons can interact with the specimen atoms and eject inner shell electrons. The atom is left in an excited state and to go back to the ground state, an electron of an outer shell can transition to fill the inner-shell vacancy. This energy difference between electron shells is a characteristic value for each element and it can be released as a photon of electromagnetic radiation called characteristic x-ray [149]. Characteristic x-rays emitted from the sample were used in energy-dispersive x-ray spectroscopy (EDX) as a routine analytical technique for qualitative elemental detection and phase assignment. For this investigation, an Apolo XV detector (EDAX Company) was used for EDX measurements at voltages of 15 and 20 kV and currents of 5.5 and 11 nA.

EDAX ZAF Quantification (Standardless)
Element Normalized
SEC Table : Default

Element	Wt %	At %	K-Ratio	Z	A	F
AlK	21.02	41.98	0.1071	1.1432	0.4445	1.0028
SiK	19.18	36.81	0.1091	1.1989	0.4739	1.0004
EuL	59.80	21.21	0.5112	0.8449	1.0118	1.0000
Total	100.00	100.00				

Element	Net Inte.	Bkgd Inte.	Inte. Error	P/B
AlK	2943.86	6.26	0.39	470.01
SiK	2628.08	4.62	0.42	569.15
EuL	1197.82	1.92	0.62	623.81
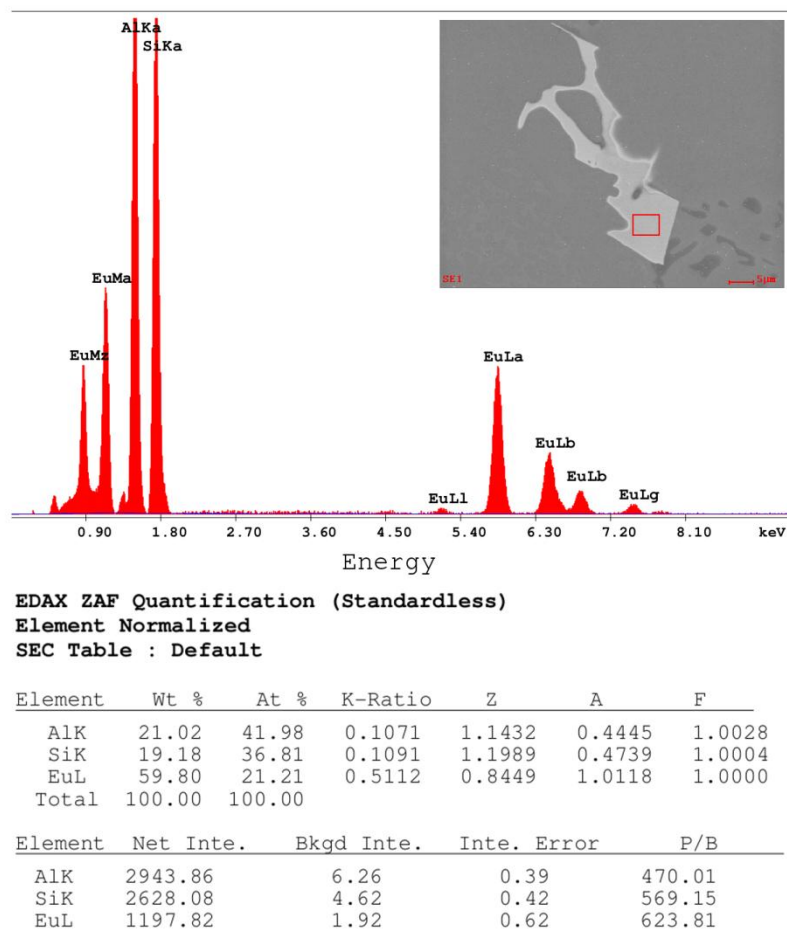
Figure 6.2: Al_2Si_2Eu phase identification by energy dispersive X-ray (EDX) spectroscopy in an Al-5 wt% Si hypoeutectic alloy with 500 ppm Eu. Acquisition with 11 nA and 15 kV electron beam.

The compositional information in EDX comes from a region ~1 μm in both diameter and depth with accuracy of approximately 1-2% in composition. At the typical beam currents in SEM, EDX spectrometers are capable of detecting x-rays of all elements above an atomic number of 4. Figure 6.2 shows an example of Al_2Si_2Eu phase recognition in an Al-5 wt% Si with 500 ppm Eu.

6.2.4 Electron backscattered diffraction – EBSD

In EBSD, the last elastic scattering event of BSE at the last plane before escaping the specimen is analyzed. To get a maximal intensity in the diffraction patterns, the surface of the specimen is tilted 70° from the horizontal. Primary electrons do not penetrate as deeply in the strongly tilted specimen and electrons with small scattering angles can escape the surface and be backscattered, increasing the backscattering coefficient. For every plane in the specimen, BSE fulfill the Bragg diffraction condition in all directions and Kossel-cones are formed. The so-called Kikuchi lines, are a section of the Kossel-cone wall on the detector's screen. For every plane in the specimen there are two Kikuchi-lines and the distance between them is determined by the crystallographic structure. A large part of the stereographic triangle is imaged at the same time which facilitates the determination of the crystal orientation. Kikuchi lines are transformed into points by a Hough transformation. Hough peaks are detected and back-transformed to index the Kikuchi lines. The relative orientation of the grains and phases in the specimen is determined with respect to a reference orientation. A charge-coupled-device (CCD) camera is used for the acquisition and a specialized software makes an automated indexing of the backscattered Kikuchi patterns received from the sample [149].

Transmission Kikuchi diffraction (TKD) was also used in this study. This is a similar technique to EBSD but uses scattered electron that are forward transmitted from a TEM sample for the diffraction analysis. The advantage of this alternative is the improved resolution due to the small interaction volume in an approximately 50 nm thick TEM lamella [150,151]. Because transmitted electrons are used, the tilt of the specimen is of 45° in the opposite direction of the 70° used for EBSD. The working distance is of 4-5 mm in comparison to the 9-11 mm used for EBSD [151].

For the analysis of results in this work, the data was presented in two ways: pole figures (PFs) and inverse pole figures (IPFs). PFs represent a stereographic projection of the crystallographic directions in the analyzed sample. A stereographic projection is a two-dimensional projection of the three-dimensional unit cell such that the angular relationship between planes and directions in the crystal can be read from the projection. Each pole shows the direction of the crystal plane normal with respect to a sample reference frame. An (hkl) pole figure shows the distribution of the {hkl} poles in the sample. IPFs are orientation maps that show the distribution of crystallographic orientations in relationship to a reference sample direction [152].

In this investigation, an EDAX Hikari detector within the FIB/SEM workstation was used to record EBSD and TKD data using an electron beam of 20 kV / 22 nA and 30 kV / 5.5 nA, respectively; and post-processing was performed using the OIM Analysis software (EDAX). IPFs were used to identify twin boundaries and $\Sigma 9$ boundaries in eutectic silicon for different samples (figure 6.3(b)); and PFs from silicon and neighboring Al_2Si_2X (X=Eu, Yb) phases were used to find parallel orientations during the growth of these phases as evidence of heterogeneous epitaxial growth. Al_2Si_2X crystal structures from literature [153–155] were added to OIM Data Collection 7 database by means of the built-in structure creation wizard. Figure 6.3 shows an example in the

Al- 5 wt% Si with 500 ppm Eu. For the calculation of pole figures, data points from the intermetallic compound and neighboring silicon were extracted using the grain highlighting feature of OIM Data Analysis 7 software. This feature allows a point-and-click selection of data points which belong to continuous grains based on a predefined tolerance angle (here 5°) (figure 6.3 (c, d)). Selected data points were then used for pole figure calculation. In contrast to classic cleanup techniques which involve a more or less severe data modification, the highlighting technique is no more than an orientation based selection of data points.
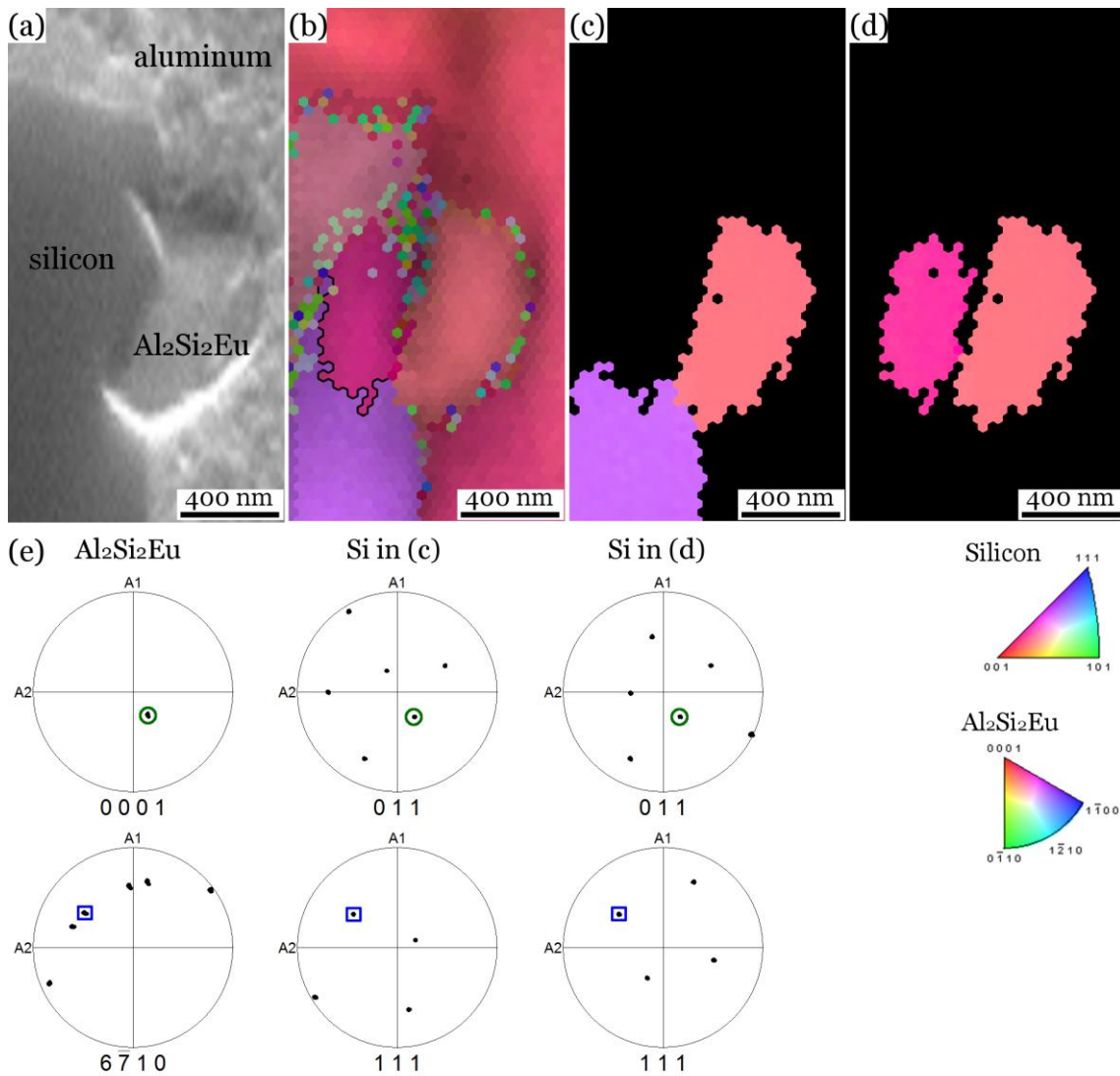
Figure 6.3: EBSD analysis in an Al-5 wt% Si with 500 ppm Eu. Crystal orientation relationship between silicon and Al_2Si_2Eu: (a) SEM image of Al_2Si_2Eu in contact with silicon and aluminum. (b) Overlaid IPF (color) and image quality (IQ) (brightness) maps of region in (a). Uncleaned raw data, step size 30 nm. Black line depicts a $\Sigma 3$ twin boundary between the silicon orientations. (c,d) Orientation-based extracted IPF maps of neighboring silicon and Al_2Si_2Eu. (e) PFs of Al_2Si_2Eu and both silicon orientations in (c) and (d). Circles and squares highlight parallel plane normals in the crystals.

6.3 Focused ion beam – FIB

A focused ion beam (FIB) with a liquid metal ion source (LMIS) allows the controlled sputtering of small volumes of material in a sample and for this reason, is especially useful for site-specific sample preparation for TEM and APT. In this work, a SEM / FIB dual-beam station Helios Nanolab 600 (FEI Company) with a gallium (Ga+) source was used.

6.3.1 Sample preparation for TEM

An in-situ lift-out procedure in the SEM/FIB dual station was used for site-specific TEM sample preparation. The region of interest (ROI) can be chosen by surface inspection with SE or BSE and the orientation of the lamella can be determined by surface EBSD. Figure 6.4 shows an example of preparation in the Al-Si eutectic phase. Electron and ion induced platinum were deposited on the ROI to protect the region from gallium implantation and avoid later curtain effect during thinning. A script was used to automatically cut-out an approximately 1 µm thick lamella and the specimen was lifted-out and transferred to a 3 mm TEM grid with an Omniprobe micromanipulator. Cleaning cross-section patterns with progressively decreasing currents are used for thinning on both sides. A last low voltage cleaning step with 2 kV is done to minimize artifacts like amorphization , ion implantation and creation of atomic defects in the lamella after thinning with 30 kV.
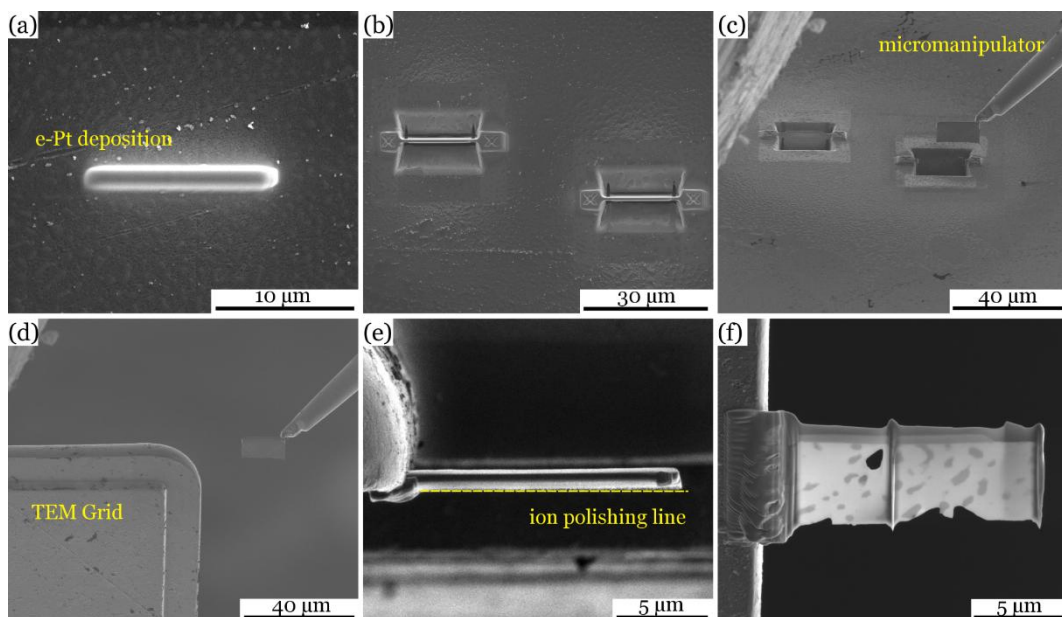
Figure 6.4: FIB sample preparation for TEM lamella. (a) Electron induced platinum deposition. (b) Lamellas after TEM-Wizard. (c) In-situ lift-out of a lamella with a micromanipulator. (d) Transfer to a TEM Grid for thinning. (e) Lamella perpendicular to the ion beam for thinning. (f) Thinned lamella ready for analysis.

6.3.2 Sample preparation for APT

APT requires a high electric field on the specimen to field evaporate atoms from its surface. For this reason, the specimen needs to be needle-shaped with an end radius smaller than 100 nm. If it is assumed that the specimen ends in a hemispherical cap of radius R and a high voltage (V) is applied, the electric field (F) at the apex of the specimen can be estimated by the idealized equation of a charged sphere:

$$F = \frac{V}{k_f R}$$

where k_f is a field factor between 3 and 5 accounting for the specimen shape and the electrostatic environment [156]. The end radius of the specimen is practically limited by the required evaporation fields of around 10 to 50 V/nm, and a maximal applied voltages of up to around 10 kV.
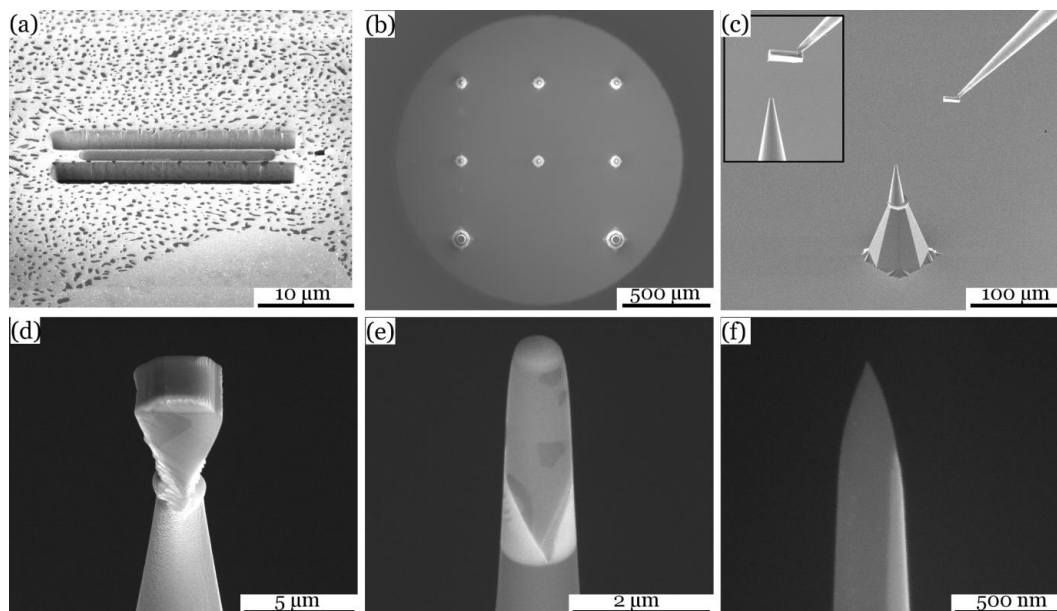
Figure 6.5: FIB sample preparation for APT. (a) Cut-out of a triangular wedge in the eutectic phase. (b) Array of micro-posts to mount the lift-out. (c) Triangular wedge attached to a micromanipulator being transferred to one of the posts shown in (b). (d) Cut piece attached by platinum deposition to the holder. (e) First thinning steps by annular milling. (f) APT specimen ready to run.

Needle-shaped specimens for APT can be prepared in two ways: electro-chemical polishing and FIB-assisted methods. The main advantages of electro-chemical polishing are avoiding the implantation of gallium ions and its low-cost; however, no site-specific preparation is possible. For Al-Si alloys, a further problem of electro-polishing is the selective etching that leads to inhomogeneities in the form of the specimen. For these reasons, FIB methods were used in this work. The lift-out method described by Thompson *et al* [157] was used to prepare specimens of

very fine eutectic structure and to study eutectic aluminum. Figure 6.5 shows the main steps of this method: a 20 μm long triangular wedge is cut-out from the sample and transferred to an APT sample holder with an array of 36 posts. The wedge is then divided into 6 to 8 pieces attached to single posts and an annular milling process is then used to gradually thin the specimens up to the final required size. A last low-energy milling step with 2 kV is used to minimize gallium induced damage.

Since this work specially focuses on the analysis of eutectic silicon, a phase-selective sample preparation method was developed to prepare silicon specimens. In this method, aluminum was deep etched and single silicon branches or plates were lifted out by FIB. Details concerning this method can be found in ***Paper V*** of this thesis.

6.4 Transmission electron microscopy – TEM

In transmission electron microscopy (TEM) and scanning transmission electron microscopy (STEM), a high-energy electron beam interacts with a thin specimen. If the specimen is thin enough to be electron transparent (~20-100 nm), beam electrons are transmitted through the specimen and collected after interacting with its atoms. Due to the small interaction volume, (S)TEM resolution is significantly increased with respect to SEM. TEM can be used to observe the crystal structure, crystal defects or grain boundaries down to the atomic scale. TEM's high-resolution makes it an adequate technique for correlation with APT. In this investigation, TEM and STEM were used to characterize the crystal defects in modified silicon. Since stacking faults (SF) / nanotwins and $\sum3$ twin boundaries, all of them on $(111)_{Si}$ planes, are the most frequent defects, selected area electron diffraction (SAED) patterns were used to align the specimens in $<110>_{Si}$ zone axes to see the defects on edge (figure 6.6).
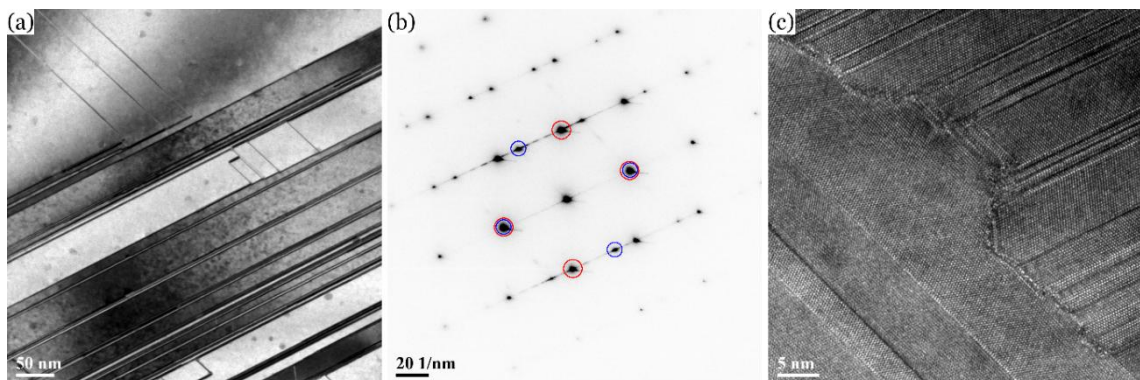
Figure 6.6: Eutectic silicon in an Al-7Si-0.3Mg with 250 ppm Sr. (a) Twinned silicon imaged with bright field diffraction contrast. Signal through a 20 μm objective aperture. (b) Selected area electron diffraction (SAED) pattern aligned in $<110>_{Si}$ zone axis. Red and blue circles highlight $\{111\}_{Si}$ reflections for the two mutually twinned silicon crystals in the specimen. (c) High resolution image showing twins, nanotwins and a grain boundary in detail.

TEM and STEM imaging and analysis in this work were performed in a Tecnai G2 TF 20 UT FEG (FEI Company) in micro and nanoprobe modes, an image-side aberration-corrected JEOL 2100F microscope and a JEM - ARM 200 F Cold FEG TEM/STEM equipped with a spherical aberration (Cs) probe and image correctors. All of them operated at 200 kV.

6.5 Atom probe tomography – APT

APT is an analytical technique that provides three-dimensional mapping of materials with atomic resolution. Surface atoms from a needle-shaped specimen are ionized, removed from the material and accelerated towards a detector. The removal of atoms from their own lattice, is field-induced by the combined effect of a standing electrostatic field and either high-voltage or laser pulses. In this investigation a LEAP 3000X HR (CAMECA Company) was used. Measurements were performed at repetition rates of 200 – 250 kHz, pressure lower than 1.33×10^{-8} Pa, evaporation rate of 5 atoms per 1000 pulses and temperatures between 40 and 60 K. Laser-pulsed APT was applied to measure silicon specimens using a laser with a wavelength of 532 nm, pulse length of 10 ps, and a pulse energy of 0.3–0.4 nJ. Voltage measurements were use to measure aluminum specimens at 20% pulse fraction. Datasets were reconstructed and analyzed with IVAS™ 3.6.8 sofware (CAMECA)

6.5.1 Working principle and experimental setup

Müller [158] explained field evaporation by the *image hump model*. In this model, a sufficiently strong electric field fully ionizes a surface atom and lowers the energy barrier of the ion to escape the surface. Later, Gomer [159,160] proposed the alternative *charge-exchange model* that assumes that ionization and escape take place simultaneously while the atom is desorbing. In any case, the energy barrier that bonds the atom to the surface is overcome by thermal activation energy, although it is possible that in low-temperature regime, ion tunneling through the energy barrier also plays a role. One further model worth mentioning is the *post-ionization theory* [161,162]. The early models, assumed the direct transition of the surface atom into an *n*-charged ion. However, in the 1980s, it was shown that the ion leaves the surface with a single charge and is then subjected to one or more field ionization processes as it moves away from the surface. The number of post-ionization events increase with field. This theory was used to calculate the relative frequency of charge-states as a function of field for several elements in the periodic system. The resultant curves are called *Kingham curves* and are used nowadays as a rough estimation of the evaporation field during a measurement. For a deeper review about field evaporation theories refer to [163].
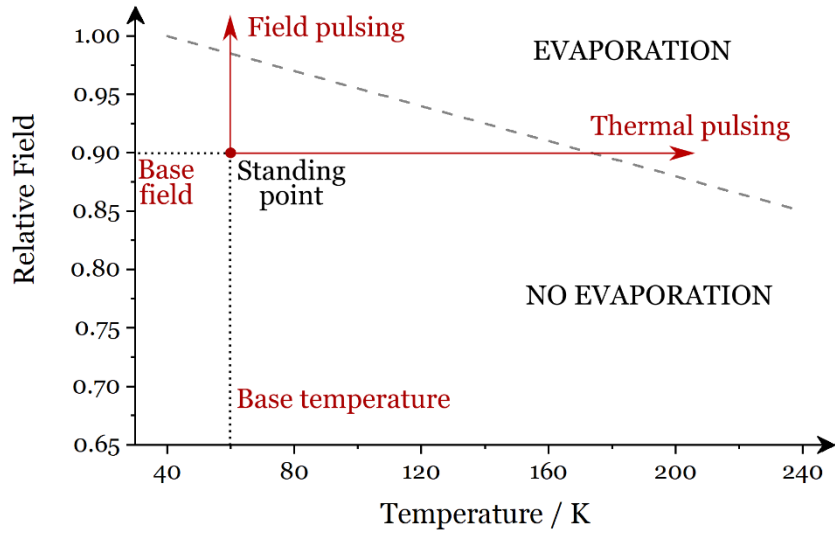
Figure 6.7: Schematic of the required electric field to evaporate as a function of temperature (thermal activation energy). Pulsing modes are depicted by arrows starting from a standing point.

In a practical sense, the removal of atoms from the specimen is a function of the applied field and temperature. Each element exhibits a characteristic behavior and a slope as shown schematically in figure 6.7. To achieve a controlled evaporation atom-by-atom, two mechanisms can be used: field-pulsing and thermal-pulsing. Starting from a standing point at a DC field (base field) and base temperature, the electric field can be increased by high-voltage pulses at a constant temperature or, on the contrary, temperature can be increased by laser pulses at a constant field. In both cases, enough energy is transferred to the specimen to evaporate an atom from the surface (figure 6.7).
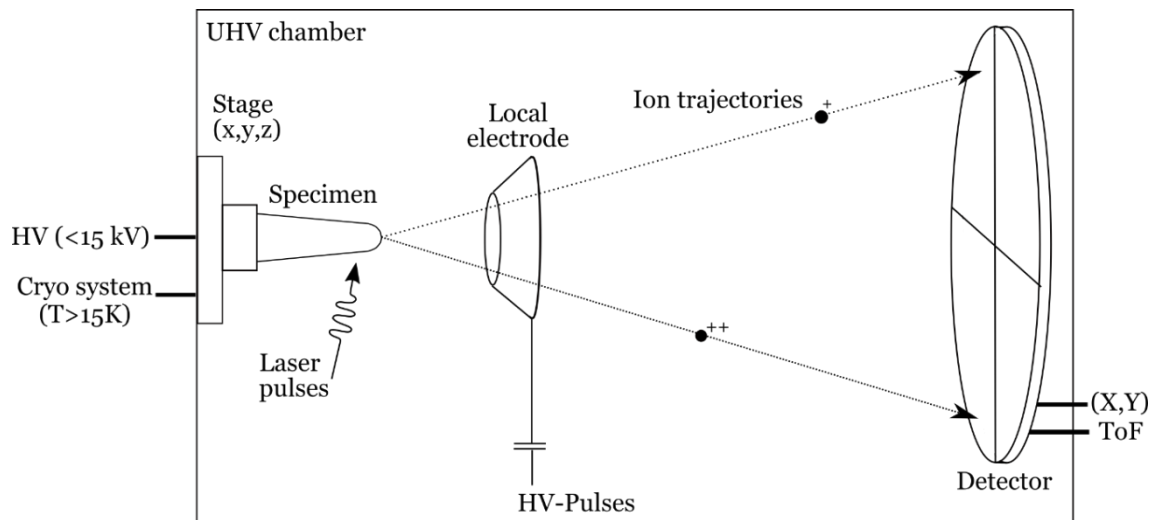
Figure 6.8: Basic experimental setup of an atom probe. [UHV: ultra-high vacuum; HV: high voltage; ToF: time of flight].

53

Figure 6.8 shows the basic experimental setup of an atom probe. The needle-shaped specimen is mounted on a three-axis translation stage and cooled to cryogenic temperatures between 20 to 80K. The base electrostatic field is generated by a high-voltage (HV) supply connected to the specimen and the voltage pulses are applied to a local electrode positioned in front of the specimen. The system operates under ultra-high vacuum (UHV) below 10^{-8} Pa.

The detection system is able to record the position of impact of each ion. Ions are converted into electrons and multiplied in a stack of microchannel plates (MCP). The electrons then come to a delay-line position-sensitive detector, where they are focused on two or three polarized conductive lines. The electrons induce electric signals on all lines and are propagated along them till the end of the line. Using the time and distance covered, the X and Y coordinates of the impact on the detector are calculated.
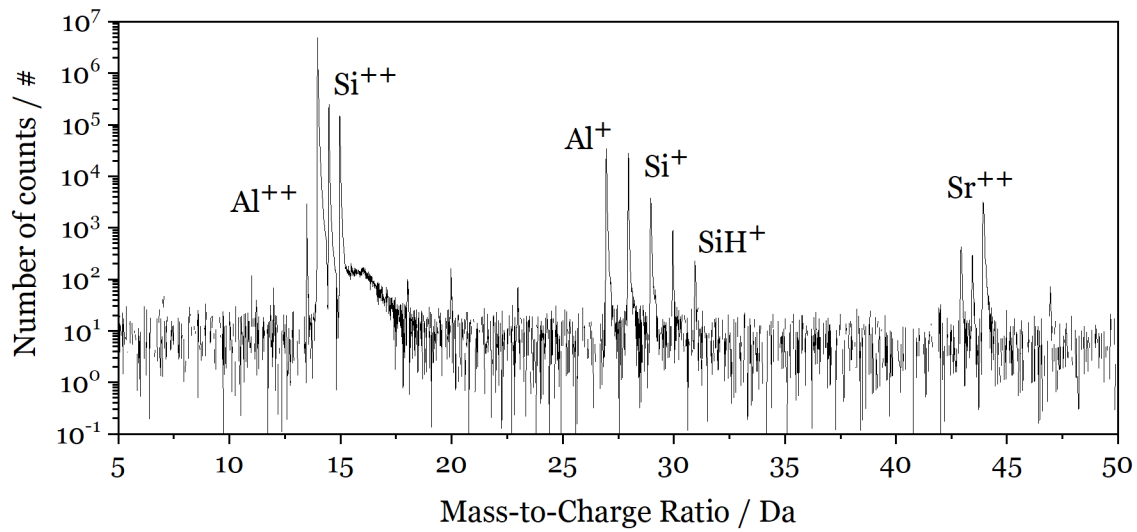
Figure 6.9: Mass-to-charge spectrum of eutectic silicon in Al- 7 wt% Si with 150 ppm Sr.

The chemical nature of the ions is determined by a time-of-flight (ToF) spectrometer. The time of flight of an ion (t_{flight}) is defined as the time between its departure from the specimen -given by the pulse that triggers evaporation- and its arrival, when the ion impacts the detector. The ion will be accelerated in the electrostatic field by the potential energy available $E_p = neV$, where V is the total voltage and ne, the charge of the ion. The total kinetic energy after departure $E_k = \frac{1}{2}mv^2$ will be equal to the potential energy, and the velocity can be defined as $v = \frac{L}{t_{flight}}$, where L is the flight length between the specimen and the detector [164]. The mass-to-charge ratio ($\frac{m}{n}$) of the ion can be then directly determined by:

$$neV = \frac{1}{2}mv^2 \;\rightarrow\; \frac{m}{n} = 2eV\left(\frac{t_{flight}}{L}\right)^2$$

By knowing the mass-to-charge ratio of each ion, it is possible to identify their chemical nature. All mass-to-charge values in a measurement are showed in a single spectrum, where the natural

isotopic abundance ratios assist in the assignment of the peaks. The peaks were ranged at the full width tenth maximum (FWTM) in this investigation. Figure 6.9 shows a mass-to-charge spectrum from a eutectic silicon specimen of an Al- 7 wt% Si with 150 ppm Sr.

6.5.2 Data reconstruction, visualization and analysis

After acquisition, the raw data is reconstructed and analyzed in the dedicated software IVAS 3.6.8 (CAMECA). This software uses an algorithm that calculates the position of the ions by assuming that they fly in a straight line from the surface of the specimen, with these lines originating from a single projection-point along the axis of the specimen [165]. The position of the projection-point depends on the compression of the field lines during evaporation, which is related to the distribution of the field at the surface of the specimen and its shape. It is also assumed that the atoms are evaporated layer-by-layer from the outermost surface inwards. This means that the sequence of detection reveals the depth position of the atoms in the specimen, the z-coordinate. This information together with the lateral position (x,y) deduced from the reverse projection of the impact coordinates given by the position-sensitive detector determine the (x,y,z) coordinates for each atom in the volume [166].

Four parameters are set by the operator during reconstruction: the evaporation field F_e, image compression factor ICF, field factor k_f (section 6.3.2) and detection efficiency. In this investigation, the detection efficiency of 37% given for the LEAP 3000 XR system was used. Silicon specimens were reconstructed with F_e of 30-33 V/nm, ICF of 1.65 and k_f of 3.3. For aluminum specimens F_e of 19 V/nm, ICF of 1.5 and k_f of 3.3 were adopted.

The tools used for visualization and analysis of the data in this investigation are iso-concentration surfaces, one-dimensional (1D) concentration profiles, proximity histograms and background corrected compositions in regions of interest (ROI).

An iso-concentration surface is a 3D representation of a threshold value. Concentrations are interpolated from average voxel values and connected triangles build an interface for a set value [167]. This is a powerful means of visualization and also the first step for the construction of proximity histograms. Proximity histograms represent concentration profiles with respect to distance from an interface allowing the analysis of sophisticated features in a reconstruction. Compositions are computed normal to the iso-surface for each point and, therefore, independent from the interface geometry [168].

1D concentration profiles are an alternative method to show the evolution of composition. Concentrations are plotted along the length of a rectangular or cylindrical ROI across a feature in the reconstruction. A fixed number of counts was used in this work to divide the ROI into slices called *blocks*. Concentrations in each block are calculated and displayed as a function of length. The *block size* was optimized to maximize the signal-to-noise ratio. In principle, proximity histograms might seem as a more advanced representation of the data, but in cases where iso-

concentration surfaces are difficult to obtain, for example due to low solute concentrations, 1D profiles are a better choice.

To count the amount of solute atoms in small clusters from one to a couple of lattice distances in size, tight ROI around each cluster were constructed and exported. The solute atoms were counted after a time-independent background subtraction included in IVAS software.

6.5.3 Trajectory aberrations and local magnification effects

Differences between the original structure and the reconstructed data may arise from a number of reasons in APT [164]. In the samples analyzed in this work, the main concern was trajectory aberrations. The deflection in the flight of the ions is related to the distribution of the electric field at the surface of the specimen. Localized variations of the electric field can induce undesirable lateral displacement of the ion just after evaporation, which induces zones of high or low density of ions in the reconstruction [169,170].

When a precipitate requires a considerably different field to evaporate than the matrix, trajectory aberrations may occur. In this work, clusters with a high content of aluminum need a significantly lower field than the silicon matrix around them. This produces a flattening of the surface and an inward deflection of the ion trajectories that causes an increased density of hits in the detector. Low-evaporation field solutes may also be evaporated prematurely, i.e. before more protruding atoms, which would result in an artefact in the depth coordinate. When considering 2 - 4 nanometer clusters, a convolution of the matrix with the precipitate may occur resulting in an overestimation of the matrix element [171–173]. Because of this uncertainty, relative solute ratios Al:M (M = Sr, Na or Eu) rather than absolute concentrations were considered in this work. The standard deviations in the Al:M ratios are attributed to the combined effect of the limited number of solute atoms in the small clusters and the detection efficiency of APT (~ 37 %).

7. Summary of included papers and contribution to the field

This investigation contributes to understand the growth change of eutectic silicon when small concentrations of modifying elements are added to hypoeutectic Al-Si alloys. Figure 7.1 shows a graphical summary of the three cases of alloys studied in this research revealing the structure and atomic distribution in the silicon phase. A model explaining the multiplication of crystal defects in silicon and its microstructural change is proposed as the outcome of this thesis.
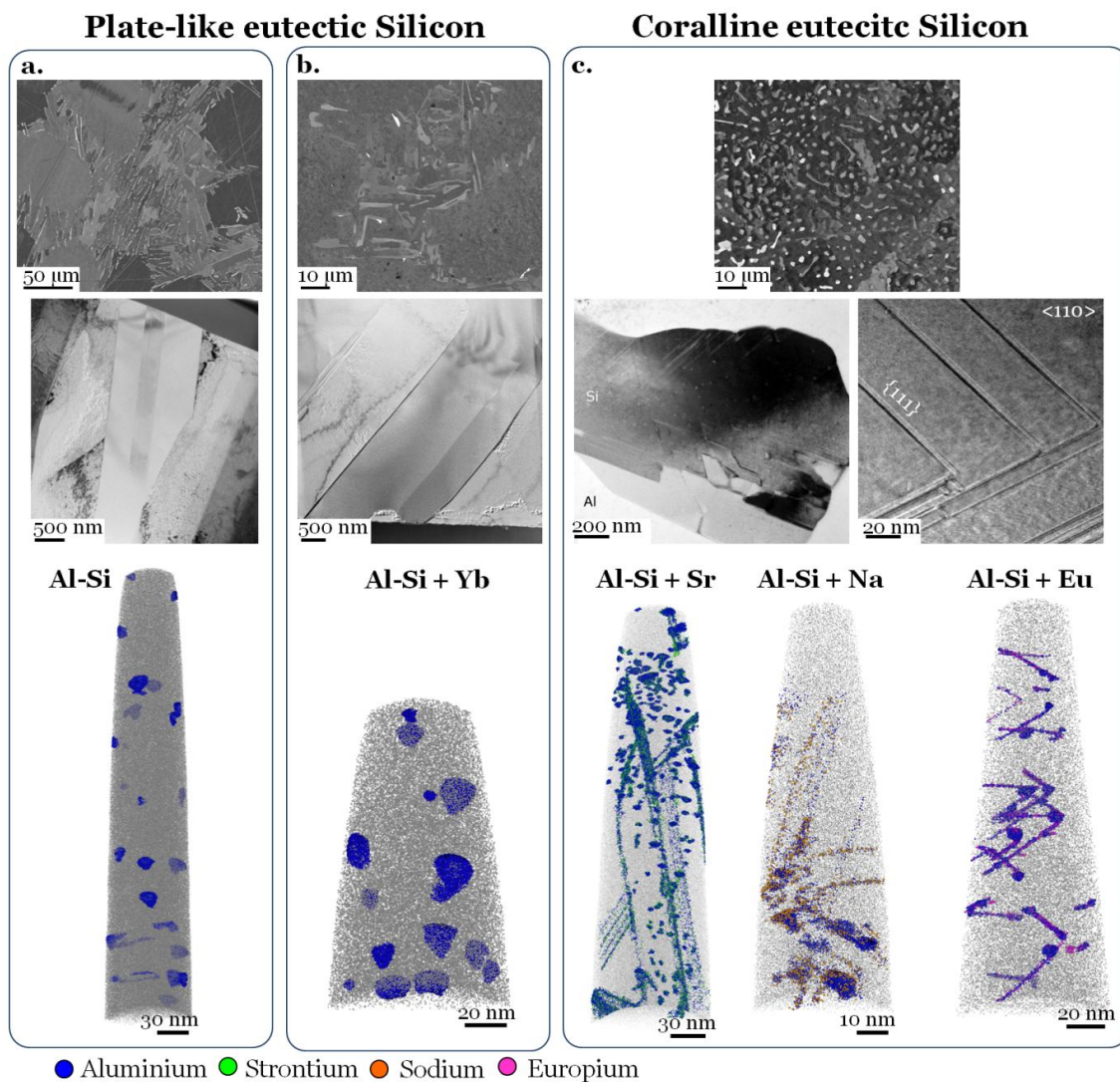
Figure 7.1: Overview of the cases studied: (a) Al-Si alloy with no addition of modifier as a reference structure; (b) Alloy with ytterbium addition. Refined plates, but no coralline structure; (c) Alloys with addition of the three most powerful modifiers known to date: sodium, strontium and europium. Coral-like structure.

Paper I. Comparison of segregations formed in unmodified and Sr-modified Al-Si alloys studied by atom probe tomography and transmission electron microscopy

The atomic distribution of solutes in eutectic silicon of an Al – 7 wt% Si alloy with and without strontium addition was studied by APT and (S)TEM.

The silicon phase in the unmodified alloy showed straight twins across the plates and spherical coherent particles. APT depicted small particles (5 to 10 nm) with 5-15 at% Al, larger particles (13-18 nm) with a core-shell structure with 40-50 at% Al in the shell, and a ring-segregation decorated with 6 at% Al. These aluminum enrichments are small pockets of liquid entrapped during solidification and impurity clouds on silicon defects such as dislocation loops.

The modified alloy with 150 ppm Sr showed irregular twin boundaries and a high density of crystal lattice defects correlated to Al-Sr-Si segregations. Depending on their morphology, the segregations were divided into three categories: rod-like, planar and particle-like (rounded). Rod-like segregations have one dimension significantly larger than the other two and often show a v-shape arrangement with precipitates at their intersection. They are responsible for changes in the silicon lattice stacking sequence and contribute to the irregular growth and smoothening of the boundary between eutectic aluminum and silicon. Planar segregations are the result of the progressive accumulation of aluminum and strontium at the silicon solid-liquid interface and favor the formation of grain boundaries and irregular twin boundaries. Rounded segregations are also found in the modified alloy, with the distinction that all contained strontium atoms together with aluminum and regions with high density of small segregations responsible for the silicon growth obstruction.

The amount of aluminum and strontium in solid solution in silicon was of 430 ± 160 at-ppm and 40 ± 10 at-ppm, respectively. The total content of aluminum trapped in silicon was nearly 4 times higher in the modified alloy and most of the strontium in the alloy segregated to the silicon phase. Based on the Al:Sr content ratio in the rod-like and planar segregations a local ternary reaction is proposed to assist in the formation and pinning of crystal defects.

Paper II. Cluster formation at the Si / liquid interface in Sr and Na modified Al-Si alloys

Atom probe tomography was used to compare the effect of strontium and sodium additions in the eutectic silicon phase of hypoeutectic Al-Si alloys. Spherical precipitates, stacking faults (SFs) and twin lamellas (TLs) depicted with TEM in both alloys show one-to-one correlation with APT results showing spherical, rod-like and planar clusters in silicon. The silicon growth is obstructed in both cases by the formation of crystal defects with solute-enriched clusters. However, the solute ratios Al:M (M= Sr or Na) in the clusters were 2.92 ± 0.46 in the case of strontium and 1.07 ± 0.23 for sodium, showing a distinctly different interaction of aluminum with each of the modifiers. The

heterogenous formation of clusters of the ternary compounds AlSiNa and Al_2Si_2Sr at the silicon / liquid interface is proposed to alter the silicon microstructure by imparting growth flexibility. These ternary compounds are reported in literature for ternary invariant reactions in Al-Si-Sr and Al-Si-Na systems at nearly the same temperature and composition as the Al-Si binary eutectic reaction. The efficiency of a modifier is suggested to be closely related to its ability to form ternary compound clusters at the faceted silicon solidification front during growth.

Paper III. Eutectic modification by ternary compound cluster formation in Al-Si alloys

The effects of europium and ytterbium additions in hypoeutectic Al-Si alloys were studied. The addition of europium modifies the eutectic silicon to a coral-like structure, while ytterbium yields a refined plate-like silicon structure. Backscattered electron images showed that both alloys form pre-eutectic and eutectic Al_2Si_2Eu and Al_2Si_2Yb phases. A substantial difference was found when comparing the silicon phases with APT. The alloy with europium addition presented numerous clusters containing europium and aluminum with the three morphologies consistent with Paper I and II: spherical, rod-like and planar. The average of the Al:Eu ratio for 35 rod-like and 4 planar clusters was of 2.25 ± 0.42, which agrees with the formation of Al_2Si_2Eu clusters at the crystallographic defects. On the contrary, no ytterbium was found in the silicon phase and only aluminum segregations similar to the unmodified alloy were present. It is proposed that the difference between these alloys is their ability to form early stage Al_2Si_2X clusters on the facets of silicon. The formation of clusters obstructs the silicon growth and increases growth flexibility causing a coral-like silicon structure. The crystallographic orientation relationship between silicon and Al_2Si_2Eu or Al_2Si_2Yb was studied by EBSD / TKD. The parallel plane normals: 111_{Si} // $6\bar{7}10_{Al2Si2Eu}$, 011_{Si} // $6\bar{7}10_{Al2Si2Eu}$ and 011_{Si} // $0001_{Al2Si2Eu}$ with misfits of the d-spacings smaller than 6 % were found between silicon and Al_2Si_2Eu, while no consistent orientation relationship was found between silicon and Al_2Si_2Yb. The interplanar spacing misfits between the $d(0002)_{Al2Si2X}$ and $d(110)_{Si}$ are 5.79% for Al_2Si_2Eu and 10.50% for Al_2Si_2Yb. The higher mismatch of the ytterbium phase adds strain energy to its nucleation, what makes Al_2Si_2Yb clusters less stable than Al_2Si_2Eu clusters on silicon facets. Based on these results, it is postulated that Al_2Si_2Yb needs a higher energy to heterogeneously form sub-critical clusters on silicon than Al_2Si_2Eu.

Paper IV. Nucleation and growth of eutectic Si in Al-Si alloys with Na addition

The nucleation and growth of sodium modified Al-Si alloys was studied in controlled sand casting and melt spun samples. TEM and APT analyses of controlled sand casting alloys showed a high density of twins and rod-like and spherical clusters containing sodium and aluminum atoms with Al:Na ratios of about 1-1.5. It is proposed that the spherical clusters might agree with the impurity induced twinning idea changing the silicon stacking sequence and promoting twin formation. The rod-like clusters can be related to the poisoning of twin plane re-entrant edges as proposed by

previous models. The rejection of sodium ahead of the solidification front was confirmed by a sodium enrichment of about 0.25 at% at the interface between eutectic aluminum and silicon.

Melt spun samples were used to study eutectic nucleation for sodium addition. DSC was used to measure the undercooling for nucleation of entrained droplets. Al-5 wt% Si without sodium showed an undercooling of 24 °C, while the addition of 19 ppm Na lead to a significant depression of the nucleation temperature (ΔT= 49 °C). This depression can be explained by the removal of AlP nucleation sites by the formation of the competing phase Na_3P. However, the entrained droplet undercooling for the alloy with 160 ppm Na decreased to 29 °C, indicating that the formation of Na_3P alone is not enough to explain the effect of sodium on nucleation.

Paper V. Phase selective sample preparation of Al-Si alloys for atom probe tomography

A method to selectively prepare eutectic silicon specimens for APT is presented. It is often said that in APT, the specimen itself is the "lens" of the microscope. The trajectory of the ions removed from the surface determine the magnification and are responsible for the later 3D-image formation. To obtain long and stable measurements of the silicon phase with a high quality mass-spectrum, aluminum eutectic surrounding the silicon branches was deep etched and silicon pieces were lifted-out attached to a micromanipulator in the SEM / FIB dual station. This specimens were transferred to an APT sample holder for final thinning. Two slightly adapted methods are given for rounded modified silicon branches and coarser unmodified silicon plates. Specimens prepared by this method had an extremely high success rate and yield during APT measurements. Density fluctuations and preferential retention due to the large difference between the evaporation field of aluminum and silicon were minimized.

7.1 Contribution to the field

The present investigation shows that all three elements that induce silicon plate-to-coral morphology transition - strontium, sodium and europium – contain nanometer sized clusters of solute atoms at the defects in silicon. The clusters have stoichiometries corresponding to compounds formed in the ternary eutectic reaction of each system. In contrast, the addition of ytterbium, which only refines the silicon plates but do not form corals, is unable to form ternary compound clusters in silicon.

The evidence of clusters containing aluminum apart from the modifying element, falsified the impurity induced twinning model which assumed the adsorption of single modifying atoms at the silicon growth interface, but confirmed the idea that the modifier is responsible for the multiplication of crystallographic defects in silicon.

We propose that the formation of ternary compounds clusters $AlSiNa$, Al_2Si_2Sr and Al_2Si_2Eu at the silicon / liquid interface during solidification restrict the silicon growth. The formation of ternary

compound clusters on silicon facets create growth steps and increase growth direction diversity. The incorporation of clusters onto the silicon surface explains the high density of crystallographic defects in silicon and the modification from plates to corals.

The parallel lattice plane-normals 011_{Si} // $0001_{Al2Si2Eu}$, 011_{Si} // $6\bar{7}10_{Al2Si2Eu}$ and 111_{Si} // $6\bar{7}10_{Al2Si2Eu}$ were found between Al_2Si_2Eu and silicon, and absent between Al_2Si_2Yb and silicon. We propose a favorable heterogeneous formation of Al_2Si_2Eu on Si. The misfit between 011_{Si} and $0002_{Al2Si2X}$ interplanar spacings shows a consistent trend with the potency of modification for several elements such as strontium, sodium, europium, calcium, barium, ytterbium and yttrium.

7.2 Outlook and future work

Based on the results obtained in this thesis some ideas for further work are presented.

7.2.1 APT analysis of modified Al-Si eutectic phase

APT proved to be a powerful analytical tool in the study of eutectic modification in Al-Si alloys. Continuing with the results in this thesis, the analysis of the silicon phase in high purity alloys with additions of calcium, yttrium and barium will give a complete outlook of the interaction of the modifying elements with aluminum and silicon at the solidification front and the formation of clusters and defects.

Further APT analysis of the Al / Si boundary in the eutectic phase for the different modification elements is also of interest. Paper IV shows an enrichment of sodium at the Al / Si interface. The comparison with additions of other modifying elements would enable a deeper understanding of the role that this enrichment plays during growth.

7.2.2 Calculation of phase diagrams and simulations

The results in this work show the relevance of phase formation in the ternary systems Al-Si-X, with X = Sr, Na, Eu or Yb. To the best of our knowledge, the Al-Si-Sr [115] and Al-Si-Na [114] phase diagrams were reported in literature, but Al-Si-Eu and Al-Si-Yb are still missing. These phase diagrams, particularly the liquidus surfaces, will assist in the interpretation of phase formation and solidification pathways during eutectic reaction.

Atomistic simulations of the crystallization at the eutectic solidification front are also needed. These simulations will unravel the structure of the melt just ahead of the crystallization interface and the cluster formation process. Li *et al* [99] performed calculations based on density functional theory with europium atoms placed in four different positions of a silicon twin boundary. However, in these calculations no aluminum atoms where considered, which differs with the experimental results shown in Paper III. Using another approach, Suzuki-Yamamoto *et al* [174] studied the stability of the crystal structure of the ternary intermetallics Al_2Si_2X (X = Ca, Sr, Ba, Eu, Y, Yb) over a wide range of temperatures showing their stability and proposing their possible

relevance for modification, but no calculation in the silicon lattice was performed. Moreover, no simulations were performed to visualize the undercooled melt in addition to the solid, with atomic-scale resolution. Force-field based molecular-dynamics (MD) simulations can be employed as an option to facilitate this [175]. Force field based simulations, rather than density-functional theory (DFT) would give access to relevant number of atoms over sufficiently large times to "equilibrate" the slightly undercooled melt close to the crystalline surface. An example of the potential of force field based simulations can be found in the work of Gao *et al* [176], who studied the moving crystallization front of CuZr from a high viscous melt.

7.2.3 Correlative characterization of the solidification front

The heterogeneous formation of clusters of ternary compounds on the eutectic solidification front is proposed to be one of the keys of modification. This hypothesis is based on "post-mortem" analysis, i.e. on completely solidified alloys. As a further study, we propose the comparison of the topology, crystal structure and concentration profile at the solidification front of unmodified and modified alloys in samples quenched during eutectic solidification. The study of the three-dimensional (3D) "frozen" solidification front at various length scales will allow the comparison of the eutectic growth modes and the clarification of the role of aluminum together with the modifier agent in the silicon crystal. Nano-CT (X-Ray computer tomography) or plasma FIB are techniques capable of giving 3D images to unveil the microstructural evolution and show the change of morphology of the solidification front. This analysis enables the study of the growth restriction due to the presence of the modifier at the growth front. EDX maps can give a rough idea of the concentration profile at both sides of the solidification front and help to recognize the exact position of the front. APT specimens at the growth front and at increasing distances from it can be used to determine the accumulation of the modifying element at the front during solidification. TEM can provide the structure of the crystallographic defects in the silicon structure and at the solidification front. The correlation of the atomic evolution at the growth front with the evolution at the micrometer scale leads to a global understanding of the solidification process and the formation of the coralline structure.

7.2.4 Interaction of modifying elements in Al-Si alloys with magnesium and iron

In this thesis, high purity binary Al-Si alloys were studied to understand the interaction between the modifying agent and silicon avoiding the effects of further impurities or alloying elements. The next step is to analyze more complex alloys such as Al-Si-Mg and Al-Si-Cu-Mg. These alloys are industrially relevant and the interaction between the modifier agent and these ternary and quaternary elements has not been studied at the atomic scale. APT analysis of the Mg_2Si and Al_2Cu phases and its boundary with eutectic aluminum and silicon would reveal whether a part of the modifying element is consumed by these phases. Additionally, the interaction of iron and its phases with the modifying elements has also not been studied at the atomic level.

8. References

[1]   J.G. Kaufman, E.L. Rooy, Aluminum Alloy Castings: Properties , Processes , and Applications., 2004.

[2]   M.M. Makhlouf, Solidification of Eutectic Alloys - Aluminum-Silicon, in: ASM Handbook, Vol. 15 Cast., 2008: pp. 312–316. doi:10.1361/asmhba0005212.

[3]   S. Khan, R. Elliott, Solidification kinetics of the unmodified aluminium-silicon flake structure, Acta Metall. Mater. 41 (1993) 2433–2439. doi:10.1016/0956-7151(93)90323-K.

[4]   W. Kurz, R. Trivedi, Overview No. 87 Solidification microstructures: Recent developments and future directions, Acta Metall. Mater. 38 (1990) 1–17. doi:10.1016/0956-7151(90)90129-5.

[5]   M.G. Day, A. Hellawell, The Microstructure and Crystallography of Aluminium-Silicon Eutectic Alloys, Proc. R. Soc. A Math. Phys. Eng. Sci. 305 (1968) 473–491. doi:10.1098/rspa.1968.0128.

[6]   A. Hellawell, The growth and structure of eutectics with silicon and germanium, Prog. Mater. Sci. 15 (1970) 3–78. doi:10.1016/0079-6425(70)90001-0.

[7]   J.E. Gruzleski, B. Closset, The treatment of liquid Aluminum-Silicon alloys, American Foundrymens Society, 1990.

[8]   A. Pacz, Alloy, 1,387,900, 1921.

[9]   V.L. Davies, J.M. West, Factors affecting the modification of the aluminium-silicon eutectic, J. Inst. Met. 92 (1963) 175–180.

[10]   H. Fredriksson, M. Hillert, N. Lange, The modification of aluminium-silicon alloys by sodium, J. Inst. Met. 101 (1973) 285–299.

[11]   D.C. Jenkinson, L.M. Hogan, The modification of aluminium-silicon alloys with strontium, J. Cryst. Growth. 28 (1975) 171–187. doi:10.1016/0022-0248(75)90233-X.

[12]   M. Shamsuzzoha, L.M. Hogan, The crystal morphology of fibrous silicon in strontium-modified Al-Si eutectic, Philos. Mag. A. 54 (1986) 459–477. doi:10.1080/01418618608243605.

[13]   J.H. Li, X.D. Wang, T.H. Ludwig, Y. Tsunekawa, L. Arnberg, J.Z. Jiang, P. Schumacher, Modification of eutectic Si in Al–Si alloys with Eu addition, Acta Mater. 84 (2015) 153–163. doi:10.1016/j.actamat.2014.10.064.

[14]   T.H. Ludwig, E. Schonhovd Dæhlen, P.L. Schaffer, L. Arnberg, The effect of Ca and P interaction on the Al-Si eutectic in a hypoeutectic Al-Si alloy, J. Alloys Compd. 586 (2014) 180–190. doi:10.1016/j.jallcom.2013.09.127.

[15]   T.H. Ludwig, P.L. Schaffer, L. Arnberg, Influence of Some Trace Elements on Solidification Path and Microstructure of Al-Si Foundry Alloys, Metall. Mater. Trans. A. 44 (2013) 3783–3796. doi:10.1007/s11661-013-1694-y.

[16]   A. Knuutinen, K. Nogita, S.D. Mcdonald, A.K. Dahle, Modification of Al – Si alloys with Ba , Ca , Y and Yb, J. Light Met. 1 (2002) 229–240. doi:10.1016/S1471-5317(02)00004-4.

[17] K. Nogita, H. Yasuda, M. Yoshiya, S.D. McDonald, K. Uesugi, a. Takeuchi, Y. Suzuki, The role of trace element segregation in the eutectic modification of hypoeutectic Al–Si alloys, J. Alloys Compd. 489 (2010) 415–420. doi:10.1016/j.jallcom.2009.09.138.

[18] J.H. Li, S. Suetsugu, Y. Tsunekawa, P. Schumacher, Refinement of Eutectic Si Phase in Al-5Si Alloys with Yb Additions, Metall. Mater. Trans. A. 44 (2012) 669–681. doi:10.1007/s11661-012-1410-3.

[19] K. Nogita, J. Drennan, A.K. Dahle, Evaluation of Silicon Twinning in Hypo-Eutectic Al-Si Alloys, Mater. Trans. 44 (2003) 625–628. doi:10.2320/matertrans.44.625.

[20] K. Nogita, S.D. McDonald, A.K. Dahle, Eutectic Modification of Al-Si Alloys with Rare Earth Metals, Mater. Trans. 45 (2004) 323–326. doi:10.2320/matertrans.45.323.

[21] R.N. Lumley, Introduction to aluminum metallurgy, in: R. Lumley (Ed.), Fundam. Alum. Metall. Prod. Process. Appl., First Edit, Woodhead Publishing, Cambridge, UK, 2011: pp. 1–20.

[22] S. Otarawanna, A.K. Dahle, Casting of aluminium alloys, in: L. R.N. (Ed.), Fundam. Alum. Metall. Prod. Process. Appl., Woodhead Publishing, Cambridge, UK, 2011: pp. 141–154.

[23] R.B.C. Cayless, Alloy and Temper Designation System for Aluminum and Aluminum Alloys, in: ASM Handbook, Vol. 2 Prop. Sel. Nonferrous Alloy. Spec. Mater., ASM International, 1990: pp. 15–28. doi:10.1361/asmhba0001058.

[24] K. Kirgin, Feeling the domino effect, Mod. Cast. 99 (2009) 34–36.

[25] European Aluminium Association. The Aluminium automotive manual - Cast alloys and products, (2002). https://www.european-aluminium.eu/media/1544/aam-products-6-cast-alloys-and-products.pdf (accessed November 15, 2018).

[26] W. Kurz, D.J. Fisher, Fundamentals of Solidification, Third Edit, Trans Tech Publications, Switzerland, 1992.

[27] S. Shankar, Eutectic Solidification - An Introduction, in: ASM Handbook, Vol. 15 Cast., ASM International, 2008: pp. 307–311. doi:10.1361/asmhba0005211.

[28] M.N. Croker, R.S. Fidler, R.W. Smith, The Characterization of Eutectic Structures, Proc. R. Soc. A Math. Phys. Eng. Sci. 335 (1973) 15–37. doi:10.1098/rspa.1973.0111.

[29] M.N. Croker, D. Baragar, R.W. Smith, Anomalous eutectic growth, J. Cryst. Growth. 30 (1975) 198–212. doi:10.1016/0022-0248(75)90090-1.

[30] K.A. Jackson, Liquid metals and solidification, American Society for metals, Cleveland, Ohio, 1958.

[31] R. Elliott, Eutectic solidification, Int. Mater. Rev. 22 (1977) 161–186. doi:10.1179/095066077791100363.

[32] D.M. Stefanescu, Science and Engineering of Casting Solidification, Second Ed., Springer, New York, 2009.

[33] M.R. Taylor, R.S. Fidler, R.W. Smith, Broken lamellar eutectic growth; Structure of the silver-bismuth eutectic, J. Cryst. Growth. 3–4 (1968) 666–673. doi:10.1016/0022-0248(68)90242-X.

[34] J.L. Murray, A.J. McAlister, The Al-Si (Aluminum-Silicon) system, Bull. Alloy Phase Diagrams. 5 (1984) 74–84. doi:10.1007/BF02868729.

[35] J. Barrirero, M. Engstler, N. Ghafoor, N. de Jonge, M. Odén, F. Mücklich, Comparison of segregations formed in unmodified and Sr-modified Al-Si alloys studied by atom probe tomography and transmission electron microscopy, J. Alloys Compd. 611 (2014) 410–421. doi:10.1016/j.jallcom.2014.05.121.

[36]   M.M. Makhluf, Solidification of Eutectic Alloys - Aluminum-Silicon, in: ASM Handbook, Vol. 15 Cast., ASM International, 2008: pp. 312–316. doi:10.1361/asmhba0005212.

[37]   H.A.. Steent, A. Hellawell, Structure and properties of aluminium-silicon eutectic alloys, Acta Metall. 20 (1972) 363–370. doi:10.1016/0001-6160(72)90030-2.

[38]   M. Shamsuzzoha, L.M. Hogan, Twinning in fibrous eutectic silicon in modified Al-Si Alloys, J. Cryst. Growth. 72 (1985) 735–737. doi:10.1016/0022-0248(85)90229-5.

[39]   S. Lu, A. Hellawell, Growth mechanisms of silicon in Al-Si alloys, J. Cryst. Growth. 73 (1985) 316–328. doi:10.1016/0022-0248(85)90308-2.

[40]   S. Lu, A. Hellawell, The mechanism of silicon modification in aluminum-silicon alloys: Impurity induced twinning, Metall. Trans. A. 18 (1987) 1721–1733. doi:10.1007/BF02646204.

[41]   M. Shamsuzzoha, L.M. Hogan, The twinned growth of silicon in chill-modified Al–Si eutectic, J. Cryst. Growth. 82 (1987) 598–610. doi:10.1016/S0022-0248(87)80004-0.

[42]   R.S. Wagner, On the growth of germanium dendrites, Acta Metall. 8 (1960) 57–60. doi:10.1016/0001-6160(60)90145-0.

[43]   D.R. Hamilton, R.G. Seidensticker, Propagation Mechanism of Germanium Dendrites, J. Appl. Phys. 31 (1960) 1165. doi:10.1063/1.1735796.

[44]   M. Shamsuzzoha, L.M. Hogan, D.J. Smith, P.A. Deymier, A transmission and high-resolution electron microscope study of cozonally twinned growth of eutectic silicon in unmodified Al-Si alloys, J. Cryst. Growth. 112 (1991) 635–643. doi:10.1016/0022-0248(91)90119-P.

[45]   K.F. Kobayashi, L.M. Hogan, The crystal growth of silicon in Al-Si alloys, J. Mater. Sci. 20 (1985) 1961–1975. doi:10.1007/BF01112278.

[46]   M. Shamsuzzoha, L.M. Hogan, Crystal morphology of unmodified aluminium-silicon eutectic microstructures, J. Cryst. Growth. 76 (1986) 429–439. doi:10.1016/0022-0248(86)90390-8.

[47]   X. Liu, Y. Zhang, B. Beausir, F. Liu, C. Esling, F. Yu, X. Zhao, L. Zuo, Twin-controlled growth of eutectic Si in unmodified and Sr-modified Al-12.7%Si alloys investigated by SEM/EBSD, Acta Mater. 97 (2015) 338–347. doi:10.1016/j.actamat.2015.06.041.

[48]   E. and P.J.H. Billig, Some observations on growth and etching of crystals with the diamond or zincblende structure, Acta Crystallogr. 8 (1955) 353–354. doi:10.1107/S0365110X55001084.

[49]   E. Billig, P.J. Holmes, New Observations on the Structure Germanium Dendrites, Acta Metall. 5 (1957) 53–54.

[50]   M. Kitamura, S. Hosoya, I. Sunagawa, Re-investigation of the re-entrant corner effect in twinned crystals, J. Cryst. Growth. 47 (1979) 93–99. doi:10.1016/0022-0248(79)90162-3.

[51]   F. Lasagni, a. Lasagni, E. Marks, C. Holzapfel, F. Mücklich, H.P. Degischer, Three-dimensional characterization of 'as-cast' and solution-treated AlSi12(Sr) alloys by high-resolution FIB tomography, Acta Mater. 55 (2007) 3875–3882. doi:10.1016/j.actamat.2007.03.004.

[52]   F. Lasagni, A. Lasagni, C. Holzapfel, F. Mücklich, H.P. Degischer, Three Dimensional Characterization of Unmodified and Sr-Modified Al-Si Eutectics by FIB and FIB EDX Tomography, Adv. Eng. Mater. 8 (2006) 719–723. doi:10.1002/adem.200500276.

[53]   A.M. Samuel, E.M. Elgallad, H.W. Doty, S. Valtierra, F.H. Samuel, Effect of metallurgical parameters on the microstructure, hardness impact properties, and fractography of Al-(6.5-11.5) wt% Si based alloys, Mater. Des. 107 (2016) 426–439.

doi:10.1016/j.matdes.2016.06.051.

[54] S. Joseph, S. Kumar, A systematic investigation of fracture mechanisms in Al-Si based eutectic alloy-Effect of Si modification, Mater. Sci. Eng. A. 588 (2013) 111–124. doi:10.1016/j.msea.2013.09.019.

[55] F. Lasagni, a. Lasagni, M. Engstler, H.P. Degischer, F. Mücklich, Nano-characterization of Cast Structures by FIB-Tomography, Adv. Eng. Mater. 10 (2008) 62–66. doi:10.1002/adem.200700249.

[56] F. Mao, G. Yan, Z. Xuan, Z. Cao, T. Wang, Effect of trace Eu addition on the microstructures and mechanical properties of A356, J. Alloys Compd. 650 (2015) 896–906. doi:10.1016/j.jallcom.2015.06.266.

[57] A.M. Samuel, G.H. Garza-Elizondo, H.W. Doty, F.H. Samuel, Role of modification and melt thermal treatment processes on the microstructure and tensile properties of Al-Si alloys, Mater. Des. 80 (2015) 99–108. doi:10.1016/j.matdes.2015.05.013.

[58] C.H. Caceres, J.R. Griffiths, Damage by the cracking of silicon particles in an Al-7Si-0.4Mg casting alloy, Acta Mater. 44 (1996) 25–33. doi:10.1016/1359-6454(95)00172-8.

[59] Q.G. Wang, C.H. Caceres, J.R. Griffiths, Damage by eutectic particle cracking in aluminum casting alloys A356/357, Metall. Mater. Trans. A Phys. Metall. Mater. Sci. 34 (2003) 2901–2912. doi:10.1007/s11661-003-0190-1.

[60] A.M.A. Mohamed, F.H. Samuel, A.M. Samuel, H.W. Doty, Influence of additives on the impact toughness of Al-10.8% Si near-eutectic cast alloys, Mater. Des. 30 (2009) 4218–4229. doi:10.1016/j.matdes.2009.04.041.

[61] J.F. Su, X. Nie, V. Stoilov, Characterization of fracture and debonding of Si particles in AlSi alloys, Mater. Sci. Eng. A. 527 (2010) 7168–7175. doi:10.1016/j.msea.2010.07.106.

[62] A. Kruglova, M. Roland, S. Diebels, T. Dahmen, P. Slusallek, F. Mücklich, Modelling and characterization of ductile fracture surface in Al-Si alloys by means of Voronoi tessellation, Mater. Charact. 131 (2017) 1–11. doi:10.1016/j.matchar.2017.06.013.

[63] M. Riestra, E. Ghassemali, T. Bogdanoff, S. Seifeddine, Interactive effects of grain refinement, eutectic modification and solidification rate on tensile properties of Al-10Si alloy, Mater. Sci. Eng. A. 703 (2017) 270–279. doi:10.1016/j.msea.2017.07.074.

[64] S.M. Jigajinni, K. Venkateswarlu, S.A. Kori, Effect of a grain refiner cum modifier on mechanical properties of Al-7Si and Al-11Si alloys, Met. Mater. Int. 19 (2013) 171–181. doi:10.1007/s12540-013-2006-1.

[65] S. Tao, Y. Pan, T. Lu, Y. Chen, J. Wu, Microstructures and mechanical properties of La added Al–Si casting alloys and mechanism of grain refinement, Int. J. Cast Met. Res. 28 (2015) 375–381. doi:10.1179/1743133615Y.0000000011.

[66] A.M. Samuel, H.W. Doty, S. Valtierra, F.H. Samuel, Effect of grain refining and Sr-modification interactions on the impact toughness of Al-Si-Mg cast alloys, Mater. Des. 56 (2014) 264–273. doi:10.1016/j.matdes.2013.10.029.

[67] S. Shivkumar, S. Ricci, J.C. Keller, D. Apelian, Influence of Solution Treatment on Tensile Properties of Cast Aluminum Alloys, J. Heat Treat. 8 (1990) 63–70.

[68] D.L. Zhang, L.H. Zheng, D.H. StJohn, Effect of a short solution treatment time on microstructure and mechanical properties of modified Al-7wt.%Si-0.3wt.%Mg alloy, J. Light Met. 2 (2002) 27–36. doi:10.1016/S1471-5317(02)00010-X.

[69] D.L. Zalensas, ed., Aluminum Casting Technology, 2nd ed., American Foundrymens Society, 1993.

[70] W. Khalifa, F.H. Samuel, J.E. Gruzleski, Iron intermetallic phases in the Al corner of the

Al-Si-Fe system, Metall. Mater. Trans. A Phys. Metall. Mater. Sci. 34 (2003) 807–825. doi:10.1007/s11661-003-1009-9.

[71] T.O. Mbuya, B.O. Odera, S.P. Ng'ang'a, Influence of iron on castability and properties of aluminium silicon alloys: Literature review, Int. J. Cast Met. Res. 16 (2003) 451–465. doi:10.1080/13640461.2003.11819622.

[72] L. Lu, A.K. Dahle, Iron-rich intermetallic phases and their role in casting defect formation in hypoeutectic Al–Si alloys, Metall. Mater. Trans. A. 36 (2005) 819–835. doi:10.1007/s11661-005-1012-4.

[73] M. Timpel, N. Wanderka, B.S. Murty, J. Banhart, Three-dimensional visualization of the microstructure development of Sr-modified Al-15Si casting alloy using FIB-EsB tomography, Acta Mater. 58 (2010) 6600–6608. doi:10.1016/j.actamat.2010.08.021.

[74] C.M. Dinnis, J.A. Taylor, A.K. Dahle, As-cast morphology of iron-intermetallics in Al-Si foundry alloys, Scr. Mater. 53 (2005) 955–958. doi:10.1016/j.scriptamat.2005.06.028.

[75] J.A. Taylor, Iron-Containing Intermetallic Phases in Al-Si Based Casting Alloys, Procedia Mater. Sci. 1 (2012) 19–33. doi:10.1016/j.mspro.2012.06.004.

[76] S.-N. Yie, S.-L. Lee, Y.-H. Lin, L. Jing-Chie, Mechanical Properties of Al-11%Si Casting Alloys Containing Trace Be and Sr, Mater. Trans. JIM. 40 (1999) 294–300.

[77] M. Tash, F.H. Samuel, F. Mucciardi, H.W. Doty, Effect of metallurgical parameters on the hardness and microstructural characterization of as-cast and heat-treated 356 and 319 aluminum alloys, Mater. Sci. Eng. A. 443 (2007) 185–201. doi:10.1016/j.msea.2006.08.054.

[78] F.H. Samuel, P. Ouellet, A.M. Samuel, H.W. Doty, Effect of Mg and Sr additions on the formation of intermetallics in Al-6 Wt Pet Si-3.5 Wt Pet Cu-(0.45) to (0.8) Wt Pet Fe 319-Type Alloys, Metall. Mater. Trans. A Phys. Metall. Mater. Sci. 29 (1998) 2871–2884. doi:10.1007/s11661-998-0194-y.

[79] M.H. Mulazimoglu, A. Zaluska, F. Paray, J.E. Gruzleski, The effect of strontium on the Mg2Si precipitation process in 6201 aluminum alloy, Metall. Mater. Trans. A. 28 (1997) 1289–1295. doi:10.1007/s11661-997-0265-5.

[80] B. Otani, Silumin and its structure, J. Inst. Met. (1926) 243–267.

[81] C.E. Ransley, H. Neufeld, The solubility relationship in the aluminium-sodium and aluminium-silicon-sodium systems, J. Inst. Met. (1950) 25–46.

[82] B.M. Thall, B. Chalmers, Modification in Aluminum-Silicon Alloys, J. Inst. Met. 77 (1949) 79–97.

[83] R.C. Plumb, J.E. Lewis, The modification of Aluminium-Silicon alloys by Sodium, J. Inst. Met. 86 (1958) 393–400.

[84] V.L. Davies, J.M. West, Influence of small additions of sodium on the Surface tension of aluminium and aluminium-silicon alloys, J. Inst. Met. 92 (1963) 208–210.

[85] S.C. Flood, J.D. Hunt, Modification of Al-Si eutectic alloys with Na, Met. Sci. 15 (1981) 287–294. doi:10.1179/030634581790426813.

[86] S.M.D. Glenister, R. Elliott, Strontium modification of Al-12.7wt-%Si alloys, Met. Sci. 15 (1981) 181–184. doi:10.1179/030634581790426732.

[87] L. Clapham, R.W. Smith, Segregation behaviour of strontium in modified and unmodified Al-Si alloys, J. Cryst. Growth. 92 (1988) 263–270. doi:10.1016/0022-0248(88)90458-7.

[88] M. Shamsuzzoha, L.M. Hogan, The role of non-cozonal twinning in the growth of fibrous silicon in strontium-modified Al–Si eutectic, J. Mater. Sci. 24 (1989) 2849–2859.

doi:10.1007/BF02385637.

[89] B. Closset, H. Dugas, M. Pekguleryuz, J.E. Gruzleski, The Aluminum-Strontium Phase Diagram, Metall. Trans. A. 17A (1986) 1250–1253.

[90] S.-M. Liang, M. Engstler, V. Groten, J. Barrirero, F. Mücklich, A. Bührig-Polaczek, R. Schmid-Fetzer, Key experiments and thermodynamic revision of the binary Al–Sr system, J. Alloys Compd. 610 (2014) 443–450. doi:10.1016/j.jallcom.2014.05.018.

[91] K. Nogita, A. Knuutinen, S.D. McDonald, A.K. Dahle, Mechanisms of eutectic solidification in Al–Si alloys modified with Ba, Ca, Y and Yb, J. Light Met. 1 (2001) 219–228. doi:10.1016/S1471-5317(02)00005-6.

[92] S.S.S. Kumari, R.M. Pillai, B.C. Pai, Role of calcium in aluminium based alloys and composites, Int. Mater. Rev. 50 (2005) 216–238. doi:10.1179/174328005X14366.

[93] S.S.S. Kumari, R.M. Pillai, B.C. Pai, Structure and properties of calcium and strontium treated Al-7Si-0.3Mg alloy: A comparison, J. Alloys Compd. 460 (2008) 472–477. doi:10.1016/j.jallcom.2007.05.085.

[94] T.H. Ludwig, J. Li, P.L. Schaffer, P. Schumacher, L. Arnberg, Refinement of Eutectic Si in High Purity Al-5Si Alloys with Combined Ca and P Additions, Metall. Mater. Trans. A Phys. Metall. Mater. Sci. 46 (2015) 362–376. doi:10.1007/s11661-014-2585-6.

[95] T. Kobayashi, J.H. Kim, M. Niinomi, Effect of calcium on mechanical properties of recycled aluminium casting alloys, Mater. Sci. Technol. 13 (1997) 497–502. doi:10.1179/mst.1997.13.6.497.

[96] S.S. Sreeja Kumari, R.M. Pillai, B.C. Pai, A study on the structural, age hardening and mechanical characteristics of Mn and Ca added Al-7Si-0.3Mg-0.6Fe alloy, J. Alloys Compd. 453 (2008) 167–173. doi:10.1016/j.jallcom.2006.11.145.

[97] S.S. Sreeja Kumari, R.M. Pillai, K. Nogita, A.K. Dahle, B.C. Pai, Influence of calcium on the microstructure and properties of an Al-7Si-O.3Mg-xFe Alloy, Metall. Mater. Trans. A Phys. Metall. Mater. Sci. 37 (2006) 2581–2587. doi:10.1007/BF02586230.

[98] A. Abdollahi, J.E. Gruzleski, An evaluation of calcium as a eutectic modifier in A357 alloy, Int. J. Cast Met. Res. 11 (1998) 145–155. doi:10.1080/13640461.1998.11819269.

[99] J. Li, F. Hage, M. Wiessner, L. Romaner, D. Scheiber, B. Sartory, Q. Ramasse, P. Schumacher, The roles of Eu during the growth of eutectic Si in Al-Si alloys, Sci. Rep. 5 (2015) 13802. doi:10.1038/srep13802.

[100] K. Nogita, H. Yasuda, K. Yoshida, K. Uesugi, a. Takeuchi, Y. Suzuki, a. K. Dahle, Determination of strontium segregation in modified hypoeutectic Al–Si alloy by micro X-ray fluorescence analysis, Scr. Mater. 55 (2006) 787–790. doi:10.1016/j.scriptamat.2006.07.029.

[101] G.K. Sigworth, Modification of Aluminum-Silicon Alloys, in: ASM Handbook, Vol. 15 Cast., 2008: pp. 240–254. doi:10.1361/asmhba0005301.

[102] A. Knuutinen, K. Nogita, S.D. McDonald, A.K. Dahle, Porosity formation in aluminium alloy A356 modified with Ba, Ca, Y and Yb, J. Light Met. 1 (2001) 241–249. doi:10.1016/S1471-5317(02)00006-8.

[103] S.D. Mcdonald, A.K. Dahle, J.A. Taylor, D.H. Stjohn, A.H. Effects, Modification-Related Porosity Formation in Hypoeutectic Aluminum-Silicon Alloys, 35 (2004) 1097–1106.

[104] L. Lu, K. Nogita, S.D. McDonald, A.K. Dahle, Eutectic solidification and its role in casting porosity formation, Jom. 56 (2004) 52–58. doi:10.1007/s11837-004-0254-8.

[105] L. Liu, A.M. Samuel, F.H. Samuel, H.W. Doty, S. Valtierra, Influence of oxides on porosity formation in Sr-treated alloys, Int. J. Met. 11 (2017) 729–742. doi:10.1007/s40962-016-

0118-3.

[106] N.S. Tiedje, J.A. Taylor, M.A. Easton, Feeding and distribution of porosity in cast Al-Si alloys as function of alloy composition and modification, Metall. Mater. Trans. A Phys. Metall. Mater. Sci. 43 (2012) 4846–4858. doi:10.1007/s11661-012-1308-0.

[107] D. Emadi, Porosity Formation in Sr-Modified Al-Si Alloys, 1995.

[108] Z. Zhang, X. Bian, X. Liu, Effect of strontium addition on hydrogen content and porosity shape of Al-Si alloys, Int. J. Cast Met. Res. 14 (2001) 31–35. doi:10.1080/13640461.2001.11819422.

[109] D. Emadi, J.E. Gruzleski, J.M. Toguri, The effect of na and Sr modification on surface tension and volumetric shrinkage of A356 alloy and their influence on porosity formation, Metall. Trans. B. 24 (1993) 1055–1063. doi:10.1007/BF02660997.

[110] M. De Giovanni, J.M. Warnett, M.A. Williams, P. Srirangam, 3D imaging and quantification of porosity and intermetallic particles in strontium modified Al-Si alloys, J. Alloys Compd. 727 (2017) 353–361. doi:10.1016/j.jallcom.2017.08.146.

[111] C.M. Dinnis, M.O. Otte, A.K. Dahle, J.A. Taylor, The influence of strontium on porosity formation in Al-Si alloys, Metall. Mater. Trans. A Phys. Metall. Mater. Sci. 35 A (2004) 3531–3541. doi:10.1007/s11661-004-0190-9.

[112] M.M. Makhlouf, H.V. Guthy, The aluminum–silicon eutectic reaction: mechanisms and crystallography, J. Light Met. 1 (2001) 199–218. doi:10.1016/S1471-5317(02)00003-2.

[113] A.G.C. Gwyer, H.W.L. Phillips, The constitution and structure of the commercial aluminium-silicon alloys, J. Inst. Met. 36 (1923) 283–324.

[114] N. Bochvar, P. Budberg, F. Hayes, Y. Liberov, R. Schmid-Fetzer, Al-Na-Si Ternary Phase Diagram, MSI, Materials Science International Services GmbH, Stuttgart, 1993.

[115] R. Ferro, O. Kubaschewski, H. Hubert, G. Ibe, Aluminium-Silicon-Strontium, VCH. 8 (1993) 270–278.

[116] J.A.E. Bell, W.C. Winegard, Structure of Pure Aluminium-Silicon Eutectics, J. Inst. Met. 93 (1964) 318–319.

[117] M.G. Day, A. Hellawell, The Structure of Modified Aluminium-Silicon Eutectic Alloy, J. Inst. Met. 95 (1967) 377.

[118] H.A.H. Steen, A. Hellawell, The growth of eutectic silicon-contributions to undercooling, Acta Metall. 23 (1975) 529–535. doi:10.1016/0001-6160(75)90093-0.

[119] M.D. Hanna, S.-Z. Lu, A. Hellawell, Modification in the aluminum silicon system, Metall. Trans. A. 15 (1984) 459–469. doi:10.1007/BF02644969.

[120] F. Yilmaz, O.A. Atasoy, R. Elliott, Growth structures in aluminium-silicon alloys II. The influence of strontium, J. Cryst. Growth. 118 (1992) 377–384. doi:10.1016/0022-0248(92)90086-X.

[121] J.H. Li, M.Z. Zarif, G. Dehm, P. Schumacher, Influence of impurity elements on the nucleation and growth of Si in high purity melt-spun Al–Si-based alloys, Philos. Mag. 92 (2012) 3789–3805. doi:10.1080/14786435.2012.687840.

[122] S.D. McDonald, A.K. Dahle, J.A. Taylor, D.H. StJohn, Eutectic grains in unmodified and strontium-modified hypoeutectic aluminum-silicon alloys, Metall. Mater. Trans. A. 35 (2004) 1829–1837. doi:10.1007/s11661-004-0091-y.

[123] S.D. McDonald, K. Nogita, A.K. Dahle, Eutectic nucleation in Al–Si alloys, Acta Mater. 52 (2004) 4273–4280. doi:10.1016/j.actamat.2004.05.043.

[124] A.K. Dahle, K. Nogita, S.D. McDonald, C. Dinnis, L. Lu, Eutectic modification and microstructure development in Al–Si Alloys, Mater. Sci. Eng. A. 413–414 (2005) 243–248. doi:10.1016/j.msea.2005.09.055.

[125] D.M. Stefanescu, ed., Modification of Aluminum-Silicon Alloys, in: ASM Met. Handb. - Vol. 15, Fourth pri, ASM INternational, 1998: pp. 1052–1064.

[126] S.-Z. Lu, A. Hellawell, Modification of Al-Si Alloys: Microstructure, Thermal Analysis, and Mechanisms, JOM. (1995) 38–40.

[127] C.R. Ho, B. Cantor, Modification of hypoeutectic Al-Si alloys, J. Mater. Sci. 30 (1995) 1912–1920. doi:10.1007/BF00353013.

[128] T.H. Ludwig, P.L. Schaffer, L. Arnberg, Influence of phosphorus on the nucleation of eutectic silicon in Al-Si alloys, Metall. Mater. Trans. A Phys. Metall. Mater. Sci. 44 (2013) 5796–5805. doi:10.1007/s11661-013-1945-y.

[129] S.-M. Liang, R. Schmid-Fetzer, Phosphorus in Al–Si cast alloys: Thermodynamic prediction of the AlP and eutectic (Si) solidification sequence validated by microstructure and nucleation undercooling data, Acta Mater. 72 (2014) 41–56. doi:10.1016/j.actamat.2014.02.042.

[130] S.M. Liang, R. Schmid-Fetzer, Validated thermodynamic prediction of AlP and eutectic (Si) solidification sequence in Al-Si cast alloys, IOP Conf. Ser. Mater. Sci. Eng. 117 (2016). doi:10.1088/1757-899X/117/1/012003.

[131] J. Eiken, M. Apel, S.-M. Liang, R. Schmid-Fetzer, Impact of P and Sr on solidification sequence and morphology of hypoeutectic Al–Si alloys: Combined thermodynamic computation and phase-field simulation, Acta Mater. 98 (2015) 152–163. doi:10.1016/j.actamat.2015.06.056.

[132] D.L. Zhang, B. Cantor, Heterogeneous nucleation of solidification of Si by solid AI in hypoeutectic Al-Si alloy, Metall. Trans. A. 24 (1993) 1195–1204. doi:10.1007/BF02657251.

[133] M. Zarif, B. Mckay, P. Schumacher, Study of Heterogeneous Nucleation of Eutectic Si in High-Purity Al-Si Alloys with Sr Addition, Metall. Mater. Trans. A. 42 (2010) 1684–1691. doi:10.1007/s11661-010-0553-3.

[134] J.H. Li, M.Z. Zarif, M. Albu, B.J. McKay, F. Hofer, P. Schumacher, Nucleation kinetics of entrained eutectic Si in Al-5Si alloys, Acta Mater. 72 (2014) 80–98. doi:10.1016/j.actamat.2014.03.030.

[135] C.M. Dinnis, A.K. Dahle, J.A. Taylor, Three-dimensional analysis of eutectic grains in hypoeutectic Al-Si alloys, Mater. Sci. Eng. A. 392 (2005) 440–448. doi:10.1016/j.msea.2004.10.037.

[136] P. Srirangam, S. Chattopadhyay, a. Bhattacharya, S. Nag, J. Kaduk, S. Shankar, R. Banerjee, T. Shibata, Probing the local atomic structure of Sr-modified Al–Si alloys, Acta Mater. 65 (2014) 185–193. doi:10.1016/j.actamat.2013.10.060.

[137] Y.H. Cho, H.-C. Lee, K.H. Oh, a. K. Dahle, Effect of Strontium and Phosphorus on Eutectic Al-Si Nucleation and Formation of β-Al5FeSi in Hypoeutectic Al-Si Foundry Alloys, Metall. Mater. Trans. A. 39 (2008) 2435–2448. doi:10.1007/s11661-008-9580-8.

[138] S. Shankar, Y.W. Riddle, M.M. Makhlouf, Nucleation mechanism of the eutectic phases in aluminum–silicon hypoeutectic alloys, Acta Mater. 52 (2004) 4447–4460. doi:10.1016/j.actamat.2004.05.045.

[139] S. Shankar, Y.W. Riddle, M.M. Makhlouf, Eutectic solidification of aluminum-silicon alloys, Metall. Mater. Trans. A. 35 (2004) 3038–3043. doi:10.1007/s11661-004-0048-1.

[140] A.K. Dahle, K. Nogita, S.D. McDonald, J.W. Zindel, L.M. Hogan, Eutectic nucleation and growth in hypoeutectic Al-Si alloys at different strontium levels, Metall. Mater. Trans. A.

32 (2001) 949–960. doi:10.1007/s11661-001-0352-y.

[141] K. Nogita, A.K. Dahle, Eutectic solidification in hypoeutectic Al-Si alloys: Electron backscatter diffraction analysis, Mater. Charact. 46 (2001) 305–310. doi:10.1016/S1044-5803(00)00109-1.

[142] J. Manickaraj, A. Gorny, Z. Cai, S. Shankar, X-ray nano-diffraction study of Sr intermetallic phase during solidification of Al-Si hypoeutectic alloy, Appl. Phys. Lett. 104 (2014). doi:10.1063/1.4865496.

[143] C.J. Simensen, Ø. Nielsen, F. Hillion, J. Voje, NanoSIMS Analysis of Trace Element Segregation during the Al-Si Eutectic Reaction, Metall. Mater. Trans. A. 38 (2007) 1448–1451. doi:10.1007/s11661-007-9165-y.

[144] M. Timpel, N. Wanderka, G.S. Vinod Kumar, J. Banhart, Microstructural investigation of Sr-modified Al-15 wt%Si alloys in the range from micrometer to atomic scale., Ultramicroscopy. 111 (2011) 695–700. doi:10.1016/j.ultramic.2010.12.023.

[145] M. Timpel, N. Wanderka, R. Schlesiger, T. Yamamoto, N. Lazarev, D. Isheim, G. Schmitz, S. Matsumura, J. Banhart, The role of strontium in modifying aluminium–silicon alloys, Acta Mater. 60 (2012) 3920–3928. doi:10.1016/j.actamat.2012.03.031.

[146] M. Timpel, N. Wanderka, R. Schlesiger, T. Yamamoto, D. Isheim, G. Schmitz, S. Matsumura, J. Banhart, Sr-Al-Si co-segregated regions in eutectic Si phase of Sr-modified Al-10Si alloy., Ultramicroscopy. 132 (2013) 216–21. doi:10.1016/j.ultramic.2012.10.006.

[147] J. Barrirero, M. Engstler, F. Mücklich, Atom Probe analysis of Sr distribution in AlSi foundry alloys, in: Light Met. 2013 - TMS, 2013: pp. 291–296. doi:10.1002/9781118663189.ch50.

[148] A.M. Garay-Tapia, A.H. Romero, G. Trapaga, R. Arróyave, First-principles investigation of the Al–Si–Sr ternary system: Ground state determination and mechanical properties, Intermetallics. 21 (2012) 31–44. doi:10.1016/j.intermet.2011.09.001.

[149] J.I. Goldstein, C.E. Lyman, D.E. Newbury, E. Lifshin, P. Echlin, L. Sawyer, D.C. Joy, J.R. Michael, Scanning Electron Microscopy and X-Ray Microanalysis, Third Edit, Kluwer Academic / Plenum Publishers, New York, NY, 2003.

[150] R.R. Keller, R.H. Geiss, Transmission EBSD from 10 nm domains in a scanning electron microscope, J. Microsc. 245 (2012) 245–251. doi:10.1111/j.1365-2818.2011.03566.x.

[151] S. Suzuki, Features of transmission EBSD and its application, Jom. 65 (2013) 1254–1263. doi:10.1007/s11837-013-0700-6.

[152] S. Suwas, R.K. Ray, Crystallographic Texture of Materials, Eng. Mater. Process. 88 (2014) 151–177. doi:10.1007/978-1-4471-6314-5.

[153] C. Kranenberg, D. Johrendt, A. Mewis, R. Pöttgen, G. Kotzyba, C. Rosenhahn, B.D. Mosel, Structure and properties of the compounds LnAl2X2 (Ln=Eu, Yb; X= Si, Ge), Solid State Sci. 2 (2000) 215–222. doi:10.1016/S1293-2558(00)00135-7.

[154] S. Bobev, P.H. Tobash, V. Fritsch, J.D. Thompson, M.F. Hundley, J.L. Sarrao, Z. Fisk, Ternary rare-earth alumo-silicides - Single-crystal growth from Al flux, structural and physical properties, J. Solid State Chem. 178 (2005) 2091–2103. doi:10.1016/j.jssc.2005.04.021.

[155] P. Villars, K. Cenzual, eds., YbAl2Si2 Crystal Structure: Datasheet from "PAULING FILE Multinaries Edition – 2012" in SpringerMaterials (https://materials.springer.com/isp/crystallographic/docs/sd_1210515), (2016).

[156] R. Gomer, Field emission, field ionization, and field desorption, Surf. Sci. 299–300 (1994) 129–152. doi:10.1016/0039-6028(94)90651-3.

[157] K. Thompson, D. Lawrence, D.J. Larson, J.D. Olson, T.F. Kelly, B. Gorman, In situ site-specific specimen preparation for atom probe tomography., Ultramicroscopy. 107 (2007) 131–9. doi:10.1016/j.ultramic.2006.06.008.

[158] E. Müller, Field Desorption, Phys. Rev. 102 (1956) 618–624. doi:10.1103/PhysRev.102.618.

[159] R. Gomer, Field desorption, J. Chem. Phys. 31 (1959) 341–345. doi:10.1063/1.1730354.

[160] R. Gomer, L.W. Swanson, Theory of field desorption, J. Chem. Phys. 38 (1963) 1613–1629. doi:10.1063/1.1776932.

[161] R. Haydock, D.R. Kingham, Post-Ionization of Field-Evaporated Ions, Phys. Rev. Lett. 44 (1980) 1520–1523. doi:10.1103/PhysRevLett.44.1520.

[162] D.R. Kingham, The post-ionization of field evaporated ions: A theoretical explanation of multiple charge states, Surf. Sci. 116 (1982) 273–301. doi:10.1016/0039-6028(82)90434-4.

[163] R. Forbes, Field evaporation theory: a review of basic ideas, Appl. Surf. Sci. 87–88 (1995) 1–11. doi:10.1016/0169-4332(94)00526-5.

[164] B. Gault, M.P. Moody, J.M. Cairney, S.P. Ringer, Atom Probe Microscopy, Springer New York, New York, NY, 2012. doi:10.1007/978-1-4614-3436-8.

[165] P. Bas, A. Bostel, B. Deconihout, D. Blavette, A general protocol for the reconstruction of 3D atom probe data, Appl. Surf. Sci. 87–88 (1995) 298–304. doi:10.1016/0169-4332(94)00561-3.

[166] D. Blavette, A. Bostel, J.M. Sarrau, B. Deconihout, A. Menand, An atom probe for three-dimensional tomography, Nature. 363 (1993) 432–435. doi:10.1038/363432a0.

[167] D.J. Larson, T.J. Prosa, R.M. Ulfig, B.P. Geiser, T.F. Kelly, Local Electrode Atom Probe Tomography, Springer New York, New York, NY, 2013. doi:10.1007/978-1-4614-8721-0.

[168] O.C. Hellman, J.A. Vandenbroucke, J. Rüsing, D. Isheim, D.N. Seidman, Analysis of Three-dimensional Atom-probe Data by the Proximity Histogram, Microsc. Microanal. 6 (2000) 437–444. doi:10.1007/s100050010051.

[169] W. Lefebvre, F. Danoix, G. Da Costa, F. De Geuser, H. Hallem, A. Deschamps, M. Dumont, 3DAP measurements of Al content in different types of precipitates in aluminium alloys, Surf. Interface Anal. 39 (2007) 206–212. doi:10.1002/sia.2516.

[170] F. Vurpillot, A. Bostel, D. Blavette, Trajectory overlaps and local magnification in three-dimensional atom probe, Appl. Phys. Lett. 76 (2000) 3127. doi:10.1063/1.126545.

[171] B. Gault, F. de Geuser, L. Bourgeois, B.M. Gabble, S.P. Ringer, B.C. Muddle, Atom probe tomography and transmission electron microscopy characterisation of precipitation in an Al-Cu-Li-Mg-Ag alloy., Ultramicroscopy. 111 (2011) 683–9. doi:10.1016/j.ultramic.2010.12.004.

[172] G. Sha, H. Möller, W.E. Stumpf, J.H. Xia, G. Govender, S.P. Ringer, Solute nanostructures and their strengthening effects in Al–7Si–0.6Mg alloy F357, Acta Mater. 60 (2012) 692–701. doi:10.1016/j.actamat.2011.10.029.

[173] J. Rüsing, J.T. Sebastian, O.C. Hellman, D.N. Seidman, Three-dimensional Investigation of Ceramic / Metal Heterophase Interfaces by Atom-probe Microscopy, Microsc. Microanal. 6 (2000) 445–451. doi:10.1007/s100050010050.

[174] Y. Suzuki-Yamamoto, R. Ozaki, M. Yoshiya, T. Nagira, H. Yasuda, Yet Another Marked Difference among Impurities as Modifier Elements for Refinement of Eutectic Si in Al-Si Alloys, 56 (2015) 1475–1483. doi:10.2320/matertrans.MA201576.

[175] M.A. González, Force fields and molecular dynamics simulations, École Thématique La

Société Française La Neutron. 12 (2011) 169–200. doi:10.1051/sfn/201112009.

[176] X.Z. Gao, M.H. Müser, L.T. Kong, J.F. Li, Atomic structure and energetics of amorphous-crystalline CuZr interfaces: A molecular dynamics study, Model. Simul. Mater. Sci. Eng. 22 (2014). doi:10.1088/0965-0393/22/6/065007.

Paper I

Comparison of segregations formed in unmodified and Sr-modified Al-Si alloys studied by atom probe tomography and transmission electron microscopy

J. Barrirero, M. Engstler, N. Ghafoor, N. de Jonge, M. Odén, F. Mücklich

Comparison of segregations formed in unmodified and Sr-modified Al–Si alloys studied by atom probe tomography and transmission electron microscopy

Jenifer Barrirero [a,b], Michael Engstler [a], Naureen Ghafoor [b], Niels de Jonge [c], Magnus Odén [b], Frank Mücklich [a,*]

[a] Department of Materials Science, Campus D3 3, Saarland University, D-66123 Saarbrücken, Germany
[b] Nanostructured Materials, Department of Physics, Chemistry and Biology, Linköping University, SE-581 83 Linköping, Sweden
[c] Innovative Electron Microscopy, INM-Leibniz Institute for New Materials, Campus D2 2, Saarland University, D-66123 Saarbrücken, Germany

ABSTRACT

The mechanical properties of Al-7 wt.% Si can be enhanced by structural modifications of its eutectic phase. Addition of low concentrations of certain elements, in this case 150 wt-ppm Sr, is enough to cause a transition from a coarse plate-like Si structure to a finer coralline one. To fully understand the operating mechanism of this modification, the composition of the eutectic Si phase in unmodified and Sr-modified alloys was analysed and compared by atom probe tomography and (scanning) transmission electron microscopy. The unmodified alloy showed nanometre sized Al-segregations decorating defects, while the Sr-modified sample presented three types of Al–Sr segregations: (1) rod-like segregations that promote smoothening of the Al–Si boundaries in the eutectic phase, (2) particle-like segregations comparable to the ones seen in the unmodified alloy, and (3) planar segregations favouring the formation of twin boundaries. Al and Sr solubilities in Si after solidification were determined to be 430 ± 160 at-ppm and 40 ± 10 at-ppm, respectively. Sr predominantly segregates to the Si phase confirming its importance in the modification of the eutectic growth.

© 2014 Elsevier B.V. All rights reserved.

1. Introduction

Al–Si are the most widely used aluminium casting alloys on account of their superior castability properties, e.g. high fluidity, low shrinkage and low thermal expansion coefficient. In this study, the hypoeutectic alloy with 7 wt.% Si, composed of α-Al dendrites and Al–Si eutectic phase will be considered. The microstructure of the irregular eutectic phase is formed by coarse Si plates embedded in an aluminium matrix. The brittle Si plates in the ductile Al matrix act as internal stress raisers and provide easy paths for cracks. By the addition of low concentrations of certain elements such as strontium (50–400 wt-ppm Sr), the microstructure of the Si phase can be modified to a coralline-like structure. In the presence of such a modifier the structure becomes finer and the brittle Si phase more rounded, contributing to higher values of ultimate tensile strength, greatly increased ductility, improved impact properties and better resistance to thermal shock [1].

These attractive properties have led to a wide industrial use of modified AlSi-based alloys in, for example, engine parts in the automotive industry. However, it remains difficult to optimize the amount of the modifier in terms of formation of intermetallic phases and homogeneity of the modification, especially for large-scale casts of complex alloys such as AlSiMg that often also contain impurities such as Fe and P. Fundamental understanding of the mechanisms governing the microstructural modification is still lacking, including how different species interact and affect the microstructure.

Na and Sr modifications of AlSi alloys have been extensively studied and numerous theories are proposed to explain the underlying phenomena [2–12]. In general, two approaches to explain the structural modification can be distinguished: the influence of the modifier on nucleation [13–16] and at the growth front of the eutectic phase [2–8,10]. The most well accepted hypotheses dealing with eutectic growth claim a Si growth restriction through the accumulation and adsorption of the modifier at the solid–liquid front. Lu and Hellawell [10] for instance, presented the impurity induced twinning (IIT) theory, through which step sources across the {1 1 1} closely packed planes in Si would be poisoned by the

modifier, promoting frequent twinning. Similarly, other authors based their explanations on a mechanism, which is believed to be operative at the modified and unmodified eutectic: the twin plane re-entrant edge (TPRE) mechanism [2,7]. This mechanism suggests that the presence of twins forms re-entrant edges that facilitate Si growth in the ⟨211⟩ direction [7]. In this case, the proposal is that the modifier will poison these re-entrant {111} twin grooves. Although based on different growth modes, both of these approaches relay on the hypothesis of a high multiplication of twins. Even if the morphology of eutectic Si appears to be almost isotropic, the underlying mechanism is believed to be an anisotropic growth with several changes of growth direction. Shamsuzzoha and Hogan [8] used this idea to propose a zigzag type of growth induced by the repeated twinning of the Si crystal during growth.

To confirm or reject the Si-growth mechanisms proposed by these theories, a more detailed investigation of the distribution of the modifier in the Si-phase, its tendency to segregate and its correlation with twins and other structural defects is needed. This verification, however, was hindered during the last decades by the lack of spatially resolved chemical information at the nanometric scale. With the advent and development of high resolution transmission electron microscopy (HR-TEM), atomically resolved scanning transmission electron microscopy (STEM) and atom probe tomography (APT), high structural and 3D chemical resolution down to parts per million [17] is now attainable. Recent studies of Sr modified samples showed evidences of segregation of the modifier together with Al inside the Si phase [18–20]. The presence of Al was not expected or predicted by any of the previously mentioned theories of modification and it remains difficult to ascertain if its presence plays a decisive role. One important missing piece to the understanding of the modified structure is a detailed characterization of the Si phase in the unmodified alloy, i.e. without Sr. The comparison of the overall Al concentration and distribution between modified and unmodified samples will help in the interpretation of its role for the modification. In addition, the measurement of the overall Sr concentration in the Si phase will give information about the necessary amount of Sr to achieve modification.

In this study, chemical and structural information about the concentration and distribution of Al and Sr in the unmodified and Sr-modified eutectic Si were obtained by means of APT, TEM and STEM. The segregations detected using APT combined with the structural features imaged by (S)TEM give a detailed three-dimensional view of the Si phase, which allowed us to trace the microstructural evolution of these alloys.

2. Materials and methods

Al-7 wt.% Si (AlSi7) samples were produced at the Foundry Institute at RWTH Aachen by directional solidification in a Bridgman furnace. All samples were fabricated with a cooling rate of 0.25 K/s at a temperature gradient of 15 K/mm. High purity Si and Al (Al5N5) were melted at the corresponding proportions. An aluminium master alloy containing 15 wt.% Sr was added to modify the samples with 150 wt-ppm Sr. Chemical compositions were determined by optical emission spectrometry and are presented in Table 1.

Cross-sectional cuts of the samples were embedded and mechanically polished. Site-specific sample preparation for TEM and APT were accomplished in a dual-beam focused ion beam/scanning electron microscopy workstation (FIB/SEM) (Helios NanoLab 600™, FEI Company, USA). In both procedures, an electron beam induced Pt-cap layer was first deposited on the eutectic area to provide protection from gallium implantation. After lift out and thinning of the samples, a low energy milling at 2 kV was performed to minimize Ga induced damage [21].

Electron back scattered diffraction (EBSD) was accomplished using an EDAX Hikari EBSD system attached to the FIB/SEM-instrument on the modified sample to assess the twin density in the Si phase. The sample polishing procedure for EBSD-measurements using colloidal silica as polishing media was optimized to get the best data quality from the Si-phase. The raw data corresponding to the Al phase was filtered out from the EBSD maps for clarity.

Overview and HR-TEM images were recorded in a Tecnai G2 TF 20 UT FEG microscope (FEI Company, USA) operated at 200 kV in micro and nanoprobe mode. STEM images were acquired using an ARM 200 microscope (JEOL, Japan) also operated at 200 kV and equipped with a corrector for spherical aberration (CEOS, Germany). The corrector was aligned for a sub-Ångstrom probe size. A beam shower procedure was applied to reduce the amount of contamination during high-resolution imaging using a high angle annular dark field (HAADF) detector. To enhance the contrast, the atom-resolved HAADF-STEM images were filtered by the image processing software Fiji [22]. The images were transformed into the frequency space by a Fast Fourier Transform (FFT). All frequencies except for the central one were individually encircled and passed through a white mask. Finally, the masked information was transformed back to the space domain by an Inverse-FFT.

Laser Pulsed APT was carried out with a LEAP™ 3000X HR (CAMECA) at a repetition rate of 250 kHz, a specimen temperature of about 40 K, a pressure lower than 1×10^{-10} Torr (1.33×10^{-8} Pa), and a laser pulse energy of 0.4–0.5 nJ. The evaporation rate of the specimen was 5 atoms per 1000 pulses. Datasets were then reconstructed and analysed with the IVAS™3.6.6 software (CAMECA). Reconstructions were calibrated by comparison with SEM images post measurement and the use of crystallographic features within the reconstruction. Localized chemical analysis was carried out using one dimensional concentration profiles and proximity histograms. The sampling of the concentration profile measurements was adjusted to minimize statistical errors using fixed number of ions per sampling block. Proximity histograms were constructed based on Al iso-concentration surfaces. Iso-concentration surfaces are shown in some figures to highlight the presence of segregations and their morphologies. The Al and Sr contents in Si and their solid solubilities were measured after background subtraction in IVAS software.

3. Results

Fig. 1 shows typical optical micrographs of the analysed AlSi7 samples. The unmodified plate-like eutectic Si phase presents a much coarser structure in comparison to the Sr-modified eutectic. Although Fig. 1(b) depicts small rounded disconnected particles in the transversal section, the three-dimensional structure consists of an interconnected coralline-like architecture [23].

The distribution and concentrations of Al and Sr in Si were analysed by APT and (S)TEM for both alloys. The different types of segregations found are summarized in Table 2. Detailed descriptions of the microstructural findings for the two alloys are presented separately in the following sections.

3.1. Unmodified alloy – AlSi7

Fig. 2 shows a transversal cut of a Si plate. The presence of twins along the plate confirms the expected twin plane re-entrant edge (TPRE) growth of eutectic Si [2,7,24]. The magnified area shown in Fig. 2(b) evidences not only twins, but also an unexpected homogeneous distribution of round precipitates. HR-TEM of these precipitates showed that they are coherent with the crystalline matrix (Fig. 2(c)). The particle's diameters measured by HR-TEM ranged between 10 and 12 nm.

For compositional insight, six eutectic Si atom probe specimens were analysed. All specimens contained Al segregations in agreement with the precipitates imaged by TEM. Fig. 3 shows one of

Table 1
Chemical composition measured by optical emission spectroscopy (wt.%).

	Si	Sr	Ti	Ca	Na	Fe, Cu, Mn, Mg, Cr, Ni, Zn, Bi, P, Pb, Sb, V
AlSi7	7.04	–	0.0006	0.0002	<0.0001	<0.001
AlSi7 + 150 wt-ppm Sr	7.04	0.015	0.0006	0.0002	<0.0001	<0.001
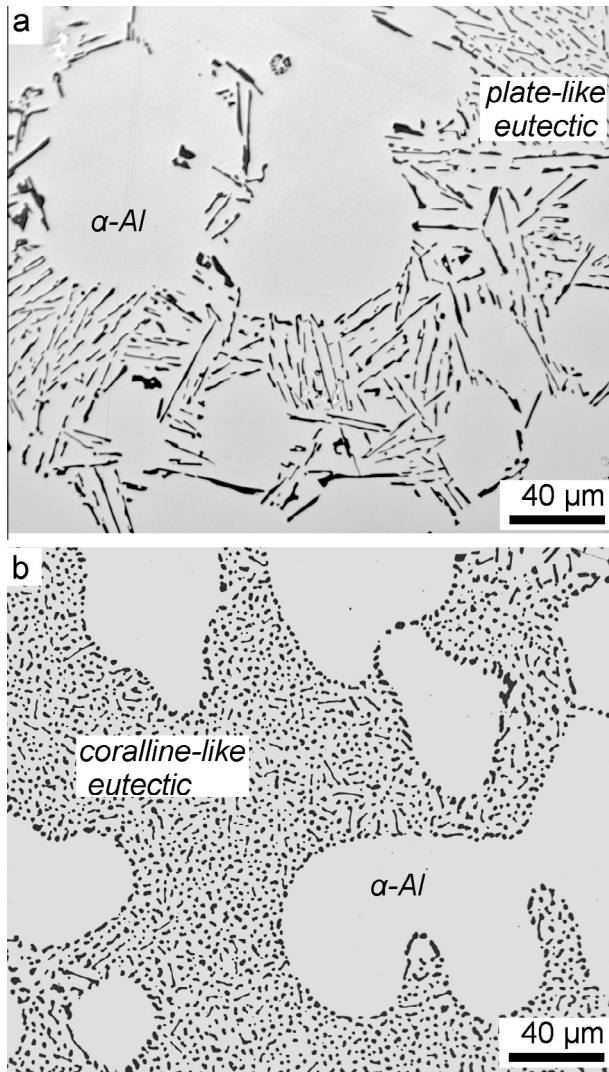
Fig. 1. Optical micrographs of the analysed samples; (a) unmodified AlSi7 alloy showing plate-like Si eutectic structure and (b) modified AlSi7 + 150ppm Sr with coralline-like Si structure (adapted from Barrirero et al. [20]).

Table 2
Summary of segregations found in the unmodified and Sr-modified AlSi7 alloy.

Segregations		AlSi7 – (unmodified)	AlSi7 + 150 ppm Sr (modified)
Particle-like	Small precipitates	<10 nm – Al (Fig. 3(b))	<10 nm – Al,Sr (Fig. 5(b))
	Larger precipitates	>10 nm – Al (Fig. 3(c))	>10 nm – Al,Sr (Fig. 8(c))
Ring-like		40 nm – Al (Fig. 3(d))	–
Rod-like		–	3 nm – Al:Sr = 2.5/4.0 (Figs. 5–7)
Planar		–	1–3 nm – Al:Sr = 2.5/4.0 (Fig. 8)

such measurements giving a representative view of the density of segregations. A total of 16 such features were analysed separately using one dimensional concentration profiles and proximity histograms in order to categorize the segregations.

Based on the results, the segregations were divided into three categories as seen in Fig. 3(b–d):
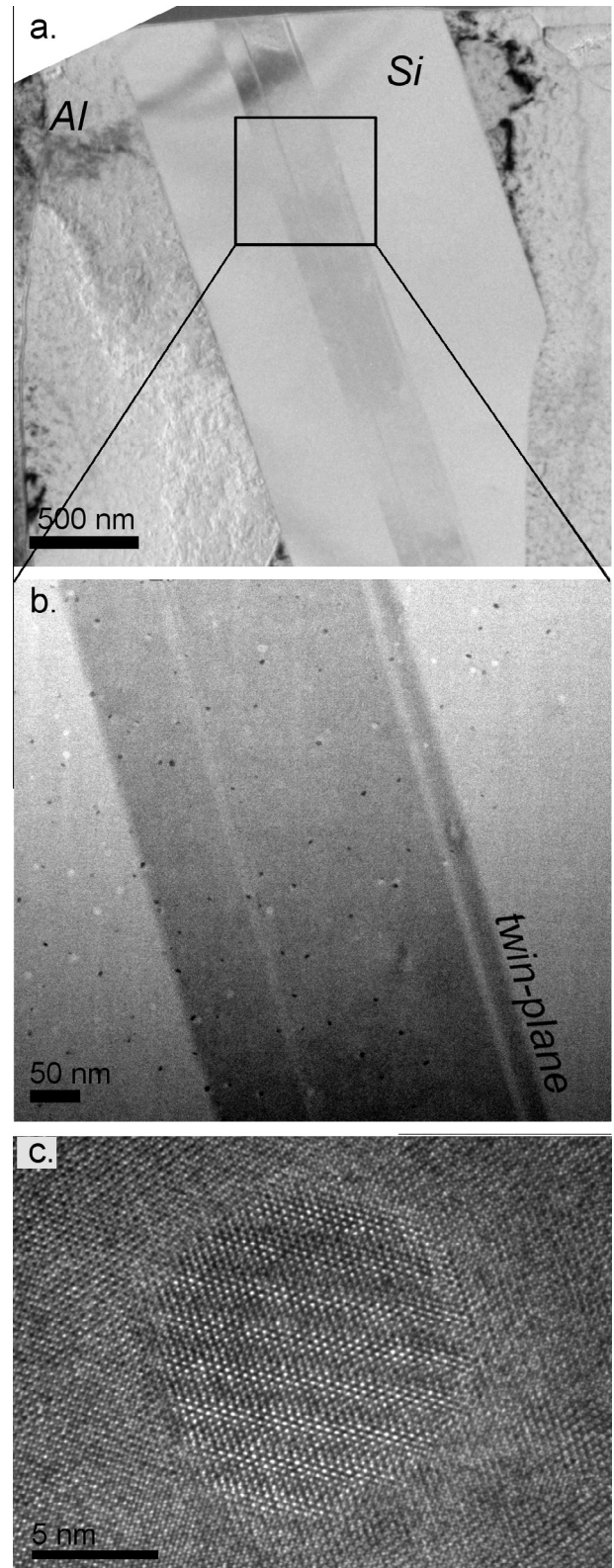
Fig. 2. Transmission electron microscopy (TEM) images of the unmodified eutectic phase; (a) transversal cut of a Si plate, (b) zoom in of the centre of the plate showing twin planes of the twin plane re-entrant edge (TPRE) type of growth and small precipitates, and (c) HR-TEM of one precipitate.

1. *Small segregations* with a diameter between 5 and 10 nm and a homogeneous Al concentration in the range of 5–15 at.% Al (Fig. 3 (b)). Three of such segregations were analysed.
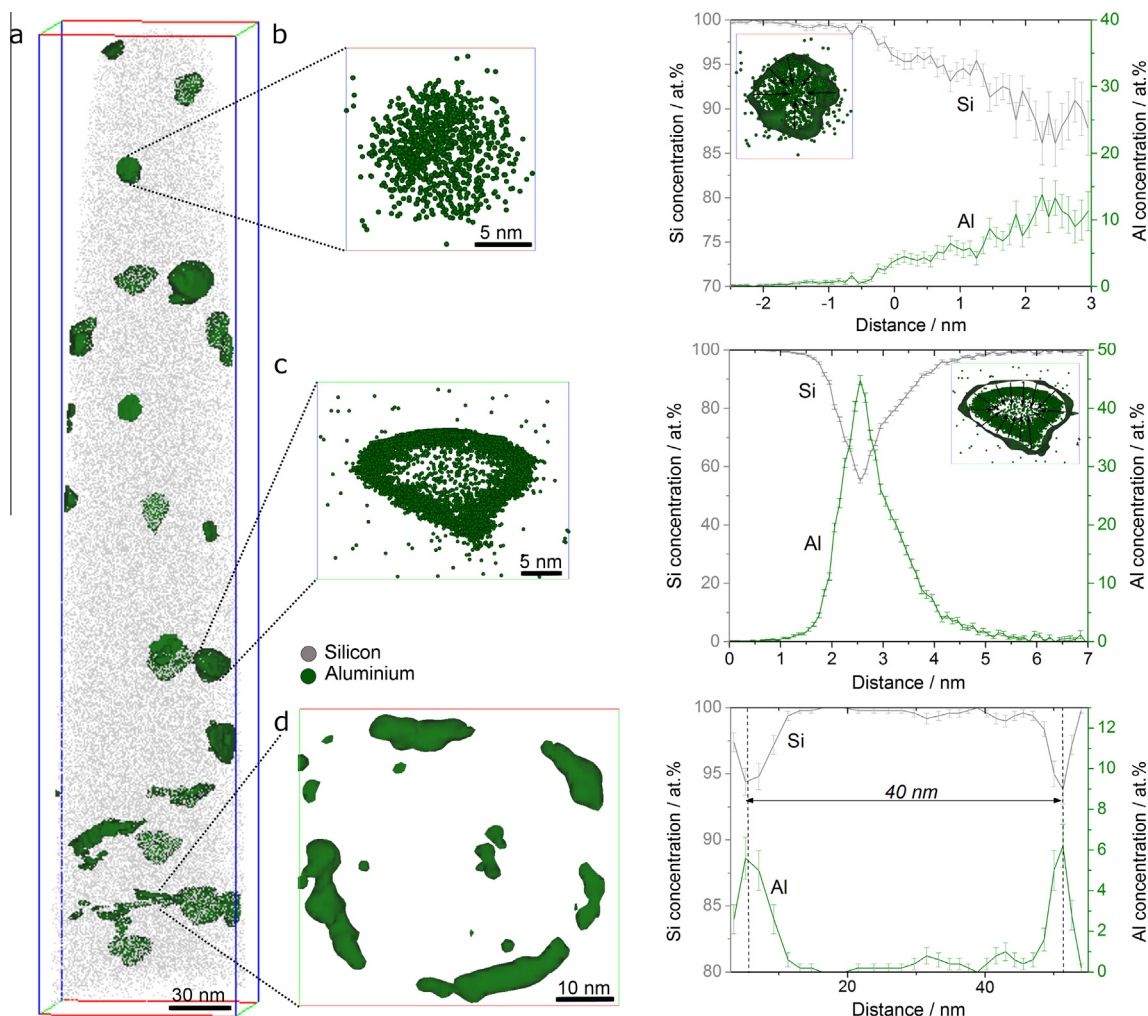
Fig. 3. Atom probe tomography (APT) of the unmodified eutectic Si with the three distinctive types of segregations; (a) complete measurement with Al segregations depicted by 2 at.% Al iso-concentration surface, (b) small Al segregation, proximity histogram showing the concentration profile as a function of the distance to an Al iso-concentration surface (2.5 at.% Al) (black arrows in the diagram depict the positive increment of the x-axis [distance]), (c) larger Al segregation showing an Al-depleted zone in the centre, proximity histogram showing the concentration profile as a function of the distance to an Al iso-concentration surface (0.5 at.% Al), and (d) ring-like segregation [top view] with one-dimensional concentration profile. (For interpretation of the references to colour in this figure legend, the reader is referred to the web version of this article.)

2. *Larger segregations* with a diameter between 13 and 18 nm. These features showed markedly uneven concentration profiles as the one depicted in Fig. 3(c) with a low Al concentration in the centre and a higher concentration at the surroundings between 40 and 50 at.% Al. 12 segregations with such an Al depleted zone in the centre were measured.

3. *Ring-like segregation* with a diameter of 40 nm and a peak concentration of 6 at.% Al. Only one of these segregations was detected (Fig. 3(d)).

The measurement of Al segregations in a Si matrix by APT is a challenging task. Al evaporates at lower field strengths than Si [25] and this fact influences the accuracy of the atoms' positions in the reconstructed volume [26]. Deflections of the ion trajectories affect primarily particle-like segregations since the uneven distribution of the electric field at the specimen surface is strongly localized in this case. This local magnification artefact results in a deformation of the segregation in the x–y direction [27]. Lefevbre et al. [28] reported a 1.5–2 nm region affected by trajectory overlaps at the interface of low-evaporation-field precipitates. Considering this biased area, we expect the significant Al depletion detected at the centre of the large segregations (13–18 nm diameter) not to be an artefact from trajectory aberrations. However, the

compositional measurements along the segregation interface, for example as shown in Fig. 3(c), can present up to ±5 at.% error.

3.2. Modified alloy – AlSi7 + 150 wt-ppm Sr

Fig. 4 shows overviews of the modified eutectic structure at two different magnifications. Fig. 4(a) shows an inverse pole figure as obtained by electron back scattered diffraction (EBSD). This map was obtained at a surface perpendicular to the solidification axis similar to the one shown in Fig. 1(b) and only shows the Si phase. This EBSD map shows the crystallographic orientations in the Si phase. The majority of the Si branches present two crystallographic orientations separated by a twin boundary highlighted in black in the figure.

Fig. 4(b and c) display TEM overview images of surfaces perpendicular to the EBSD map. Both of these images also show two Si crystallographic orientations separated by a twin boundary. A clear difference between the twin boundaries seen in the unmodified (Fig. 2) and in the modified alloy is that, in the modified case there is no unique twin plane. Instead, the twin boundary displays several different directions indicating repeated changes of the growth front direction during solidification, i.e. the modified alloy
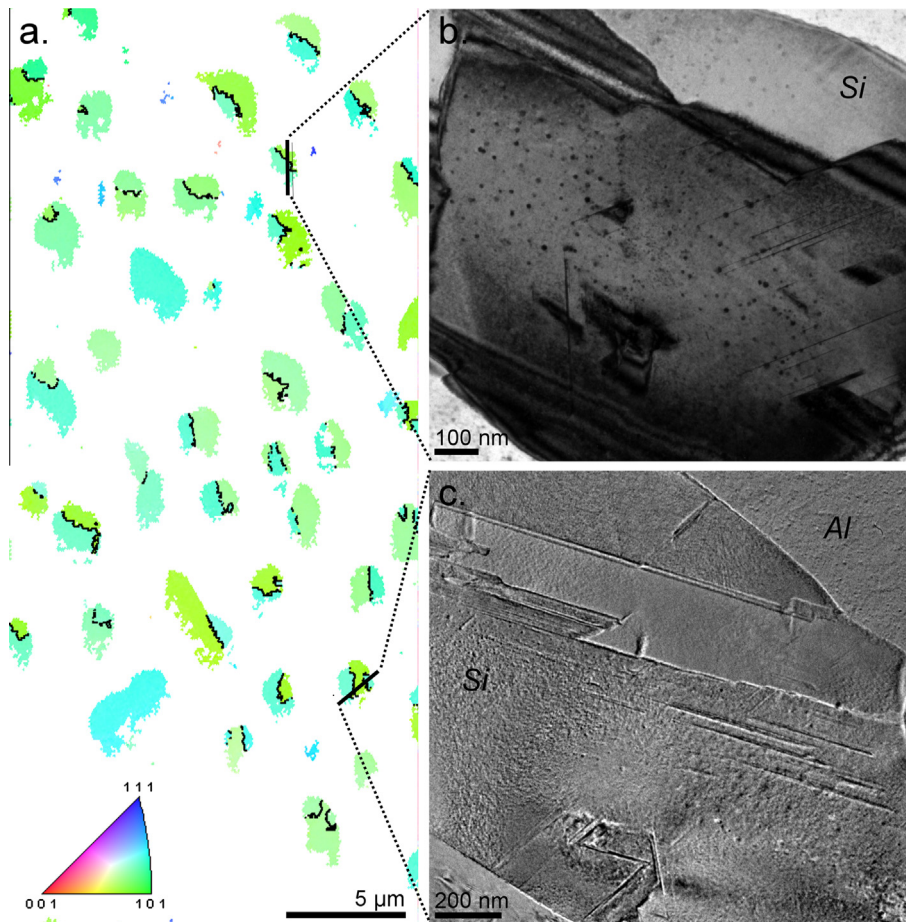
Fig. 4. Overview of the modified eutectic phase (AlSi7 + 150 ppm Sr); (a) inverse pole figure map (electron backscattered diffraction – EBSD) perpendicular to the sample's growth direction. The map shows the crystallographic orientations of the silicon phase. Twin boundaries are shown in black. White areas correspond to the Al matrix which was filtered out for clarity, (b) diffraction contrast bright-field and (c) bright-field TEM overview images of Si modified branches. Each image shows two different crystallographic orientations in Si in agreement with the EBSD data. Nanometric rod-like and particle-like defects can be seen. (For interpretation of the references to colour in this figure legend, the reader is referred to the web version of this article.)

is characterised with a higher degree of growth flexibility compared to the unmodified alloy.

In addition to these coarse changes of growth direction, the modified alloy presents a high density of nanometre sized features embedded in the single-crystalline Si lattice. These features include precipitates as found in the unmodified alloy, twins involving just a few tens of crystallographic planes, and faults in the Si stacking sequence involving a few inter-planar distances. These features were analysed by (S)TEM and correlated to Al–Sr segregations measured by APT. No segregations presenting Al or Sr alone were detected. Depending on their morphology, the segregations were categorized into three types: *rod-like*, *particle-like* and *planar*.

3.2.1. Rod-like segregations

Rod-like segregations are here defined as segregations having one dimension significantly larger than the other two. Fig. 5 shows a complete APT reconstruction of a Si specimen where rod-like segregations containing Al and Sr are the dominating features (see supplementary data Video 1 for a full three-dimensional view). Fig. 5(a) shows a top- and lateral-view of an 8 nm thick slice through the measurement. This slice presents numerous rod-like segregations rich in Al and Sr. In the upper part of the reconstruction, a V-shaped arrangement with a precipitate at its intersection is seen; while at the lower part, several parallel segregations separated by 10 to 30 nm are shown. Fig. 5(b) shows the top- and lateral-view of a 90° rotation of this reconstruction. This image

shows further segregations branching out and illustrates the three-dimensional complexity of the phase. Top- and lateral magnifications of these segregations are displayed in Fig. 5(c) with Al and Sr atoms represented as spheres. These segregations are separated by 5–10 nm. Rod-like segregations were always longer than the field of view of the tomographies. The maximal lengths that could be measured by APT were about 200 nm.

Concentration profiles obtained along these segregations showed between 2–4 at.% Al and 0.5–1 at.% Sr. Fig. 5(d) depicts one example of such concentration profile calculated in a cylindrical region of interest (ROI). The diameter size has a critical influence on the concentration measured, and therefore, it was chosen as close as possible to the segregation with a diameter of 3 nm. Since the background noise signal cannot be identified in the 3D space data, it cannot be subtracted from the concentration profiles. To evaluate the background level, we extracted the mass spectrum data inside the selected ROI. This mass spectrum data shows 0.87 ± 0.09 at.% Sr and 3.16 ± 0.17 at.% Al in agreement with the profile measurement and indicating a minor influence of the background. Concentrations measured in such small regions in the reconstructions should be treated carefully due to the limited detection efficiency of the instrument [29]. As a consequence, we report Al:Sr ratio rather than concentrations. Here, all rod-like segregations present between 2.5 and 4 times more Al than Sr, which is what to expect if local ternary reactions have formed intermetallic phases.
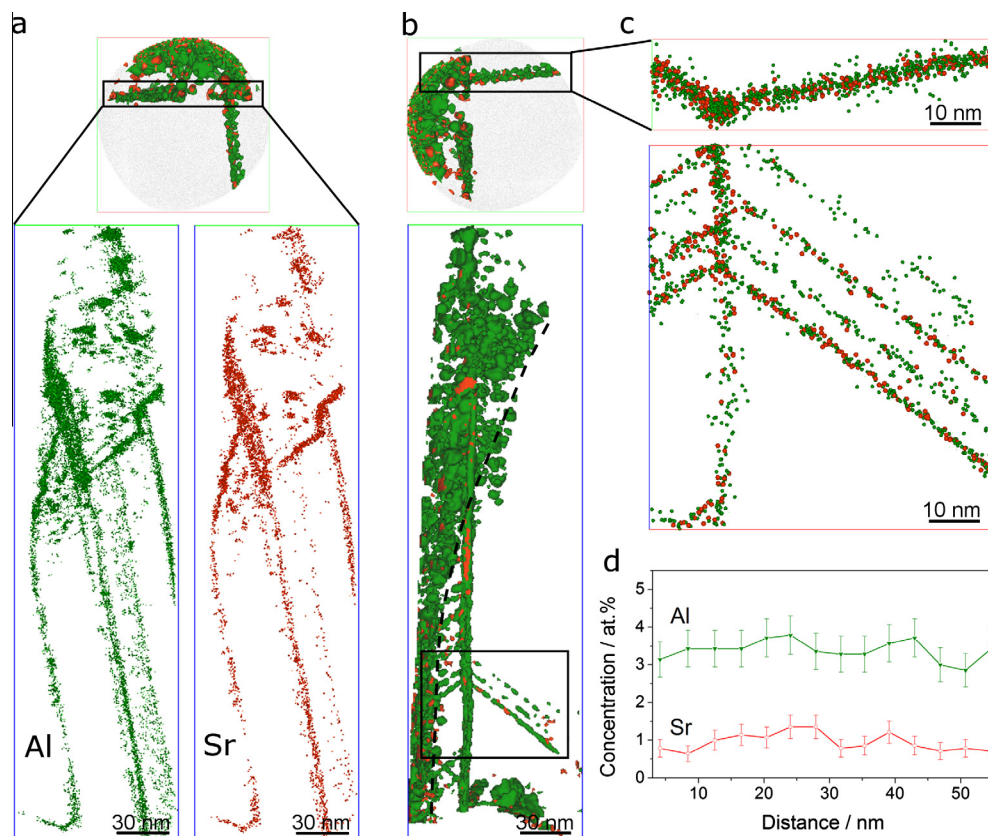
Fig. 5. APT of the modified Si eutectic phase; (a) top- and lateral-view of an 8 nm slice in the APT measurement. Rod-like segregations rich in Al and Sr are shown, (b) 90° rotation of the same specimen showing particle-like segregations and further rod-like segregations (iso-concentration surfaces at 0.5 at.% Sr and 0.6 at.% Al), (c) magnified region of interest depicting the three-dimensional relations and complexity of the structure (Al and Sr atoms are represented by spheres), and (d) concentration profile along one single rod-like segregation showing an Al:Sr ratio of about 3. (For interpretation of the references to colour in this figure legend, the reader is referred to the web version of this article.)

Fig. 6(a) shows a dark field TEM image of a Si branch containing a high amount of V-shaped defects. These features start in the inner part of the Si branch and extend towards the Al–Si boundary. Fig. 6(b) illustrates the correlation with the Al–Sr segregations presented in Fig. 5 by APT. These features were frequently found in the samples.

Fig. 7(a) shows an APT region of interest containing V-shaped Al-Sr segregations with spheroidal segregations heterogeneously nucleating along them and at their intersections. Fig. 7(b) is a HRTEM image viewed along the $\langle 0 1 1 \rangle$ zone axis of the Si crystal displaying V-shaped defects along two $\langle 1 1 1 \rangle$ directions at an angle of 70.5°. This defect consists of faults in the stacking sequence involving a few lattice planes. We note that this is not a twin type defect since the Si lattice orientation is the same on both sides of the defect. This is further confirmed by the atomically resolved HAADF-STEM image in Fig. 7(c). The atomic structure aligned in the $\langle 1 1 0 \rangle$ zone axis depicts the Si arrangement into the characteristic dumbbells of the diamond structure. The Si structure is maintained at both sides of the segregation and the distortion of the crystal structure corresponds to three lattice planes.

3.2.2. Particle-like segregations

Particle-like segregations containing Al and Sr were found in all APT reconstructions and (S)TEM images. Similarly as in the unmodified alloy, two size-ranges of particle-like segregations are present:

1. *Segregations* smaller than 10 nm. These features can be seen in Fig. 5(b). The difference to the unmodified sample is not only the presence of Sr together with Al, but also a very high density of these segregations only in one part of the specimen. Fig. 5(b) shows a dotted line highlighting the "virtual plane" behind which the segregations are accumulated.

2. Larger segregations (>10 nm). Several of these segregations are presented in the APT reconstruction of Fig. 8(a). Fig. 8(c) shows a magnification of one of them. Al and Sr present similar fluctuations in concentration as in the unmodified sample with an Al-depleted zone in the centre of the feature.

The Al and Sr concentrations in the segregations vary and ranges from 7 to 20 at.% Al and 0.2 to 0.8 at.% Sr. In some precipitates there is up to 30 times more Al than Sr.

3.2.3. Planar segregations

Planar segregations are the third type of features found by APT measurements. They are described by having two dimensions significantly larger than the third one. Due to their large size a definite correlation to the TEM images is not straightforward for this type of segregations. However, they are probably situated at grain boundaries and irregular twin boundaries as the one presented in Fig. 4.

Fig. 8(b) shows one example of a planar segregation that is 1 nm thick (see supplementary data Video 2 for a full three-dimensional view). The segregation crosses the entire atom probe specimen, which has a diameter of approximately 70 nm. The size of this segregation is larger than the field of view and can therefore not be estimated. The Al and Sr distributions are constant such that an Al:Sr ratio of about 2.5 is maintained throughout the segregation
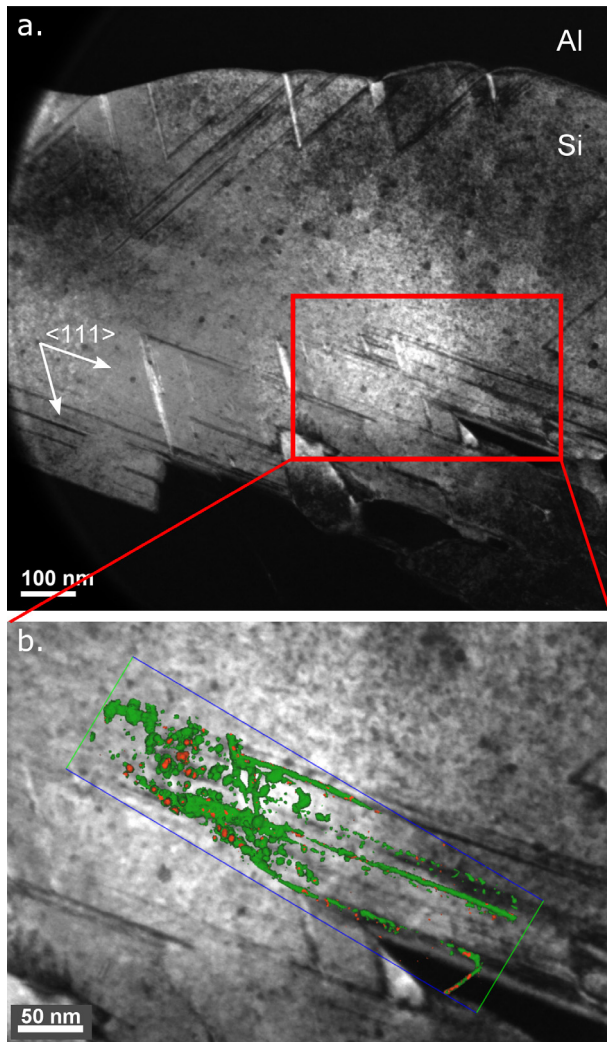
Fig. 6. TEM-APT correlation; (a) dark-field TEM overview of a Si branch with numerous V-shaped defects along two $\langle 1\,1\,1 \rangle$ directions, (b) magnified area of (a) and superimposed correlation with the segregations presented in APT in Fig. 5(a). (For interpretation of the references to colour in this figure legend, the reader is referred to the web version of this article.)

with peak contents of 5 at.% Sr and 12 at.% Al at the segregation centre. We note that the Al:Sr ratio is comparable to that measured for the rod-like segregations.

3.3. Al and Sr concentrations in Si

The data of 7 specimens of the modified and 6 specimens of the unmodified alloy were averaged to obtain the Al and Sr concentrations in the Si-phase of each alloy.

The amount of Al and Sr in solid solution in each alloy are reported in Table 3 and are 430 ± 160 at-ppm for Al and 40 ± 10 at-ppm for Sr. These values represent a measure of the solubility of Al and Sr in Si after solidification.

The total amount of Al and Sr trapped in the Si-phase during solidification is also reported in Table 3. The Al content of the unmodified plate-like Si-phase is nearly 4 times lower than the Al content in the modified coralline-like Si-phase. The total content of Sr in the Si-phase of the modified alloy is 860 ± 560 at-ppm. It should be noted here that the values reporting the total amount of Al and Sr in the Si phase present larger deviations than the solubility values because they strongly depend on the amount of segregations found in each tomography.
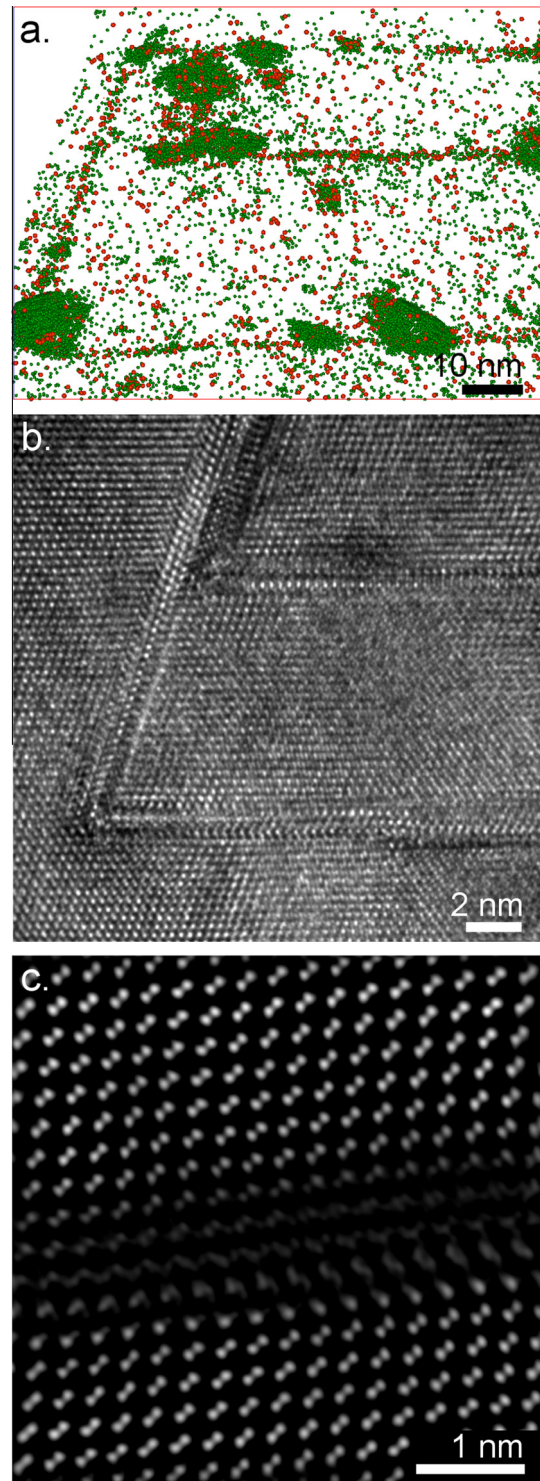
Fig. 7. High resolution images of the rod-like defects in the Si phase; (a) rod-like and particle-like segregations containing Al (green) and Sr (red) atoms. Si atoms are not shown for clarity, (b) HR-TEM of two V-shape defects along $\{1\,1\,1\}$ planes, and (c) HR-STEM showing a 1 nm-thick defect involving 3 lattice planes and no change of orientation at both sides of the defect. (For interpretation of the references to colour in this figure legend, the reader is referred to the web version of this article.)

4. Discussion

4.1. Unmodified alloy

Doping and impurity atoms present in Si have been extensively investigated due to the importance of Si as a material for
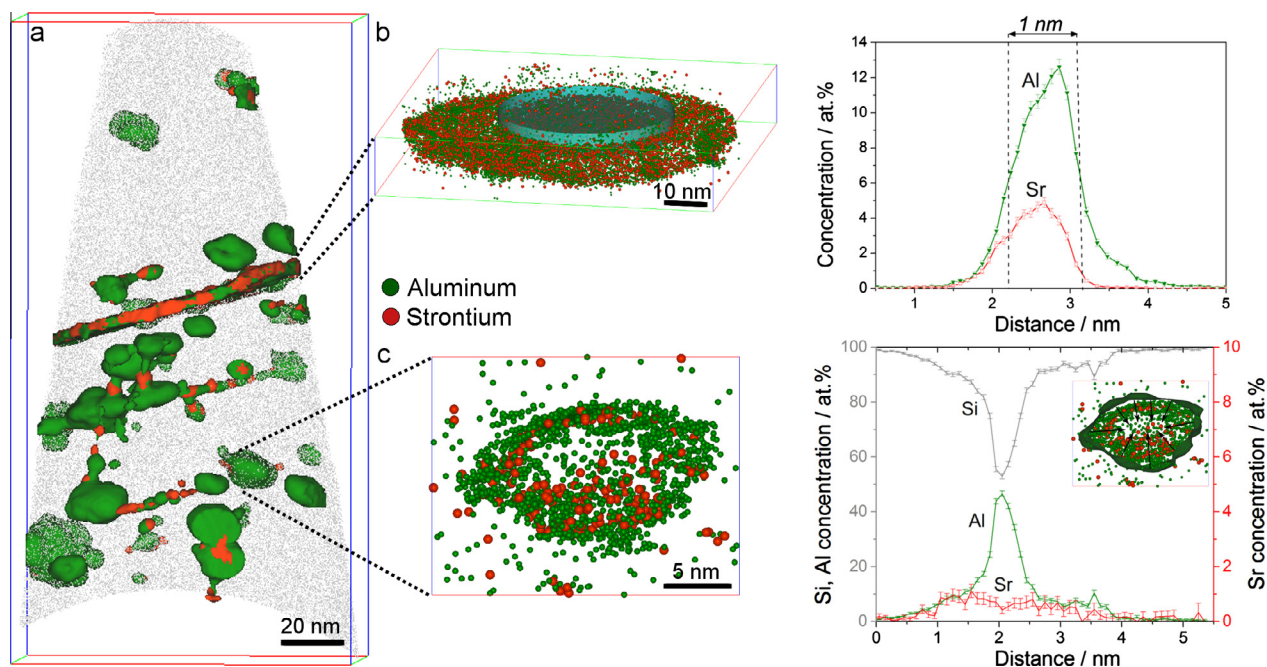
Fig. 8. APT of the modified eutectic Si phase; (a) complete reconstruction highlighting Al–Sr segregations by iso-concentration surfaces (1.2 at.% Al; 0.4 at.% Sr). All three types of segregations are present, i.e. rod-like, particle-like and planar, (b) magnified planar segregation with a cylindrical region of interest – ROI (40 nm in diameter) used to measure the concentration profile, and (c) slice of a particle-like segregation depicting an Al and Sr depleted region in the centre, proximity histogram showing Si, Al and Sr concentration profiles as a function of the distance to an Al iso-concentration surface (2.5 at.% Al) (black arrows in the diagram depict the positive increment of the x-axis [distance]).(For interpretation of the references to colour in this figure legend, the reader is referred to the web version of this article.)

Table 3
Minor elements' content in the eutectic Si phase (at.%).

	Al in the specimens	Al dissolved in the Si matrix	Sr in the specimens	Sr dissolved in the Si matrix
AlSi7	0.161 ± 0.109	0.036 ± 0.009	–	–
AlSi7 + 150 wt-ppm Sr	0.616 ± 0.233	0.047 ± 0.012	0.086 ± 0.056	0.004 ± 0.001

microelectronic applications. Carrier concentration profiles of heavily implanted Al in Si shows that only a small fraction of Al atoms contributes to the electrical activity in Si suggesting that part of the Al atoms are segregated or related to lattice defects [30]. This was supported by transmission electron microscopy showing dislocation loops and coherent precipitates 5–10 nm in size [30]. Such defects are also found in Si implanted by As, B or P [30–32]. Washburn et al. [31] for example, shows a large number of small defects which could be dislocation loops or planar clusters of P atoms that are accompanied by lattice strain. Recently, Thompson et al. [33] showed As-Cottrell atmospheres surrounding silicon interstitials and their evolution into decorated dislocation loops as a function of annealing. When interstitial and impurity atoms migrate into the proximity of a defect, the strain field around the defect will be relaxed, producing an energetically more favourable state. Similarly, Al segregations are formed in the Si eutectic phase of Al–Si alloys. The eutectic phase grows under an externally imposed cooling rate. Under such solidifying conditions, Al is incorporated in the Si lattice with a higher concentration than at thermodynamic equilibrium. Below the eutectic temperature, as the crystal is cooling down, there is a time period with high enough temperature to facilitate mobility and clustering of the excess Al. Preferential sites for these atoms are in the proximity of defects where the Si lattice is strained.

Nanometre sized defects in Si can be caused by the aggregation of Si interstitials into more complex defects [33,34], or due to the entrapment of nanosized crystals forming pockets at the growth front. In the unmodified alloy, Si grows ahead of the solidifying front by the TPRE mechanism [24]. Given this anisotropic growth mode and due to the low solubility and low distribution coefficient of Al in Si ($k = 0.002$) [35], Al will be accumulated at the growth front. At a certain Al concentration, entrapment of this Al-rich layer in small pockets of high Al concentration can occur [34,36]. Moreover, Si clusters which were not completely dissolved in the melt can also be incorporated at the solidifying growth front resulting in interstitial lattice defects [37]. Such interstitials may aggregate and produce a strain field towards which Al will diffuse. As a consequence, the three types of Al segregations found by APT are impurity clouds surrounding defects in the Si lattice. Depending on the type of defect in the Si lattice and the time given for the Al segregation to evolve during cooling, different types of segregations are formed. They range from small Al clusters to larger clouds surrounding a Si-rich core, and finally to the decoration of even larger defects such as dislocation loops as seen in the ring-like segregation.

4.2. Modified alloy

The modification of the flaky eutectic structure in favour of a more fibrous or coralline one is thought to be a consequence of the competing growth of the Al and Si phases [4,5,7]. It is well documented that the unmodified plate-like Si structure grows in advance with respect to the Al phase [2,3,7]. When the flake-to-fibrous transition takes place this growth rate advantage is lost. As a result, both phases grow simultaneously at a common growth front, which changes the final microstructure.

One way to obtain such condition is to force the growth rate to exceed 400–500 μm/s by, for example, rapid cooling [5]. Thall and Chalmers [38] suggested that under such conditions the microstructural refinement is a consequence of the balance between heat flow from the liquid to the solid and heat evolved during solidification. The solid–liquid interface will advance more rapid when the thermal conductivity is high and the latent heat of fusion is low. For the present phases, the thermal conductivity of Si is lower than Al, while the latent heat of fusion is higher. Because of these differences the growth rate will be similar or even faster for the Al phase.

An alternative way to produce a similar change in the growth front profile is by the addition of a minor element, e.g. Sr. This type of modification occurs at much lower solidification rates and, thus, it is more relevant for industrial processes. In this case, the phenomenon is explained by a reduction of the Si growth rate by mechanical obstruction and adsorption of the modifier into the Si crystal. This will produce a common growth front of the Al and Si eutectic phases [2,10]. The analysis of the nanometre sized features present in the Si phase is a key to understand how Sr is incorporated and how this translates into the microstructural modification.

4.2.1. Rod-like segregations

The modification of the Si-phase due to Sr addition is generally explained by a high multiplication of twins causing repeated changes in the crystallographic growth direction. Based on this interpretation, several twin boundaries and multiple crystallographic orientations would be expected in a transversal cut to the growth direction. The EBSD overview presented in Fig. 4(a), however, shows that most of the Si branches present only two different crystallographic orientations. This is corroborated in the TEM images (Fig. 4(b and c); Fig. 9(a)) where also only two orientations are evident, even if the Si crystal presents a high density of defects.

Although changes of the overall growth direction due to twinning are seen in almost all branches, they are not as frequent as one would expect in order for twins to cause the entire change of morphology. In fact, over the years, the discrepancy between predicted and observed twin density has been given attention to elucidate if the presence of twins is really a determining factor for the modification. Shamsuzzoha and Hogan [8], for instance, showed that the twin density changed with cooling rate while a modified structure was observed for all studied cooling rates. Another example was presented by Nogita et al. [39], who reported modification

by Ba and Ca, which produce a well modified structure with a lower amount of twins than expected.

In the present study, TEM and STEM images show that the most frequent features in the analysed sample are narrow defects embedded in the Si single crystal. These rod-like segregations involve only a few inter-planar distances and not necessarily an overall twinning of the crystal. This is supported by high-resolution images in Fig. 7(b and c) where no twin boundary is formed, and instead, only the stacking sequence of a few planes is changed. APT reveals an enrichment of Al and Sr pinning these features. To understand the influence of these rod-like defects on the modified structure we need to trace their origin and understand their composition.

Rod-like segregations have been observed in previous APT studies [18–20]. However, the three-dimensional complexity of the segregations was not captured until now when wider field of views were obtained. The reconstructed volume shown in Fig. 5 presents rod-like segregations in several different crystallographic orientations. Such measurement also permitted spatial correlation between APT and TEM. It should be born in mind that these APT and TEM images originate from different samples prepared from the same alloy. Nevertheless, there is a 1:1 correlation in the thickness of each single segregation and the distances between them (Fig. 6) manifesting the high frequency of rod-like segregations in the structure.

Numerous rod-like segregations found in both APT and TEM show a V-shaped morphology as the ones depicted in the overview and high-resolution images in Figs. 5–7. So-called hairpin dislocations may form when an advancing solid–liquid interface encounters small nanometre sized crystalline clusters with a slightly different crystallographic orientation than the growing crystal. When such crystalline pockets are incorporated into the Si single crystal, their misorientation favour the formation of stacking faults or half loop dislocations [40–42]. Al–Si–Sr clusters were frequently found at the intersection of rod-like defects as shown in Fig. 7(a). Timpel et al. [18,19] reported similar defects showing segregations of Al and Sr at their intersections using energy dispersive X-ray spectroscopy, while atom-resolved STEM confirmed that the overall direction of the Si crystal was not changed.

The misoriented pockets and consequent formation of hairpin dislocations will interrupt the Si growth. The lattice planes emerging from such disturbance will be favourable sites for Al and Sr accumulated at the solid–liquid interface to be adsorbed and incorporated into the Si lattice. Once these elements are adsorbed, the defects are stabilized or pinned, not having the
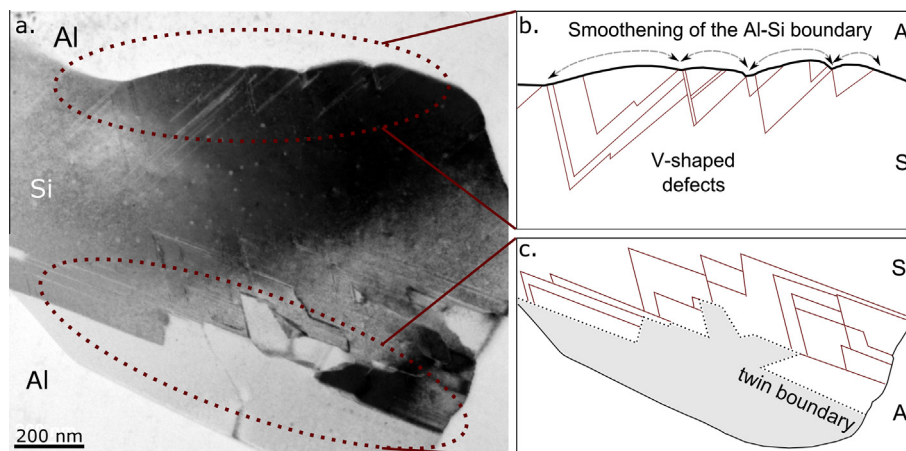
Fig. 9. Influence of the V-shaped defects on the Si growth; (a) TEM overview of a modified Si branch, (b) illustration of the smoothening of the Al–Si boundary by the presence of V-shaped defects, and (c) formation of an irregular twin boundary following the growth front determined by V-shaped defects.

possibility to annihilate during the further cooling of the alloy. This proposed mechanism adheres to the well-accepted theories claiming adsorption of the modifier at the growth front [2,10]. However, we propose that these segregations restrict the Si growth and generate localized disturbances over a few inter-planar distances, instead of causing overall changes of the growth direction by repeated twinning as proposed by earlier theories.

The remaining item to address is related to the formation of the nanometre sized clusters that induce V-shape defects. Some insight to the nucleation of these clusters can be found in the build-up of a layer at the growth front during solidification. It is reasonable to assume that both Al and Sr are accumulated ahead of the growth front given their low solubility in Si. This is further supported by Kobayashi et al. [43] who studied overmodified Al–Si samples by the addition of Na and reported the formation of an Al–Si–Na rich layer along the solidification interface. In the case of Sr-modification we propose a similar but subtler effect, with a thin Al–Si–Sr layer forming at the growth front. This layer will act as a mechanical obstruction for the growth of the Si-phase and favour a nearly planar growth front.

On this basis, local ternary phase reactions within this layer will assist in the nucleation of nanometre sized clusters responsible for V-shaped defects. Whether these clusters are crystalline or not, was not proven in the present study. However, based on our assumption that these clusters are a consequence of ternary phase reactions, we assume that they are crystalline. Such ternary reactions were studied, for example by Hanna and Hellawell [44] who determined the liquidus surface for the Al–Si–Sr phase diagram from 0 to 20 wt.% Si and 0 to 5 wt.% Sr. Their study presented a ternary reaction et Al – 12.9 at.% Si – 0.6 at.% Sr (Al – 13.2 wt.% Si – 1.8 wt.% Sr) around 2–3 K below the binary Al–Si eutectic. The Si concentration for this reaction to occur is near the binary eutectic point at 12.2 at.% Si [45] and the Sr concentration of 0.6 at.% can be easily reached at the growth front considering that all segregations measured by APT showed higher values (Figs. 5(d) and 8(b)). Another evidence supporting local ternary reactions is the range of Al:Sr ratios found in the segregations. These ratios coincide with two known intermetallic phases related to this system: Al_4Sr and Al_2Si_2Sr. A recent investigation reports that Sr atoms segregate towards Si-rich regions and that the addition of trace levels of Sr results in the formation of Al_2Si_2Sr-like clusters [46]. Formation of such clusters ahead of the solidification front and their incorporation in the Si-crystal to generate V-shaped defects would be consistent with the APT and TEM results. The reason why different elements have distinctive modifying efficiencies remains an open question. It is well known, for instance, that complete modification with Na can be achieved with lower Na concentration than with Sr. Different local ternary reactions for each element may be a factor determining these efficiencies.

One of the most important structural changes responsible for the enhanced crack resistance of the Sr-modified alloy is that Si branches become more rounded and smoother in comparison to the elongated plates with sharp or angular edges of the unmodified alloy. Fig. 9 presents two ways how rod-like segregations affect the structure at the microscopic level.

The first way is schematically shown in Fig. 9(b). It shows the direct influence of the rod-like segregations at the Al–Si phase boundary. Rod-like defects corresponding to Al–Sr segregations extend from the inner part of the branch until the Al–Si interface. During growth, the aggregation rate of Si is retarded at these defects by the adsorption of Al and Sr. Consequently, the regions between the rod-like segregations at the phase boundary have a slightly higher growth rate and, therefore, the boundary seems to be pinned by the defects which are marked by the arrows in Fig. 9(b). The net result of these types of features is a smoothening of the Al–Si phase boundary.

The second way the rod-like segregations appear to affect the modification is by influencing the twinned surface inside the Si branch. Almost all Si branches present one shift of the overall growth direction by a twin boundary (Fig. 4). Twin boundaries inside the Si phase were also seen for the unmodified sample. The difference between these alloys is that for the unmodified plate-like structure, the twin boundary is a unique plane which runs through the complete plate (Fig. 2), while in the Sr-modified sample the twinned boundary is irregular and changes directions repeatedly. This is schematically presented in Fig. 9(c) and it is frequently observed in the TEM samples, e.g. in Fig. 4(c). The changes of the growth rate and the irregular growth front determined by the rod-like segregations will favour the accumulation of Al–Si–Sr layers in certain crystallographic directions over others. When the growth is completely obstructed by this layer, formation of a twin is favoured. This can be seen in Fig. 9(a and c) where the irregular twin boundary follows the directions imposed by the V-shaped defects. Although the cause of the twin will be the segregation of Al and Sr at the front (see Section 4.2.3), the irregularities of this boundary are a consequence of the growth front given by the rod-like segregations. The growth flexibility of the Si branches given by these boundaries favours a more isotropic growth of the Si branches.

4.2.2. Particle-like segregations

Two types of particles were distinguished in the Sr-modified sample: small precipitates under 10 nm in diameter, and larger ones over this size. In contrast to the unmodified Si-phase where all particles were homogeneously distributed, the Sr-modified Si phase presents regions with very high density of small precipitates (<10 nm) (Fig. 5(b)). This high density of segregations shows how the Si-growth pushes Al and Sr ahead of the solidification front until a threshold level is reached and they are incorporated in the Si-phase. It is likely that the agglomeration of these segregations affects the advancement of the solidification front and contributes to the modification. In contrast, the larger particles have a similar density and distribution as in the unmodified alloy and they do not show any relevant correlation to the structural modification. Similarly as seen in the unmodified alloy, excess Al trapped in the Si-phase diffuses to strained regions of the lattice forming impurity clouds.

4.2.3. Planar segregations

Planar segregations are considered to be a result of the progressive accumulation of Al and Sr at the solidifying interface. As it was explained in Section 4.2.1, rod-like segregation will cause instabilities at the growing interface. These perturbations in the shape of the solid–liquid interface of the Si faceted phase grow faster in certain crystallographic directions and become tangential to low-index faceting planes [34]. Al and Sr will be continuously rejected at these facets ending up in the formation of an enriched surface (planar segregation). Further growth of the Si crystal in this direction is hindered until this enriched layer is overgrowth and trapped in the Si lattice. Such planar segregations favour the formation of grain boundaries and irregular twin boundaries crossing through the entire Si branch as the one depicted in Fig. 9(c).

4.3. Al and Sr concentrations in the Si phase

The solubility of Al in Si is low and sometimes for practical reasons it is even considered to be zero. It is clear, however, that this practical assumption is not valid if the Si phase is analysed at a more detailed level. Data measured by diffusion [47] and temperature-gradient zone melting [48] showed solubilities lower than 0.035 at.% at all temperatures. Trumbore [35] reviewed a number of conflicting studies showing discrepancies as high as three or

four orders of magnitude in the solid solubility of Al in Si. In this study, Trumbore measured a solid solubility of 0.03 at.% at 720 °C by spectrophotometric and spectroscopic analyses on crystals grown in thermal gradient experiments. In addition, he calculated the solidus curve by reinterpreting Gudmundsen and Maserjian's [49] low temperature curve by taking Backenstoss' mobility data [50] into account resulting in an Al solid-solubility near 6×10^{18} at./cm^3 ($\sim$0.035 at.%) at 600 °C. These data agree with the values obtained by APT in this study. The amount of Al in solid solution in the Si phase is nearly the same in both alloys and ranges between $\sim$300 and 600 at-ppm.

The total amount of Al in the Si-phase is higher than the solubility limit for the unmodified and modified alloys (Table 3). The total amount of Al in the unmodified alloy is $\sim$0.161 at.%, while in the modified is of $\sim$0.616 at.%. As both alloys were directionally solidified under the same temperature gradient and growth rate, the fourfold increase of Al content in the modified alloy as compared to the unmodified, can be explained by the presence of Sr. This finding supports the hypothesis that Al and Sr are incorporated together into the Si-phase in the form of nanometre sized phases as proposed in Section 4.2.1.

The content of Sr in the Si-phase of the modified alloys was determined by APT. Just as for Al, the amount of Sr in solid solution (40 ± 10 at-ppm) is considerably lower than the total amount of Sr trapped in the Si-phase (860 ± 560 at-ppm). This indicates that most of the Sr contained in the alloy is related to segregations. It is commonly accepted that Sr segregates to the Si phase of these alloys [12,51]. The total amount of Sr in the alloy is 46 at-ppm (150 wt-ppm) and if all this Sr was contained in the Si phase, the total Sr concentration in Si would be nearly 680 at-ppm. This concentration lies in the range measured by APT confirming that Sr predominantly segregates to the Si phase. This is vital information for the optimization of the alloy.

5. Conclusion

AlSi7 alloys with and without Sr modification were analysed by APT, TEM and STEM. The composition and distribution of Al and Sr in the Si phase were studied and correlated to structural defects.

The unmodified Si structure presented nanometre size Al segregations. The amount of Al trapped in Si during solidification is over its solubility limit, what makes Al to diffuse and decorate defects. These segregations do not influence the plate-like type of growth of the Si microstructure.

The coralline-like microstructure of the modified sample showed high density of defects enriched by Al–Sr segregations. Three distinctive features inherent to the structural modification were identified:

a. Rod-like segregations which frequently showed a V-shape. These segregations influence the final round section and smoothening of the Si branches and the formation of irregular twin boundaries.
b. Regions with high density of small particle-like segregations. These regions result from the accumulation of Al and Sr at the solidification front, what hinders the Si growth.
c. Planar segregations at grain and twin boundaries.

Compositional analysis of the Si phase show solubilities of 430 ± 160 at-ppm Al and 40 ± 10 at-ppm Sr. The total amount of Al trapped in the Si phase is four times higher in the Sr modified alloy than in the unmodified, confirming that a large fraction of Al is incorporated together with Sr into the Si phase. Sr segregates predominantly to the Si phase confirming its importance in the modification of the eutectic growth.

The present study shows that high density of defects enriched by Al and Sr in the Si phase plays a decisive role in the modification of the Si microstructure. We propose that the nucleation of Al–Si–Sr/Al–Sr nanoclusters by local ternary reactions assists in the formation and pinning of defects.

Although changes in the Si crystallographic orientation by twinning is a relevant characteristic of this modification, different types of defects including stacking faults and hairpin dislocations should also be taken into account.

Appendix A. Supplementary material

Supplementary material associated with this article can be found, in the online version, at http://dx.doi.org/10.1016/j.jallcom.2014.05.121.

References

[1] J.E. Gruzleski, B. Closset, The Treatment of Liquid Aluminum–Silicon Alloys, American Foundrymens Society, 1990.
[2] M.G. Day, A. Hellawell, The microstructure and crystallography of aluminium–silicon eutectic alloys, Proc. R. Soc. A Math. Phys. Eng. Sci. 305 (1968) 473–491.
[3] A. Hellawell, The growth and structure of eutectics with silicon and germanium, Prog. Mater. Sci. 15 (1970) 3–78.
[4] H.A. Steent, A. Hellawell, Structure and properties of aluminium–silicon eutectic alloys, Acta Metall. 20 (1972) 363–370.
[5] D.C. Jenkinson, L.M. Hogan, The modification of aluminium–silicon alloys with strontium, J. Cryst. Growth. 28 (1975) 171–187.
[6] M.D. Hanna, S.-Z. Lu, A. Hellawell, Modification in the aluminum silicon system, Metall. Trans. A. 15 (1984) 459–469.
[7] K.F. Kobayashi, L.M. Hogan, The crystal growth of silicon in Al–Si alloys, J. Mater. Sci. 20 (1985) 1961–1975.
[8] M. Shamsuzzoha, L.M. Hogan, The crystal morphology of fibrous silicon in strontium-modified Al–Si eutectic, Philos. Mag. A. 54 (1986) 459–477.
[9] M. Shamsuzzoha, L.M. Hogan, Crystal morphology of unmodified aluminium–silicon eutectic microstructures, J. Cryst. Growth 76 (1986) 429–439.
[10] S. Lu, A. Hellawell, The mechanism of silicon modification in aluminum–silicon alloys: impurity induced twinning, Metall. Trans. A 18 (1987) 1721–1733.
[11] M. Shamsuzzoha, L.M. Hogan, The twinned growth of silicon in chill-modified Al–Si eutectic, J. Cryst. Growth 82 (1987) 598–610.
[12] L. Clapham, R.W. Smith, Segregation behaviour of strontium in modified and unmodified Al–Si alloys, J. Cryst. Growth 92 (1988) 263–270.
[13] S.D. McDonald, K. Nogita, A.K. Dahle, Eutectic nucleation in Al–Si alloys, Acta Mater. 52 (2004) 4273–4280.
[14] A.K. Dahle, K. Nogita, S.D. McDonald, J.W. Zindel, L.M. Hogan, Eutectic nucleation and growth in hypoeutectic Al–Si alloys at different strontium levels, Metall. Mater. Trans. A 32 (2001) 949–960.
[15] A.K. Dahle, K. Nogita, S.D. McDonald, C. Dinnis, L. Lu, Eutectic modification and microstructure development in Al–Si Alloys, Mater. Sci. Eng. A 413–414 (2005) 243–248.
[16] S.D. McDonald, A.K. Dahle, J.A. Taylor, D.H. StJohn, Eutectic grains in unmodified and strontium-modified hypoeutectic aluminum–silicon alloys, Metall. Mater. Trans. A 35 (2004) 1829–1837.
[17] M.E. van Dalen, R.A. Karnesky, J.R. Cabotaje, D.C. Dunand, D.N. Seidman, Erbium and ytterbium solubilities and diffusivities in aluminum as determined by nanoscale characterization of precipitates, Acta Mater. 57 (2009) 4081–4089.

[18] M. Timpel, N. Wanderka, R. Schlesiger, T. Yamamoto, N. Lazarev, D. Isheim, et al., The role of strontium in modifying aluminium–silicon alloys, Acta Mater. 60 (2012) 3920–3928.

[19] M. Timpel, N. Wanderka, R. Schlesiger, T. Yamamoto, D. Isheim, G. Schmitz, et al., Sr-Al–Si co-segregated regions in eutectic Si phase of Sr-modified Al–10Si alloy, Ultramicroscopy 132 (2013) 216–221.

[20] J. Barrirero, M. Engstler, F. Mücklich, Atom probe analysis of Sr distribution in AlSi foundry alloys, in: Light Met., vol. 2013, TMS, 2013, pp. 291–296.

[21] K. Thompson, D. Lawrence, D.J. Larson, J.D. Olson, T.F. Kelly, B. Gorman, In situ site-specific specimen preparation for atom probe tomography, Ultramicroscopy 107 (2007) 131–139.

[22] J. Schindelin, I. Arganda-Carreras, E. Frise, V. Kaynig, M. Longair, T. Pietzsch, et al., Fiji: an open-source platform for biological-image analysis, Nat. Methods 9 (2012) 676–682.

[23] F. Lasagni, A. Lasagni, C. Holzapfel, F. Mücklich, H.P. Degischer, Three dimensional characterization of unmodified and Sr-modified Al–Si eutectics by FIB and FIB EDX tomography, Adv. Eng. Mater. 8 (2006) 719–723.

[24] D.R. Hamilton, R.G. Seidensticker, Propagation mechanism of germanium dendrites, J. Appl. Phys. 31 (1960) 1165.

[25] C.M. Eichfeld, S.S. a Gerstl, T. Prosa, Y. Ke, J.M. Redwing, S.E. Mohney, Local electrode atom probe analysis of silicon nanowires grown with an aluminum catalyst, Nanotechnology 23 (2012) 215205.

[26] B. Gault, M.P. Moody, J.M. Cairney, S.P. Ringer, Atom Probe Microscopy, Springer New York, New York, NY, 2012.

[27] C. Oberdorfer, G. Schmitz, On the field evaporation behavior of dielectric materials in three-dimensional atom probe: a numeric simulation, Microsc. Microanal. 17 (2011) 15–25.

[28] W. Lefebvre, F. Danoix, G. Da Costa, F. De Geuser, H. Hallem, A. Deschamps, et al., 3DAP measurements of Al content in different types of precipitates in aluminium alloys, Surf. Interface Anal. 39 (2007) 206–212.

[29] T.F. Kelly, M.K. Miller, Invited review article: atom probe tomography, Rev. Sci. Instrum. 78 (2007) 031101.

[30] D.K. Sadana, M.H. Norcott, R.G. Wilson, U. Dahmen, Transmission electron microscopy of aluminum implanted and annealed ⟨1 0 0⟩ Si: direct evidence of aluminum precipitate formation, Appl. Phys. Lett. 49 (1986) 1169.

[31] J. Washburn, G. Thomas, H.J. Queisser, Diffusion-induced dislocations in silicon, J. Appl. Phys. 35 (1964) 1909.

[32] C. Carter, W. Maszara, D.K. Sadana, G.a. Rozgonyi, J. Liu, J. Wortman, Residual defects following rapid thermal annealing of shallow boron and boron fluoride implants into preamorphized silicon, Appl. Phys. Lett. 44 (1984) 459.

[33] K. Thompson, P.L. Flaitz, P. Ronsheim, D.J. Larson, T.F. Kelly, Imaging of arsenic Cottrell atmospheres around silicon defects by three-dimensional atom probe tomography, Science 317 (2007) 1370–1374.

[34] D.T.J. Hurle, Crystal Pulling From the Melt, Springer Berlin Heidelberg, 1993.

[35] F.A. Trumbore, Solid solubilities of impurity elements in germanium and silicon*, Bell Syst. Tech. J. 39 (1960) 205–233.

[36] G.A. Chadwick, Eutectic alloy solidification, Prog. Mater. Sci. 12 (1963) 99–182.

[37] J. Zhang, H. Yu, S.B. Kang, J.H. Cho, G. Min, Modification of horizontal continuous casting Al–12%Si alloy using FSM master alloy, Mater. Charact. 75 (2013) 44–50.

[38] B.M. Thall, B. Chalmers, Modification in aluminum–silicon alloys, J. Inst. Met. 77 (1950) 79–97.

[39] K. Nogita, J. Drennan, A.K. Dahle, Evaluation of silicon twinning in hypo-eutectic Al–Si alloys, Mater. Trans. 44 (2003) 625–628.

[40] L.D. Glowinski, K.N. Tu, P.S. Ho, Direct observations of defects in implanted and postannealed silicon wafers, Appl. Phys. Lett. 28 (1976) 312.

[41] T. Sands, J. Washburn, E. Myers, D.K. Sadana, On the origins of structural defects in BF2+implanted and rapid-thermally-annealed silicon: conditions for defect-free regrowth, Nucl. Instrum. Methods Phys. Res. Sect. B Beam Interact. Mater. Atoms 7–8 (1985) 337–341.

[42] K.S. Jones, S. Prussin, E.R. Weber, A systematic analysis of defects in ion-implanted silicon, Appl. Phys. A Solids Surf. 45 (1988) 1–34.

[43] K. Kobayashi, P. Shingu, R. Ozaki, Banded Structure in aluminium–silicon eutectic alloy, Trans. Jpn. Inst. Met. 21 (1980) 417–424.

[44] M.D. Hanna, A. Hellawell, Modification of Al–Si microstructure – the Al–Si–Sr phase diagram from 0–20 wt.% Si and 0–5.0 wt.% Sr, in: L.H. Bennett, T.B. Massalski, B.C. Giessen (Eds.), Alloy Phase Diagrams, Elsevier Science Publishing, New York, 1983, pp. 411–416.

[45] J.L. Murray, A.J. McAlister, The Al–Si (Aluminum–Silicon) system, Bull. Alloy Phase Diagrams 5 (1984) 74–84.

[46] P. Srirangam, S. Chattopadhyay, A. Bhattacharya, S. Nag, J. Kaduk, S. Shankar, et al., Probing the local atomic structure of Sr-modified Al–Si alloys, Acta Mater. 65 (2014) 185–193.

[47] R.C. Miller, A. Savage, Diffusion of aluminum in single crystal silicon, J. Appl. Phys. 27 (1956) 1430.

[48] D. Navon, V. Chernyshov, Retrograde solubility of aluminum in silicon, J. Appl. Phys. 28 (1957) 823.

[49] R.A. Gudmundsen, J. Maserjian, Semiconductor properties of recrystallized silicon in aluminum alloy junction diodes, J. Appl. Phys. 28 (1957) 1308.

[50] G. Backenstoss, Conductivity mobilities of electrons and holes in heavily doped silicon, Phys. Rev. 108 (1957) 1416–1419.

[51] K. Nogita, H. Yasuda, K. Yoshida, K. Uesugi, A. Takeuchi, Y. Suzuki, et al., Determination of strontium segregation in modified hypoeutectic Al–Si alloy by micro X-ray fluorescence analysis, Scr. Mater. 55 (2006) 787–790.

Paper II

Cluster formation at the Si/liquid interface in Sr and Na modified
Al–Si alloys

J. Barrirero, J. Li, M. Engstler, N. Ghafoor, P. Schumacher, M. Odén,
F. Mücklich

Cluster formation at the Si/liquid interface in Sr and Na modified Al–Si alloys

Jenifer Barrirero [a,b], Jiehua Li [c], Michael Engstler [a], Naureen Ghafoor [b], Peter Schumacher [c], Magnus Odén [b], Frank Mücklich [a,*]

[a] Department of Materials Science, Campus D3.3, Saarland University, D 66123 Saarbrücken, Germany
[b] Nanostructured Materials, Department of Physics, Chemistry, and Biology (IFM), Linköping University, SE 581 83 Linköping, Sweden
[c] Montanuniversität Leoben, A 8700 Leoben, Austria

ARTICLE INFO

ABSTRACT

Atom probe tomography was used to compare Na and Sr modified Al–Si hypoeutectic alloys. Both Na and Sr promote the formation of nanometre-sized clusters in the Si eutectic phase. Compositional analyses of the clusters show an Al:Sr ratio of 2.92 ± 0.46 and an Al:Na ratio of 1.07 ± 0.23. It is proposed that $SrAl_2Si_2$ and NaAlSi clusters are formed at the Si/liquid interface and take part in the modification process by altering the eutectic Si growth.

© 2016 Elsevier B.V. All rights reserved.

To meet the evolving demands of current high-performance industrial applications, ultimate tensile strength, ductility, impact and thermal-shock properties of Al–Si alloys can be effectively favoured by a morphological modification of the eutectic phase [1]. Na and Sr are known to segregate into the eutectic Si phase and effectively induce a transition from a plate- to a coralline-like structure [2–5].

Since Pacz discovered this effect in 1921 [6], large efforts have been directed towards understanding the underlying mechanisms. During the first half of the last century, Na modification was in focus [7–12]. Later, Sr emerged as an attractive alternative to Na since it is easier to control the Sr-content during the casting process. Na has high volatility and oxidizes easily, which affects the Na addition control [8]. Sr has a lower tendency to fade and can be added in the form of Al–Sr master alloys, making the addition of the alloying element easier and more precise [1].

The effects of Na and Sr on the morphological modification have often been considered indistinctively [13–15]. Both elements produce multiplication of twins and lattice defects in the Si phase, as well as the same coralline-like eutectic microstructure.

Recent investigations have revealed that Al forms segregations with Sr or Na in the Si eutectic phase [16–18]. The presence of Al in combination with the modifier was not considered in previous theories when explaining the origin of the modification [5,11]. These findings open

for new interpretations on the role of Al and the mechanisms causing the change in the microstructure.

In this paper, atom probe tomography (APT) combined with transmission electron microscopy (TEM) is used to compare the structure and the Al content in Sr- and Na-rich clusters in the Si eutectic phase. It is proposed that $SrAl_2Si_2$ and NaAlSi clusters form at the Si/liquid interface and take part in the modification of the eutectic Si growth to form a coralline-like microstructure.

Al–Si hypoeutectic alloys modified with Sr and Na were manufactured by high purity Si (5 N, 99.999) and Al (5 N). An Al-5 wt.% Si alloy was modified by 160 ppm Na. Na was added using elemental Na in vacuum packed Al foils before casting. An Al-7 wt.% Si alloy was modified by 150 ppm Sr added using an Al-10 wt.% Sr master alloy.

TEM sample preparation was performed by successive mechanical grinding, polishing, and dimpling to a thickness of about 30 μm followed by Ar ion-beam milling to electron transparency using a Gatan Precision Ion Polishing System (PIPS) model 691. Additional TEM and APT samples were prepared in a dual-beam focused ion beam/scanning electron microscopy workstation (FIB/SEM) (Helios NanoLab 600™, FEI Company, USA). After lift out and thinning of the samples, a low energy milling at 2 kV was performed to minimize gallium induced damage [19].

TEM analysis was performed using a FEI Tecnai G2 microscope operated at 200 kV in micro and nanoprobe mode and an image-side aberration-corrected JEOL 2100F microscope operated at 200 kV. Laser Pulsed APT was carried out with a LEAP™ 3000X HR (CAMECA) at repetition rates of 160 kHz and 250 kHz, a specimen temperature of about

* Corresponding author.

40 K, a pressure lower than 1.33×10^{-8} Pa, and a laser pulse energy in the range of 0.4–0.5 nJ. The evaporation rate of the specimen was 5 atoms per 1000 pulses. Datasets were reconstructed and analysed with IVAS™ 3.6.8 software (CAMECA). Al, Sr and Na contents in Si were measured after background subtraction performed with the IVAS software.

The eutectic Si structure of both alloys, modified either by the addition of Sr or Na, presents a high density of lattice defects (Fig. 1). These defects are necessary for the repeated change of Si growth direction and growth rate that give rise to the desired coralline-structure [16]. It was observed that the defects in the Si lattice are enriched by the modifier (Sr/Na) and Al by correlating TEM and APT data. TEM images in Fig. 1 show spherical-precipitates, stacking faults (SFs) and twin lamellas (TLs) which have a one-to-one correspondence to the three categories of solute clusters detected by APT: spherical, rod-like and planar (Figs. 2 and 3).

TEM images of both alloys reveal that spherical precipitates are often located at the intersection of SFs and TLs on {111}Si planes (Fig. 1 b, c and d). APT confirms the presence of spherical precipitates and shows solute enrichment of Al and modifiers (Fig. 2). This suggests that the spherical precipitates may assist the formation of SFs and TLs. Based on this, the phenomena causing the modified microstructure appear to be the same for both Sr and Na additions, i.e. an obstructed Si growth as a result of the formation of a high number of solute-enriched clusters and crystallographic defects.

Despite the structural similarities between Sr and Na modifications, it is important to point out a significant difference in the composition of the Sr- and Na-rich clusters recorded by APT. Since the clusters are located in the Si phase, their Si content could not be determined and instead the focus was put on the content of Al and modifier. The local

composition of the clusters measured by APT can be influenced by ion trajectory overlaps due to local magnification effects [20]. When considering 2–5 nm sized segregations present in these alloys, this artefact may lead to a convolution of the matrix with the precipitate resulting in an overestimation of the matrix element [20–24]. Given this uncertainty, reporting relative solute ratios Al:M (M = Sr or Na) is more adequate than the absolute concentrations. Each single cluster of solutes was exported in tightly fitted regions of interest (ROIs) for separate analysis. The bulk composition inside the ROI was measured after optimization of the elemental ranges in the mass-to-charge spectrum. The number of solute atoms in the clusters was measured after background subtraction. Fig. 4 shows the Al:M ratios for each cluster. The ratios for Sr- and Na-modified alloys are distinctly different, i.e. the ratio datasets have no overlap and no outliers. In the Sr-modified alloy, the average of 14 rod-like and 5 planar segregations from 6 APT specimens yields an Al:Sr ratio of 2.92 ± 0.46. In the Na-modified alloy, the average of 9 rod-like and 2 planar segregations from 5 APT specimens results in an Al:Na ratio of 1.07 ± 0.23. The standard deviations in the Al:M ratios can be attributed to the combined effect of the limited number of solute atoms involved in such small clusters and the detection efficiency of APT (~37%). The ratios indicate that Al is needed to form these segregations and that Al interacts differently with Na and Sr.

Inferring the role of Al on the modification and understanding the Al:M ratios is not straight forward given the required extrapolation from an observed "post-mortem" microstructure to the dynamic scenario occurring at a moving solid/liquid interface in a temperature gradient during solidification.

The high density of defects has historically been explained by the impurity induced twinning (IIT) mechanism and the poisoning of the twin plane re-entrant edge (TPRE) mechanism suggesting an inhibition of
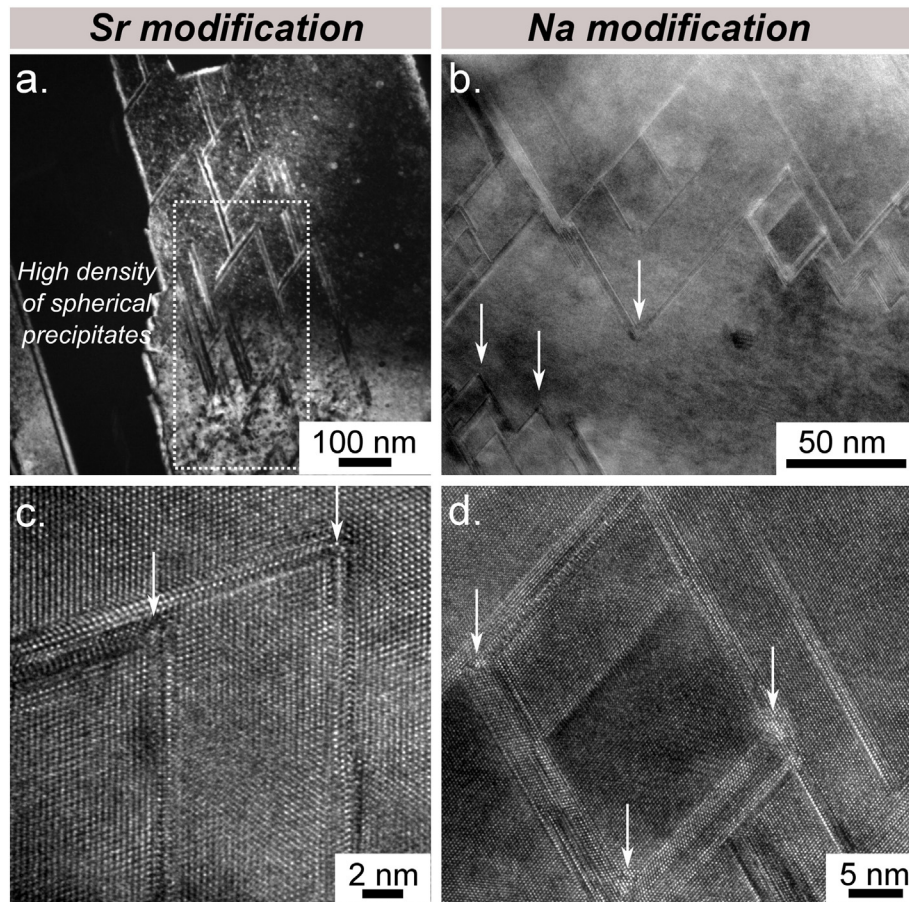
Fig. 1. TEM images of the eutectic Si phase. (a) Dark-field image of Sr-modified Si phase recorded along <111> zone axis. (b) Bright-filed image of Na-modified Si phase recorded along <011> zone axis. (c,d) High resolution images of the Sr- and Na-modified alloys, respectively. White arrows highlight particles at the intersections of SFs and TLs.
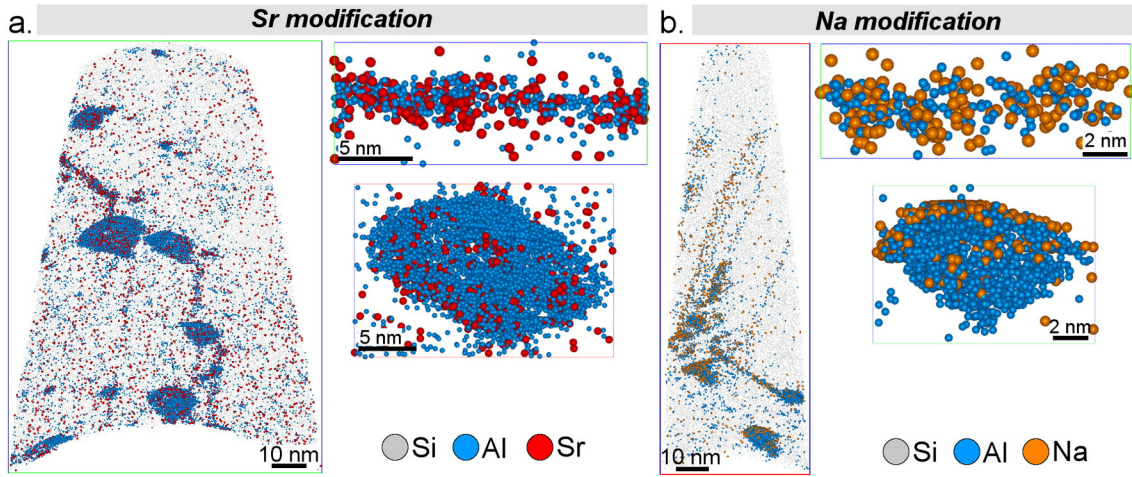
Fig. 2. APT datasets of the eutectic Si phase and magnified regions of interest of rod-like and particle-like segregations: (a) Sr-modified alloy, b) Na-modified alloy.

the Si growth by adsorption of single atoms of the modifier at the solid/liquid interface [5,11]. This led to the proposal that the atomic radius (r) of the modifiers satisfy a geometrical factor of $r_M/r_{Si} = 1.646$. However, this way of explaining the origin for modification does not consider the presence of Al nor the defined Al:M ratios found in this investigation.

Recently, Li et al. [25] proposed that the adsorption of Sr (or Na) atoms causes the changes in growth direction and multiplication of twins, while the entrainment of Al together with the modifier is an artefact rather than an active factor for the modification. They propose that the formation of Al–Si–Sr-rich clusters takes place after the adsorption of Sr (or Na) atoms during the subsequent overgrowth of Si. Another way of explaining the presence of Al, however, would be to consider the formation of such clusters at the growth front just before the overgrowth of Si. To address the different Al:M ratios, one can first consider the invariant reactions reported in literature for the Al–Si [26], Al–Si–Na [27] and Al–Si–Sr [28] systems (Table 1). Due to the low concentration of modifier in both systems, they present ternary eutectic reactions very near to the binary Al–Si eutectic composition and temperature (Table 1). In the system containing Na, the NaAlSi (τ) ternary compound

forms together with Si and Al [27]; while for the alloy containing Sr, $SrAl_2Si_2$ phase is predicted [28]. Such compounds are consistent with the Al:M ratios measured by APT in the rod-like and planar segregations in the Si phase. The stoichiometry of the clusters (Al:Na ~ 1, Al:Sr ~ 2) corresponds to the compounds expected for each alloy, i.e. NaAlSi for Na modification and $SrAl_2Si_2$ for Sr modification.

In the case of the alloy containing Sr, even though thermodynamic calculations predict the formation of $SrAl_2Si_2$ at the ternary eutectic reaction [28], this will only be possible if there is a local Sr concentration of about 20 at.% Sr. Since the content of the modifier in the alloy is much lower, the nucleation and growth of this intermetallic phase will not be always feasible. However, locally at a length scale just involving a few thousand atoms the situation might be dramatically different. Ahead of the growing Si crystal a diffusion profile is formed by segregation leading to constitutional undercooling. The solubilities of Al and Sr in Si are ~400 at-ppm and ~40 at-ppm, respectively [16], which is less than the expected concentration in the liquid. Therefore, both these elements are expected to be enriched ahead of the solidification front. That is, over a distance of a few nanometres in front of the growth front, the local concentrations of Sr and Al are sufficiently high to
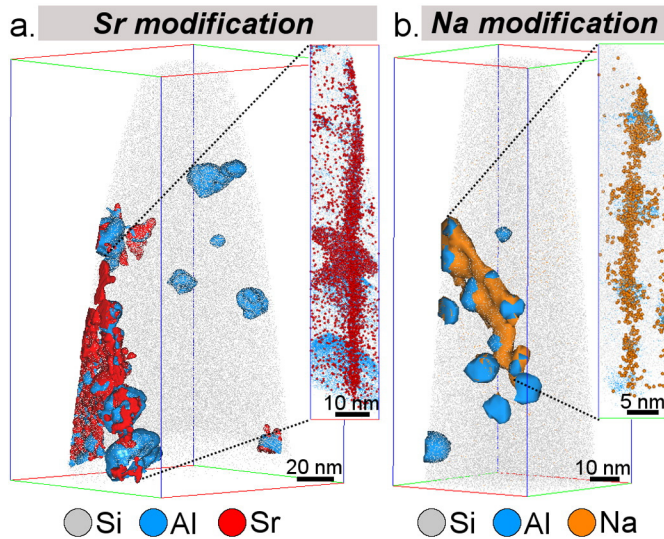
Fig. 3. APT datasets of the eutectic Si phase. Segregations are highlighted by iso-concentration surfaces. Single atoms are only shown in the insets. (a) Sr-modified alloy. Iso-concentration surfaces at 2 at.% Al and 0.4 at.% Sr, (b) Na-modified alloy. Iso-concentration surfaces at 3 at.% Al and 1 at.%Na.

Fig. 4. Al:M (M: Sr, Na) ratios for rod-like and planar segregations.
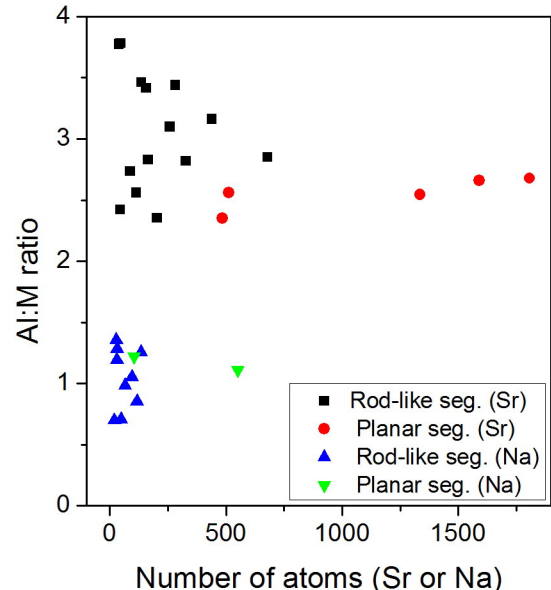
Table 1
Eutectic reactions in the binary Al-Si and ternary Al–Si–Na and Al–Si–Sr alloys.

Reaction	T (°C)	Composition (at.%)		
(Al–Si) system [26]			Al	Si
L ↔ (Al) + (Si)	577		87.8	12.2
(Al–Si–Na) system [27]		Na	Al	Si
L ↔ AlSiNa (τ) + (Al) + (Si)	576	0.01	87.35	12.64
(Al–Si–Sr) system [28]		Sr	Al	Si
L ↔ Al$_2$Si$_2$Sr (τ_1) + (Al) + Si	575	0.03	~86.8	13.1

allow for the formation of atomic clusters of compounds. Recently, Srirangam et al. [29] showed that the local coordination environment of Sr in Al–Si alloys is consistent with the formation of SrAl$_2$Si$_2$ clusters in the eutectic phase supporting the concept that nanometre-sized clusters can be formed in these alloys. According to the classical homogenous nucleation theory clusters of this size are subcritical, and the local ordering in the melt would be that of fluctuating clusters. For stable clusters to occur, heterogeneous substrates and/or high undercooling must be present. Thus, during growth of the eutectic Si, two competing processes are active at the solid/liquid interface, i.e. segregation of Sr and Al out of the Si crystal and the formation of clusters where the interface acts as a heterogeneous substrate. In the case of conventional solidification, segregation dominates. However, if adsorption of a modifying element (Sr or Na) is possible, it would be energetically favourable to form clusters at the interface. These clusters are continuously incorporated into the growing Si crystal, which also seals their size and composition. The same reasoning can be used for the alloy modified by Na with the difference that the compound forming is NaAlSi. This means all of the three phases that results from the ternary eutectic reactions (Table 1) are present in the alloys, although the SrAl$_2$Si$_2$ and NaAlSi compounds cannot be resolved by optical microscope or even SEM. It remains unclear whether single modifier atoms or Al–Si–M-rich clusters induce multiplication of crystallographic defect. However, both cases highlight the interaction between the modifier and Si. Furthermore, APT shows that Al is present in all defects [16], even when the defect is only one atomic monolayer [18].

The presence of Al–Si–M-rich clusters in the eutectic phase suggests that the efficiency of a modifier depends on its ability to form ternary compound clusters at the Si/liquid interface near the binary eutectic point, and furthers the understanding of the eutectic modification of Al–Si alloys. Other elements such as Eu [30,31], Ba [32], Ca [33] and Yb [34] which are known to alter the microstructure either to fibrous Si or a refined plate-like structure can also form ternary compounds, i.e. EuAl$_2$Si$_2$, BaAlSi, BaAl$_2$Si$_2$, CaAl$_2$Si$_2$ and YbAl$_2$Si$_2$. Studies of these systems by means of APT will provide additional information towards the understanding of the eutectic modification.

In conclusion, APT chemical analysis showed that Sr and Na additions in Al–Si alloys form clusters with fixed and distinctly different Al:M ratios. Based on these results, it is proposed that SrAl$_2$Si$_2$ and NaAlSi clusters formed at the Si/liquid interface alter the Si growth and consequently modify the microstructure. This investigation emphasizes the importance of considering compound formation when evaluating elements for modification and optimization of manufacturing processes.

References

[1] J.E. Gruzleski, B. Closset, The Treatment of Liquid Aluminum–Silicon Alloys, American Foundrymens Society, 1990.
[2] F. Lasagni, A. Lasagni, C. Holzapfel, F. Mücklich, H.P. Degischer, Adv. Eng. Mater. 8 (2006) 719–723.
[3] L Clapham, R.W. Smith, J. Cryst. Growth 92 (1988) 263–270.
[4] K. Nogita, H. Yasuda, K. Yoshida, K. Uesugi, A. Takeuchi, Y. Suzuki, A.K. Dahle, Scr. Mater. 55 (2006) 787–790.
[5] S. Lu, A. Hellawell, Metall. Trans. A 18 (1987) 1721–1733.
[6] A. Pacz, Alloy 1 (1921) 387,900.
[7] A.G.C. Gwyer, H.W.L. Phillips, J. Inst. Met. 36 (1923) 283–324.
[8] B.M. Thall, B. Chalmers, J. Inst. Met. 77 (1950) 79–97.
[9] R.C. Plumb, J.E. Lewis, J. Inst. Met. 86 (1958) 393–400.
[10] V.L. Davies, J.M. West, J. Inst. Met. 92 (1963) 175–180.
[11] M.G. Day, A. Hellawell, Proc. R. Soc. A Math. Phys. Eng. Sci. 305 (1968) 473–491.
[12] H. Fredriksson, M. Hillert, N. Lange, J. Inst. Met. 101 (1973) 285–299.
[13] D.C. Jenkinson, L.M. Hogan, J. Cryst. Growth 28 (1975) 171–187.
[14] M.D. Hanna, S.-Z. Lu, A. Hellawell, Metall. Trans. A 15 (1984) 459–469.
[15] K.F. Kobayashi, L.M. Hogan, J. Mater. Sci. 20 (1985) 1961–1975.
[16] J. Barrirero, M. Engstler, N. Ghafoor, N. de Jonge, M. Odén, F. Mücklich, J. Alloys Compd. 611 (2014) 410–421.
[17] M. Timpel, N. Wanderka, R. Schlesiger, T. Yamamoto, D. Isheim, G. Schmitz, S. Matsumura, J. Banhart, Ultramicroscopy 132 (2013) 216–221.
[18] J.H. Li, J. Barrirero, M. Engstler, H. Aboulfadl, F. Mücklich, P. Schumacher, Metall. Mater. Trans. A 46 (2014) 1300–1311.
[19] K. Thompson, D. Lawrence, D.J. Larson, J.D. Olson, T.F. Kelly, B. Gorman, Ultramicroscopy 107 (2007) 131–139.
[20] W. Lefebvre, F. Danoix, G. Da Costa, F. De Geuser, H. Hallem, A. Deschamps, M. Dumont, Surf. Interface Anal. 39 (2007) 206–212.
[21] G. Sha, H. Möller, W.E. Stumpf, J.H. Xia, G. Govender, S.P. Ringer, Acta Mater. 60 (2012) 692–701.
[22] B. Gault, F. de Geuser, L. Bourgeois, B.M. Gabble, S.P. Ringer, B.C. Muddle, Ultramicroscopy 111 (2011) 683–689.
[23] J. Rüsing, J.T. Sebastian, O.C. Hellman, D.N. Seidman, Microsc. Microanal. 6 (2000) 445–451.
[24] H.K. Hasting, W. Lefebvre, C. Marioara, J.C. Walmsley, S. Andersen, R. Holmestad, F. Danoix, Surf. Interface Anal. 39 (2007) 189–194.
[25] J.H. Li, M. Albu, F. Hofer, P. Schumacher, Acta Mater. 83 (2015) 187–202.
[26] J.L. Murray, A.J. McAlister, Bull. Alloy Phase Diagr. 5 (1984) 74–84.
[27] N. Bochvar, P. Budberg, F. Hayes, Y. Liberov, R. Schmid-Fetzer, Al–Na–Si Ternary Phase Diagram, MSI, Materials Science International Services GmbH, Stuttgart, 1993.
[28] R. Ferro, O. Kubaschewski, H. Hubert, G. Ibe, VCH 8 (1993) 270–278.
[29] P. Srirangam, S. Chattopadhyay, A. Bhattacharya, S. Nag, J. Kaduk, S. Shankar, R. Banerjee, T. Shibata, Acta Mater. 65 (2014) 185–193.
[30] J.H. Li, X.D. Wang, T.H. Ludwig, Y. Tsunekawa, L. Arnberg, J.Z. Jiang, P. Schumacher, Acta Mater. 84 (2015) 153–163.
[31] J. Li, F. Hage, M. Wiessner, L. Romaner, D. Scheiber, B. Sartory, Q. Ramasse, P. Schumacher, Sci. Rep. 5 (2015) 13802.
[32] A. Knuutinen, K. Nogita, S.D. Mcdonald, A.K. Dahle, 1 (2002) 229–240.
[33] T.H. Ludwig, P.L. Schaffer, L. Arnberg, Metall. Mater. Trans. A 44 (2013) 3783–3796.
[34] J.H. Li, S. Suetsugu, Y. Tsunekawa, P. Schumacher, Metall. Mater. Trans. A 44 (2012) 669–681.

Paper III

Eutectic modification by ternary compound cluster formation in Al-Si alloys

J. Barrirero, C. Pauly, M. Engstler, J. Ghanbaja, N. Ghafoor, J. Li, P. Schumacher, M. Odén, F. Mücklich

PAPER III

SCIENTIFIC REP⚙RTS

OPEN

Eutectic modification by ternary compound cluster formation in Al-Si alloys

J. Barrirero[1,2], C. Pauly[1], M. Engstler[1], J. Ghanbaja[3], N. Ghafoor[2], J. Li[4], P. Schumacher[4], M. Odén[2] & F. Mücklich[1]

Al-alloys with Si as the main alloying element constitute the vast majority of Al castings used commercially today. The eutectic Si microstructure in these alloys can be modified from plate-like to coral-like by the addition of a small amount of a third element to improve ductility and toughness. In this investigation the effects of Eu and Yb are studied and their influence on the microstructure is compared to further understand this modification. The two elements impact the alloy differently, where Eu modifies Si into a coral-like structure while Yb does not. Atom probe tomography shows that Eu is present within the Si phase in the form of ternary compound Al_2Si_2Eu clusters, while Yb is absent in the Si phase. This indicates that the presence of ternary compound clusters within Si is a necessary condition for the formation of a coral-like structure. A crystallographic orientation relationship between Si and the Al_2Si_2Eu phase was found, where the following plane normals are parallel: $011_{Si}//0001_{Al2Si2Eu}$, $111_{Si}//6\bar{7}10_{Al2Si2Eu}$ and $011_{Si}//6\bar{7}10_{Al2Si2Eu}$. No crystallographic relationship was found between Si and Al_2Si_2Yb. The heterogeneous formation of coherent Al_2Si_2Eu clusters inside the Si-phase is suggested to trigger the modification of the microstructure.

The use of light-weight castings in the automotive sector results in higher energy efficiency and reduced fuel consumption. Al-Si alloys are frequently used for such castings because of their excellent fluidity, castability, and corrosion resistance[1]. Al-Si alloys have an irregular eutectic phase with faceted Si plates in a non-faceted aluminium matrix. The Si plates act as crack propagation paths that deteriorate the ductility and toughness of the material[2,3]. To improve these properties, the Si plate-like morphology is modified to a coral-like microstructure[4,5]. Small amounts of certain elements such as Na, Sr, or Eu are added to the alloy to completely change the Si-plates to finer, rounded coral branches. The reduced size and geometric aspect ratio of the modified eutectic enhances the toughness of the alloy by reducing the local stress concentrations such that crack initiation is suppressed and crack propagation resistance is increased[3,6,7]. The secondary dendrite arm spacing (SDAS) of the Si-phase is affected by the cooling rate during casting and by combining appropriate casting conditions with additions of modifier and grain refiner, significant improvements in tensile[8–10] and impact properties[2,6,11] are obtained.

Understanding the exact underlying mechanism for this remarkable change in structure has been an outstanding research topic ever since the discovery of the modification, almost 100 years ago[12] and the interaction between Al, Si, and the modifying agents is not yet fully elucidated. Without such knowledge it is impossible to control the homogeneity of the modification for more complex alloys such as Al-Si-Mg and Al-Si-Mg-Cu.

Several studies have considered the effect of the modifier during nucleation and growth of the eutectic phase[13–19]. One of the most distinctive characteristics of the modified Si-phase is the large amount of crystallographic defects[17,20,21]. A well accepted hypothesis by Lu and Hellawell[19] for the multiplication of defects is the so called impurity induced twinning (IIT). They proposed poisoning of step sources across the closely packed {111} planes in Si by the adsorption of atoms of the modifying agent at the solidification front. They formulated a geometric model to predict the optimal ratio between the atomic radius of the modifying agent and Si such that the adsorption of this impurity on a {111}$_{Si}$ step would cause a displacement resulting in a different stacking sequence and

[1]Functional Materials, Department of Materials Science, Saarland University, D-66123, Saarbrücken, Germany. [2]Nanostructured Materials, Department of Physics, Chemistry and Biology (IFM), Linköping University, SE-58183, Linköping, Sweden. [3]Institut Jean Lamour, UMR CNRS 7198, Université de Lorraine, F-54042, Nancy, France. [4]Institute of Casting Research, Montanuniversität Leoben, A-8700, Leoben, Austria. Correspondence and requests for materials should be addressed to J.B. (email: j.barrirero@mx.uni-saarland.de)
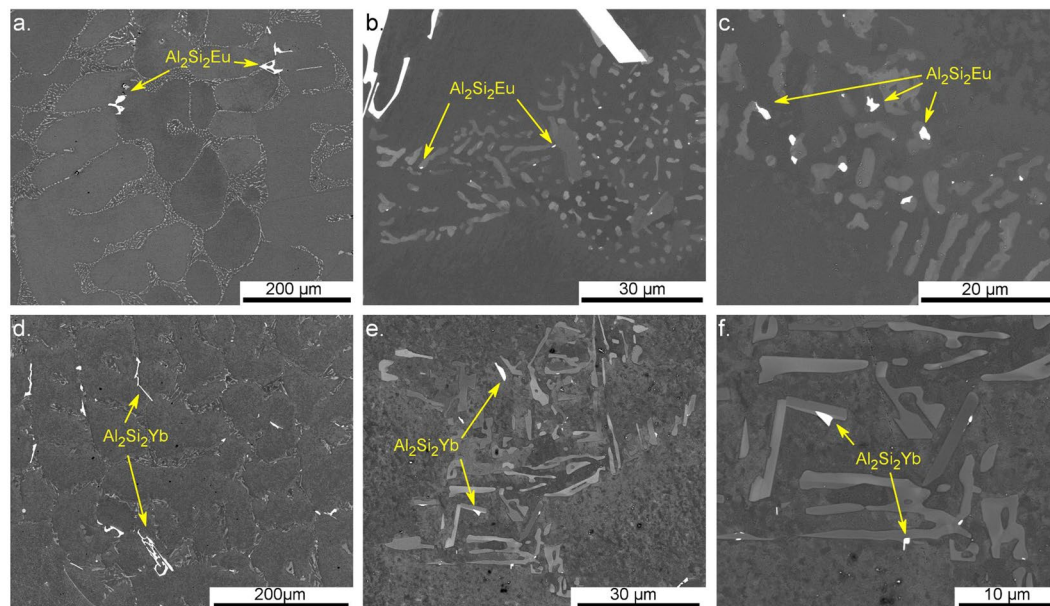
Figure 1. SEM micrographs of Al-5 wt.%Si with either Eu (**a**–**c**) or Yb (**d**–**f**) additions. (**a**) Coral-like eutectic phase and pre-eutectic coarse Al$_2$Si$_2$Eu intermetallics; (**b,c**) smaller Al$_2$Si$_2$Eu intermetallic phases formed during eutectic growth. (**d**) Refined structure resembling the plate-like eutectic phase of unmodified alloys and coarse Al$_2$Si$_2$Yb intermetallics; (**e,f**) smaller intermetallic phases forming during eutectic growth.

promoting frequent twinning. According to this model the optimal atomic radius of the modifying agent should be 1.65 times larger than the one of Si.

Based on the IIT-model, several elements other than the well-known Na and Sr have been tested as possible alloy modifiers[22–24]. Nogita *et al.*[24], studied the microstructure of the eutectic phase after addition of almost all rare earth metals and found that, although all of them caused suppressed eutectic growth temperature, the only element able to form the coral-like structure was europium (Eu). In fact, ytterbium (Yb), which is the element with the best fit to the IIT-model ($r_{Yb}/r_{Si} = 1.66$) shows, similar to many other rare earth metals, only a refinement of the Si plate-like structure. This shows that the atomic radius alone is not capable of predicting the morphological transition of the eutectic structure and the reason why they behave differently remains an open question.

Recent studies using atom probe tomography (APT) with the possibility of obtaining spatially resolved chemical information from crystallographic defects in the Si-phase have shown co-segregation of Al atoms and the modifier agent in alloys modified with Sr and Na[25–28]. The defects showed chemical compositions consistent with Al$_2$Si$_2$Sr and AlSiNa[26]. Based on this, the formation of the coral-like Si structure was proposed to be related to the formation of clusters of ternary compounds at the solidification front rather than the adsorption of single atoms.

The present study investigates and compares the effect of Eu and Yb additions on the microstructure of an Al-Si alloy at different length scales. The aim is to confirm whether the formation of ternary compounds plays a role during the growth of Si corals by Eu addition and highlight the difference of the Si crystal growth with the addition of elements that only refine the Si plate structure such as Yb. Li *et al.*[29] have shown the presence of Eu at crystallographic defects in the Si phase by high resolution scanning transmission electron microscopy (STEM). The difficulty faced with this technique is that Al atoms in the Si lattice cannot be identified due to the small difference in atomic weight between Al and Si. They also used electron energy loss spectroscopy (EELS) to determine the distribution of Eu atoms within Si but were not able to chemically resolve Al atoms present in the Si crystal. To overcome this problem we used APT, which offers the possibility to study and compare the three-dimensional distribution of Al, Eu and Yb in the Si phase. Transmission electron microscopy (TEM), electron back-scattered diffraction (EBSD), transmission Kikuchi diffraction (TKD) and back-scattered electron (BSE) imaging are also used as complementary techniques to compare the eutectic microstructures at different length scales and to study the orientation relationship between the phases.

Results

Figure 1 shows two distinct microstructures when adding 0.05 wt.% Eu (Fig. 1(a–c)) or 0.61 wt.% Yb (Fig. 1(d–f)) to an Al-5 wt.% Si alloy. Eu addition results in a homogeneously modified coral-like Si structure, while Yb addition shows less drastic morphological change with a coarser microstructure similar to the plate-like structure of the unmodified alloys. Several studies report that Yb acts just as a refiner of the unmodified plate-like structure[22,24,30,31]. Our results show a mixed structure with straight elongated Si-branches similar to plates together with more rounded ones.

The regions giving bright contrast by backscattered electrons on the polished surfaces are Al$_2$Si$_2$Eu and Al$_2$Si$_2$Yb intermetallic phases. The presence of the intermetallic compounds was confirmed by standardless quantitative EDS and their EBSD Kikuchi patterns were successfully indexed to match the crystallographic structure
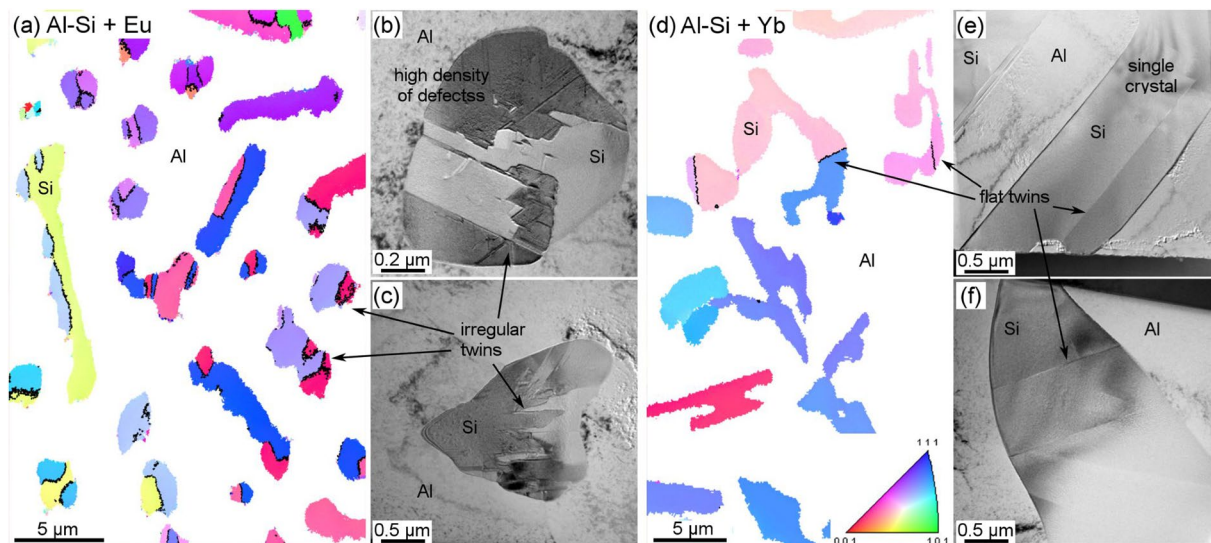
Figure 2. Inverse pole figures of EBSD maps in Al-5 wt.%Si alloys modified by: (**a**) Eu (step size 30 nm) and (**d**) Yb (step size 90 nm). Black lines show twin boundaries in Si. White areas correspond to the Al matrix which was filtered out for clarity. TEM images show high density of crystallographic defects in the Si structure of the Eu modified alloy (**b,c**); and only flat twin planes across the Si crystal in the alloy with Yb addition (**e,f**).

of Al_2Si_2Eu and Al_2Si_2Yb, respectively[32–34]. Figure 1 shows how these ternary compound particles are present with two different sizes. In Fig. 1(a,d), coarse (tens of micrometres) pre-eutectic intermetallic particles are present, while Fig. 1(b,c,e,f) show particles formed during eutectic solidification with sizes ranging from sub-micrometre to a few micrometres.

Figure 2 shows the difference between the eutectic Si structures of the two alloys investigated. Black lines in the EBSD images (Fig. 2(a,d)) highlight irregular Σ3 twin boundaries for Eu addition, which is similar to that in Sr modified alloys[25]. Yb addition shows a lower density of twins in coarser Si branches. The EBSD map in Fig. 2(d) confirms that twin boundaries are straight, which is similar to what have been seen in the unmodified alloy[25].

The TEM micrographs in Fig. 2 show the crystallographic structure of Si. All micrographs were recorded along the Si<011> zone axis in order to have edge-on alignment of defects on {111} planes. Figure 2(b,c) shows a high density of nanotwins or stacking faults (SF) and v-shaped defects in the alloy with Eu addition, which is consistent with what has been reported for Sr and Na modifications[25,26]. Moreover, the boundaries between the areas with different contrast in the Si phase show irregular shaped twin boundaries. The alloy with Yb addition presents only straight twins through the crystal (Fig. 2(e,f)).

APT reconstructions in Fig. 3 display differences in the solutes' distribution in the two alloys. The alloy with Eu addition contains clusters of Eu and Al in the Si structure. Similar to Sr and Na modified alloys[25,26], solute clusters with three different morphologies are distinguished: rod-like, planar, and rounded (Fig. 3(a)). No clusters containing only Eu or only Al could be found in the Si phase and instead Al and Eu atoms always appear together. Figure 3(b) shows an inset of one such planar cluster of solute atoms with a quantitative one-dimensional concentration profile through the cluster showing the spatial distribution of the atoms. In contrast, no rod-like or planar clusters were found in the alloy with Yb addition (Fig. 3(c)). In fact, no traces of Yb could be detected in the Si phase, i.e. Yb was not even found as solid solution in the Si-crystals. The rounded clusters found in this alloy contain Al and Si, and most of them have a core-shell structure, similar to the unmodified alloy[25].

To determine the composition of the ternary compound clusters formed in the Eu modified alloy, each single rod-like and planar cluster present in three different APT specimens were isolated in tightly fitted regions of interest (ROIs) and the number of Al and Eu atoms was counted after optimization of the mass spectrum and background subtraction, following the procedure outlined in[26]. The details of a rod-like cluster are shown in Fig. 4(d), and the measured Al:Eu ratios for 35 rod-like and 4 planar clusters are plotted in Fig. 4(e). The average Al:Eu ratio for all these clusters is 2.25 ± 0.42. When considering 2–5 nanometre thick clusters, the atomic positions in APT can be influenced by ion trajectory overlaps due to local magnification effects[35]. This artefact may lead to a convolution of the matrix, in this case Si, with the cluster resulting in an overestimation of the matrix element[35–39]. Given this uncertainty, it is not possible to discriminate between the "matrix Si" and Si in the cluster. Because of this reason, only Al and Eu atoms are considered and reporting relative solute ratios Al:Eu is more adequate than absolute concentrations in the clusters.

Figure 4(a,b,c) shows three perspectives of one APT specimen with a high density of rod-like clusters. All rounded clusters and dissolved solutes in the specimen were masked out to reveal the structure of the rod-like defects. In Fig. 4(a), the specimen is oriented to display the v-shape character of the defects in a similar way to how they are seen by TEM. Figure 4(b,c) are obtained by rotating the specimen. These images reveal the three-dimensional structure of the crystallographic defects in the Si lattice and show how misleading the two-dimensional projection obtained by TEM can be. In several occasions, what we see and denote as v-shaped
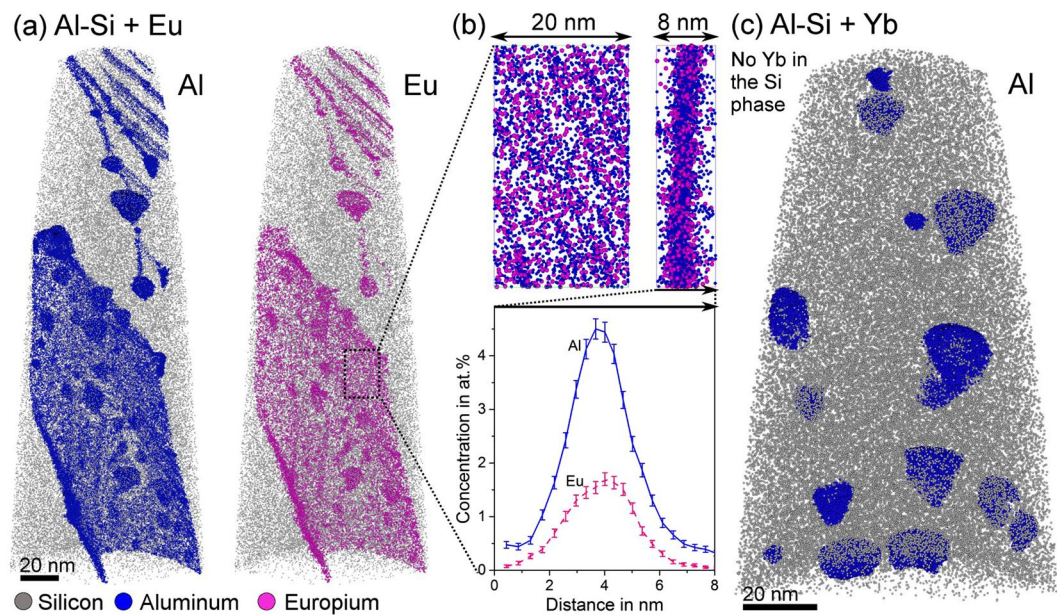
Figure 3. APT comparison of the solute distribution in Si. (**a**) Alloy modified by Eu presenting rod-like, planar and round clusters, all of them containing Al and Eu; (**b**) inset of the planar atomic clustering with a one-dimensional concentration profile across the segregation plane. (**c**) Alloy with Yb addition presenting only Al rounded clusters in Si. No Yb peaks were detected in the mass spectrum of the Si phase.
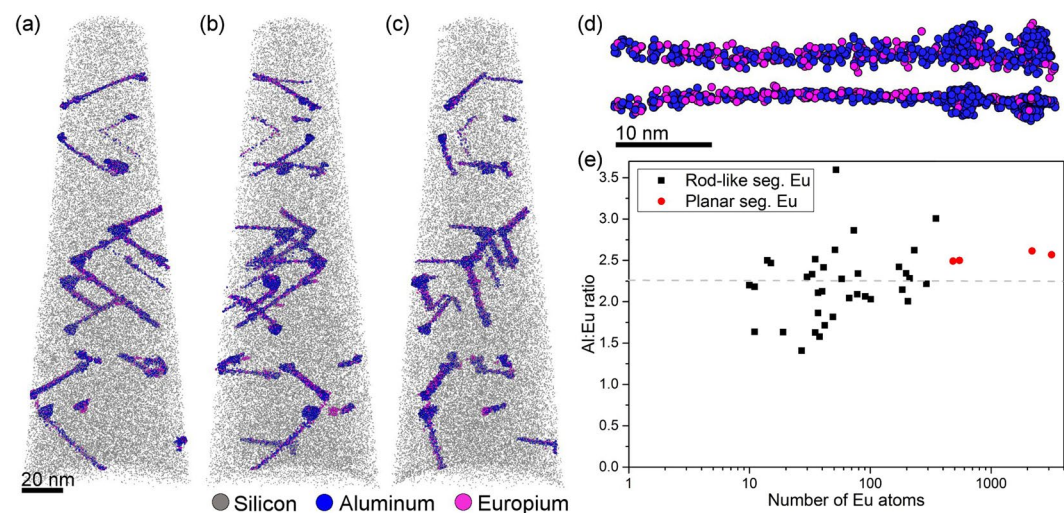
Figure 4. APT analysis of eutectic Si. (**a**), (**b**), and (**c**) are views of the same specimen at different rotation angles showing the scaffold of rod-like segregations in the Si lattice. (**d**) Shows one isolated rod-like segregation viewed from the top and the side. (**e**) Al:Eu ratios as a function of the number of Eu-atoms in each of the 39 clusters (35 rod-like and 4 planar).

defects are actually three rod-like clusters originating from one point or two different clusters positioned at different planes in space. Instead of v-shaped defects, APT shows a complex three-dimensional structure of the crystallographic defects in Si. For clarity, videos are included as supplementary material to get complete 3D-views (Supplementary Video S1 and S2).

APT specimens of eutectic Al were analysed and no traces of Eu and Yb were detected with a detection limit of 50 at. ppm showing a negligible solubility of these elements in Al.

The crystallographic orientations between Si and the micrometre sized eutectic Al_2Si_2Eu or Al_2Si_2Yb phases were analysed by EBSD and TKD. For this analysis, 17 different Si/Al_2Si_2Eu boundaries and 10 Si/Al_2Si_2Yb boundaries were scanned. Pole figures of the low index plane-normals 001, 011 and 111 in Si were constructed and compared with the pole figures of the low index plane-normals 0001, $11\bar{2}0$, $01\bar{2}2$ and $11\bar{2}1$ in Al_2Si_2X (X = Eu,Yb). This comparison allows looking for crystallographic orientation relationships between the ternary phases and the Si crystal. The spatial coincidences of poles from the two phases show parallel plane-normals, or

what is the same, parallel planes of the two phases. Alloys modified by Eu showed coincidence of 011_{Si} and $0001_{Al2Si2Eu}$ poles in 15 out of the 17 cases analysed, while the alloy with Yb addition only showed this orientation relationship in 2 out of 10 cases.

TKD/EBSD datasets were then rotated to have the $0001_{Al2Si2Eu}$ plane-normal at the centre of the pole figure, i.e. at the normal direction (ND), to find a further orientation relationship perpendicular to the $(0001)_{Al2Si2Eu}$ lattice plane. Two mutually perpendicular orientation relationships between the crystals define a fixed three-dimensional orientation relationship. Figure 5 shows an example of three Si crystals next to an Al_2Si_2Eu phase which fulfil the $011_{Si}//0001_{Al2Si2Eu}$ orientation relationship (Fig. 5(b,c,d,e)). In this condition, pole coincidences depicting parallel plane-normals between the low index {011}, {111} Si plane-families and the {$6\bar{7}10$} Al_2Si_2Eu plane-family were determined (Fig. 5(c,d,e)). The simultaneous orientation relationships $011_{Si}//0001_{Al2Si2Eu}$ and $111_{Si}//6\bar{7}10_{Al2Si2Eu}$ or $011_{Si}//6\bar{7}10_{Al2Si2Eu}$ describe a fixed growth orientation between Si and Al_2Si_2Eu which is not present in the case of Si and Al_2Si_2Yb.

The three Si crystals shown in Fig. 5 are mutually related by coherent twin boundaries $\sum 3$ and the special grain boundary $\sum 9$ (marked in black and green in Fig. 5(b), respectively). We note that all three Si grain-orientations have parallel low index planes to some plane in the {$6\bar{7}10$} family of the same Al_2Si_2Eu grain. $(6\bar{7}10)_{Al2Si2Eu}$ plane deviates 7.6° from the low index plane $(1\bar{1}00)_{Al2Si2Eu}$.

The misfits of the interplanar spacings between Si and Al_2Si_2Eu were calculated to prove the feasibility of a coherent growth of the phases in the orientations found in the pole figures. Table 1 shows misfits smaller than 6% between multiples of the d-spacings. Several other pole coincidences were found involving the Si low index planes and Al_2Si_2Eu {$12\bar{3}0$}, {$1\bar{1}00$} and {$1\bar{1}03$} plane-families. Not all coincidences are shown in Fig. 5 for clarity. The relationship between the two mutually perpendicular sets of planes in both lattices is enough to describe the fixed orientation relationship between the crystals.

Discussion

The addition of eutectic modifiers in Al-Si castings affects solidification in several aspects. Eutectic nucleation sites are poisoned causing a depression of the nucleation and growth temperatures, and a strong decrease in the density of eutectic grains[15,40–46]. Fewer and larger grains have a smaller total solid/liquid surface area. To account for a given cooling rate the modified eutectic phase solidifies with a higher interface velocity and, therefore, the microstructure inside the eutectic grains is refined[13,14]. However, the plate-to-coral morphology transition of Si was shown to be independent of alterations in nucleation mode and frequency[47]. The morphology transformation is rather a consequence of an additional effect of the modifier during Si growth. A significant increase of crystallographic defects in Si has been explained by the poisoning of re-entrant twins' edges[48–52] and by the impurity induced twinning (IIT) model[19]. The latter points out several atomic species as potential eutectic modifiers of Al-Si alloys[19]. This theory is based on single atoms modifying the structure by poisoning preferred growth orientations. The poisoning atom should optimally be 1.65 times larger than the Si-atom, which would interrupt the growth such that one monolayer in the regular close packed plane stacking sequence is skipped and instead a twin is formed.

Today we know that, although the modifier agent influences the formation of crystallographic defects, the atomic radius itself cannot be taken as an indication of potency of modification. This is exemplified as just some of the elements proposed in IIT form Si-corals. For example, Yb has the ideal ratio $r_{Si}/r_{Yb} = 1.65$ but it only refines the plate-like Si structure[22,30,31], while Eu having a ratio of 1.72 is as potent as Na and Sr to form Si-corals[30,53]. Further, in this paper we show that an efficient modifier like Eu always appears together with Al in the defects of the Si lattice (Figs 3 and 4) and never as single atoms. This is in accordance with other efficient modifiers such as Sr and Na, which showed compositions inside the defects consistent with Al_2Si_2Sr and $AlSiNa$[25,26]. In the present work, the average Al:Eu ratio of nearly 2 (Fig. 4(e)) suggests that the ternary compound Al_2Si_2Eu is formed at the defects and in this case the geometric IIT model is no longer valid. The presence of clusters of Al_2Si_2Eu at the defects in the Si lattice stresses the importance of atomic interaction between Si, the third element (in this case Eu), and Al during solidification.

The formation of the eutectic ternary compounds Al_2Si_2Eu and Al_2Si_2Yb (Figs 1(b,c,e,f); 5(a)) indicates that there is sufficient driving force for nucleation and growth of these phases during solidification. To the best of our knowledge, the liquidus surfaces for Al-Si-Eu and Al-Si-Yb ternary systems are not known. However, the liquidus surfaces for alloys with other modifiers such as Al-Si-Sr[54], Al-Si-Na[55] and Al-Si-Ca[56] show a ternary eutectic point close to the temperature and composition of the binary Al-Si and at low amounts of Sr (0.03 at.%), Na (0.01 at.%), or Ca (0.7 at.%). Based on the back-scattered-electron images in Fig. 1 and other studies[29–31,53], it is reasonable to assume that Al-Si-Eu and Al-Si-Yb alloys also present such eutectic point. At the ternary eutectic point, three phases are expected: Al, Si, and a ternary compound inherent to each system.

Examining the ternary eutectic solidification path and keeping in mind that the amount of the third element (Eu, Yb) in the alloy is low, there is a simultaneous solidification of the two major phases (Al and Si) during the entire eutectic reaction. The third phase will only form when the third element's local concentration is high enough. APT results show that almost no Eu or Yb is dissolved in the eutectic Al or Si. Instead, these elements are expected to be accumulated ahead of the solidification front resulting in a concentration gradient of Eu or Yb perpendicular to the growth front. Such accumulation of the modifying element has been proposed in several studies[50,57–59] and it gives the necessary conditions of constitutional undercooling and supersaturation for ternary compounds to form. The Gibbs free energy for nucleation of embryos is a function of the undercooling and the local supersaturation of the elements. At the eutectic temperature, the diffusion boundary layer at the solid/liquid interface has an increased amount of the third element causing the melt to locally be more undercooled[22,31,53]. Under these conditions, sub-critical clusters (embryos) of the ternary phase will form and re-melt in the liquid until there is enough supersaturation for a cluster to reach a critical size and grow to a micrometre-sized grain as
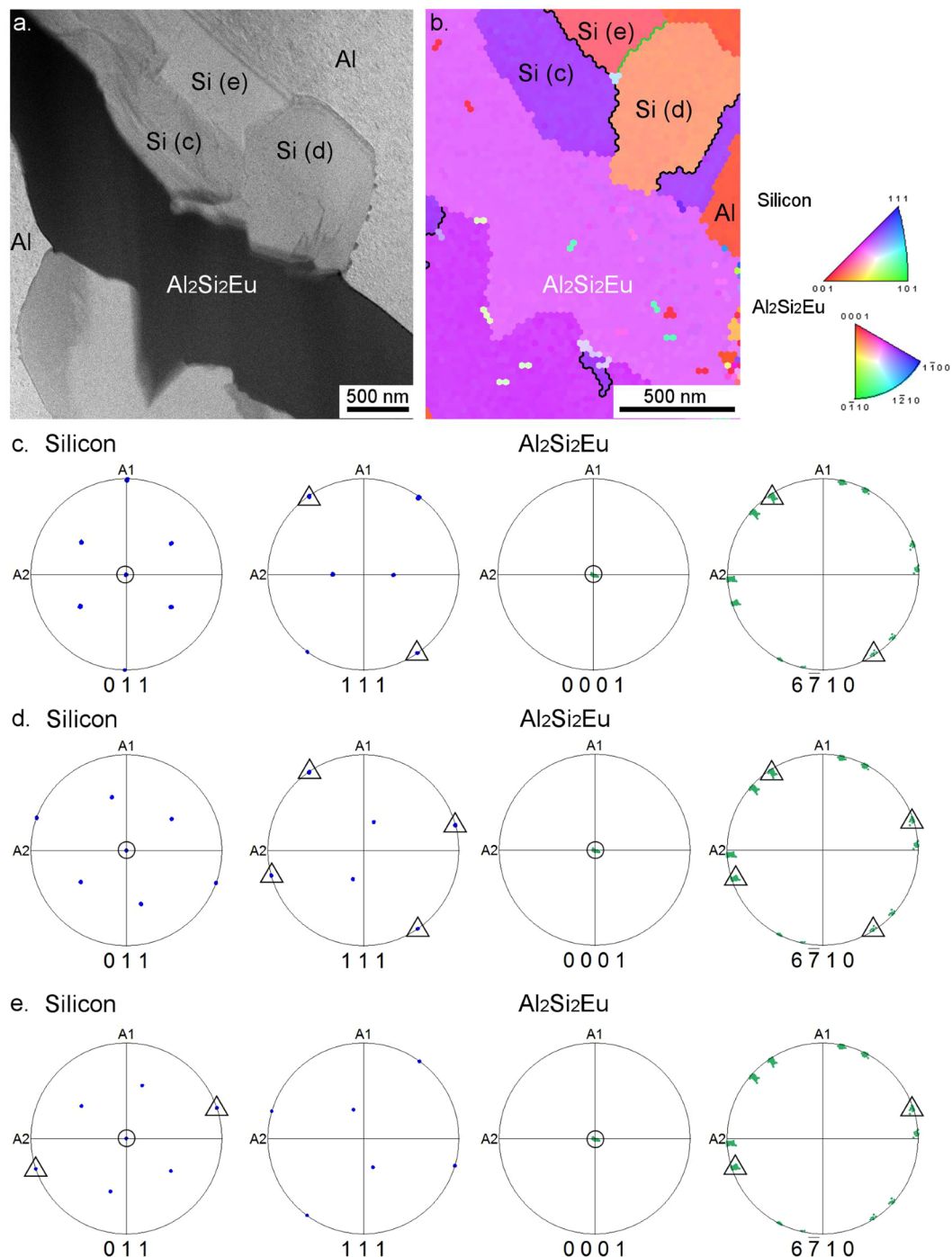
Figure 5. Crystallographic orientation relationship between Si and eutectic Al_2Si_2Eu: (**a**) bright field TEM image showing eutectic Al_2Si_2Eu surrounded by Si; (**b**) inverse pole figure of a TKD map showing mutually twinned Si crystal orientations. Black boundaries between Si grains show $\sum3$ twin (60° @<111>), and the green boundary highlights a $\sum9$ twin (38.9° @<110>). (**c**–**e**) Pole figures (PF) corresponding to the three Si crystals marked in (**b**). All PF were re-oriented to the $(0001)_{Al2Si2Eu}$ in the normal direction (ND) for convenience. Circles depict coincident poles (parallel plane-normals) between 011_{Si} and $0001_{Al2Si2Eu}$. Triangles depict coincident poles in 011_{Si}, 111_{Si} and $6\bar710_{Al2Si2Eu}$.

seen in Fig. 1(b,c,e,f). Figures 1(c,f) and 5(a) highlight how the eutectic ternary phase is formed on the Si phase and do not grow independently or as a part of eutectic Al. This observation emphasizes that these phases are most probably heterogeneously nucleated at the Si interface. This is reasonable because the Al_2Si_2X phases normally have an ordered hexagonal structure (space group P-3m1 (164)) and grow in a faceted manner such as Si. This tendency towards faceted growth can be seen in the polyhedral morphology of the pre-eutectic coarse particles (Fig. 1(a,d)).

d-Spacings and multiples (nm)		
	d-$\{6\overline{7}10\}$Al$_2$Si$_2$Eu $= 0.0552$	Misfit δ (%)
d-$\{111\}$Si $= 0.314$	(6×) d-$\{6\overline{7}10\} = 0.331$	−5.19
d-$\{011\}$Si $= 0.384$	(7×) d-$\{6\overline{7}10\} = 0.386$	0.62
	d-$\{011\}$Si $= 0.384$	
d-$\{0001\}$Al$_2$Si$_2$Eu $= 0.726$	(2×) d-$\{011\}$Si $= 0.768$	−5.79

Table 1. Misfits of Al$_2$Si$_2$Eu related to Si for the parallel planes found in EBSD/TKD.

	Space group	Lattice parameters		d-spacing (nm)	Misfit δ %	Si structure
		a,b (nm)	c (nm)			
Si	Fd-3m (227)	0.543	0.543	d(110) = 0.384	—	—
Al$_2$Si$_2$Sr[63]	P-3m1 (164)	0.418	0.743	d(0002) = 0.372	−3.36	Coral
AlSiNa[64]	P4/nmmO2 (129)	0.414	0.738	d(002) = 0.369	−4.07	Coral
Al$_2$Si$_2$Eu[33]	**P-3m1 (164)**	**0.418**	**0.726**	**d(0002) = 0.363**	**−5.79**	**Coral**
Al$_2$Si$_2$Ca[63]	P-3m1 (164)	0.413	0.715	d(0002) = 0.358	−7.41	Mixed
Al$_2$Si$_2$Ba[65]	I4/mmm (139)	0.423	0.698	d(0002) = 0.349	−10.03	Mixed
Al$_2$Si$_2$Yb[33]	**P-3m1 (164)**	**0.414**	**0.695**	**d(0002) = 0.348**	**−10.50**	**Refined plates**
Al$_2$Si$_2$Y[66]	P-3m1 (164)	0.418	0.656	d(0002) = 0.328	−17.07	Refined plates

Table 2. Crystal structure and misfit of ternary compounds related to Si.

The microstructural comparison between the two alloys studied here shows that they have similar solidification paths. Both alloys have a ternary eutectic point with formation of Al$_2$Si$_2$X (Eu,Yb) (Fig. 1). The difference between the two alloys is Eu's ability to form early stage Al$_2$Si$_2$Eu clusters on the facets of the Si crystal, while such clusters are absent in the alloy containing Yb (Figs 3 and 4). The formation of clusters on the Si-facets during solidification affects the Si-growth by local obstruction, causing steps on the facets and increasing growth direction diversity. This growth restriction model is different to the IIT model, as it incorporates the much larger ternary clusters as growth obstacle on the Si surfaces explaining more readily the high density of crystallographic defects in Si and the modification from Si plates to corals.

We postulate that the difference between the effect of Eu and Yb stems from the difference in the energy needed for sub-critical clusters of Al$_2$Si$_2$Eu and Al$_2$Si$_2$Yb to form on solidified Si surfaces. In other words, Al$_2$Si$_2$Eu clusters need less energy to form on Si in comparison to Al$_2$Si$_2$Yb clusters. The strong accumulation of the modifier together with Al and Si on the first tens of nanometres ahead of the solidification front, gives the necessary condition of constitutional undercooling and supersaturation for the ternary clusters to form. Eu and Yb atoms will be eventually trapped at the Si surface as part of ternary clusters formed heterogeneously at the interface. However, the cluster formation is only energetically favourable for a good lattice match onto the Si surface. The presence of Al$_2$Si$_2$Eu clusters showed by APT suggests a good lattice match with Si, in contrast to Al$_2$Si$_2$Yb. Although Yb atoms may sit shortly onto the Si interface, the lattice mismatch of the ternary cluster cost too much energy and dissolves or cannot form.

Direct determination of the formation energy of heterogeneous clusters of Al$_2$Si$_2$Eu and Al$_2$Si$_2$Yb on different facets of the Si crystal during eutectic solidification is challenging, both experimentally and by simulations. Instead, we have adopted an indirect approach to test our arguments by studying the crystallographic orientation relationships between Si and each of the two ternary phases. The expected crystallographic orientation relationship between fcc and hcp is the alignment of the close packed planes 111$_{fcc}$//0001$_{hcp}$. However, Fig. 5 shows EBSD/TKD pole figures of Al$_2$Si$_2$Eu in contact with Si, showing unexpected parallel plane-normals: 111$_{Si}$//$6\overline{7}10_{Al2Si2Eu}$, 011$_{Si}$//$6\overline{7}10_{Al2Si2Eu}$ and 011$_{Si}$//0001$_{Al2Si2Eu}$ with misfits of the d-spacings smaller than 6% (Table 1). This result indicates heterogeneous formation of Al$_2$Si$_2$Eu with an epitaxial relationship to the Si surface, while such relationship is not present in the case of Al$_2$Si$_2$Yb. Both ternary compounds, Al$_2$Si$_2$Eu and Al$_2$Si$_2$Yb, have the same hexagonal P-3m1 crystal structure with a = b lattice parameters that differ less than 1%, while c differs more than 4% (Table 2). Considering the orientation relationship reported in Fig. 5, the different potency of heterogeneous nucleation for these two phases on Si is evaluated on the basis of the misfit between the Si-surface and the nucleating phases. The interplanar spacings d(0002)$_{Al2Si2Eu}$ = 0.363 nm and d(0002)$_{Al2Si2Yb}$ = 0.348 nm can be compared to d(110)$_{Si}$ = 0.384 nm. This comparison shows misfits of 5.79% for Al$_2$Si$_2$Eu and 10.50% for Al$_2$Si$_2$Yb towards Si. The higher mismatch of the Yb phase adds strain energy to its nucleation, which makes Al$_2$Si$_2$Yb clusters less stable than Al$_2$Si$_2$Eu clusters on Si facets.

This calculation can be applied to similar ternary phases present in the Al-Si alloys with addition of other elements. Table 2 shows how the three systems forming Si corals (addition of Na, Sr or Eu), have ternary phases with a misfit smaller than 6%. Ca and Ba, elements which can induce the formation of fibrous Si similar to the coral structure when higher amounts of these elements are added[22,23], have a higher misfit, while Yb and Y ternary phases show the highest misfits and also the lowest potency as modifiers[22,31].

The reason why clusters with a rod-like morphology are the most frequently found is likely an effect of different misfits in different orientations on the Si-surface. Such dispersion in misfit favors growth of the cluster in specific orientations. These results show a consistent difference between the elements tested as possible modifiers in literature and the degree of Si microstructural modification into corals. Li et al.[29] showed by high resolution STEM imaging how columns of Eu atoms match every second Si pair of dumbbells on a 111_{Si} plane. The approximated distance between Eu columns that can be measured from their image is ~0.7 nm, i.e. the c distance of Al_2Si_2Eu. Al and Si atoms between Eu columns cannot be differentiated in HAADF-STEM mode because of the projection of the entire thickness of the TEM sample on the image (about 20 nm with more than 20 Al and Si atomic layers) and because of the small Z difference between Al and Si. However, the distance between Eu columns can be explained by the early stage formation of atomic layers of the Al_2Si_2Eu ternary compound on a 111_{Si} plane as postulated in this work.

Conclusion

- This study shows clusters of Eu co-segregated with Al in eutectic Si matching the stoichiometry of Al_2Si_2Eu ternary compound. On the contrary, no Yb in the Si crystal was found. This result suggests that the existence of nanometre sized clusters of ternary compounds is a necessary condition for the formation of a coral-like structure.
- The formation of Al_2Si_2Eu and Al_2Si_2Yb during eutectic solidification proves the presence of a ternary eutectic reaction for these alloys.
- The parallel lattice plane-normals $011_{Si}//0001_{Al2Si2X}$, $011_{Si}//6\overline{7}10_{Al2Si2X}$ and $111_{Si}//6\overline{7}10_{Al2Si2X}$ found only for the sample with Eu addition and not for Yb proves a favourable heterogeneous formation of Al_2Si_2Eu on Si. This explains the formation and adsorption of clusters of this phase in the alloy with Eu addition and not in the alloy with Yb addition.
- The misfit between 011_{Si} and $0002_{Al2Si2X}$ interplanar spacings shows a consistent trend with the potency of modification for several elements such as Sr, Na, Eu, Ca, Ba, Yb and Y.

In the present work, the growth restriction of eutectic Si by the formation of ternary clusters is proposed. The formation of such clusters on Si-facets creates growth steps increasing growth direction diversity. The incorporation of cluster onto the Si surface explains the high density of crystallographic defects in Si and the modification from Si plates to corals.

Methods

Ingots of about 1 kg Al-5Si-0.05Eu and Al-5Si-0.61Yb alloys (wt. %) were produced by electric resistance melting of the charge material in a boron-nitride coated clay-graphite crucible at 750 °C and then casted using gravity die casting. Prior to casting, no degassing treatment was performed. High purity Al (5N) and Si (5N) were used as starting materials. Master alloys, Al-2Eu and Al-5Yb, were used to add Eu and Yb when the starting materials (Al and Si) were fully molten. The modifier amounts were chosen to yield optimal modification based on previous studies[22,24,29,31,53].

Microscopy samples were prepared from the casts by metal machining, followed by grinding and polishing to a mirror-like finish, where the last step was vibrational polishing in a colloidal silica suspension (Struers OP-S - 0.04 μm) for 2 hours. TEM and APT samples were prepared in a dual-beam focused ion beam/scanning electron microscopy workstation (FIB/SEM) (Helios NanoLab 600™, FEI Company, USA). APT specimen of the eutectic Si phase were prepared by the phase selective sample preparation method described in[60]. After lift out and thinning of the samples, a low energy milling at 2 kV was performed to minimize gallium induced damage[61].

An EDAX Hikari detector within the FIB/SEM workstation was used to record EBSD and TKD data using an electron beam of 20 kV/22 nA and 30 kV/5.5 nA, respectively. Al_2Si_2Eu and Al_2Si_2Yb crystal structures from literature[32–34] were added to OIM Data Collection 7 database by means of the built-in structure creation wizard. Post-processing of the data was performed using the OIM Analysis software (EDAX). Results are shown in the form of pole figures and inverse pole figure maps. In case of the TKD measurement shown in Fig. 5, a pseudosymmetry clean-up followed by a grain dilation was performed for visual representation. Pole figures were calculated from uncleaned data. Conventional EBSD scans in reflection mode yielded better pattern quality. Data points for pole figure calculation were extracted from uncleaned raw data using the grain highlight function of OIM Data Analysis software. This allows a point-and-click selection of data points belonging to a continuous grain based on a misorientation threshold (here 5°). Data points from the intermetallic phase (Al_2Si_2Eu or Al_2Si_2Yb) and the neighbouring Si phase were highlighted and used for the calculation of pole figures. No clean-up was used.

TEM and STEM imaging was performed in a Tecnai G2 TF 20 UT FEG (FEI) in micro and nanoprobe modes and a JEM - ARM 200 F Cold FEG TEM/STEM operating at 200 kV and equipped with a spherical aberration (Cs) probe and image correctors (point resolution 0.12 nm in TEM mode and 0.078 nm in STEM mode).

APT was carried out in a LEAP 3000X HR (CAMECA) in laser mode to measure eutectic Si and voltage mode to measure eutectic Al. All measurements were performed at repetition rate of 200 kHz, pressure lower than 1.33×10^{-8} Pa, and evaporation rate of 5 atoms per 1000 pulses. Laser-pulsed APT was accomplished using a laser with a wavelength of 532 nm, pulse length of 10 ps, and a pulse energy of 0.3–0.4 nJ while keeping a specimen temperature of about 40 K. Voltage measurements were performed at 20% pulse fraction and a specimen temperature between 50 and 60 K. Datasets were reconstructed and analysed with IVAS™3.6.8 software (CAMECA). Al and Eu contents in Si were measured after background subtraction performed with IVAS software. The cleaning of the datasets for visualization purposes was performed with the open source software Blender 2.76 and the open access AtomBlend plugin developed by Peter Felfer and Vavara Efremova[62].

Data Availability

The datasets analysed during the current study are available from the corresponding author on reasonable request.

References

1. Kaufman, J. G. & Rooy, E. L. *Aluminum Alloy Castings: Properties, Processes, and Applications* (*ASM International*, 2004).
2. Samuel, A. M., Elgallad, E. M., Doty, H. W., Valtierra, S. & Samuel, F. H. Effect of metallurgical parameters on the microstructure, hardness impact properties, and fractography of Al-(6.5–11.5) wt% Si based alloys. *Mater. Des.* **107**, 426–439 (2016).
3. Joseph, S. & Kumar, S. A systematic investigation of fracture mechanisms in Al-Si based eutectic alloy-Effect of Si modification. *Mater. Sci. Eng. A* **588**, 111–124 (2013).
4. Gruzleski, J. E. & Closset, B. *The treatment of liquid Aluminum-Silicon alloys* (American Foundrymens Society, 1990).
5. Samuel, A. M., Garza-Elizondo, G. H., Doty, H. W. & Samuel, F. H. Role of modification and melt thermal treatment processes on the microstructure and tensile properties of Al-Si alloys. *Mater. Des.* **80**, 99–108 (2015).
6. Mohamed, A. M. A., Samuel, F. H., Samuel, A. M. & Doty, H. W. Influence of additives on the impact toughness of Al-10.8% Si near-eutectic cast alloys. *Mater. Des.* **30**, 4218–4229 (2009).
7. Caceres, C. H. & Griffiths, J. R. Damage by the cracking of silicon particles in an Al-7Si-0.4Mg casting alloy. *Acta Mater.* **44**, 25–33 (1996).
8. Riestra, M., Ghassemali, E., Bogdanoff, T. & Seifeddine, S. Interactive effects of grain refinement, eutectic modification and solidification rate on tensile properties of Al-10Si alloy. *Mater. Sci. Eng. A* **703**, 270–279 (2017).
9. Jigajinni, S. M., Venkateswarlu, K. & Kori, S. A. Effect of a grain refiner cum modifier on mechanical properties of Al-7Si and Al-11Si alloys. *Met. Mater. Int.* **19**, 171–181 (2013).
10. Tao, S., Pan, Y., Lu, T., Chen, Y. & Wu, J. Microstructures and mechanical properties of La added Al–Si casting alloys and mechanism of grain refinement. *Int. J. Cast Met. Res.* **28**, 375–381 (2015).
11. Samuel, A. M., Doty, H. W., Valtierra, S. & Samuel, F. H. Effect of grain refining and Sr-modification interactions on the impact toughness of Al-Si-Mg cast alloys. *Mater. Des.* **56**, 264–273 (2014).
12. Pacz, A. Alloy. U.S. Patent No. 1,387,900 (1921).
13. McDonald, S. D., Dahle, A. K., Taylor, J. A. & StJohn, D. H. Eutectic grains in unmodified and strontium-modified hypoeutectic aluminum-silicon alloys. *Metall. Mater. Trans. A* **35**, 1829–1837 (2004).
14. Dahle, A. K., Nogita, K., McDonald, S. D., Dinnis, C. & Lu, L. Eutectic modification and microstructure development in Al–Si Alloys. *Mater. Sci. Eng. A* **413–414**, 243–248 (2005).
15. Cho, Y. H., Lee, H.-C., Oh, K. H. & Dahle, A. K. Effect of Strontium and Phosphorus on Eutectic Al-Si Nucleation and Formation of β-Al5FeSi in Hypoeutectic Al-Si Foundry Alloys. *Metall. Mater. Trans. A* **39**, 2435–2448 (2008).
16. Flood, S. C. & Hunt, J. D. Modification of Al-Si eutectic alloys with Na. *Met. Sci.* **15**, 287–294 (1981).
17. Kobayashi, K. F. & Hogan, L. M. The crystal growth of silicon in Al-Si alloys. *J. Mater. Sci.* **20**, 1961–1975 (1985).
18. Shamsuzzoha, M. & Hogan, L. M. Twinning in fibrous eutectic silicon in modified Al-Si Alloys. *J. Cryst. Growth* **72**, 735–737 (1985).
19. Lu, S. & Hellawell, A. The mechanism of silicon modification in aluminum-silicon alloys: Impurity induced twinning. *Metall. Trans. A* **18**, 1721–1733 (1987).
20. Shamsuzzoha, M. & Hogan, L. M. The crystal morphology of fibrous silicon in strontium-modified Al-Si eutectic. *Philos. Mag. A* **54**, 459–477 (1986).
21. Shamsuzzoha, M. & Hogan, L. M. The role of non-cozonal twinning in the growth of fibrous silicon in strontium-modified Al–Si eutectic. *J. Mater. Sci.* **24**, 2849–2859 (1989).
22. Knuutinen, A., Nogita, K., Mcdonald, S. D. & Dahle, A. K. Modification of Al–Si alloys with Ba, Ca, Y and Yb. *J. Light Met.* **1**, 229–240 (2002).
23. Ludwig, T. H., Schaffer, P. L. & Arnberg, L. Influence of Some Trace Elements on Solidification Path and Microstructure of Al-Si Foundry Alloys. *Metall. Mater. Trans. A* **44**, 3783–3796 (2013).
24. Nogita, K., McDonald, S. D. & Dahle, A. K. Eutectic Modification of Al-Si Alloys with Rare Earth Metals. *Mater. Trans.* **45**, 323–326 (2004).
25. Barrirero, J. *et al*. Comparison of segregations formed in unmodified and Sr-modified Al-Si alloys studied by atom probe tomography and transmission electron microscopy. *J. Alloys Compd.* **611**, 410–421 (2014).
26. Barrirero, J. *et al*. Cluster formation at the Si/liquid interface in Sr and Na modified Al–Si alloys. *Scr. Mater.* **117**, 16–19 (2016).
27. Li, J. H. H. *et al*. Nucleation and Growth of Eutectic Si in Al-Si Alloys with Na Addition. *Metall. Mater. Trans. A* **46**, 1300–1311 (2014).
28. Timpel, M. *et al*. Sr-Al-Si co-segregated regions in eutectic Si phase of Sr-modified Al-10Si alloy. *Ultramicroscopy* **132**, 216–21 (2013).
29. Li, J. *et al*. The roles of Eu during the growth of eutectic Si in Al-Si alloys. *Sci. Rep.* **5**, 13802 (2015).
30. Nogita, K. *et al*. The role of trace element segregation in the eutectic modification of hypoeutectic Al–Si alloys. *J. Alloys Compd.* **489**, 415–420 (2010).
31. Li, J. H., Suetsugu, S., Tsunekawa, Y. & Schumacher, P. Refinement of Eutectic Si Phase in Al-5Si Alloys with Yb Additions. *Metall. Mater. Trans. A* **44**, 669–681 (2012).
32. Kranenberg, C. *et al*. Structure and properties of the compounds LnAl2X2 (Ln = Eu, Yb; X = Si, Ge). *Solid State Sci.* **2**, 215–222 (2000).
33. Bobev, S. *et al*. Ternary rare-earth alumo-silicides - Single-crystal growth from Al flux, structural and physical properties. *J. Solid State Chem.* **178**, 2091–2103 (2005).
34. YbAl2Si2 Crystal Structure: Datasheet from 'PAULING FILE Multinaries Edition – 2012' in Springer Materials (https://materials.springer.com/isp/crystallographic/docs/sd_1210515).
35. Lefebvre, W. *et al*. 3DAP measurements of Al content in different types of precipitates in aluminium alloys. *Surf. Interface Anal.* **39**, 206–212 (2007).
36. Sha, G. *et al*. Solute nanostructures and their strengthening effects in Al–7Si–0.6Mg alloy F357. *Acta Mater.* **60**, 692–701 (2012).
37. Gault, B. *et al*. Atom probe tomography and transmission electron microscopy characterisation of precipitation in an Al-Cu-Li-Mg-Ag alloy. *Ultramicroscopy* **111**, 683–9 (2011).
38. Rüsing, J., Sebastian, J. T., Hellman, O. C. & Seidman, D. N. Three-dimensional Investigation of Ceramic/Metal Heterophase Interfaces by Atom-probe Microscopy. *Microsc. Microanal.* **6**, 445–451 (2000).
39. Hasting, H. K. *et al*. Comparative study of the β″-phase in a 6xxx Al alloy by 3DAP and HRTEM. *Surf. Interface Anal.* **39**, 189–194 (2007).
40. Dahle, A. K., Nogita, K., McDonald, S. D., Zindel, J. W. & Hogan, L. M. Eutectic nucleation and growth in hypoeutectic Al-Si alloys at different strontium levels. *Metall. Mater. Trans. A* **32**, 949–960 (2001).
41. Zarif, M., Mckay, B. & Schumacher, P. Study of Heterogeneous Nucleation of Eutectic Si in High-Purity Al-Si Alloys with Sr Addition. *Metall. Mater. Trans. A* **42**, 1684–1691 (2010).
42. Li, J. H., Zarif, M. Z., Dehm, G. & Schumacher, P. Influence of impurity elements on the nucleation and growth of Si in high purity melt-spun Al–Si-based alloys. *Philos. Mag.* **92**, 3789–3805 (2012).

43. Ho, C. R. & Cantor, B. Modification of hypoeutectic Al-Si alloys. *J. Mater. Sci.* **30**, 1912–1920 (1995).
44. Ludwig, T. H., Schonhovd Dæhlen, E., Schaffer, P. L. & Arnberg, L. The effect of Ca and P interaction on the Al-Si eutectic in a hypoeutectic Al-Si alloy. *J. Alloys Compd.* **586**, 180–190 (2014).
45. Li, J. H. *et al.* Nucleation kinetics of entrained eutectic Si in Al-5Si alloys. *Acta Mater.* **72**, 80–98 (2014).
46. Eiken, J., Apel, M., Liang, S.-M. & Schmid-Fetzer, R. Impact of P and Sr on solidification sequence and morphology of hypoeutectic Al–Si alloys: Combined thermodynamic computation and phase-field simulation. *Acta Mater.* **98**, 152–163 (2015).
47. McDonald, S. D., Nogita, K. & Dahle, A. K. Eutectic nucleation in Al–Si alloys. *Acta Mater.* **52**, 4273–4280 (2004).
48. Day, M. G. & Hellawell, A. The Microstructure and Crystallography of Aluminium-Silicon Eutectic Alloys. *Proc. R. Soc. A Math. Phys. Eng. Sci.* **305**, 473–491 (1968).
49. Hellawell, A. The growth and structure of eutectics with silicon and germanium. *Prog. Mater. Sci.* **15**, 3–78 (1970).
50. Jenkinson, D. C. & Hogan, L. M. The modification of aluminium-silicon alloys with strontium. *J. Cryst. Growth* **28**, 171–187 (1975).
51. Hanna, M. D., Lu, S.-Z. & Hellawell, A. Modification in the aluminum silicon system. *Metall. Trans. A* **15**, 459–469 (1984).
52. Yilmaz, F., Atasoy, O. A. & Elliott, R. Growth structures in aluminium-silicon alloys II. The influence of strontium. *J. Cryst. Growth* **118**, 377–384 (1992).
53. Li, J. H. *et al.* Modification of eutectic Si in Al–Si alloys with Eu addition. *Acta Mater.* **84**, 153–163 (2015).
54. Ferro, R., Kubaschewski, O., Hubert, H. & Ibe, G. Aluminium-Silicon-Strontium. *VCH* **8**, 270–278 (1993).
55. Bochvar, N., Budberg, P., Hayes, F., Liberov, Y. & Schmid-Fetzer, R. *Al-Na-Si Ternary Phase Diagram* (MSI, Materials Science International Services GmbH, 1993).
56. Kumari, S. S. S., Pillai, R. M. & Pai, B. C. Role of calcium in aluminium based alloys and composites. *Int. Mater. Rev.* **50**, 216–238 (2005).
57. Davies, V. L. & West, J. M. Factors affecting the modification of the aluminium-silicon eutectic. *J. Inst. Met.* **92**, 175–180 (1963).
58. Steen, H. A. H. & Hellawell, A. The growth of eutectic silicon-contributions to undercooling. *Acta Metall.* **23**, 529–535 (1975).
59. Clapham, L. & Smith, R. W. Segregation behaviour of strontium in modified and unmodified Al-Si alloys. *J. Cryst. Growth* **92**, 263–270 (1988).
60. Barrirero, J., Engstler, M., Odén, M. & Mücklich, F. Phase selective sample preparation of Al-Si alloys for Atom Probe Tomography. *Pract. Metallogr.* **56**, 76–90 (2019).
61. Thompson, K. *et al. In situ* site-specific specimen preparation for atom probe tomography. *Ultramicroscopy* **107**, 131–9 (2007).
62. https://github.com/annacegu/atomblend - Accessed on 01.11.2018. 01.11.2018. Available at: https://github.com/annacegu/atomblend (Accessed: 1st November 2018).
63. Gladyshevskii, E. I., Kripyakevich, P. I. & Bodak, O. I. Crystal structure of CaAl2Si2 and its analogs. *Ukr. Phys. J.* **12**, 447–452 (1967).
64. Westerhaus, W. & Schuster, H.-U. Darstellung und Struktur von NaAlSi und NaAlGe. *Tl. B Anorg. chemie, Org. chemie* **34B**, 352–353 (1979).
65. Yamanaka, S., Kajiyama, M., Sirakumar, S. N. & Fukuoka, H. Preparation and single crystal structure of a new high-pressure modification of BaAl2Si2. *High Press. Res.* **24**, 481–490 (2004).
66. Muraveva, A. A., Zarechnyuk, O. S. & Gladyshevskii, E. I. The systems Y-Al-Si(Ge,Sb) in the range 0–33.3 at.% Y. *Inog. Mater.* **7**, 34 (1971).

Acknowledgements

Author Contributions

J.L. fabricated the samples. J.B. and M.E. performed SEM imaging and APT acquisition and analysis. C.P. and J.B. performed EBSD/TKD acquisition and analysis. J.G., N.G. and J.B. performed TEM acquisition and analysis. J.B. and M.O. wrote the first draft of the manuscript. J.B. prepared all images. All authors (J.B., C.P., M.E., J.G., N.G., J.L., P.S., M.O., F.M.) contributed substantially to the concepts, ideas and design of the experiments and to the discussion of the results. All authors reviewed and contributed to the manuscript.

Additional Information

Supplementary information accompanies this paper at https://doi.org/10.1038/s41598-019-41919-2.

Competing Interests: The authors declare no competing interests.

Publisher's note: Springer Nature remains neutral with regard to jurisdictional claims in published maps and institutional affiliations.

Paper IV

Nucleation and Growth of Eutectic Si in Al-Si Alloys with Na Addition

J.H.H. Li, J. Barrirero, M. Engstler, H. Aboulfadl, F. Mücklich, P. Schumacher

PAPER IV

Nucleation and Growth of Eutectic Si in Al-Si Alloys with Na Addition

J.H. Li[1], J. Barrirero[2], M. Engstler[2], H. Aboulfadl[2], F. Mücklich[2] and P. Schumacher[1]

[1]Institute of Casting Research, Montanuniversität Leoben, 8700 Leoben, Austria.

[2]Department of Materials Science, Saarland University, Campus D3.3, 66123 Saarbrücken, Germany.

Abstract

Al-5 wt pct Si-based alloys with Na additions (19 and 160 ppm) have been produced by controlled sand casting and melt spinning. Entrained droplet technique and differential scanning calorimetry were employed to investigate the nucleation behavior of eutectic Si. High-resolution transmission electron microscopy and atom probe tomography were used to investigate the distribution of Na atoms within eutectic Si and at the interfaces between eutectic Si and eutectic Al. It was found that (i) only 19 ppm Na addition results into a high undercooling (49 K (49 °C)) of the entrained eutectic droplet. However, further increasing Na addition up to 160 ppm exerts no positive effect on the nucleation of eutectic Si, instead a decreased undercooling (29 K (29 °C)) was observed. (ii) Na addition suppresses the growth of eutectic Si due to the Na segregation at the interface between eutectic Si and eutectic Al, and (iii) Na addition promotes significant multiple Si twins, which can be attributed to the proposed adsorption of Na atoms at the intersection of Si twins and along the $<112>_{Si}$ growth direction of Si. The present investigation demonstrates, for the first time, a direct observation on the distribution of Na atoms within eutectic Si and thereby provides strong experimental supports to the well-accepted impurity-induced twinning growth mechanism and poisoning of the twin plane re-entrant edge growth mechanism.

1. Introduction

Na has been firstly used to modify the eutectic Si in Al-Si alloys since 1921 [1]. However, Na modification has been replaced, or is being reduced, by Sr modification due to the inherent disadvantages of Na modification, i.e., evaporation, high volatility, rapid fade from the melt, and a tendency to overmodification [1]. Compared with Sr modification, the effects of Na addition on the nucleation and growth of eutectic Si are still not fully understood due to the lack of a detailed experimental investigation on Na modification.

Similar to Sr modification, it is generally accepted that impurity-induced twinning (IIT) growth mechanism [2], twin plane re-entrant edge (TPRE) growth mechanism[3,4] as well as poisoning

of the TPRE [5] are also valid for Na modification under certain conditions. The IIT mechanism postulates that the modifier can be adsorbed on the growing $\{111\}_{Si}$ planes producing frequent multiple Si twins. The TPRE mechanism proposes that Si growth occurs more readily at the re-entrant edge along the $<112>_{Si}$ growth direction of Si while poisoning of the TPRE assumes that the modifier retards the Si growth by selectively adsorbing at the TPRE, thus deactivating the growth advantage of the TPRE and forcing new growth of the TPRE. However, in contrast to detailed investigations on Sr modification [6, 7, 8, 9, 10, 11, 12, 13, 14], there is still a lack of, if any, detailed experimental investigations on the distribution of Na atoms within eutectic Si. This is mainly due to the very low Na content (less than 50 ppm) and the difficulties of Na observation within eutectic Si using scanning transmission electron microscopy (STEM) due to their very close Z atomic numbers (Z_{Na} = 11, Z_{Al} = 13, Z_{Si} = 14) and thereby the weak contrast in STEM high-angle annular dark field (HAADF) image.

It has been reported [15] that Na atoms were adsorbed on $\{111\}_{Si}$ physically and homogeneously using X-ray photoelectron spectroscopy (XPS) and Auger electron spectroscopy (AES) analyses in hypereutectic Al-22 wt pct Si alloys with 0.25 and 0.6 wt pct Na additions. The existence of Na-enriched regions within primary Si crystals has also been reported in Al-16 wt pct Si alloy with Na addition using electron probe microanalysis (EPMA) and back-scattered electron images [16]. Na-enriched regions were observed in narrow regions which spread from the center to the periphery of the multifaceted Si particle which appeared rounded in morphology. However, the distribution of Na atoms within eutectic Si has not been reported yet at an atomic scale. Therefore, in the case of Na modification, IIT, TPRE, or poisoning of the TPRE has not been supported experimentally.

In terms of the nucleation of eutectic Si, similar to Sr modification [6,17], the poisoning effect of Na modification on the AlP compound has also been reported by Mondolfo[18] in hypoeutectic Al-Si alloys. Na addition was found to force the nucleation of Si to larger undercoolings. Similar results were also obtained by Ho and Cantor[19] in hypoeutectic Al-Si alloys doped with different levels of P and Na using entrained droplet experiments. Adding Na (80 to 850 ppm) was found to lead to the formation of Na_3P in preference to AlP. It is the formation of Na_3P compound that reduces the amount of the potent AlP phase [20]. Clearly, there is an important interaction between Na and AlP in Al-Si alloys. However, whether such type of interaction affects the growth of eutectic Si, and thereby the modification of eutectic Si is still not fully understood.

In the present investigation, the entrained droplet technique, which can be used to investigate the impurity effect on heterogeneous nucleation [6]. was employed to investigate the nucleation of eutectic Si in Al-5 wt pct Si alloy with Na addition (19 and 160 ppm). In order to compare the observations under different solidification conditions, the samples produced using controlled sand casting and melt spinning were investigated using differential scanning calorimetry (DSC) and multi-scale microstructure characterization techniques from μm to sub-nm scales. In particular, high-resolution transmission electron microscopy (TEM) and atom probe tomography (APT) were used to investigate the distribution of Na atoms within eutectic Si and along the interfaces between eutectic Si and eutectic Al, with the aim to further elucidate the modification mechanism caused by Na addition.

2. Experimental Methods

Al-5 wt pct Si alloys (wt pct, used throughout this paper unless otherwise noted) with and without Na addition were prepared, respectively, using high purity (HP) Al (5N, 99.998), HP Si chips (5N), and elemental Na (2N8, 99.8) supplied in vacuum-packed Al foils. The purity level of the used elemental Na is 2N8 (99.8). Other impurities (*i.e.*, Fe) may be also present. However, it can be expected that these possible impurities may have no significant effect on the nucleation and growth of eutectic Si because of the fact that the content of the possible impurities is very low (the Na content is about 19 and 160 ppm). The chemical concentration of Na was determined by inductively coupled plasma atomic emission spectrum (ICP-AES) apparatus. The chemical concentration of P, due to the Al and Si addition, even with a high purity level, was determined with a Finnigan ELEMENT GD glow discharge mass spectrometer (GD-MS). Due to the fact that P comes from the Al and Si used, even with a high purity level (5N Al, 5N Si), repeated measurements (at least three times) of Al-5Si alloys with and without Na additions using GD-MS give a consistent value (about 0.44 ppm) if the used Al and Si remain the same impurity level, *i.e.*, 5N Al, 5N Si. Therefore, 0.44 ppm was used as an average P content.

The measured compositions of both alloys are given in Table I. The balance in Table I is Al. Although a trace Fe (about 10 ppm, coming from used Al and alloy melting and casting process) may be present, Fe has no significant effect on the nucleation and growth on eutectic Si, as reported in Reference 6.

Table I: The Measured Compositions of Al-5Si-Based Alloy with Na Addition (wt pct)

Alloys	Elements			
	Si	Na (ppm)	P (ppm)	Al
Alloy 1	5.00	--	0.44	balance
Alloy 2	5.00	19	0.44	balance
Alloy 3	5.00	160	0.44	balance

In the case of controlled sand casting, experimental alloys were melted in an electric resistance furnace, and the temperature of the melt was kept at about 993 K (720 °C). Elemental Na in vacuum-packed Al foils was added before casting. No degassing was performed prior to casting. At least two samples for each condition were taken to perform thermal analysis using a Quik-Cup method in resin bounded sand molds. The dimensions of Quik-Cup are about 30 mm in length, 30 mm in width, and 30 mm in height. The average cooling rate is about 20 K min^{-1} (20 °C min^{-1}), which is very close to the conventional sand casting even with a larger scale. Please note that the sample prepared using controlled sand casting method is in contrast to the work by Ho and Cantor [19], where the samples were prepared using arc melting.

In the case of melt spinning, two Na-containing alloys (about 15 g) were re-melted under high vacuum conditions and ejected onto a rotating copper wheel (20 m s^{-1}). A power-compensated

PerkinElmer PYRIS Diamond DSC under an Ar atmosphere was used to measure the entrained droplet undercooling with a constant heating from 673 K to 873 K (400 °C to 600 °C), holding for 1 minute at 873 K (600 °C), and subsequent cooling to 673 K (400 °C) with a rate of 10 K min⁻¹ (10 °C min⁻¹). At least two DSC measurements (about 8 mg) were performed. Note that only the cooling curves were used to measure the entrained droplet undercooling because the instrument (DSC) calibration was performed during the cooling stage. For comparison, a similar DSC measurement was also performed for the controlled sand cast alloys.

Optical microscopy (OM), TEM, and APT were employed to characterize the as-cast microstructure in Al-5Si alloy with Na addition (19 and 160 ppm, Table I). Samples were taken from the center parts at the vicinity of the thermal couple. The specimens for OM investigation were mechanically ground, polished, and then etched using a mixture of 13 g boric acid, 35 g HF, and 800 ml H_2O. The specimens (ribbons in the melt spun condition and bulk samples in the controlled sand casting condition) for TEM investigation were mechanically ground, polished, and dimpled to about 30 μm, and then ion beam milled using a Gatan Precision Ion Polishing System (PIPS, Gatan model 691). During PIPS, the sample was cooled to about 253 K (–20 °C) and rotated with a speed of 3 r min⁻¹. Double guns with an accelerating voltage of about 4 kV and an angle of about +4 deg (left or right) and –4 deg (the other side) were used. TEM was performed using a Philips CM12 microscopy operated at 120 kV and an image-side Cs-corrected JEOL-2100F operated at 200 kV.

Sample preparation for APT (bulk samples produced by controlled sand casting) was performed in a dual-beam focused ion beam/scanning electron microscopy workstation (FIB/SEM) (Helios NanoLab 600™, FEI Company, USA) by the standard lift-out technique [21]. After thinning of the samples, a low energy milling at 2 kV was performed to minimize the possible damage induced by Ga. APT was carried out in a LEAP™ 3000X HR (CAMECA). Specimens containing only eutectic Si were measured in laser-assisted mode with a pulse energy of 0.5 nJ and a repetition rate of 160 kHz. Specimens containing both eutectic Si and eutectic Al were measured in voltage mode at a pulse fraction of 20 pct and a repetition rate of 200 kHz. A specimen temperature of about 40 K, a pressure lower than 1×10^{-10} Torr (1.33×10^{-8} Pa), and an evaporation rate of 5 atoms per 1000 pulses were used for all measurements. Datasets were reconstructed and analyzed with the IVAS™3.6.6 software (CAMECA). The Al and Na contents were measured after background noise subtraction. Note that more than 5 samples have been investigated using TEM and APT in each condition (controlled sand casting and melt spinning). A consistent result can be obtained.

3. Results

3.1. Controlled Sand Casting

3.1.1. The as-cast structure for the samples produced by controlled sand casting

Figure 1 shows eutectic structures observed by optical microscopy at a low magnification. Either 19 ppm (Figure 1(b)) or 160 ppm (Figure 1(c)) Na addition results in a very good modification on

the eutectic Si, when compared with Al-5Si alloy (Figure 1(a)). In both cases, eutectic Si appears as a fine fibrous morphology. Due to the very similar modified eutectic Si microstructure, further characterization investigations (TEM and APT) mainly focus on the sample with the 160 ppm Na addition.
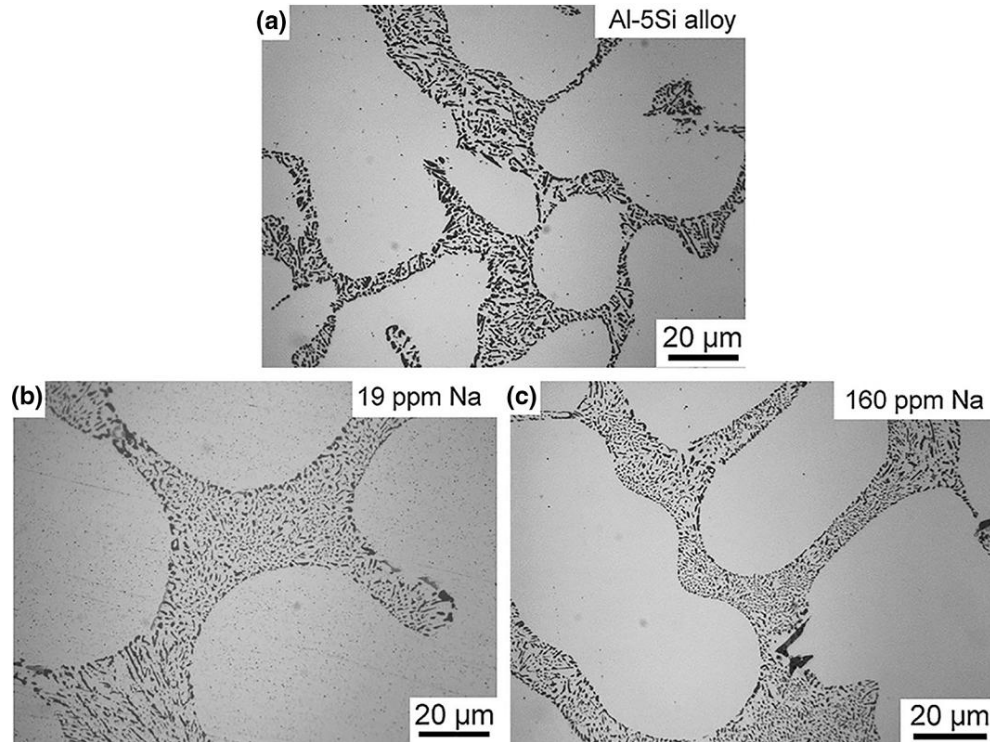
Fig. 1: The as-cast microstructures observed by optical microscopy in Al-5Si-based alloys, (a) without Na addition, (b) with 19 ppm Na addition, and (c) with 160 ppm Na addition

3.1.2. TEM observation for the samples produced by controlled sand casting

Figure 2(a) shows two Si particles in Al-5Si alloy with 160 ppm Na addition. One Si particle (top) was tilted to the principal twinning orientation of Si ($<110>_{Si}$, Figure 2(b)) to observe Si twinning. The Si particle was multiply twinned. The twinning plane is $\{111\}_{Si}$. The weaker reflections can be attributed to the double diffraction of Si caused by the multiply Si twins, as reported in Reference 7. When the Si particle was tilted to $<112>_{Si}$ (Figure 2(d)), which is the typical Si growth direction according to TPRE, the Si twins appear to be not very sharp, as shown in Figure 2(c), when compared with Figure 2(a), viewed from $<011>_{Si}$. However, the zig-zag geometry and the growth steps were clearly observed.
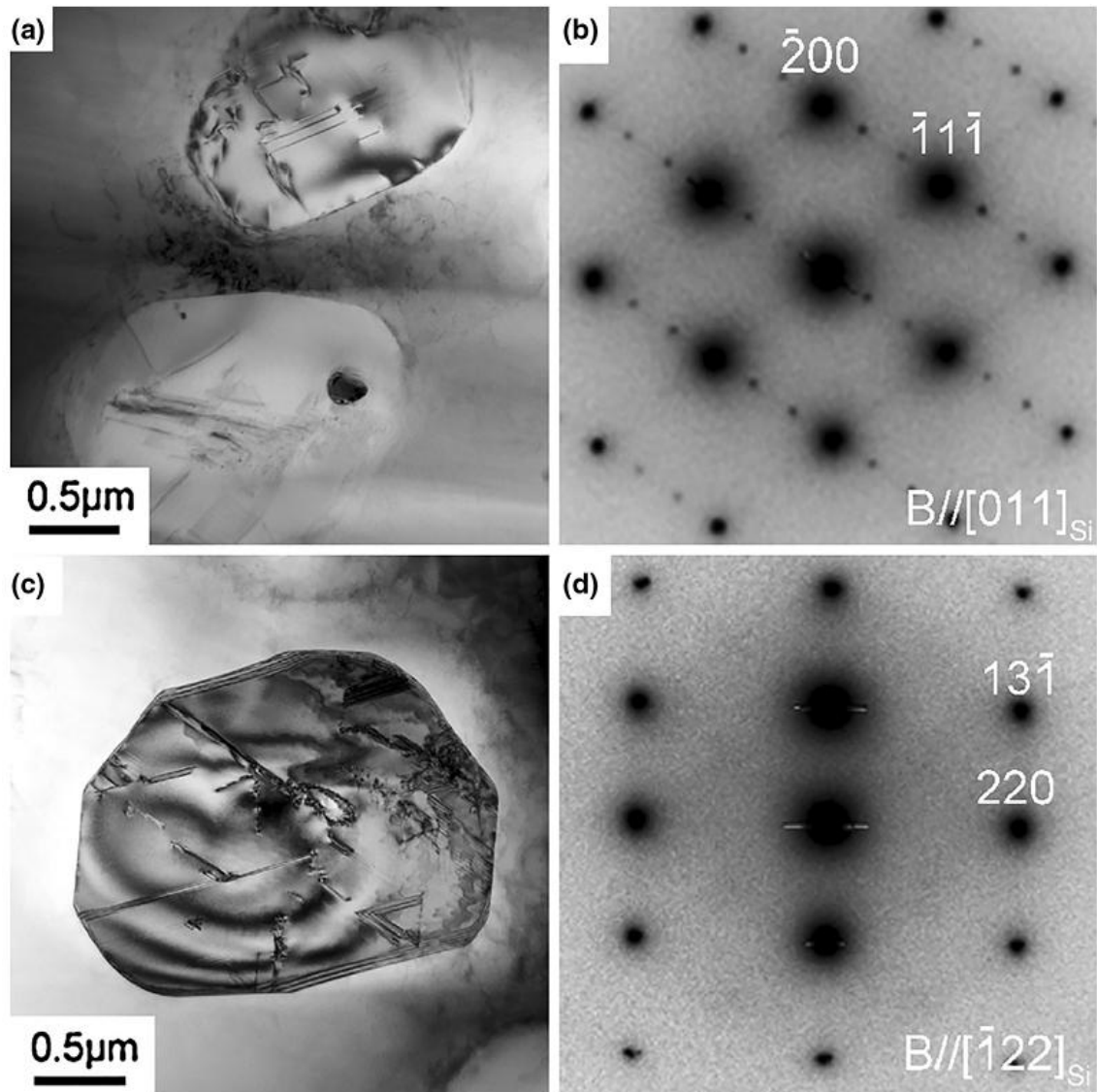
Fig. 2: (a) TEM bright field image, (b) corresponding $[011]_{Si}$ selected area diffraction pattern (SADP), (c) TEM bright field image, (d) corresponding $[112]_{Si}$ SADP, taken from Al-5Si alloy with 160 ppm Na addition

Figure 3 shows another Si particle in Al-5Si alloy with 160 ppm Na addition. Multiple Si twins with a high density were observed, as shown in Figure 3(a). Typical multiple Si twins are enlarged in Figure 3(b). Structural defects that can be correlated to Na-rich clusters appear to be present along the $<112>_{Si}$ growth direction of Si and at the intersection of two $\{111\}_{Si}$ twins, as marked with a white arrow in Figure 3(b). However, it should be noted that no further STEM-HAADF image was taken because of the very close atomic number Z ($Z_{Na} = 11$, $Z_{Al} = 13$, $Z_{Si} = 14$) and thereby the weak contrast in STEM-HAADF image. Instead, APT was employed to elucidate the distribution of Na atoms within eutectic Si.
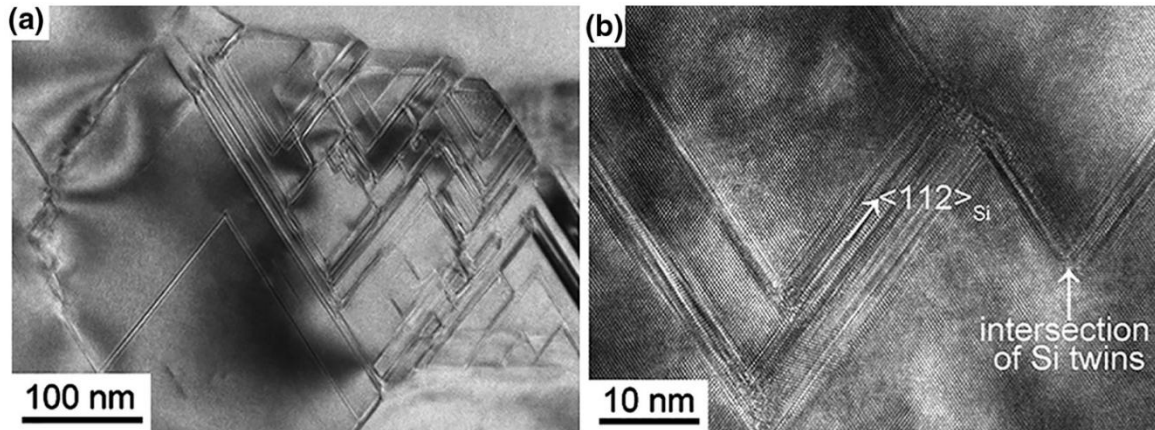
Fig. 3: (a) TEM bright field image, (b) high-resolution TEM image taken from Al-5Si alloy with 160 ppm Na addition. The beam is parallel to $[011]_{Si}$

3.1.3. APT observation for the samples produced by controlled sand casting

In order to further elucidate the distribution of Na atoms within eutectic Si, APT was performed in the bulk samples produced by controlled sand casting. Since APT analysis for such investigation is very time consuming, only one composition was analyzed; however, it is expected a similar distribution of Na in the eutectic Si phase can be observed for both compositions (19 and 160 ppm). Figure 4(a) shows an elemental map of eutectic Si in Al-5Si alloy with 160 ppm Na addition. Magnifications of three different clusters enriched in Al and Na are presented in Figures 4(b) and (c). Figure 4(b) shows two views of an elongated rod-like cluster with a size of about $4 \times 6 \times 16$ nm. Totally, 99 Al atoms and 92 Na atoms were detected in the elongated rod-like cluster. The ratio of Al:Na is close to 1. Figure 4(c) shows two round particle-like clusters with a diameter of about 4 to 6 nm. Within one round particle-like cluster, about 75 Al atoms and 51 Na atoms were detected, while, in the other round particle-like cluster, about 75 Al and 53 Na atoms were detected. The ratio of Al:Na in these two round particle-like clusters is close to 1.5. Reporting the amount of detected atoms is preferred in contrast to concentrations, because of the small amount of atoms involved in the clusters and the difficulty of setting a region of interest to measure the concentrations. It should be noted that only about 37 pct of the total atoms in the sample can be detected in the APT instrument used [22]. Therefore, the number of atoms reported here should not be regarded as the total amount of each species in the clusters. However, the ratio of Al and Na atoms remains unchanged.
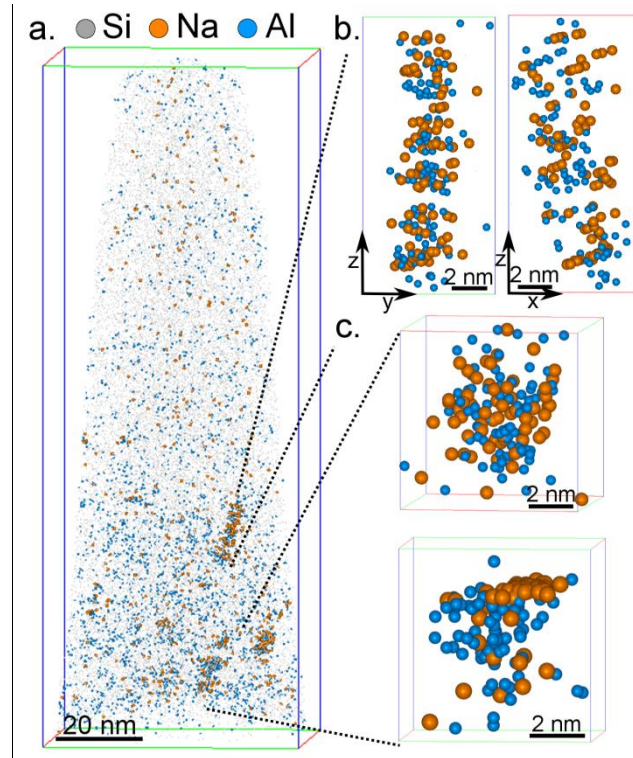
Fig. 4: Atom probe tomography of eutectic Si in Al-5Si alloy with 160 ppm Na addition, (a) complete 3D reconstruction of the data (atoms of each element are shown in different sizes for visualization purposes), (b) magnified image of a rod-like cluster, (c) magnified images of two particle-like clusters

Figure 5(a) shows an elemental map of eutectic Al and eutectic Si in the Al-5Si alloy with 160 ppm Na addition. Figure 5(b) highlights an elongated rod-like cluster in the eutectic Si, which extends up to the interface between eutectic Al and eutectic Si. Within the elongated rod-like cluster, Al and Na atoms were observed along one atomic monolayer (z–y view). When the cropped volume is viewed from another direction (x–y view), the Al and Na atoms are seen to extend over an area of approximately 4 × 30 nm2. Figure 5(c) shows only the Na atoms in the reconstruction. A clear enrichment of Na at the interface between eutectic Al and eutectic Si was detected. For a quantitative analysis, a concentration profile at the interface between eutectic Si and eutectic Al was performed by a proximity histogram, which is constructed on an Al iso-concentration surface. An iso-surface value of 50 at. pct Al was chosen (iso-surface not shown here). Figure 5(d) shows an enrichment of ~0.25 at. pct Na along the interface.

The enrichment of Na seems to be slightly displaced toward the eutectic Al phase (Figure 5(d)); however, this is most probably an artifact in the APT measurement. It is theoretically known that Al atoms evaporate at a lower field than Si during APT acquisition (19 V nm^{-1} at 77 K (−196 °C) for Al and 33 V nm^{-1} at 77 K (−196 °C) for Si [23]). This results in a slightly higher field evaporation rate of Al than Si during measurement. Therefore, for such spatial configurations of two phases with different values of evaporation field within the specimen, a step in the surface morphology of the specimen curvature is formed at the interface. A slight morphological change along an

interface may lead to broadening of segregated elements at the interface as a result of ion-trajectory aberrations. A recent field evaporation simulation by C. Oberdorfer *et al*[24] explains such effects in detail.
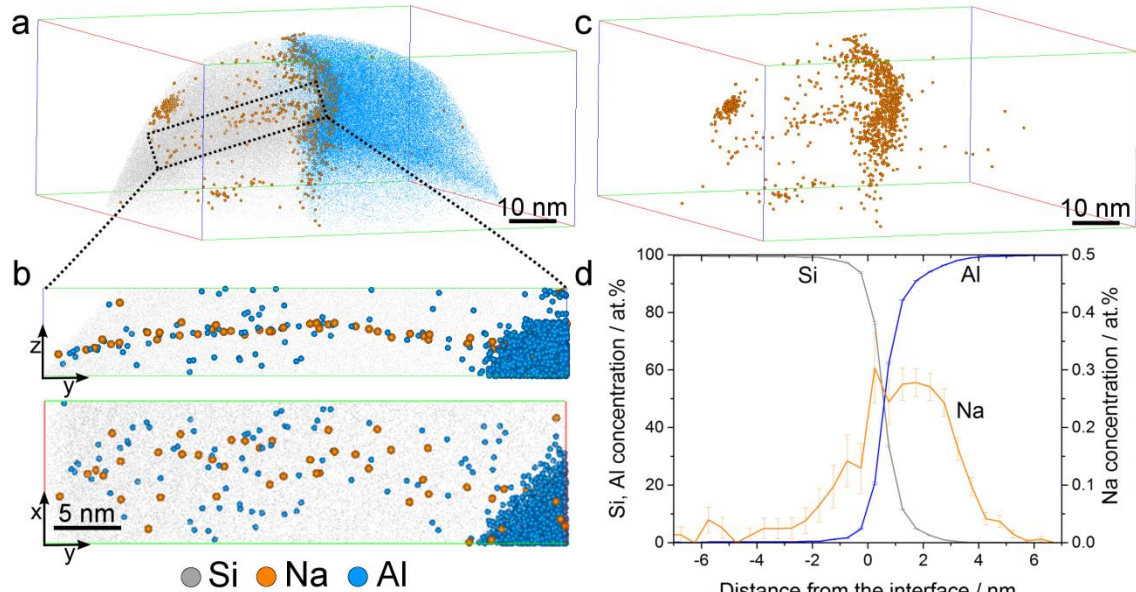
Fig. 5: Atom probe tomography of eutectic Al and eutectic Si in Al-5Si alloy with 160 ppm Na addition, (a) complete 3D reconstruction of the data with Na atoms represented as sphere, (b) a sub-volume highlighting a rod-like cluster composed of an atomic monolayer, (c) atomic map of Na atoms showing Na enrichment at the interface between eutectic Al and eutectic Si, (d) concentration profile across the interface constructed using proximity histogram, showing the enrichment of Na at the interface

3.2. Entrained Si after Melt Spinning and DSC

3.2.1. DSC

Figure 6 shows a DSC trace taken from Al-5Si alloys produced by controlled sand casting. Only the eutectic Si [about 850 K (577 °C)] was reflected in DSC curve. It is not possible to investigate the nucleation of eutectic Si using DSC analyses for the samples produced by controlled sand casting. Therefore, no further detailed investigation was performed. In contrast, Figure 7 shows DSC traces taken from Al-5Si alloys without (Figure 7(a)) and with 19 ppm Na (Figure 7(b)) and 160 ppm Na (Figure 7(c)) additions, respectively. Two distinct solidification exotherms were observed. The first exotherm corresponds to the solidification of the eutectic Si along the grain boundaries [6]. The second exotherm is associated with the solidification of entrained eutectic droplets embedded in the α-Al matrix. The undercooling of the entrained eutectic droplets (ΔT) was defined as the difference between the onset temperatures of these two exotherms. Therefore, only the onset temperatures are marked in Figure 7. The peak temperature is very helpful to elucidate the nucleation kinetics at different cooling rates (DSC heating and cooling rates). However, in the present manuscript, only one cooling rate (10 K min⁻¹) was used. Therefore, no further analysis on

the peak temperature is included here. The entrained eutectic undercooling can be obtained reliably with a reproduction of about 0.2 K to 0.5 K (0.2 °C to 0.5 °C). In the case of Al-5Si alloy without Na addition, the measured undercooling of the entrained eutectic droplets (ΔT) is about 24 K (24 °C), as shown in Figure 7(a). In the case of Al-5Si alloy with 19 ppm Na addition, the measured undercooling of the entrained eutectic droplets (ΔT) is about 49 K (49 °C). Clearly, 19 ppm Na addition does lead to a significant depression on the nucleation of entrained eutectic droplets. However, further increasing Na addition up to 160 ppm decreases the undercooling [29 K (29 °C)]. Furthermore, it should be noted that the second exotherm in Na-containing samples (Figures 7(b), (c)) is much wider than that of Na-free sample (Figure 7(a)), indicating a wider size distribution of the entrained eutectic droplets [6]. Such typical observation is always present after four DSC runs, as shown in Figure 8. However, it should be pointed out that the shape of the second exotherm has no significant effect on the measurement of the entrained eutectic undercooling because the entrained eutectic undercooling is measured using the onset temperature of the exotherms.

3.2.2. TEM observation for the samples produced by melt spinning

Similar to the case of the controlled sand casting, TEM characterization mainly focuses on the sample with the 160 ppm Na addition. Figure 9 shows a TEM bright field image of two Si particles in melt spun Al-5Si alloy with 160 ppm Na addition. Parallel Si twins (left Si particle) and multiple Si twins (right Si particle) were observed, as shown in Figure 9(a), and can be seen more clearly in Figures 10(b) and (c). The parallel Si twins can be interpreted according to TPRE growth mechanism, while multiple Si twins can be interpreted according to IIT growth mechanism. The TPRE growth mechanism appears to form a much finer twin structure in the $<112>_{Si}$ directions respective facets in the case of melt spinning, when compared with the case of controlled sand casting (Figure 3(a)). However, no or little change of directions was observed. In contrast, the IIT growth mechanism appears not to provide such a fine structure but facilitates a change of growth direction in non-constrained solidification conditions. This is fully consistent with the TEM observation in the case of controlled sand casting (Figures 2, 3). Furthermore, the number density of Si twins in melt spun condition appears to be much higher due to the high cooling rates during melt spinning.
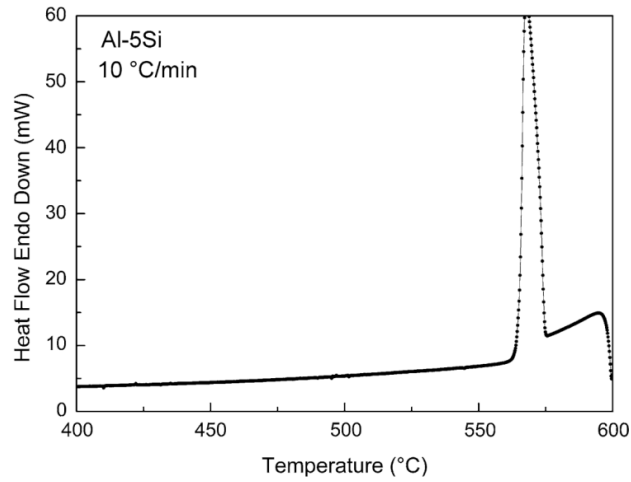
Fig. 6: DSC solidification exotherms of Al-5Si alloy produced by controlled sand casting at a cooling rate of 10 K min⁻¹ (10 °C min⁻¹)
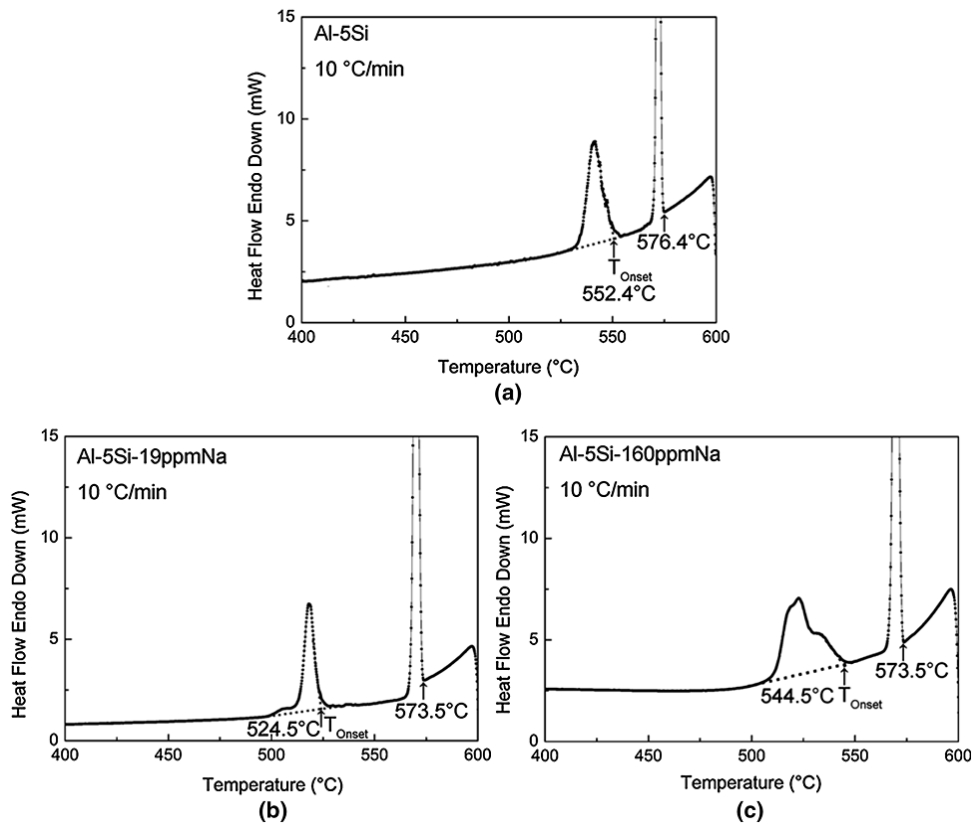
Fig. 7: DSC solidification exotherms of melt spun Al-5Si alloys without Na addition (a) and with 19 ppm Na (b), 160 ppm Na (c) additions at a cooling rate of 10 K min⁻¹ (10 °C min⁻¹)
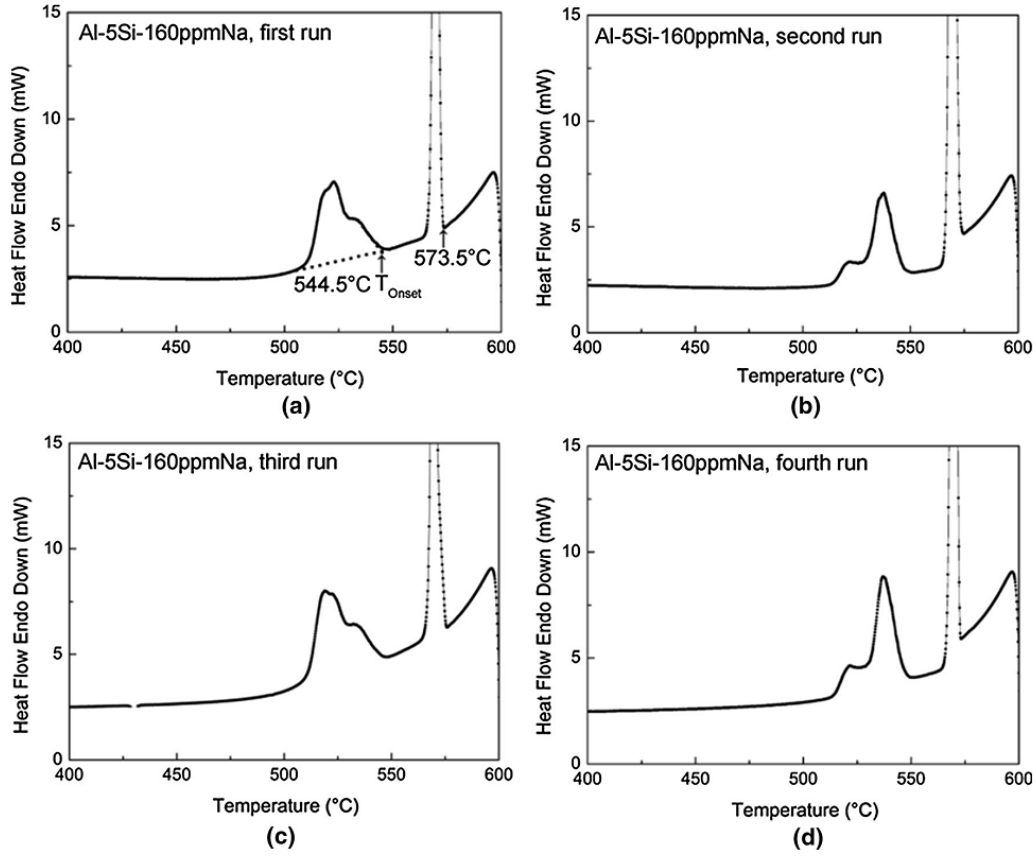
Fig. 8: DSC solidification exotherms of melt spun Al-5Si alloys with 160 ppm Na addition after the first (a), second (b), third (c), and fourth (d) DSC run at a cooling rate of 10 K min⁻¹ (10 °C min⁻¹)
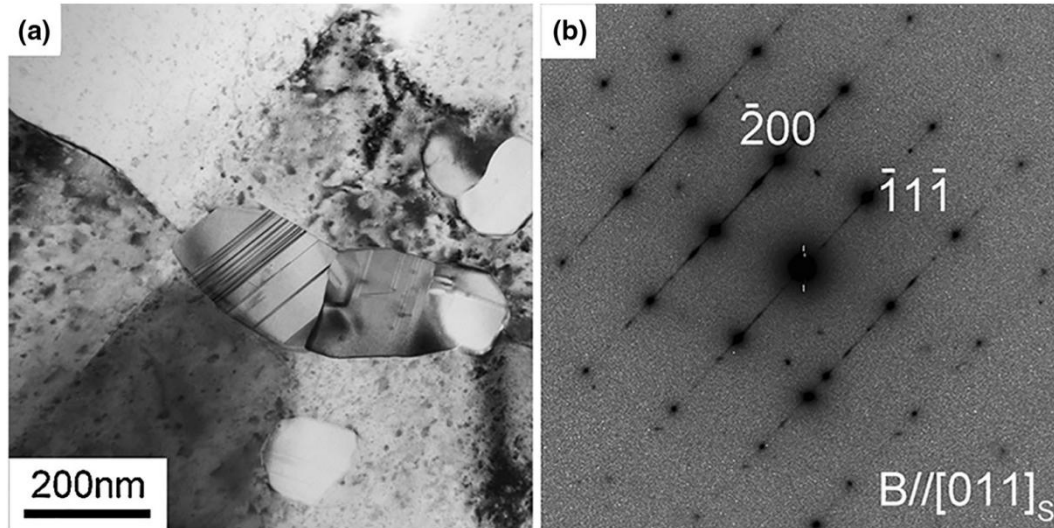
Fig. 9: (a) TEM bright field image, (b) corresponding [011]Si SADP of Si particles taken from melt spun Al-5Si alloy with 160 ppm Na addition. The beam is parallel to [011]$_{Si}$
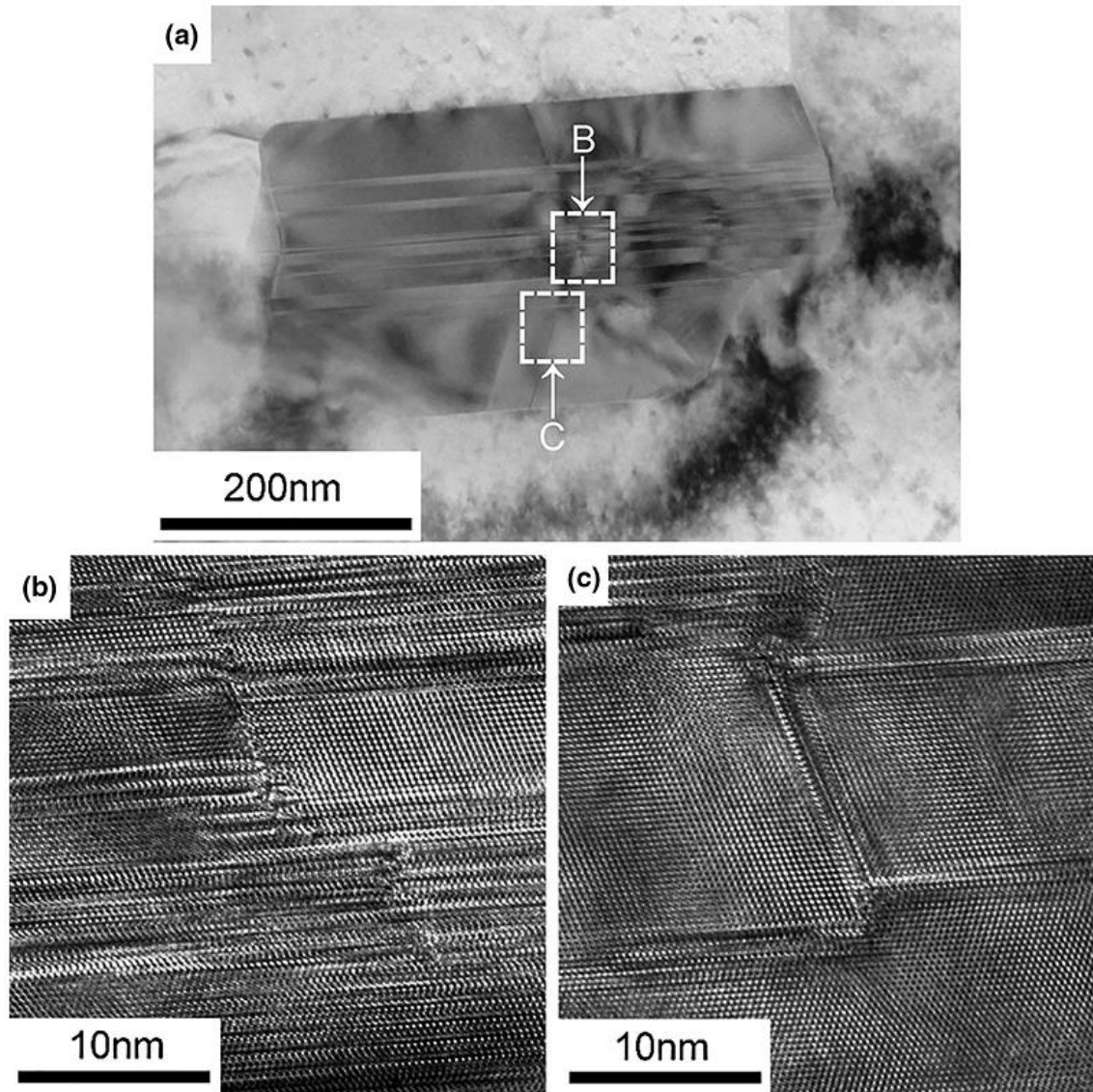
Fig. 10: (a) TEM bright field image of a multiple twinned Si particle taken from melt spun Al-5Si alloy with 160 ppm Na addition. (b), (c) are enlarged from the areas as marked with white boxes ((B) and (C)) in (a), respectively, showing Si twinning. The beam is parallel to $[011]_{Si}$

Several APT attempts have also been made to measure the Na distribution in melt spun samples. However, melt spun samples have an extremely fine Si structure which makes site-specific sample preparation for APT very challenging. Although further APT measurement is still required for melt spun samples, a similar Na distribution can be expected in both samples produced by melt spinning and controlled sand casting.

4. Discussion

4.1. Growth of Eutectic Si

In terms of the growth of eutectic Si, 160 ppm Na addition into Al-5Si alloy promotes significant Si twins both in the cases of controlled sand casting (Figures 2, 3) and melt spun condition (Figures 9, 10), respectively. This is very similar to the case of Sr addition, indicating that the modification mechanism can be interpreted in a similar way. As reported in Reference 7, the twin density (*i.e.*, number of twins per length) can be evaluated by counting the number of the twins intersecting a perpendicular reference line. An analysis of at least ten twinned Si particles in melt spun Al-5Si-based alloy yields an average twin density of about $1.6 \pm 0.4 \times 10^{-4}$ nm^{-1}. In contrast, a total analysis of at least ten twinned Si particles in Al-5Si-based alloy with 160 ppm Na addition provides a value of $4.8 \pm 0.85 \times 10^{-2}$ nm^{-1} for the average twin density, which is two orders of magnitude higher than that of melt spun Al-5Si-based alloy, strongly indicating that 160 ppm Na addition indeed promotes significant Si twins.

For the first time, the adsorption of Na atoms within eutectic Si was clearly observed by APT. The elongated rod-like clusters and round particle-like clusters were found to be enriched with Al and Na atoms, which are fully consistent with the previous report [19] using STEM X-ray elemental mapping that Na is localized in small particles, rather than being adsorbed uniformly in the eutectic Al or eutectic Si. Although no detailed structural information (*i.e.*, orientations) of such types of clusters can be easily extracted from APT data, the elongated rod-like clusters can be proposed to be oriented along the $<112>_{Si}$ growth direction of Si when correlated to the high-resolution TEM image (Figure 3(b)). Indeed, the length (about 20 nm, Figure 3(b)) and the width (about 2 to 3 nm, Figure 3(b)) of Si twins observed by TEM are very close to that of the elongated rod-like cluster ($4 \times 6 \times 16$ nm) observed by APT. The round particle-like clusters can be proposed to be located at the intersection of the two $\{111\}_{Si}$ twins when the APT and high-resolution TEM image (Figure 3(b)) are compared.

The difference of cluster types can be further supported by the fact that the ratio of Al:Na (1.5) within the round particle-like clusters is higher than that (1) within the elongated rod-like clusters, strongly indicating that a possible different segregation pattern may occur. It should be noted here that, from TEM images, the crystallographic orientation and location of TPRE mechanism are identical to that of the IIT mechanism and cannot be differentiated by the crystallography alone because the intersection of Si twins for IIT and the corner for TPRE appear as single points, when viewed in $<011>_{Si}$ direction. However, from APT, the IIT segregation pattern appears to be round particle-like clusters enriched with Al, Si, and Na atoms, while the poisoning of the TPRE segregation pattern appears to be elongated rod-like clusters or segregation line along the $<112>_{Si}$ growth direction of Si enriched with Al, Si, and Na atoms (Figures 4(b), 5(b)). For clarity, two types of the segregation patterns within eutectic Si, corresponding to poisoning of the TPRE and IIT segregation patterns, are marked in Figures 11(a) and (b), respectively.

The elongated rod-like clusters result as a segregation pattern of the poisoning of the TPRE mechanism. Na atoms are adsorbed at the TPRE hindering growth but are quickly overgrown by subsequent Si growth on $\{111\}_{Si}$ facets. Excess Al can segregate out ahead of the growing interface, as marked with a red arrow in Figure 11(a), leading to lower Al concentrations in the elongated

rod-like clusters. The round particle-like clusters can be related to the multiple IIT events on {111}$_{Si}$ facets. When newly formed {111}$_{Si}$ facets grow subsequent to the IIT event, a secondary IIT of Na atoms may occur on these {111}$_{Si}$ facets, as marked with dashed Na atoms in Figure 11(b). Subsequently, these {111}$_{Si}$ facets grow toward each other and entrap the solute-rich diffusion fields ahead of the {111}$_{Si}$ facets. Once entrapped, the liquid has no path for Al to segregate out, and thereby higher Al concentration was observed in the round particle-like clusters. The entrapped liquid itself forms clusters, which can be caused by the surface minimization and ripening exhibiting a more spherical morphology.
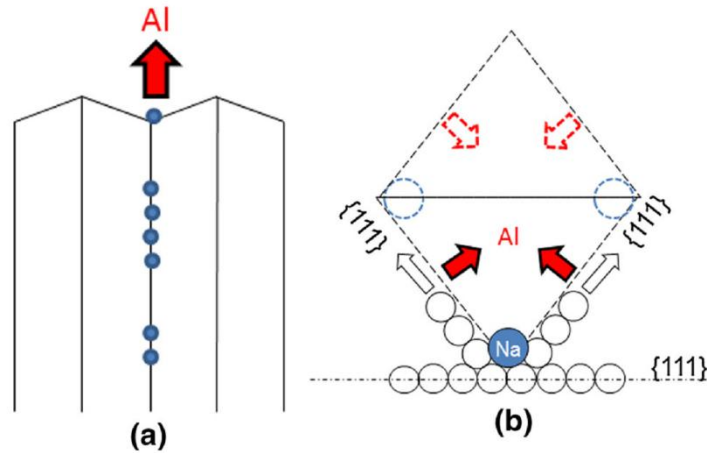
Fig. 11: Schematic representation of the adsorption of Na atoms along the <112>$_{Si}$ growth direction of Si (poisoning of the TPRE) (a) and at the intersection of Si twins (IIT) (b) within eutectic Si

Comparing the information collected from the high-resolution experimental analysis with the IIT and poisoning of the TPRE growth mechanism, one question arises how Na atoms are adsorbed on {111}$_{Si}$ growth planes. It is still not clear whether the Na adsorption occurs within one monolayer. The adsorption of Na atoms was observed within one monolayer, as shown in Figure 5(b). Although, viewed from the other direction (x–y view), Al and Na atoms were observed to extend over an area of approximately 4×30 nm^2, this planar monolayer of Na and Al atoms can be therefore assumed to correspond to a region of narrow twins, as shown in Figure 3(b). Thus, it can be proposed that only one monolayer of Na atoms can induce the poisoning of the TPRE growth mechanism. The Na-rich segregation line (Figure 5(b)) is indicative of the repeated poisoning of the TPRE growth mechanism. Similarly, the adsorption of Na atoms within one monolayer at the intersection of two {111}$_{Si}$ twins can also induce the IIT growth mechanism. The formation of Na-rich clusters with different compositions and morphologies can be attributed to the continuous solute segregation and entrapment of Al, Si, and Na atoms during continuous Si growth. Further detailed discussion on the solute adsorption and entrapment has been made elsewhere [25].

The adsorption of Na atoms at the interface between Al and Si was also clearly observed, as shown in Figure 5(c), (d). An enrichment of Na (about 0.25 at. pct) was, for the first time, measured, as

shown in Figure 5(d). It should be pointed out that this observation is fully consistent with the previous report [26] that Na atoms are rejected by the Al and Si phase during solidification because of the low solubility of Na in Al and Si. Such type of Na enrichment provides a direct experimental support to the assumption that Na atoms are segregated ahead of the solidification front and hinder the growth of eutectic Si.

4.2. Nucleation of Eutectic Si

In terms of the nucleation of eutectic Si, the measured entrained eutectic undercooling [24 K (24 °C)] in Al-5Si alloy is consistent with the previous report [6] that the undercooling of Al-5Si binary alloy is about 20.5 K (20.5 °C) (4N Si) and 31 K (31 °C) (5N Si), respectively. However, given the used materials (5N Si) in the present investigation, some impurities may be present. 19 ppm Na addition does lead to a significant depression on the nucleation of entrained eutectic droplets in high purity Al-5Si alloy. The measured undercooling of the entrained eutectic droplets (ΔT) is about 49 K (49 °C), which is fully consistent with the previous report [about 48 K (48 °C)] [19]. However, a decreased undercooling [29 K (29 °C)] was observed in the case of 160 ppm Na addition, indicating that the nucleation kinetic of entrained eutectic Si may be related to the Na content.

According to the calculation of the required Na to form the Na_3P phase instead of AlP [19], about two times of the Na content (*e.g.* $c_{Na}=2c_p$, 0.88 ppm) are needed to fully react with the P (0.44 ppm, Table I). 19 or 160 ppm Na addition in the present investigation is sufficient to completely remove the effect of P on the nucleation of eutectic Si. However, this is not the case. The undercooling does not further reduce with increasing Na content, indicating that the nucleation mechanism may be not simply due to the formation of Na_3P phase. The solubility of Na atoms in eutectic Al and eutectic Si should be taken into consideration, as suggested in Reference 19. Following discussion will be made in terms of the remaining AlP phase, which can form AlP patches to nucleate Si.

As to the remaining AlP phase, it has been reported [6,27] that the Gibbs free energy (ΔG) of the Na_3P phase (−200 kJ/mol) is less than that of AlP phase (−115 kJ/mol), indicating that the Na_3P phase is thermodynamically more stable and must be preferentially formed. However, the less stable AlP phase is not fully transformed to the stable Na_3P phase because there is a competition between the stable and less stable compounds. The equilibrium reaction (AlP ↔ Al + P) determined the AlP available for the nucleation of eutectic Si.

Through the interaction between AlP and Na_3P phase (AlP + 3Na ↔ Na3P + Al), the activity of AlP varies greatly with respect to the original concentration. Furthermore, Na content may also affect the activity of AlP. The activity of AlP can be measured by the activity coefficient. The equilibrium fraction between the competing phases establishes itself by the formula [28,29]:

$$k_{AlP} = \frac{a_{AlP}}{x_{AlP}} = \frac{Activity\ of\ AlP}{Real\ concentration\ of\ AlP} \qquad [1]$$

where a_i and k_{AlP} are the activity and activity coefficient of AlP, respectively. This formula determines the remaining AlP which can form AlP patches to nucleate eutectic Si within the droplet. However, activity (a_i) and activity coefficient (k_{AlP}) are often not known for phosphide compounds. Thus, despite the presence of more stable phosphide compounds (*i.e.*, Na_3P phase), AlP patches may still be present. Their amount could be estimated if the thermodynamic data are known [6]. Their size or size distribution will be dependent on the adsorption kinetics such as a line tension and other factors [20]. This argument is fully consistent with the observed undercooling of entrained eutectic droplets in the present investigation, indicating that sufficient AlP is still available for the nucleation of eutectic Si despite the presence of the sufficient Na (160 ppm). Detecting AlP particle (in the center of Si particle) is extremely challenging, due to the very low P content (about 0.44 ppm), as listed in Table I. Although it is more likely to detect such type AlP particle with higher P contents (*e.g.* 10 ppm P or higher), the present investigation focuses on the case of low P contents. Further investigation on AlP particle is still required.

5. Conclusions

1. The adsorption of Na atoms was, for the first time, observed at an atomic scale. The adsorption of Na atoms was further proposed to occur at the intersection of multiple Si twins and along the $<112>_{Si}$ growth direction of Si, which provides a strong experimental support to the IIT growth mechanism and poisoning of the TPRE growth mechanism.

2. The adsorption of Na atoms within one monolayer can induce the IIT growth mechanism and poisoning of the TPRE growth mechanism, while the formation of round particle-like Na-rich clusters at the intersection of multiply Si twins and elongated rod-like Na-rich clusters along the $<112>_{Si}$ growth direction of Si can be attributed to the continuous solute segregation and entrapment of Al, Si, and Na atoms during continuous Si growth.

3. The adsorption of Na atoms was, for the first time, observed at the interface between eutectic Si and eutectic Al, which is believed to hinder the growth of eutectic Si and thereby affect its morphology.

4. 19 ppm Na addition results into a high-entrained eutectic undercooling. However, further increasing Na addition up to 160 ppm exerts no positive effects on the nucleation of eutectic Si. Instead a slight decrease of undercooling was observed. The formation of thermodynamic stable Na_3P phase was proposed to deteriorate the AlP potency in Al-Si alloys. However, the remaining AlP phase can still nucleate Si.

References

1. A. Pacz: US Patent No. 1387900, 1921.

2. Shu-Zu Lu and A. Hellawell: Metall. Trans. A, 1987, vol. 18, pp.1721-1733.

3. R.S. Wanger: Acta Metall., 1960, vol. 8, p. 57.

4. R.D. Hamilton and R.G. Seidensticker: J. Appl. Phys., 1960, vol. 31, p. 1165.

5. M.G. Day and A. Hellawell: Proc. R Soc. Lond A, 1968, vol. 305, pp. 473-491.

6. J.H. Li, M. Zarif, M. Albu, B. McKay, F. Hofer and P. Schumacher: Acta Mater., 2014, vol. 72, pp. 80-98.

7. J.H. Li, M. Zarif, G. Dehm and P.Schumacher: PHIL. Mag., 2012, vol. 92, pp. 3789-3805.

CrossRefGoogle Scholar

8. M. Zarif, B. McKay and P. Schumacher: Metall. Mater. Trans. A., 2011, vol. 42, pp. 1684-1691.

9. K. Nogita, H. Yasuda, K. Yoshida, K. Uesugi, A. Takeuchi, Y. Suzuki and A.K.Dahle: Scripta Mater., 2006, vol. 55, pp. 787-790.

10. K. Nogita, H. Yasuda, M. Yoshiya, S.D. McDonald, K. Uesugi, A. Takeuchi and Y. Suzuki: J. Alloys Compd., 2010, vol. 489, pp. 415-420.

11. M. Timpel, N. Wanderka, R. Schlesiger, T. Yamamoto, N. Lazarev, D. Isheim, G. Schmitz, S. Matsumura and J. Banhart: Acta Mater., 2012, vol. 60, pp. 3920-3928.

12. M. Timpel, N. Wanderka, R. Schlesiger, T. Yamamoto, D. Isheim, G. Schmitz, S. Matsumura and J. Banhart. Ultramicroscopy, 2013, vol. 132, pp. 216-221.

13. J. Barrirero, M. Engstler, N. Ghafoor, N. de Jonge, M. Odén and F. Mücklich:. Alloys Compd., 2014, vol. 611, pp. 410-421.

14. M. Faraji and L. Katgerman: Micron., 2010, vol. 41, pp. 554-559.

15. Q.Y. Liu, Q.C. Li and J.R. Zhang: Scripta Metall., 1988, vol. 22, pp. 789-791.

16. K. Kobayashi, P.H. Shingu and R. Ozaki: J. Materials Science., 1975, vol. 10, pp. 290-299.

17. H. Cho, H.C. Lee, K.H. Oh and A.K. Dahle: Metall. Mater. Trans. A., 2008, vol. 10, p.2435.

18. P.B. Crosley and L.F. Mondolfo: Modern Castings, 1966, vol. 49, p.63.

19. C.R. Ho and B. Cantor: J. Materials Science, 1995, vol. 30, pp. 1912-1920.

20. C.R. Ho and B. Cantor: Acta Metall. Mater., 1995, vol. 43, pp.3231-3246.

21. K. Thompson, D. Lawrence, D.J. Larson, J.D. Olson, T.F. Kelly and B. Gorman: Ultramicroscopy, 2007, vol.107, pp.131-139.

22. T.F. Kelly and M.K. Miller: Review of Scientific Instruments, 2007, vol. 78, p. 031101.

23. M.K. Miller: Atom Probe Tomography: Analysis at the Atomic Level. New York, Kluwer Academic/Plenum, 2000.

24. C. Oberdorfer, S.M. Eich and G. Schmitz: Ultramicroscopy, 2013, vol. 128, pp. 55-67.

25. J.H. Li, M. Albu, F. Hofer and P.Schumacher: Acta Mater., 2015, vol. 83, pp. 187-202.

26. L. Clapham and R.W. Smith: in Partitioning of Strontium Modifier to Individual Phases in Al-Si Eutectic, J. Beech and H. Jones, eds., Proc. 4th Decenn. Int. Conf. Solidif. Process, Sheffield, 1987.

27. M.E. Schlesinger: Chem. Rev., 2002, vol. 102, pp. 4267-4301.

28. DA Porter, KE Easterling, MY Sherif (2009) Phase Transformation in Metals and Alloys, 3rd ed., CRC Press, Boca Raton, FL.

29. E.B. Smith: Basic Chemical Thermodynamics, 4th ed., Oxford University Press, New York, 1990.

Paper V

Phase Selective Sample Preparation of Al-Si alloys for Atom Probe Tomography

J. Barrirero, M. Engstler, M. Odén, F. Mücklich

PAPER V

J. Barrirero, M. Engstler, M. Odén, F. Mücklich

Phase Selective Sample Preparation of Al-Si alloys for Atom Probe Tomography

Phasenselektive Probenpräparation von Al-Si-Legierungen für die Atomsondentomographie

Abstract

We present how the conventional focused ion beam (FIB) lift-out method can be modified to obtain phase selective specimens for atom probe tomography (APT). The modified method combines selective deep etching with site-specific lift-out using a micromanipulator in a FIB/SEM workstation. This method is used for phase-selective sample preparation in alloys with complex microstructures such as the coral- and plate-like silicon structures in the eutectic phase of Al-Si castings. The method proves to be both, practical and robust, with a high success rate of high-quality phase-specific APT specimens.

Kurzfassung

In dieser Arbeit wird gezeigt, wie das konventionelle Liftout-Verfahren mit fokussiertem Ionenstrahl (FIB) so verändert werden kann, dass phasenselektive Proben, die für die Atomsondentomographie (APT, *Atom Probe Tomography*) geeignet sind, hergestellt werden können. Das modifizierte Verfahren kombiniert die selektive Tiefenätzung mit einem ortsspezifischen Liftout unter Verwendung eines Mikromanipulators in einer FIB/REM-Workstation. Dieses Verfahren wird für die phasenselektive Probenvorbereitung bei Legierungen mit komplexen Gefügen verwendet wie z. B. den korallenartigen und plattenartigen Siliziumstrukturen in der eutektischen Phase von Al-Si-Gussteilen. Das Verfahren erweist sich als zweckmäßig und zuverlässig aufgrund der hohen Erfolgsrate bei phasenspezifischen APT-Proben von hoher Qualität.

Authors:

Jenifer Barrirero, Michael Engstler, Frank Mücklich   Chair of functional materials, Department of materials science, Saarland University, D-66123 Saarbrücken, Germany; e-mail: j.barrirero@mx.uni-saarland.de
Magnus Odén   Nanostructured Materials, Department of Physics, Chemistry and Biology (IFM), Linköping University, SE-581 83 Linköping, Sweden

1. Introduction

Atom probe tomography (APT) is a powerful technique that provides three-dimensional analytical mapping of materials with atomic resolution [1]. To be able to reach such a high resolution, only limited volumes can be measured. Specimens have a sharp needle-shape with a diameter in the order of 100 nm to enable field evaporation. Since the feature of interest must be positioned near the apex region of the specimen, sample preparation is often a critical and challenging step [2].

Two commonly used methods for sample preparation for APT are electrochemical polishing and focused ion beam (FIB) milling. Electrochemical polishing has the advantage of being a rather simple technique that does not require expensive and sophisticated devices. However, the material investigated should have sufficient conductivity, it is not possible to prepare site-specific specimens, and samples with more than one phase may display selective etching causing an uneven removal of material.

FIB assisted methods can be more time consuming and challenging but any material can be prepared and it is suitable for site-specific preparation. In the commonly used lift-out technique, a triangular wedge is cut out, lifted with an in-situ manipulator, transferred and attached to pre-fabricated posts to be thinned to the final needle shape [3]. From one lift-out approximately 20 µm long, 6 to 8 specimens can be prepared. For example, this method allows for preparing surface samples of coatings or choosing the region of interest, such as a particular grain in an alloy. The challenge arises when the phase of interest is far smaller than the size of the lift-out or

1. Einleitung

Die Atomsondentomographie (APT) ist ein leistungsstarkes Verfahren, das zur dreidimensionalen analytischen Darstellung von Werkstoffen mit atomarer Auflösung dient [1]. Um eine solch hohe Auflösung erreichen zu können, können nur begrenzte Volumen gemessen werden. Die Proben haben eine spitze Nadelform mit einem Durchmesser in der Größenordnung von 100 nm, um Feldverdampfung zu ermöglichen. Da der Bereich, der von Interesse ist, im vorderen Bereich der Probenspitze platziert werden muss, erweist sich die Probenvorbereitung oft als anspruchsvoller und kritischer Vorgang [2].

Bei APT gibt es zwei weitverbreitete Methoden für die Probenpräparation: Elektrochemisches Polieren und Ionendünnen mittels FIB. Der Vorteil des elektrochemischen Polierens besteht darin, dass es sich um eine relativ einfache Methode handelt, für die keine teuren und anspruchsvollen Geräte notwendig sind. Jedoch sollte der zu untersuchende Werkstoff eine ausreichend hohe Leitfähigkeit besitzen. Das Herstellen von ortsspezifischen Proben ist nicht möglich und bei Proben mit mehr als einer Phase könnte es zur selektiven Ätzung kommen, was zu einem ungleichmäßigen Materialabtrag führt.

FIB-gestützte Methoden können sich als zeitintensiver und schwieriger erweisen, jedoch können aus jedem Werkstoff Proben hergestellt werden und die Methode eignet sich auch für die ortsspezifische Präparation. Bei der häufig verwendeten Liftout-Methode wird ein dreieckiger Keil ausgeschnitten und mit einem in-situ-Manipulator herausgehoben. Danach erfolgt der Transfer und die Anbringung an einem vorgefertigten Träger und schließlich das Dünnen der Probe bis zur endgültigen Nadelform [3]. Aus einem Liftout mit einer Länge von etwa 20 µm können 6 bis 8 Proben präpariert werden. Mit dieser Methode können zum Beispiel Oberflächenproben von Beschichtungen präpariert oder ein Bereich ausgewählt werden,

when the three-dimensional (3D) structure of the phase is difficult to predict from a 2D-section.

In this work, we show an alternative for phase-selective sample preparation in the eutectic phase of Al-Si casting alloys. This eutectic phase consists of hard and brittle Si plates in a ductile Al matrix. To avoid cracking along the Si plates and to increase the overall ductility of the alloy, the morphology of the eutectic Si phase can be modified to a coral-like structure instead of a plate-like one [4]. This is achieved by adding low concentration of certain elements which cluster in the Si phase and cause a change in the growth mechanism during solidification such that rounded Si branches form [5, 6]. We show here a practical solution for sample preparation in order to increase the success rate and the volume of data acquired by APT. Although this paper is concentrated in this particular alloy, the method used here can be applied to a wide range of materials with similar microstructures.

2. Method of Phase-Selective Sample Preparation

The microstructure of alloys is frequently intricate and contains several phases. In the case of Al-Si alloys, the eutectic microstructure is composed by α-Al and Si. These two phases cannot be electropolished for APT sample preparation, because there is no electrolyte able to polish both phases with a similar rate. As a result, the specimens present an irregular surface and lack of overall robustness and stability. Instead, FIB sample preparation is needed for this eutectic phase.

der von Interesse ist, wie etwa ein bestimmtes Korn in einer Legierung. Herausfordernd wird es, wenn die interessante Phase weit kleiner als die Größe des Liftouts ist oder wenn sich die dreidimensionale (3D) Struktur der Phase, ausgehend von einem 2D-Schnitt, nur schwer vorhersagen lässt.

In dieser Arbeit wird eine Alternative für die phasenselektive Probenpräparation der eutektischen Phase von Al-Si-Gusslegierungen präsentiert. Diese eutektische Phase besteht aus harten und spröden Si-Platten in einer duktilen Al-Matrix. Um ein Brechen entlang der Si-Platten zu vermeiden und um die allgemeine Duktilität der Legierung zu erhöhen, kann die Morphologie der eutektischen Si-Phase zu einer korallenartigen statt einer plattenförmigen Struktur veredelt werden [4]. Dies wird durch die Zugabe geringer Konzentrationen bestimmter Elemente erreicht, die in der Si-Phase Cluster bilden und eine Änderung des Wachstumsmechanismus während der Erstarrung hervorrufen, so dass sich rundliche Si-Zweige bilden [5, 6]. In dieser Arbeit wird eine praktische Lösung für die Probenpräparation vorgestellt, mit der eine höhere Erfolgsrate und eine größere Datenmenge mit Hilfe von APT erreicht werden. Obwohl sich diese Arbeit auf eine bestimmte Legierung konzentriert, kann das vorgestellte Verfahren auf eine Vielzahl von Werkstoffen mit ähnlichen Gefügen angewandt werden.

2. Methode der phasenselektiven Probenpräparation

Das Gefüge von Legierungen ist häufig kompliziert und enthält mehrere Phasen. Im Fall von Al-Si-Legierungen besteht das eutektische Gefüge aus α-Al und Si. Diese beiden Phasen können für die APT-Probenpräparation nicht elektrochemisch poliert werden, da kein Elektrolyt existiert, der beide Phasen mit einer ähnlichen Rate polieren kann. Daher weisen die Proben eine unregelmäßige Oberfläche auf und es fehlt ihnen allgemein an Robustheit und Stabilität. Für diese eutektische Phase ist stattdessen die Probenpräparation mittels FIB notwendig.

When the intention of the study is to elucidate the mechanisms of the Si growth, the sample preparation should yield as much Si phase as possible within the APT specimen. Volumes reconstructed by APT are in the order of $\sim (100\ nm)^3$. A large fraction of Si-phase gives a good representation and, in order to maximize the reliability of the statistics extracted from the reconstruction, the amount of Si-phase should be maximized. In this context and recognizing that Si in the eutectic phase grows in an Al matrix and only represents around 11 % of the eutectic phase volume, the selection of a 100 nm Si specimen from a 20 µm long FIB lift out is nontrivial. A majority of the specimens will be the Al phase if one works blindly. Even if one aims for the Si phase by visual inspection from the surface, the complex 3D morphology of the Si phase in the third dimension remains unknown and the chances of extracting specimens containing mainly Si are low.

Apart from the challenge of a site-specific preparation in FIB, there is an additional challenge during APT measurement. APT is a technique based on the removal of surface atoms induced by field evaporation. In this process, an ion needs to overcome an energy barrier reduced by applying an electric field and by thermal activation [7]. Müller [8] described the activation energy for field evaporation by a field dependent energy barrier characteristic for each chemical element. Based on this model, the predicted evaporation fields for Al and Si are 19 V/nm and 33 V/nm, respectively. The large difference between the fields required for evaporation, induce trajectory aberrations of the ions. These aberrations can cause apparent density fluctuations [9] and / or preferential retention [7, 10]. The best approach to minimize such aberrations is to prepare

Liegt das Ziel einer Untersuchung in der Beschreibung des Wachstumsmechanismus von Si, sollte die Probenpräparation so viel Si-Phase wie möglich in der APT-Probe erzielen. Volumen, die mittels APT rekonstruiert wurden, liegen in der Größenordnung von $\sim (100\ nm)^3$. Durch einen großen Anteil an Si-Phase wird eine gute Darstellung erzielt und, um eine hohe statistische Aussagekraft der Werte, die im Zuge der Rekonstruktion gewonnen werden, zu erreichen, sollte die Menge an Si-Phase maximiert werden. In diesem Kontext und in Anbetracht dessen, dass Si in der eutektischen Phase in einer Al-Matrix wächst und nur etwa 11 % des eutektischen Phasenvolumens darstellt, ist die Auswahl einer 100 nm langen Si-Probe aus einem 20 µm langen FIB-Liftout nicht-trivial. Eine Mehrheit der Proben wird die Al-Phase enthalten, falls nicht gezielt gearbeitet wird. Sogar wenn durch visuelle Begutachtung der Oberfläche die Si-Phase anvisiert wird, bleibt die komplexe 3D-Morphologie der Si-Phase in der dritten Dimension unbekannt und die Wahrscheinlichkeit, Proben zu entnehmen, die hauptsächlich Si enthalten, ist gering.

Abgesehen von der Herausforderung einer ortsspezifischen Präparation mittels FIB gibt es eine weitere Hürde während der APT-Messung. APT ist ein Verfahren, das auf dem durch Feldverdampfung induzierten Abtrag von Oberflächenatomen beruht. Bei diesem Vorgang muss ein Ion eine Energieschwelle überwinden, die durch Anlegen eines elektrischen Feldes und durch thermische Aktivierung gesenkt wird [7]. Müller [8] beschreibt die Aktivierungsenergie für die Feldverdampfung als eine feldabhängige Energieschwelle, die für jedes chemische Element charakteristisch ist. Nach diesem Modell betragen die prognostizierten Verdampfungsfelder für Al und Si 19 V/nm bzw. 33 V/nm. Die große Differenz zwischen den Feldern, die für die Feldverdampfung notwendig sind, rufen Abweichungen in der Flugbahn der Ionen hervor. Diese Abweichungen können scheinbare Dichteschwankungen [9] und / oder Vorzugs-

specimens containing only one phase, in this case, Si.

Samples

High purity Si and Al (Al5N5) were melted to produce unmodified Al-7 wt.% Si and Sr-modified alloys with 150 wt. ppm Sr by directional solidification in a Bridgman furnace. The samples were fabricated with a cooling rate of 0.25 K/s at a temperature gradient of 15 K/mm. Sr was added from an aluminium master alloy containing 15 wt.% Sr. Chemical compositions were determined by optical emission spectrometry. A cross-section of each sample was hot embedded in a conductive resin for SEM and mirror polished.

Deep Etching

In order to free the eutectic Si, the α-Al matrix was deep etched. A three steps procedure was used:

- Deep etching of the α-Al to satisfactorily reveal the Si phase with a 2.5N (5M) NaOH aqueous solution for 15 min in an ultrasonic bath at room temperature.

- Chemical neutralization to stop the etching process using a HCl 0.005N aqueous solution for 2 min in an ultrasonic bath.

- Rinsing the samples subsequently in water and iso-propanol.

The etched structure can be seen in Figs. 1 (a–c) and 2 (a–c).

FIB / SEM

The embedded samples were further prepared in a dual-beam focused ion beam / scanning electron microscopy workstation (FIB/SEM) (Helios NanoLab 600™, FEI) equipped with a OmniProbe 100 microma-

retention [7, 10] verursachen. Der beste Ansatz zur Minimierung solcher Abweichungen liegt in der Präparation von Proben, die nur eine Phase enthalten, im vorliegenden Falle Si.

Proben

Die Herstellung von unveredelten Legierungen mit Al-7 Gew.-%Si und von Sr-veredelten Legierungen mit 150 Gew.-ppm Sr erfolgte durch Aufschmelzen von hochreinem Si und Al (Al5N5) und durch gerichtete Erstarrung in einem Bridgman-Ofen. Die Proben wurden mit einer Abkühlgeschwindigkeit von 0,25 K/s bei einem Temperaturgradienten von 15 K/mm hergestellt. Sr stammt aus einer Aluminium-Vorlegierung mit 15 Gew.-% Sr. Die chemischen Zusammensetzungen wurden mit Hilfe der optischen Emissionsspektrometrie ermittelt. Ein Schliff jeder Probe wurde in leitfähigem Harz warmeingebettet und für die Untersuchung im REM hochglanzpoliert.

Tiefenätzung

Um das eutektische Si freizulegen, wurde die α-Al-Matrix tiefgeätzt. Hierzu wurde ein dreistufiges Verfahren eingesetzt:

- Tiefenätzung des α-Al bis zur zufriedenstellenden Sichtbarmachung der Si-Phase mit 2,5N (5M) NaOH in wässriger Lösung über 15 min in einem Ultraschallbad bei Raumtemperatur.

- Chemisches Neutralisieren zum Abbruch des Ätzvorgangs mittels HCl 0,005N in wässriger Lösung über 2 min im Ultraschallbad.

- anschließendes Abspülen der Proben in Wasser und Isopropanol.

Das geätzte Gefüge ist in Bild 1 (a–c) und 2 (a–c) zu sehen.

FIB / REM

Die eingebetteten Proben wurden in einer Workstation mit dualem fokussierten Ionenstrahl / Rasterelektronenmikroskop (FIB/REM) (Helios NanoLab 600™, FEI) und einem OmniProbe 100 Micromanipulator (Oxford Instruments) weiter
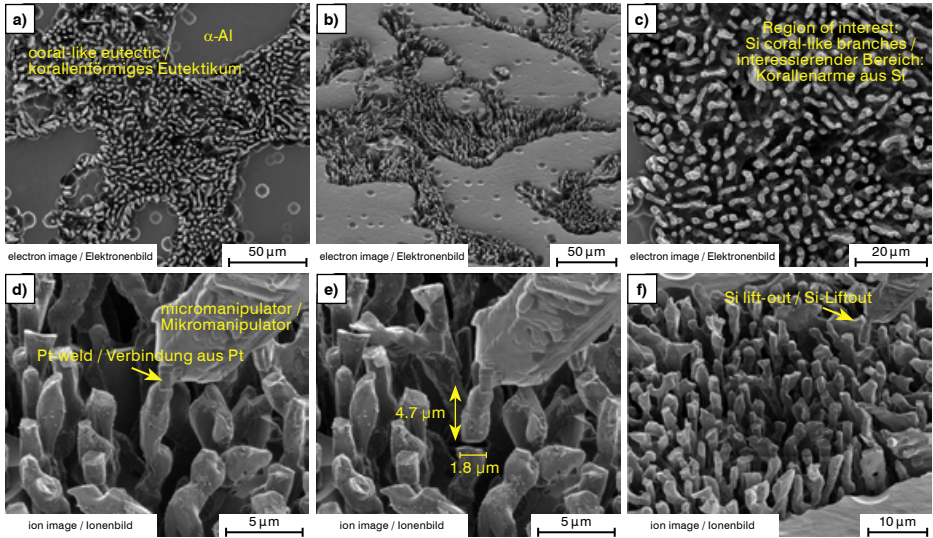
Figs. 1 a to f: *Phase selective sample preparation of Si in a Sr modified Al-Si alloy: a), b) 0° and 52° tilted overviews of a deep etched sample. α-Al dendrites and eutectic Si branches can be seen; c) Top-view of free standing eutectic Si branches; d) Micromanipulator attached by Pt deposition to a Si branch oriented perpendicular to the surface of the sample. The total length of the branches before separation is larger than 5 µm; e) Si branch after separation by cutting with Ga ion-beam at 0° tilt angle; f) Lift-out of the Si branch by retracting the micromanipulator.*

Bilder 1 a bis f: *Phasenselektive Probenpräparation von Si bei einer Sr-veredelten Al-Si-Legierung: a), b) um 0° und 52° geneigte Übersichten der tiefgeätzten Probe. α-Al-Dendrite und eutektische Si-Zweige sind zu erkennen; c) Draufsicht: freistehende eutektische Si-Zweige; d) Durch Pt-Deposition an einen Si-Zweig angebrachter Mikromanipulator; der Zweig ist senkrecht zur Probenoberfläche ausgerichtet. Die Gesamtlänge der Zweige vor dem Abtrennen beträgt mehr als 5 µm; e) Si-Zweig nach dem Abtrennen mittels Ga-Ionenstrahl in einem Neigungswinkel von 0°; f) Liftout des Si-Zweigs durch Zurückziehen des Mikromanipulators.*

nipulator (Oxford Instruments). Please note that images are recorded by detecting either secondary electron or ions. The two image types are recorded using different geometries (52° rotation around the sample surface normal) of gun, sample, and detector, which makes the two types of images look mirrored, cf. Fig. 2 c and d.

Modified Al – 7 wt.% Si with 150 wt-ppm Sr

The Sr modified Si microstructure is composed of branches with circular cross-section. Fig. 1 shows branches with a diameter of 1–2 µm. Consequently, each APT speci-

präpariert. Es ist zu beachten, dass die Bildgebung auf dem Einfang von Sekundärelektronen oder Ionen basiert. Beide Bildarten werden mit Hilfe verschiedener Geometrien (52° Rotation um die Normale der Probenoberfläche) der Teilchenquelle, Probe und des Detektors erzielt. Die beiden Bildarten liefern dabei spiegelverkehrte Ergebnisse, vgl. Bild 2 c und d.

Veredelte Legierung Al – 7 Gew.-% Si mit 150 Gew.-ppm Sr

Das Sr-veredelte Si-Gefüge besteht aus Zweigen mit rundem Querschnitt. Bild 1 zeigt Zweige mit einem Durchmesser von 1–2 µm. Folglich entspricht jede APT-Probe einem
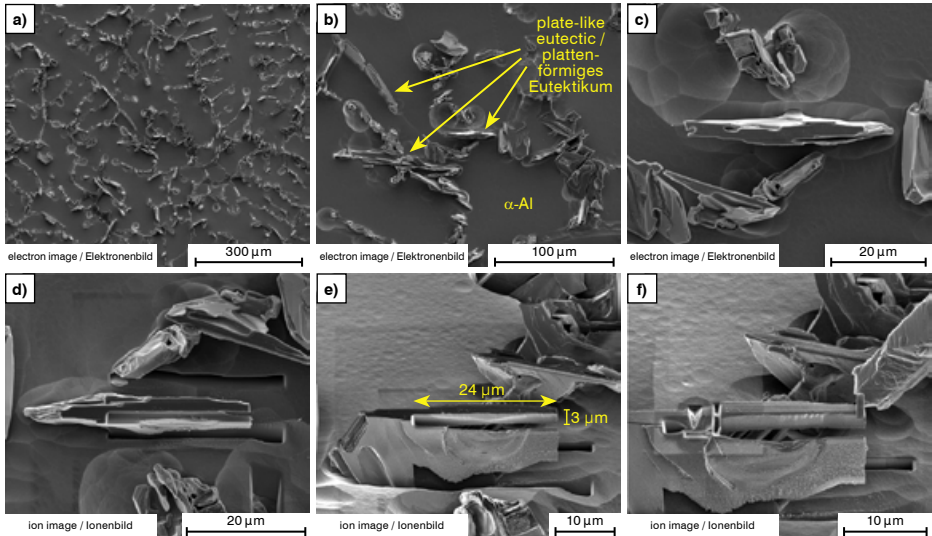
Figs. 2 a to f: *Phase selective sample preparation of Si in an unmodified Al-Si alloy: a), b) Overview of a deep etched sample; c), d) Horizontal Si plate chosen for lift out at the center of the image; d) ,e) 0° and 52° tilted views of the cut out of the Si wedge from both sides forming an inverted equilateral triangle; f) Welded micromanipulator by Pt deposition and separation by cutting with Ga ion-beam at 0° tilt angle.*

Bilder 2 a bis f: *Phasenselektive Probenpräparation von Si bei einer unveredelten Al-Si-Legierung: a), b) Übersicht der tiefgeätzten Probe; c), d) Für den Liftout ausgewählte horizontale Si-Platte in der Bildmitte; d), e) um 0° und 52° geneigte Ansicht des von beiden Seiten ausgeschnittenen Si-Keils in der Form eines umgedrehten gleichseitigen Dreiecks; f) Durch Pt-Deposition angeschweißter Mikromanipulator und Abtrennen mittels Ga-Ionenstrahl in einem Neigungswinkel von 0°.*

men corresponds to a separate lift-out. This is different from the conventional lift-out technique, for which 6–8 specimens can be lifted out at once. The disadvantage of a longer preparation time is compensated by the improved accuracy of choosing a region of interest (ROI).

1. Selecting a region of interest (ROI)

The deep etched sample enables the operator to select Si branches that have convenient perpendicular orientation to the surface. Such branches are advisable for an easier subsequent attachment to a prefabricated post and annular thinning. Besides, the operator is able to choose a region of particular interest for the analysis, for instance the place where

einzelnen Liftout. Hierin liegt der Unterschied zur konventionellen Liftout-Methode, bei der 6–8 Proben auf einmal entnommen werden können. Der Nachteil einer längeren Vorbereitungszeit wird durch die höhere Präzision bei der Auswahl einer Region of Interest (ROI) ausgeglichen.

1. Auswahl einer Region of Interest (ROI)

Die tiefgeätzte Probe ermöglicht dem Bediener die Auswahl von geeigneten Si-Zweigen mit einer Orientierung senkrecht zur Oberfläche. Solche Zweige sind empfehlenswert, da sie die anschließende Anbringung auf dem vorgefertigten Träger und das ringförmige Dünnen erleichtern. Außerdem kann der Bediener einen Bereich auswählen, der für die Untersuchung

a branch bends. By tilting the sample in different directions an even better understanding of the Si morphology can be obtained such that the choice of ROI is well founded.

2. Electron-induced Pt deposition

The next step is to protect the surface of the chosen region by electron induced sputtering of Pt. This step is necessary if the studied material is susceptible to Ga implantation during the thinning process or if the branches are too short then additional height can be provided by a Pt deposit. In the example shown in this paper, Pt deposition was not needed. Ga implantation is negligible in Si and the length of the branches is larger than 4 µm (Fig. 1).

3. Coarse milling of the region

If the selected branch is densely packed within the rest of the Si structure, a rough annular milling with the sample positioned perpendicular to the ion beam (52° tilted in the Helios Nanolab, FEI) is recommended. This coarse milling provides space around the ROI for the subsequent cutting step.

Since the Si branch will be transferred and attached to a post, it is important to fit the diameter of the lift-out to the diameter of the post. This facilitates the welding. In cases when the selected region is too thick, a thinning step it is advisable.

4. Attachment to the micromanipulator

Fig. 1(d) shows the attachment of the ROI to the micromanipulator by ion induced Pt deposition. This is done at 0° tilt angle and intending to affect a region

von besonderem Interesse ist, zum Beispiel die Stelle, an der ein Zweig eine Biegung aufweist. Durch das Neigen der Probe in verschiedene Richtungen kann ein noch besseres Verständnis der Si-Morphologie erreicht werden, so dass es sich bei Auswahl der ROI um eine fundierte Entscheidung handelt.

2. Elektroneninduzierte Pt-Deposition

Der nächste Schritt besteht darin, die Oberfläche des ausgewählten Bereichs durch elektroneninduziertes Sputtern von Pt zu schützen. Dieser Schritt ist notwendig, wenn der zu untersuchende Werkstoff anfällig für die Einbringung von Ga während des Dünnens ist oder wenn die Zweige zu kurz sind und durch die Deposition von Pt eine ausreichende Länge erzielt werden kann. Für das in dieser Arbeit gezeigte Beispiel war eine Deposition von Pt nicht notwendig. Die Einbringung von Ga in Si ist vernachlässigbar und die Länge der Zweige liegt bei über 4 µm (Bild 1).

3. Grobes Dünnen der Region

Ist der ausgewählte Zweig innerhalb des Si-Gefüges dicht gepackt, wird ein grobes ringförmiges Dünnen der Probe empfohlen, die senkrecht zum Ionenstrahl (52° geneigt innerhalb der Helios Nanolab, FEI) ausgerichtet ist. Für den anschließenden Schneidvorgang schafft dieses grobe Dünnen um die ROI herum den erforderlichen Raum.

Da der Si-Zweig auf einen Träger transferiert und an diesem befestigt wird, ist es wichtig, den Durchmesser des Liftouts an den Durchmesser des Trägers anzupassen. Dies erleichtert das Anschweißen. Für den Fall, dass der ausgewählte Bereich zu dick ist, ist ein Dünnungsvorgang ratsam.

4. Befestigung am Mikromanipulator

Bild 1(d) zeigt die Befestigung der ROI am Mikromanipulator durch ioneninduzierte Pt-Deposition. Dies geschieht in einem Neigungswinkel von 0°und dient dazu, nur

as small as possible of the sample. The top part of the Si branch which is in contact with the weld will be sacrificed when the sample is separated from the micromanipulator.

5. Separation of the Si-branch from the deep etched sample

Fig. 1(e) shows how the Si branch is separated from the deep etched sample. This cut is done with ion bombardment in a line pattern or, eventually, a rectangular pattern with a high aspect ratio. Since this cut is performed at 0°, the cutting Ga ion beam will be 52° tilted with respect to the surface of the sample. This has to be taken into consideration when placing the cutting pattern in order to ensure the separation of the branch. It is advisable that the length of the extracted branch is not smaller than 3 µm to obtain a final APT specimen originating far enough from the Pt-deposit.

6. Transfer the Si-branch to a post on a holder suitable for APT

The transfer process is shown in Fig. 3(a). The Si branch needs to be attached from both sides with enough material to guarantee robustness during the APT measurement (Fig. 3(b)). At this point, it is important to inspect the material for possible cracks or defects that can result from the etching process and might weaken the material and cause early fracture during APT measurement.

7. Thinning to reach the final diameter

The annular milling process is the same as the one used for conventional thinning, while keeping in mind that milling of the Pt-attachments that connects the specimen to the post should be avoided to ensure sufficient stability. Fig. 3 (c) and (d) show the APT specimen after thinning.

einen möglichst kleinen Bereich der Probe zu beanspruchen. Der obere Teil des Si-Zweigs, der in Kontakt mit der Schweißnaht ist, wird geopfert, wenn die Probe vom Mikromanipulator abgetrennt wird.

5. Abtrennen des Si-Zweigs von der tiefgeätzten Probe

Bild 1(e) zeigt, wie der Si-Zweig von der tiefgeätzten Probe abgetrennt wird. Dieser Schnitt erfolgt durch Ionenbeschuss in einem linienförmigen Muster oder später in einem rechteckigen Muster mit großem Seitenverhältnis. Da der Schnitt in einem Winkel von 0° durchgeführt wird, ist der schneidende Ga-Ionenstrahl im Verhältnis zur Probenoberfläche um 52° geneigt. Dies muss berücksichtigt werden, wenn das Schnittmuster angelegt wird, um die Abtrennung des Zweigs zu gewährleisten. Es wird empfohlen, dass die Länge des entnommenen Zweigs nicht kleiner als 3 µm ist, sodass die finale APT-Probe aus einem Bereich stammt, der weit genug von der Pt-Deposition entfernt ist.

6. Transfer des Si-Zweigs auf einen APT-geeigneten Halter

Der Übertragungsprozess wird in Bild 3(a) gezeigt. Der Si-Zweig muss mit genügend Material von beiden Seiten befestigt werden, um dessen Stabilität während der APT-Messung zu gewährleisten (Bild 3(b)). Bei diesem Schritt ist es wichtig, den Werkstoff auf Risse oder Fehler zu prüfen, die möglicherweise durch den Ätzvorgang verursacht wurden, und die den Werkstoff schwächen und zum frühzeitigen Bruch während der APT-Messung führen können.

7. Dünnen bis zum finalen Durchmesser

Der Vorgang des ringförmigen Dünnens ist identisch mit dem konventionellen Dünnen; hier ist zu beachten, dass das Dünnen der Pt-Verbindungen, die die Probe am Halter befestigen, vermieden werden sollte, um eine ausreichende Stabilität zu gewährleisten. Bild 3 (c) und (d) zeigen die APT-Probe nach dem Dünnen.
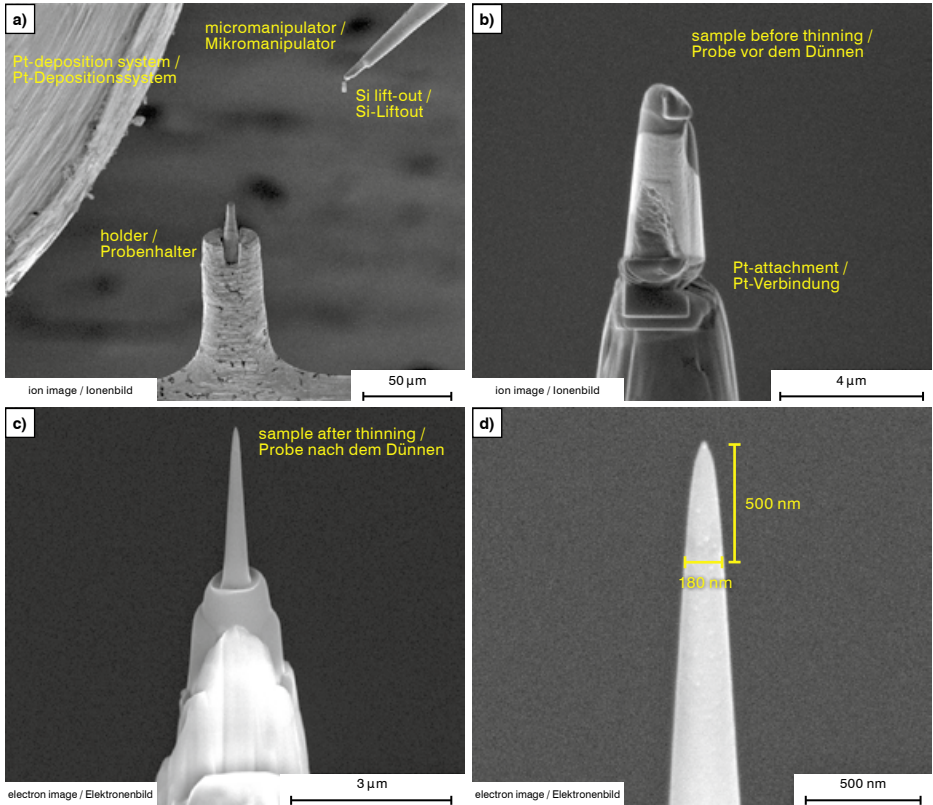
Figs. 3a to d: *Sample transfer and final preparation: a) Modified Si-branch transferred in a micromanipulator to a suitable APT holder; b) Si specimen attached by Pt-deposition before annular milling; c) Thinned APT specimen; d) Inset of the specimen ready to run in APT.*

Bilder 3a bis d: *Probenübertragung und finale Präparation: a) Veredelter Si-Zweig beim Transfer auf einen geeigneten APT-Halter mit einem Mikromanipulator; b) Durch Pt-Deposition befestigte Si-Probe vor dem ringförmigen Dünnen; c) Gedünnte APT-Probe; d) Teil der Nadelspitze der Probe für den Einsatz von APT.*

Unmodified Al – 7 wt.% Si alloy

The unmodified eutectic Si phase shows a structure containing relatively large Si-plates (Fig. 2(a–c)) that makes the preparation fairly simple as compared to the previous case (modified alloy). Similarly to the conventional preparation method described in [3], the operator can lift out material for 6–8 specimens at once.

Unveredelte Legierung Al – 7 Gew.-% Si

Die unveredelte eutektische Si-Phase weist eine Struktur mit relativ großen Si-Platten auf (Bild 2(a–c)), die die Präparation im Vergleich zum vorherigen Fall (veredelte Legierung) recht einfach macht. Ähnlich wie beim konventionellen Präparationsverfahren, das in [3] beschrieben wurde, kann der Bediener Material für 6–8 Proben gleichzeitig herausheben.

1. Choice of the region of interest

   The most convenient plates for the preparation are those oriented perpendicularly to the surface, length larger than 20 µm, thickness and depth of at least 2 and 5 µm, respectively. Rotate the sample to align the Si plate horizontally from a top view (Fig. 2(b,c)).

2. Electron induced Pt deposition

   Similarly as the previous case, a protective Pt layer can be applied depending on the sensitivity of the sample to Ga implantation. In this case, no Pt was deposited on the Si Plate.

3. Milling of the sides in preparation for lift out

   Just as in the conventional lift-out, the sample is tilted 22° with respect the surface, so that the Ga ion beam cuts with an orientation of 30° to the surface (52° – 22° = 30°). Rotate the sample 180° (tilt 22°) and cut from the other side so that the lift-out has the well-known "Toblerone" shape (inverted equilateral triangle) (Fig. 2(d, e)). Since there is no bulk material surrounding the Si plate, this process is faster than in conventional preparation and it has not only the advantage of phase selective preparation, but also the possibility of a clear visualization of the cutting process during milling. If the patterns are positioned at one of the edges of the plate, the final wedge for lift out is free from one side and one step is spared (Fig. 2(e)).

4. Welding of the sample to the manipulator

   Fig. 2(f) shows the manipulator to the right side in the ion image. The manipulator is welded to the wedge by ion induced Pt-deposition with the sample at 0° tilt angle.

1. Auswahl der Region of Interest

   Für die Präparation eignen sich am besten solche Platten, die senkrecht zur Oberfläche ausgerichtet sind, und die eine Länge von mehr als 20 µm und eine Dicke bzw. Tiefe von mindestens 2 bzw. 5 µm aufweisen. Die Probe wird dann gedreht, um die Si-Platte horizontal zur Draufsicht (Bild 2(b,c)) auszurichten.

2. Elektroneninduzierte Pt-Deposition

   Ähnlich wie beim vorherigen Fall kann eine Schutzschicht aus Pt aufgebracht werden, je nach Anfälligkeit die Probe für eine Einbringung von Ga. In diesem Fall wurde kein Pt auf der Si-Platte aufgebracht.

3. Dünnen der Seiten als Vorbereitung für den Liftout

   Wie beim konventionellen Liftout ist die Probe im Verhältnis zur Oberfläche um 22° geneigt, so dass der Ga-Ionenstrahl mit einer Ausrichtung von 30° zur Oberfläche (52° – 22° = 30°) schneidet. Die Probe wird dann um 180° (Neigung 22°) gedreht und von der anderen Seite geschnitten, so dass der Liftout der allgemein bekannte „Toblerone"-Form (umgekehrtes gleichseitiges Dreieck) aufweist (Bild 2(d, e)). Da kein Vollmaterial um die Si-Platte herum existiert, ist dieser Vorgang schneller als bei der konventionellen Präparation und bietet nicht nur den Vorteil der phasenselektiven Präparation, sondern auch die Möglichkeit einer visuellen Überwachung des Schneidvorgangs während des Dünnens. Wenn die Muster an einer der Kanten der Platte positioniert werden, ist der finale Keil für den Liftout von einer Seite frei und ein Schritt wird eingespart (Bild 2(e)).

4. Befestigen der Probe am Manipulator

   Bild 2(f) zeigt den Manipulator auf der rechten Seite des Ionenbildes. Der Manipulator wurde durch ioneninduzierte Pt-Deposition bei einer Probenneigung von 0° mit dem Keil verschweißt.

5. Separation of the wedge form the deep etched sample

   The wedge of material is separated from the sample by cutting the left side of the lift out with a rectangular pattern with the sample at 0° tilt angle (Fig. 2(f)).

6. Transfer of the wedge to a post in a holder suitable for APT

   Six to eight APT-specimens can be prepared from the ~20 µm long wedge. Sections, ~2 µm long, are welded and separated from the wedge until the whole wedge is consumed. Welding from both sides is needed to stabilize the specimens to the post.

7. Thinning

   Regular thinning of the specimens to reach a final diameter of ~100 nm.

3. Outcome and Discussion

The use of this method for phase selective sample preparation gave nearly 100 % success rate and high yield during APT measurements. Artefacts due to the large difference in evaporation field between Al and Si were almost completely eliminated. Fig. 4 (a) and (b) show examples of the eutectic Si-phase present in Sr-modified and unmodified alloys, respectively. Al and Sr represent less than 1 at.% of the total number of atoms in the specimen. Thus, field evaporation artefacts are confined to small regions.

Fig. 4 (a) shows Al and Sr clustering together at crystallographic defects such as nanotwins and stacking faults in the Si phase. The addition of Sr, similarly as the addition of other elements such as Na or Eu, induce the formation of ternary compound clusters at the solidification front of the eutectic phase in these alloys. These pre-nucleation clusters formed at the Si

5. Herausheben des Keils aus der tiefgeätzten Probe

   Der Materialkeil wird aus der Probe durch Schneiden der linken Seite des Liftouts mit einem rechteckigen Muster und einem Neigungswinkel der Probe von 0° (Bild 2(f)) herausgetrennt.

6. Transfer des Keils auf einen Träger in einem APT-geeigneten Halter

   Sechs bis acht APT-Proben können aus einem ~20 µm langen Keil präpariert werden. Abschnitte von ~2 µm Länge werden verschweißt und aus dem Keil herausgetrennt, bis der gesamte Keil aufgebraucht ist. Ein Anschweißen von beiden Seiten ist notwendig, um die Probe auf dem Halter stabil zu befestigen.

7. Dünnen

   Gleichmäßiges Dünnen der Proben bis zu einem finalen Durchmesser von ~100 nm.

3. Ergebnis und Diskussion

Der Einsatz dieses Verfahrens für die phasenselektive Probenpräparation erzielte eine fast 100 %-ige Erfolgsquote und eine hohe Ausbeute bei den APT-Messungen. Artefakte, bedingt durch die große Differenz der Verdampfungsfelder bei Al und Si, wurden fast vollständig beseitigt. Bild 4 (a) und (b) zeigen Beispiele der eutektischen Si-Phase, wie sie in den Sr-veredelten bzw. unveredelten Legierungen vorliegt. Al und Sr stellen weniger als 1 At.-% der Gesamtzahl der Atome in der Probe dar. Somit sind Artefakte der Feldverdampfung auf nur kleine Bereiche beschränkt.

Bild 4 (a) zeigt Al und Sr, die an kristallographischen Defekten, z. B. Nanozwillinge und Stapelfehler in der Si-Phase, Cluster bilden. Die Zugabe von Sr, ähnlich wie die Zugabe anderer Elemente wie Na oder Eu, induzieren die Bildung von ternären Clustern an der Erstarrungsfront der eutektischen Phase bei diesen Legierungen. Diese Cluster, die eine Vorstufe der Keimbildung darstellen, entstanden an der Fest-Flüssig-Grenz-
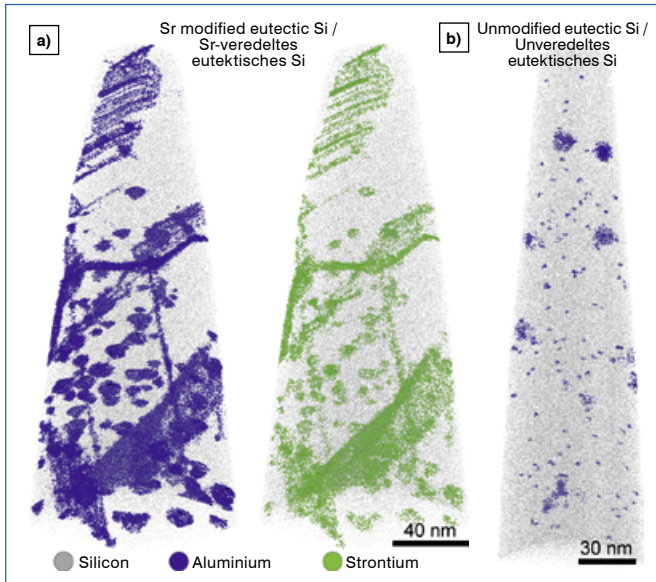
Figs. 4a and b: Atom probe tomography (APT) atomic maps of the Si eutectic phase in Al-Si alloys: a) Sr-modified Si phase showing Al and Sr clustering in crystallographic defects such as nanotwins and stacking faults; b) Unmodified Si phase showing rounded Al clusters only.

Bilder 4a und b: Atomare Analyse der eutektischen Phase Si in Al-Si-Legierungen mittels Atomsondentomographie (APT): a) Sr-veredelte Si-Phase mit Al und Sr, die Cluster an kristallographischen Defekten, z.B. Nanozwillinge und Stapelfehler, bilden; b) Unveredelte Si-Phase nur mit rundlichen Al-Clustern.

liquid / solid interface are responsible for changing the growth direction of Si by the formation of crystallographic steps resulting in a coral-like Si microstructure [5, 6]. On the contrary, Fig. 4 (b) presents an example of eutectic Si in the unmodified alloy, where only rounded clusters of Al can be seen. In this case, no formation of nanotwins, stacking faults or other defects is detected. The Si crystal grows anisotropically with a highest growth rate in the ⟨112⟩ orientation and the slowest perpendicular to (111) planes [11].

fläche des Si und sind verantwortlich für die Änderung der Wachstumsrichtung von Si aufgrund der Bildung von kristallographischen Stufen, die zur Ausbildung des korallenartigen Si-Gefüges führen [5, 6]. Im Gegensatz dazu zeigt Bild 4 (b) ein Beispiel von eutektischem Si in der unveredelten Legierung, bei der nur rundliche Cluster von Al zu sehen sind. In diesem Fall konnte keine Bildung von Nanozwillingen, Stapel- oder anderen Fehlern festgestellt werden. Der Si-Kristall wächst anisotrop mit der höchsten Wachstumsrate in der ⟨112⟩-Richtung und der niedrigsten senkrecht zu den (111)-Ebenen [11].

4. Conclusion

The use of phase selective sample preparation by deep etching proved to have an extremely high success rate and yield in APT measurements. The method was applied here for eutectic Si in Al-Si alloys, but can be taken one to one for sample preparation of other alloys to approach metallurgical questions involving specific phases.

4. Schlussfolgerung

Der Einsatz der phasenselektiven Probenpräparation durch Tiefenätzung erbrachte eine extrem hohe Erfolgsrate und Ausbeute bei APT-Messungen. Das Verfahren wurde im vorliegenden Fall bei eutektischem Si in Al-Si-Legierungen angewandt, kann jedoch auch eins zu eins für die Probenpräparation anderer Legierungen verwendet werden, wenn es um metallurgische Fragestellungen und um spezifische Phasen geht.

Acknowledgments

Danksagung

References / Literatur

[1] Miller, M.K.; Forbes, R.G.: Mater. Charact. 60 (2009) 461–469.
DOI: 10.1016/j.matchar.2009.02.007

[2] Gault, B.; Moody, M. P.; Cairney, J. M.; Ringer S. P.: Mater. Today 15 (2012) 378–386.
DOI: 10.1016/S1369-7021(12)70164-5

[3] Thompson, K.; Lawrence, D.; Larson, D. J.; Olson, J. D.; Kelly, T. F.; Gorman, B.: Ultramicroscopy 107 (2007) 131–9.
DOI: 10.1016/j.ultramic.2006.06.008

[4] Gruzleski, J. E.; Closset, B.: The Treatment of Liquid Aluminum-Silicon Alloys, American Foundrymens Society, USA, 1990.

[5] Barrirero, J.; Engstler, M.; Ghafoor, N.; de Jonge, N.; Odén, M.; Mücklich, F.: J. Alloys Compd. 611 (2014) 410–421.
DOI: 10.1016/j.jallcom.2014.05.121

[6] Barrirero, J.; Li, J.; Engstler, M.; Ghafoor, N.; Schumacher, P.; Odén, M.; Mücklich, F.: Scr. Mater. 117 (2016) 16–19.
DOI: 10.1016/j.scriptamat.2016.02.018

[7] Gault, B.; Moody, M. P.; Cairney, J. M.; Ringer, S. P.: Atom Probe Microscopy, Springer New York, NY, 2012.
DOI: 10.1007/978-1-4614-3436-8

[8] Müller, E.: Phys. Rev. 102 (1956) 618–624.
DOI: 10.1103/PhysRev.102.618

[9] Vurpillot, F.; Bostel, A.; Blavette, D.: Appl. Phys. Lett. 76 (2000) 3127.
DOI: 10.1063/1.126545

[10] Felfer, P. J.; Gault, B.; Sha, G.; Stephenson, L.; Ringer, S. P.; Cairney, J. M.: Microsc. Microanal. 18(2) (2012) 359–364.

[11] Hellawell, A.: Prog. Mater. Sci. 15 (1970) 3–78.
DOI: 10.1016/0079-6425(70)90001-0

Jenifer Barrirero

did a joint European master in materials science at Saarland University and the Polytechnic University of Catalonia. She is currently part of a joint Phd program at Saarland University and Linköping University and specializes on the study of eutectic modification in Al-Si casting alloys. She leads the Atom Probe Tomography group at the Chair of Functional Materials, Saarland University.

Michael Engstler

studied Material Science and Engineering at Saarland University in Saarbrücken. He is currently PhD-student at the Institute for Functional Materials at Saarland University and heads the 3D Microstructure Research Group. He is also project leader at the Steinbeis Material Engineering Center Saarland (MECS) in Saarbrücken.